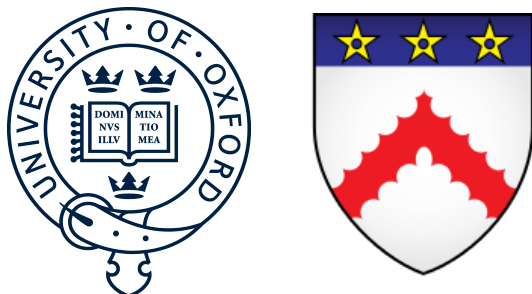


**First Measurement of Reactor Antineutrinos in  
Scintillator at SNO+ and Study of Alternative Designs for  
Large-Scale Liquid Scintillator Detectors**

Iwan Morton-Blake

A thesis presented for the degree of  
*Doctor of Philosophy*



Keble College  
University of Oxford

Michelmas 2021

To my parents

## Abstract

This thesis presents the first measurement of oscillation in antineutrinos from nuclear reactor cores, detected in liquid scintillator at SNO+. The small cluster of reactor cores along the Canadian-American border creates a distinct oscillated antineutrino energy spectrum, from which oscillation parameter values can be extracted. A likelihood analysis is presented, measuring the sensitivity to neutrino oscillation parameter  $\Delta m_{21}^2$  based on 100 tonne-years exposure. The Covid-19 pandemic forced a halt of the SNO+ scintillator fill, however stable data was recorded over 127 days in an approximately half-full detector. BiPo214 coincidence pairs provided an in-situ calibration of the LAB + 0.5g/L PPO scintillator cocktail. The reduced scintillator volume and livetime in the partially filled detector lead to limited sensitivity to the neutrino oscillation parameter  $\Delta m_{21}^2$ . Strong agreement was seen between the 44 events measured in data and the total  $45 \pm 6.7_{\text{stat}}$  events expected due to signal reactor antineutrinos and background geoneutrinos and  $\alpha$ -n. Due to the limited statistics, two values of  $\Delta m_{21}^2$  were favoured,  $8.8_{-1.3}^{+1.1}$  and  $12.6_{-1.3}^{+1.6} \times 10^{-5} \text{ eV}^2$ . The current global PDG value of  $\Delta m_{21}^2 = 7.53 \pm 0.18 \times 10^{-5} \text{ eV}^2$  was found to be within a  $1\sigma$  frequentist confidence interval of the smaller of the best-fit  $\Delta m_{21}^2$  value. Following a successful first measurement of reactor antineutrinos, the analysis will be continued into the fully filled scintillator phases of SNO+. Simulation studies show that a precise measurement of  $\Delta m_{21}^2$  may be possible, where the current global uncertainty (dictated primarily by the KamLAND measurement) can be surpassed in 3-5 years of livetime in the Te-loaded scintillator phase, depending primarily on continued reactor activity and  $\alpha$ -n levels. The uncertainty in  $\Delta m_{21}^2$  impacts the interpretation of neutrino beam experimental results, making its measurement particularly relevant. Also discussed in this work, is a novel design for the next generation of large-scale liquid scintillator detectors (comparable to JUNO in size). The proposed ‘SLIPS’ design may allow for a much more simple and economical construction of large-scale liquid scintillator detectors, potentially impacting a number of areas,  $0\nu\beta\beta$  and solar, supernova and geoneutrinos along with long baseline monitoring of reactors. Potential detector designs are discussed, with simulation studies demonstrating the possible quality of event reconstruction.

# Acknowledgements

I would first like to thank my supervisor Steve Biller, for all the knowledge and advice he was able to share, but equally, having the ability to crack a good joke with (as well of course put up with my occasionally crude language). My thanks to Armin Reichold, who could always lighten the mood and give sound advice towards any difficulties inside and out of PhD work (and has influenced me to greet people with ‘Howdy doody’). Jeff Tseng always provided an opportunity for fun conversation, and none can compare to him and his ability in preventing group meetings from doubling in duration due to some physics-related dispute.

I was enormously lucky to have shared an office with Esther Turner, Tereza Kroupová, Jia-Shian Wang and Josie Paton. I’m glad to be able to call them proper friends, sharing many laughs and gaffs inside and out of the workplace. Esther and Tereza have become shining lights in my life and I have come to cherish the streak of Zoom weekly chats with them since the beginning of the lockdowns, it has to be some kind of world record. Jeffrey Lidgard will always be one of my favourite people, but combination of apple pie dipped in a McFlurry is not, and will never be, ‘a thing’. I am appreciative of Ed Leming, Billy Liggins and Jack Dunger, for putting up with my puppy-dog energy in my first year and for all they were able to share. I have formed fond memories of the time spent in frozen tundra of Sudbury, thanks especially to the folk I got to spend it with, Michal Rigan, Rhea Gaur, Vinny Albanese, Cindy Lin, Ben Tam and Leon ’KFC’ Pickard.

I was able to live with Kla Karava (just about) while we were all confined to our homes, and for all those filming practice shoots, he best include me in the credits of one of his future films. I am very appreciative of Angela Wu for the lifetime’s worth of friendship, as well as all the assistance and companionship over the difficult periods of lockdowns combined with thesis writing. I will also always care for the folks from back home (even if I don’t show it directly) in Emmet Byrne, Naiyie Lamb, Yashaswi Nalawade and Brendan Griffin, who’ve consistently kept me grounded and reminded me what being home-sick feels like.

Lastly but not leastly, I’d like to thank my parents, for just about everything in life, I cannot thank you enough (let me buy you lunch or something sometime).

# Table of Contents

<b>1</b>	<b>Introduction</b>	<b>8</b>
1.1	The Neutrino . . . . .	8
1.1.1	Neutrino Mass - Beyond the Standard Model . . . . .	10
1.2	Neutrino Oscillation in a Vacuum . . . . .	12
1.2.1	CP violation . . . . .	16
1.2.2	Two Neutrino Example . . . . .	17
1.3	Oscillation in Matter . . . . .	17
1.4	Neutrino Oscillation Experiments . . . . .	21
1.4.1	Mass Hierarchy Uncertainty . . . . .	22
1.4.2	Experimentally Accessing Mixing Matrix Components . . . . .	22
1.4.2.1	Solar Oscillations . . . . .	23
1.4.2.2	Atmospheric/Accelerator Oscillations . . . . .	23
1.4.2.3	Reactor Oscillations . . . . .	25
1.4.2.4	Current Measurements of $\Delta m_{21}^2$ . . . . .	27
1.4.3	The KamLAND and SNO+ Reactor Antineutrino Analyses . . . . .	28
<b>2</b>	<b>The SNO+ Experiment</b>	<b>31</b>
2.1	The SNO+ Detector . . . . .	31
2.2	SNO+ Experimental Phases . . . . .	34
2.3	Optics . . . . .	36
2.3.1	Water Phase - Cherenkov Radiation . . . . .	36
2.3.2	Liquid Scintillator Phases - Scintillation . . . . .	37
2.3.2.1	SNO+ Scintillator cocktail . . . . .	39
2.3.2.2	Scintillation Time Emission Profile . . . . .	41
2.3.2.3	Scintillator Quenching . . . . .	42
2.4	Differences Between Water and Scintillator . . . . .	42
2.4.1	Addition of Te . . . . .	43
2.5	PMTs . . . . .	44
2.6	Data Acquisition System . . . . .	46

---

## TABLE OF CONTENTS

---

2.6.1	Global Triggers . . . . .	47
2.6.2	Instrumentals . . . . .	48
2.6.3	Detector Runs . . . . .	48
2.7	Detector Calibration . . . . .	49
2.7.1	Optical Calibration . . . . .	49
2.7.1.1	Laserball . . . . .	49
2.7.1.2	ELLIE Systems . . . . .	50
2.7.2	Radioactive Calibration Sources . . . . .	50
2.7.2.1	N16 . . . . .	50
2.7.2.2	AmBe . . . . .	51
2.7.3	Cover Gas System . . . . .	51
2.8	Event Simulation . . . . .	51
<b>3</b>	<b>Event Reconstruction</b>	<b>53</b>
3.1	Position and Time Fit . . . . .	53
3.1.1	Time Residuals . . . . .	53
3.1.2	Event Position and Time Reconstruction . . . . .	54
3.2	Direction (Water Phase) . . . . .	56
3.3	Energy Fit . . . . .	57
3.4	Light Yield Across the Phases . . . . .	58
3.5	Beyond Position and Energy . . . . .	59
<b>4</b>	<b>In-Situ Measurement of BiPo214 and Scintillator Calibration in the Partial Fill Phase</b>	<b>61</b>
4.1	BiPo214 Event Rates in the Partial Fill Phase . . . . .	61
4.1.1	$^{238}\text{U}$ and $^{232}\text{Th}$ Decay Chains . . . . .	62
4.1.2	Tagging BiPo214 during the Partial Fill Phase . . . . .	64
4.1.2.1	Analysis Cuts . . . . .	65
4.1.2.2	BiPo214 Sample Purity - Accidental Contamination .	65
4.2	Scintillator Supported Contamination Measurement in the Partial Fill . . .	67
4.2.1	Separation from External $^{222}\text{Rn}$ . . . . .	67
4.2.2	Partial Fill Result . . . . .	68

---

## TABLE OF CONTENTS

---

4.2.3	Rn Leaking: Evolution in Time and Space . . . . .	70
4.2.3.1	Motivation for Positional Cuts . . . . .	71
4.2.4	BiPo214 Rate Measurement Conclusion . . . . .	72
4.3	Scintillation Emission Calibration with BiPo214 . . . . .	73
4.3.1	Scintillator Emission Prior to Calibration with BiPo214 . . . . .	74
4.3.1.1	Assumed Other Optical Parameters . . . . .	75
4.3.2	Results of Scintillator Emission Time Tuning . . . . .	76
4.3.3	Discrepancies Between In-Situ and Benchtop Measurements . . . . .	77
4.4	Position Reconstruction Post-Calibration . . . . .	79
4.5	Calibration of Light Yield and $\alpha$ Quenching from BiPo214 events . . . . .	81
4.5.1	Results of Light Yield Parameter Tuning . . . . .	82
4.5.2	Position Dependent Energy Corrections for the Reactor Antineutrino Analysis . . . . .	84
4.5.2.1	Method . . . . .	86
4.5.2.2	Result of Energy Corrections . . . . .	86
4.6	Conclusion . . . . .	87
<b>5</b>	<b>Reactor Antineutrino Signal Calculation</b>	<b>89</b>
5.1	Antineutrino Emission in Nuclear Fission . . . . .	89
5.1.1	Nuclear Reactor Fuel . . . . .	89
5.1.1.1	Radioisotope Emission Spectra . . . . .	90
5.1.1.2	Reactor Types - Fuel Composition . . . . .	91
5.1.2	Reactor Thermal Powers . . . . .	92
5.1.2.1	Time Variation . . . . .	93
5.2	Neutrino Propagation . . . . .	94
5.3	Inverse Beta Decay . . . . .	94
5.3.1	The IBD Interaction Process in Liquid Scintillator . . . . .	95
5.3.1.1	Positron Energy . . . . .	96
5.3.2	Inverse Beta Decay Cross Section . . . . .	97
5.3.3	Target Protons in the Scintillator . . . . .	98
5.4	Expected Reconstructed Energy Spectrum . . . . .	98

---

## TABLE OF CONTENTS

---

<b>6 Reactor Antineutrino Signal Extraction</b>	<b>100</b>
6.1 Dataset and Livetime . . . . .	100
6.2 Antineutrino Coincident Pair Event Selection . . . . .	101
6.2.1 Position and Time Correlation . . . . .	101
6.2.2 Coincidence Pair Analysis Cuts . . . . .	102
6.2.2.1 Correction Factors for Energy Cuts . . . . .	102
6.3 Backgrounds . . . . .	103
6.3.1 Correlated Background: Geoneutrinos . . . . .	103
6.3.1.1 Expected Geoneutrino Flux . . . . .	104
6.3.2 Correlated Background: $\alpha$ -n . . . . .	106
6.3.2.1 $\alpha$ -n Prompt Energy Spectrum . . . . .	107
6.3.2.2 $^{210}\text{Po}$ Rate . . . . .	108
6.3.2.3 $\alpha$ to $\alpha$ -n Conversion . . . . .	109
6.3.2.4 $^{13}\text{C}(\alpha, n)^{16}\text{O}$ Spectrum Shape . . . . .	111
6.3.2.5 Surface $\alpha$ -n events . . . . .	113
6.3.3 Uncorrelated Background - Accidental s . . . . .	114
6.3.3.1 Accidental Rate Contamination Calculations . . . . .	114
6.3.3.2 BiPo214 Removal - Accidental s . . . . .	115
6.3.4 Atmospherics . . . . .	116
6.3.4.1 Atmospheric Neutrinos . . . . .	116
6.3.4.2 Muon Induced Backgrounds . . . . .	117
6.3.4.3 Removal of Atmospheric-Induced Antineutrino Candidates . . . . .	119
6.4 Measured Antineutrino Candidates in Partial Fill . . . . .	120
6.4.1 Conclusion . . . . .	122
<b>7 Results - Sensitivity Analysis</b>	<b>123</b>
7.1 Energy Spectrum Likelihood Framework . . . . .	123
7.1.1 Pdf Generation . . . . .	123
7.1.1.1 Oscillating Reactor Reconstructed Energy Spectra . . . . .	124
7.1.2 Binned Likelihood Expression . . . . .	125

---

## TABLE OF CONTENTS

---

7.1.2.1	Pdf Distortion: Systematic Uncertainties . . . . .	126
7.1.3	Test Statistic - Profile Likelihood Calculation . . . . .	128
7.1.3.1	Wilks' Theorem . . . . .	129
7.2	Systematics . . . . .	130
7.2.1	Calculation of Energy Scaling and Smearing Systematics . . . . .	130
7.2.2	Summary of Likelihood Nuisance Parameters . . . . .	131
7.2.2.1	Nuisance Parameter Summary . . . . .	133
7.3	Likelihood Fitting Results . . . . .	134
7.3.1	Bayesian vs Frequentist Confidence Intervals . . . . .	137
7.3.2	Nuisance Parameters . . . . .	137
7.3.3	Conclusion . . . . .	138
<b>8</b>	<b>Future Sensitivity and <math>\alpha</math>-n Discrimination</b>	<b>139</b>
8.1	SNO+ Oscillation Sensitivity in Future Phases . . . . .	139
8.1.1	Asimov Dataset Generation . . . . .	140
8.1.2	Oscillation Parameter Sensitivity . . . . .	141
8.1.2.1	Assumed Backgrounds and Systematics . . . . .	142
8.1.3	Geoneutrino Sensitivity . . . . .	144
8.2	$\alpha$ -n Event Classification . . . . .	145
8.2.1	Pulse Shape Discrimination - Time Residuals . . . . .	146
8.2.2	$\alpha$ -n Discrimination : Proton Recoils vs Positrons . . . . .	146
8.2.2.1	Origins of Differences in Simulated Time Residuals . . . . .	147
8.2.3	$\alpha$ -n/IBD Classifier: Likelihood and Fisher Discriminant . . . . .	149
8.2.3.1	Likelihood Ratio . . . . .	150
8.2.3.2	Fisher Discriminant . . . . .	150
8.2.4	$\alpha$ -n and IBD Separation Prospects . . . . .	152
8.2.5	Conclusion . . . . .	153
<b>9</b>	<b>Stratified LIquid Plane Scintillator - SLIPS Detector</b>	<b>155</b>
9.1	Current Liquid Scintillator Detector Designs . . . . .	155
9.2	SLIPS Detector Design . . . . .	156
9.3	Detector Simulation . . . . .	157

---

## TABLE OF CONTENTS

9.3.1	PMTs . . . . .	158
9.3.2	Simulated Liquid Scintillator and Buffer Liquid . . . . .	159
9.4	Performance Testing in Simulation . . . . .	160
9.4.1	Light Yield . . . . .	160
9.4.2	Position Reconstruction . . . . .	161
9.4.2.1	Vertical Position Determination with PMT Hit Times .	162
9.4.2.2	Reconstruction using PMT Hit Densities . . . . .	165
9.4.3	Faster Scintillators & Faster PMTs . . . . .	166
9.4.4	Light Collecting Concentrators . . . . .	167
9.5	Alternative SLIPS Detector Shape . . . . .	169
9.5.1	Cuboid Detector Minimum Width . . . . .	170
9.6	Conclusion . . . . .	170
<b>10</b>	<b>Conclusion</b>	<b>172</b>
<b>Appendix A</b>	<b>Neutrino Mass</b>	<b>173</b>
A.1	Neutrino Mass Scale . . . . .	173
A.2	Neutrino Mass . . . . .	173
A.2.1	Dirac Neutrinos . . . . .	174
A.2.2	Majorana Neutrinos . . . . .	175
A.2.3	Dirac-Majorana Mixing . . . . .	177
A.2.3.1	The Seesaw Mechanism . . . . .	179
A.3	Neutrino-less Double Beta Decay . . . . .	180
A.3.1	Double Beta Decay . . . . .	180
<b>Appendix B</b>	<b>Measurement of the SNO+ Ropes Background in the Water Phase</b>	<b>183</b>
B.1	Background Events Originating from the Ropes . . . . .	184
B.2	Method to Isolate Rope Events . . . . .	185
B.2.1	Positional and Energy Cuts . . . . .	186
B.2.2	The Stacking Method . . . . .	189
B.2.2.1	Approach to Non-rope Backgrounds . . . . .	190
B.2.3	Constraining the Non-rope Backgrounds . . . . .	192

---

**TABLE OF CONTENTS** 0.0

B.2.4	Results . . . . .	194
B.2.5	Calculation of Systematic Uncertainties . . . . .	195
B.2.5.1	Further checks of stacking method in data . . . . .	198
B.2.6	Conclusion . . . . .	202
<b>Appendix C Reactor Core Information</b>		<b>203</b>
<b>Appendix D IBD Cross Section</b>		<b>204</b>

# Thesis Outline

This thesis is organised as follows:

**Chapter 1** — A whistle-stop tour of the history of the neutrino, introductions to the theory behind neutrino oscillations and the current status of neutrino experiments.

**Chapter 2** — SNO+, the different phases of the experiment and an introduction to the detector and its components.

**Chapter 3** — Summary of the methods used to reconstruct key parameters of the events that trigger the SNO+ detector, in both the water and scintillator phases.

**Chapter 4** — Measurement of the supported concentration  $^{222}\text{Rn}$ , from the  $^{238}\text{U}$  chain in the partial fill scintillator phase, using BiPo214 events. Also shown is the calibration of the scintillator's emission times and light yield, also using BiPo214, for  $\alpha$  and  $\beta$  particles.

**Chapter 5** — Chronicle of the calculations used to calculate the expected antineutrino energy spectrum at SNO+.

**Chapter 6** — The analysis methods used to extract signal reactor antineutrino events from the partial fill data. Also shown, are the calculations of the background contamination in the reactor antineutrino analysis, namely  $\alpha$ -n and geoneutrinos.

**Chapter 7** — Results of the reactor antineutrino analysis, showing fits of the antineutrino energy spectrum and the sensitivity to oscillation parameters  $\Delta m_{21}^2$  and  $\theta_{12}$ .

**Chapter 8** — Prospects of the antineutrino analysis continued in the fully filled scintillator phases of the experiment.

**Chapter 9** — Presentation of the ‘SLIPS’ large-scale liquid scintillator detector and its performance in simulation.

**Appendix A** — Introduction to the theory behind Dirac and Majorana neutrinos and the mechanisms behind their mass, leading to the search for neutrino-less dou-

ble beta decay in the SNO+ experiment.

**Appendix B** — Background analysis carried out in the water phase, applying a novel method to extract the contamination present in the SNO+ ropes system.

**Appendix C** — Summary of the reactor core information used in the partial fill reactor antineutrino analysis.

**Appendix D** — Summary of the IBD cross-section calculation used to calculate the reactor and geo-antineutrino interaction rates in liquid scintillator.

# List of Figures

1.1	Neutrino Scattering - Oscillation in Matter . . . . .	17
1.2	MSW Resonance Demonstration . . . . .	21
1.3	Neutrino Mass Hierarchy . . . . .	22
1.4	Reactor Spectrum Weighted Survival Probability . . . . .	26
1.5	Antineutrino Survival Probability vs Energy . . . . .	27
1.6	JUNO Antineutrino Energy Spectrum Signal . . . . .	27
1.7	Precision Measurement of Neutrino Oscillation Parameters with KamLAND . . . . .	29
1.8	Nuclear Reactors Surrounding SNO+ . . . . .	30
2.1	SNOLAB Location and Depth . . . . .	32
2.2	Schematic and Photograph of the SNO+ Detector . . . . .	32
2.3	SNO+ Phases . . . . .	34
2.4	Photo of SNO+ water-scintillator interface . . . . .	35
2.5	Sketch of Cherenkov Radiation . . . . .	37
2.6	Sketch of delocalised pi-bonds in benzene . . . . .	38
2.7	Sketch of Scintillator Molecule Energy Levels . . . . .	39
2.8	Molecular Structure of LAB and PPO. . . . .	41
2.9	Absorption and Emission spectra for the SNO+ scintillator cocktail . . . . .	41
2.10	Schematics of the r1408 Hamamatsu Photomultiplier Tube . . . . .	44
2.11	The measured r1408 Hamamatsu PMT transit time distribution . . . . .	45
2.12	r1408 Hamamatsu PMT efficiency and charge spectrum . . . . .	46
3.1	Key Refractive Indices in SNO+ . . . . .	55
3.2	Demonstration of Time Residuals . . . . .	55
3.3	Water Direction Fit PDF . . . . .	57
3.4	Nhits vs Electron Energy . . . . .	58
4.1	$0\nu\beta\beta$ Energy Spectrum Region of Interest . . . . .	62
4.2	Uranium and Thorium Decay Chains . . . . .	63

4.3	$^{214}\text{Bi}$ and $^{212}\text{Bi}$ Decay Chains . . . . .	63
4.4	BiPo214 Nhits Spectra and Time Residuals in Partial Fill Data . . . . .	66
4.5	BiPo214 $\Delta t$ distribution . . . . .	66
4.6	BiPo214 Rn Exponential Decay Fit . . . . .	68
4.7	Partial Fill Daily BiPo214 Rate vs Time . . . . .	70
4.8	$^{214}\text{Bi}$ ( $\beta$ ) and $^{214}\text{Po}$ ( $\alpha$ ) time residuals . . . . .	77
4.9	$^{214}\text{Bi}$ time residuals vs z . . . . .	78
4.10	$^{214}\text{Bi}$ time residuals vs radius . . . . .	79
4.11	radial distances between $^{214}\text{Bi}$ and $^{214}\text{Po}$ events . . . . .	80
4.12	Distances in x, y and z position between $^{214}\text{Bi}$ and $^{214}\text{Po}$ events . . . . .	80
4.13	BiPo214 Nhit Spectra Pre-calibration . . . . .	82
4.14	Data/simulation median nhits ratio vs position following the update to light yield . . . . .	83
4.15	Energy reconstruction following light yield updates . . . . .	84
4.16	$^{214}\text{Bi}$ reconstructed energy distributions . . . . .	85
4.17	$^{214}\text{Bi}$ reconstructed energy distributions following the position-dependent $^{214}\text{Bi}$ energy scaling . . . . .	85
4.18	Energy scaling corrections to $^{214}\text{Bi}$ and $^{214}\text{Po}$ . . . . .	87
5.1	Reactor Fuel Antineutrino Emission Spectra . . . . .	91
5.2	The Inverse Beta Decay Interaction . . . . .	95
5.3	IBD Feynman diagram . . . . .	97
5.4	Flux Cross Section Product . . . . .	97
5.5	1 year Asimov dataset for reactors and geoneutrinos . . . . .	99
6.1	$\Delta t$ and $\Delta r$ distributions for simulated reactor antineutrino events . . . . .	102
6.2	Geoneutrino U and Th Emission Spectra . . . . .	105
6.3	Partial fill Asimov dataset of reactor antineutrinos and geoneutrinos . . . . .	106
6.4	Pdf and sketch of $\alpha$ -n interaction . . . . .	108
6.5	Low energy peak fit for the $^{210}\text{Po}$ rate . . . . .	109
6.6	$\alpha$ capture on $^{13}\text{C}$ cross section . . . . .	110
6.7	Partial fill Asimov dataset of reactors, geoneutrinos and $\alpha$ -n . . . . .	111

6.8	$\alpha$ -n Neutron Energy Spectrum	113
6.9	Accidental event energy distribution	116
6.10	Antineutrino candidates in partial fill data	121
7.1	Example of energy scaling and smearing systematic	127
7.2	Evolution of energy reconstruction with time	132
7.3	Partial fill spectral fit for $\Delta m_{21}^2$ and $\theta_{12}$	136
7.4	Bayesian contours in $\Delta m_{21}^2$ and $\theta_{12}$	137
8.1	1 year Te-loaded scintillator phase Asimov dataset	140
8.2	Te-loaded scintillator $\Delta m_{21}^2$ and $\theta_{12}$ sensitivity	141
8.3	$\Delta m_{21}^2$ sensitivity vs time	142
8.4	$\alpha$ -n impact to $\Delta m_{21}^2$ sensitivity	143
8.5	Sensitivity to geoneutrinos in 1 year of Te scintillator	145
8.6	Time residual pdfs in partial fill for positrons and proton recoil	147
8.7	Sketch of energy deposition for IBD and $\alpha$ -n events	148
8.8	Event size for IBD and $\alpha$ -n events	149
8.9	Likelihood and Fisher test statistic separation of $\alpha$ -n and IBD events	150
8.10	ROC curves for likelihood ratio and Fisher discriminant in partial fill	151
9.1	Designs of some recent, current and future scintillator detectors	156
9.2	3d rendering of the SLIPS detector	157
9.3	SLIPS Detector Dimensions	158
9.4	r12860 Hamamatsu PMT quantum efficiency	160
9.5	SLIPS light yield vs position	161
9.6	PMT hit times vs PMT position	162
9.7	Vertical position fits using PMT hit times	164
9.8	PMT hit density plots vs horizontal displacement	165
9.10	Faster PMTs and scintillator wavefront resolution	167
9.11	HepRep renderings of light concentrators	169
9.12	Hit times with concentrators	169
9.13	Cuboid SLIPS Detector 3D renderings	170

9.14 Pancake vs Cuboid Comparison: PMT Hit Times vs Position . . . . .	171
A.1 Double Beta Decay Isobars . . . . .	180
A.2 $0\nu\beta\beta$ Feynman Diagram . . . . .	181
A.3 Effective Majorana Mass . . . . .	181
A.4 $0\nu\beta\beta$ Spectrum Sketch . . . . .	182
B.1 Drawings of the SNO+ ropes . . . . .	185
B.2 side-on view of AV . . . . .	187
B.3 $\vec{u}.\vec{r}$ distributions . . . . .	188
B.4 Top-down view of AV with Hd ropes . . . . .	188
B.5 Histograms of $\phi$ using reconstructed events, in simulations . . . . .	189
B.6 top-down view of a portion of the detector around the equator of the AV .	189
B.7 Total Simulated Summed Rope Peaks in $\phi$ . . . . .	190
B.8 Peak Integral Demo . . . . .	191
B.9 Non-rope Backgrounds Stacking in $\phi$ . . . . .	193
B.10 Data and simulation Results for stacked $\phi$ . . . . .	195
B.12 Data/simulation peak integral ratio vs $E_{\min}$ . . . . .	199
B.14 Stacking in $\phi$ for data, around the bottom hemisphere region of the detector	201
B.15 Stacking in $\phi$ $E_{\min} = 3.1\text{MeV}$ . . . . .	201

# 1 | Introduction

## 1.1 The Neutrino

The neutrino and its properties have been under the microscope of physicists since their existence was first postulated by Wolfgang Pauli in 1930. Pauli proposed the existence of a spin-half, neutral, weakly interacting particle to rectify the apparent non-conservation of energy and angular momentum suggested in measurements of a continuous  $\beta$ -decay energy spectrum [1]. Following James Chadwick's discovery of a much more massive neutral particle (later appointed as the neutron) [2], the neutral particle discovered by Pauli was famously labelled by Enrico Fermi as the neutrino [3].

Fermi would soon develop his theory of weak interactions, successfully interpreting the continuous  $\beta$ -decay energy spectrum [4]. Fermi modelled the weak interaction involved in the decay of a neutron to a proton  $n \rightarrow p + e^- + \nu_e$ , as a 4-fermion vertex interaction, denoting the strength of the vertex interaction with Fermi's coupling constant  $G_F$ . Pauli had commented on his proposal of a neutral weakly interacting, tiny mass particle as being something 'no theorist should ever do', presuming it was so weakly interacting that it would be impossible to experimentally measure.

Wang Ganchang in 1942 proposed inverse beta decay ( $\bar{\nu} + p \rightarrow n + e^+$ ) as a method for their detection [5]. Neutrinos were eventually first experimentally measured by Clyde Cowan and Fred Reines in 1956, measuring  $\bar{\nu}_e$  events in a liquid scintillator detector situated beside a nuclear reactor core [6]. Reactor cores provided a large source of antineutrinos due to nuclear fission interactions occurring at sufficiently large rates to overcome the tiny neutrino interaction cross section.

Also 1956 Tsung-Dao Lee and Chen-Ning Yang proposed the need to investigate if there was violation of parity in weak interactions, having calculated parity violation in the decay of  $K$  mesons (known as the  $\theta - \tau$  puzzle at the time) [7]. Parity violation in weak interactions was famously verified in experiment by Chien-Shiung Wu and collaborators, measuring  $\beta$ -decay of aligned  $^{60}\text{Co}$  nuclei, in the same year as the Lee and Yang literature review [8]. Richard Garwin and Leon Lederman also alternatively measured in 1957,

parity violation in the decay of polarised muon beams [9].

Following the discovery of parity violation in weak interactions, the modelling of the interactions using a V-A theory maximally violating parity [10], was developed in 1958 by Richard Feynman and Murray Gell-Mann [11], Ennackal Sudarshan and Robert Marshak [12] and J.J. Sakurai [13]. Lev Landau [14], Lee and Yang [15], and Abdus Salam [16] incorporated V-A theory into the lepton sector and described the neutrino's role in weak interactions, proposing the ‘two-component theory of massless neutrinos’. The theory proposed that neutrinos are massless and only have left-hand chiral components and antineutrinos right-hand chiral, allowing for V-A interactions. In 1958, Goldhaber, Grodzins and Sunyar measured the helicity of neutrinos in electron capture experiments [17]. The result was found to agree with the massless two-component neutrino theory, measuring neutrinos within measurement uncertainties, to have 100% negative helicity i.e. spins anti-aligned with their momentum.

The single neutrino particle known up to this point was later found to be part of a family of neutrino flavours, where the Cowan and Reines experiment had measured the electron neutrino  $\nu_e$ . The muon neutrino  $\nu_\mu$  was first experimentally measured in 1962 by Lederman, Schwartz and Steinberger [18], while the tau neutrino  $\nu_\tau$  flavour was eventually measured in 2000 by the DONUT experiment [19]. Shortly after the Cowan and Reines result in 1957, Bruno Pontecorvo presented a theory of oscillation between neutrino and antineutrino, inspired by the first measurement of kaon particle-antiparticle oscillation [20]. Following the measurement of  $\nu_\mu$ , Pontecorvo had completed his theory, allowing for oscillation between two neutrino flavours [21].

The Standard Model of particle physics (SM) was developed through many years of international collaboration between theorists and experimentalists, describing the interactions between fundamental particles and three (of the four) fundamental forces, the electromagnetic, weak and strong forces. The SM is renormalisable, Lorentz invariant and defined by the local gauge invariance of the symmetry group  $SU(3)_C \times SU(2)_L \times U(1)_Y$ , subscripts denoting colour, left-hand chirality and weak hypercharge respectively. The model’s name was coined in 1975 and has been hugely successful in the prediction of experimental data in particle physics, to extreme levels of precision. Focusing on the

role of neutrinos in the SM, the electroweak theory developed by Glashow, Weinberg and Salam [22][23][24] (awarded the Nobel prize in 1979), unified the electromagnetic and weak forces and gave experimentally correct predictions of the weak interaction. The electroweak theory included the presence of a fundamental scalar Higgs field, which allowed for massive gauge bosons and fermions through spontaneous breaking of the  $SU(2)_L \times U(1)_Y$  symmetry. Fermionic fields can be broken down into the left and right chiral states. Due to the parity violation observation in the Wu experiment, only the left-handed  $SU(2)$  doublet components participate in weak interactions, leaving the right-handed components as  $SU(2)$  singlets. It will be seen in section A.2 that fermion masses arise from the coupling between these left and right-handed components, through interactions with the Higgs field. Neutrinos are included in the SM as massless particles [25] and assumes that only left-handed neutrinos exist. The right-handed neutrino is left as a currently hypothetical particle. While the SM was able to describe all the strong and electroweak experimental data to this point, the first experimental delineation from the SM was the discovery of neutrino mass.

### 1.1.1 Neutrino Mass - Beyond the Standard Model

For time evolution and oscillation between neutrino flavours, finite neutrino masses are required. The first measurement that saw the impact of neutrino oscillation was in the Homestake solar neutrino experiment, headed by Ray Davis and John Bahcall, beginning in 1970 using  $^{37}\text{Cl}$  as the detection medium, detecting  $\nu_e$  [26]. The experiment saw approximately a third of the neutrino flux predicted by the solar theoretical model provided by Bahcall. This discrepancy between experiment and theory would be known as the ‘solar neutrino problem’. Anomalies were also seen in the area of atmospheric neutrinos in large Cherenkov neutrino experiments in the late 1980’s. Kamiokande-II [27] and IMB [28] both measured significant deficits in the expected ratio of  $\nu_\mu$  to  $\nu_e$ .

The next breakthrough in the measurement of neutrino oscillation was seen by Super-Kamiokande, a large-scale Cherenkov experiment, measuring to a high degree of accuracy, the asymmetry in the flux  $\nu_\mu$  for those travelling through the Earth compared to those produced in the atmosphere above the detector. The oscillation of  $\nu_\mu \rightarrow \nu_\tau$  was

inferred from the precise measurements [29].

The predecessor to the SNO+ experiment, SNO, would soon follow the Super-Kamiokande result, with a measurement that would solve the solar neutrino problem seen originally in the Homestake experiment by Davis and Bahcall. SNO was the first experiment to definitively demonstrate in 2002 that  $\nu_e$  produced in  $^8\text{B}$  decays in the solar core, undergo flavour transition in the sun, resolving the solar neutrino problem [30][31]. The heavy water target volume, a design proposed by H. Chen [32], allowed for the measurement of the  $\nu_e$  flux through the charged-current (CC) process, along with the total  $\nu$  flux through the neutral current (NC) interaction. Heavy water allowed for both CC and NC interactions with deuterium ( $d$ ):

$$\begin{aligned} \nu_e + d &\rightarrow p + p + e^- \\ \nu_x + d &\rightarrow p + n + \nu_x, \end{aligned} \tag{1.1}$$

where  $\nu_x$  represent the three neutrino flavours ( $\nu_{e/\mu/\tau}$ ). Previous to this, no experiment had sensitivity to all neutrino flavours and relied upon measuring deficits in neutrino flux compared to expectation, to infer neutrino oscillation. The decay of  $d$  produces a neutron ( $n$ ) which is detectable by the  $\gamma$  particle it produces upon capturing on a free hydrogen atom in the detector. In measuring the electron neutrino flux  $\phi_{\nu_e}$  alongside the total neutrino flux  $\phi_\nu$ , the SNO result confirmed the standard solar model and the observable mixing between  $\nu_e$ ,  $\nu_\mu$  and  $\nu_\tau$ .

The KamLAND experiment would subsequently publish a measurement of reactor antineutrinos in 2004, who similarly saw a deficit in the expected  $\bar{\nu}_e$  flux without oscillations [33]. Super-Kamiokande and SNO were recognized with the Nobel Prize in 2015 for their measurements of neutrino oscillation, now providing explanations to  $\nu_e$  flux deficits measured in previous neutrino experiments that were sensitive only to the CC  $\nu_e$  channel.

The discovery of massive neutrinos has shed light on incomplete nature of the Standard Model. As a result, the area of neutrino physics has become a centre of research activity as physicists attempt to find answers to the most basic, yet alluring questions in

physics. How many neutrinos are there? What is the mechanism that gives birth to their mass? Can they explain the matter-antimatter asymmetry in the universe? Might they provide answers for the evidence of dark matter? The reactor antineutrino oscillation analysis presented in this thesis, attempts to eventually assist in answering some of these questions. The primary goal of the SNO+ experiment is to uncover the mechanism that gives rise to the neutrino mass, by searching for the rare neutrino-less double beta decay, discussed further in section A.2. Background rate measurements presented in this work are also expected to contribute towards this eventual goal. The following sections will outline the theoretical groundwork and describe the current experimental status and the motivation for the physics analyses presented in this thesis. Neutrino oscillation and the associated experiments are examined, followed by discussion on the possible neutrino mass mechanisms that allow for neutrino oscillation.

## 1.2 Neutrino Oscillation in a Vacuum

The three known flavours of neutrinos  $\nu_e, \nu_\mu, \nu_\tau$  are each produced, by definition, alongside their charged leptonic partners, the  $e, \mu$  and  $\tau$  particles respectively in CC interactions<sup>1</sup>. Neutrinos can be described by the Lagrangian density:

$$\begin{aligned} \mathcal{L}_\nu \subset & \sum_{\alpha=e,\mu,\tau} [\bar{\nu}_\alpha i\not{\partial} \nu_\alpha + \frac{g_W}{\sqrt{2}} (\bar{\nu}_{\alpha,L} \gamma^\mu e_{\alpha,L} W_\mu^+ + \text{h.c.}) + \frac{g_W}{2 \cos \theta_W} \bar{\nu}_{\alpha,L} \gamma^\mu \nu_{\alpha,L} Z_\mu] \\ & - \sum_{\alpha,\beta=e,\mu,\tau} (m_{\alpha\beta} \bar{\nu}_{\alpha,L} \nu_{\beta,R} + \text{h.c.}) \end{aligned} \quad (1.2)$$

The first three terms are included in the SM, where the first term is the neutrino kinetic term and the second and third describe the coupling of neutrinos to the W and Z gauge bosons, representing the CC and NC interactions respectively. The last term represents the neutrino mass, and so is not a SM term. Mass matrix  $m_{\alpha\beta}$  in general has non-zero off-diagonal terms, such that flavour eigenstates  $\nu_e, \nu_\mu, \nu_\tau$  do not have definite mass. The non-equivalence of flavour eigenstates and neutrino mass eigenstates, allows for neutrino mixing. For the case of a non-diagonal mass matrix, it is possible to diagonalise  $m_{\alpha\beta}$

---

<sup>1</sup>Neutrinos are also produced in the NC weak interactions in  $Z$  boson decays, however these neutrinos are not produced with definite flavour [10]

using two appropriate  $3 \times 3$  unitary matrices  $U$  and  $V$ , yielding  $m_D = \text{diag}(m_1, m_2, m_3)$ :

$$m_D = V^\dagger m U, \quad (1.3)$$

such that neutrino mass eigenstates flavour eigenstates (labelled  $\alpha$ ) can be written in terms of a linear combination of mass eigenstates (labelled  $j$ ):

$$\begin{aligned} \nu_{j,L} &= \sum_\alpha U_{\alpha j}^* \nu_{\alpha,L} \\ \nu_{j,R} &= \sum_\alpha V_{\alpha j}^* \nu_{\alpha,R} \end{aligned} \quad (1.4)$$

Rewriting the Lagrangian for neutrino interactions in 1.2 in terms of mass eigenstates:

$$\begin{aligned} \mathcal{L}_\nu = \sum_{j=1,2,3} [\bar{\nu}_j i \not{\partial} \nu_j + \frac{g_W}{\sqrt{2}} (\bar{\nu}_{j,L} U_{\alpha,j}^* \gamma^\mu e_{\alpha,L} W_\mu^+ + \text{h.c.}) + \frac{g_W}{2 \cos \theta_W} \bar{\nu}_{j,L} \gamma^\mu \nu_{j,L} Z_\mu] \\ - \sum_{j=1,2,3} (m_j \bar{\nu}_{j,L} \nu_{j,R} + \text{h.c.}), \end{aligned} \quad (1.5)$$

it can be seen in the second term of the expression, that a given charged-current interaction may yield a charged lepton and neutrino pair of a certain flavour, where the neutrino is produced as superposition of mass eigenstates. As seen in experiment, there exists interference between mass and flavour eigenstates. Treating neutrino wave functions as plane-waves, the evolution of a massive neutrino state with a well-defined mass  $\nu_j$  can be described using the Schrödinger equation, with a free-particle Hamiltonian  $\mathcal{H}$ . For a neutrino mass eigenstate  $\nu_j$  at time  $t$  and distance  $L$  from its creation point:

$$|\nu_j(t, L)\rangle = \mathcal{H} |\nu_j\rangle = \exp[-iE_j t + ip_j L] |\nu_j\rangle. \quad (1.6)$$

Converting from the mass basis to the flavour basis using equation 1.4, yields the evolution of the flavour eigenstate:

$$|\nu_\alpha(t, L)\rangle = \sum_j U_{\alpha j}^* \exp[-iE_j t + ip_j L] |\nu_j\rangle. \quad (1.7)$$

The energy  $E_j$  and momentum  $p_j$  are defined by the mass of the mass eigenstates, for which the kinematics are well-defined.

Following this, the oscillation probability for the flavour transition  $\alpha \rightarrow \beta$  can be calculated. Final flavour state  $\langle \nu_\beta |$  can be written as a superposition of mass eigenstates  $\langle \nu_\beta | = \sum_j U_{\beta j} \langle \nu_j |$ . The amplitude of measuring a neutrino with flavour state  $\beta$  at time  $t$  and distance  $L$  is:

$$\begin{aligned}\langle \nu_\beta | \nu_\alpha(t, L) \rangle &= \sum_{j,k} U_{\alpha j}^* U_{\beta k} \exp[-iE_j t + ip_j L] \langle \nu_k | \nu_j \rangle \\ &= \sum_j U_{\alpha j}^* U_{\beta j} \exp[-iE_j t + ip_j L],\end{aligned}\tag{1.8}$$

yielding oscillation probability:

$$P_{\alpha\beta}(t, L) = |\langle \nu_\beta | \nu_\alpha(t, L) \rangle|^2 = \sum_{j,k} U_{\alpha j}^* U_{\beta j} U_{\alpha k} U_{\beta k}^* \exp[-i(E_j - E_k)t + i(p_j - p_k)L].\tag{1.9}$$

In the measurement of neutrinos, the precise creation time of the neutrino is an unknown. Integrating over time  $t$  yields the oscillation probability in terms of propagation distance  $L$ :

$$\begin{aligned}P_{\alpha\beta}(L, E) &= \sum_{j,k} U_{\alpha j}^* U_{\beta j} U_{\alpha k} U_{\beta k}^* \exp[i(\sqrt{E^2 - m_j^2} - \sqrt{E^2 - m_k^2})L] \delta(E_j - E_k) \\ &\approx \sum_{j,k} U_{\alpha j}^* U_{\beta j} U_{\alpha k} U_{\beta k}^* \exp[-i\frac{\Delta m_{jk}^2 L}{2E}]\end{aligned}\tag{1.10}$$

where in the second line, a Taylor expansion in the mass square difference and the approximation that the neutrino mass difference is much smaller than the neutrino energy  $|m_j - m_k| \ll E = E_j = E_k$  were applied. This can also be written as:

$$P_{\alpha\beta}(L, E) \approx \left| U \begin{pmatrix} 1 & 0 & 0 \\ 0 & \exp[-i\frac{\Delta m_{21}^2 L}{2E}] & 0 \\ 0 & 0 & \exp[-i\frac{\Delta m_{31}^2 L}{2E}] \end{pmatrix} U^\dagger \right|^2\tag{1.11}$$

The  $3 \times 3$  mixing matrix  $U$  in equation 1.4 transforms between the flavour and mass eigenstates:

$$\begin{pmatrix} \nu_e \\ \nu_\mu \\ \nu_\tau \end{pmatrix} = \begin{pmatrix} U_{e1} & U_{e2} & U_{e3} \\ U_{\mu 1} & U_{\mu 2} & U_{\mu 3} \\ U_{\tau 1} & U_{\tau 2} & U_{\tau 3} \end{pmatrix} \begin{pmatrix} \nu_1 \\ \nu_2 \\ \nu_3 \end{pmatrix} \quad (1.12)$$

For a general  $3 \times 3$  complex matrix, there are 18 real, independent parameters. The unitarity of  $U$  causes the loss of 9 parameters. This can be written in terms of 3 real angles and 6 complex phases. A further 5 complex phases can be removed with field rephasing  $\nu_j \rightarrow e^{i\phi_j} \nu_j$ , where  $\nu_\alpha \rightarrow e^{i\phi_\alpha} \nu_\alpha$  leaves the Lagrangian in 1.2 unchanged. This leaves 4 independent physical parameters, summarised in the Pontecorvo-Maki-Nakagawa-Sakata (PMNS) matrix, with 3 real parameters in the form of mixing angles  $\theta_{12}, \theta_{13}, \theta_{23}$  and 1 complex phase  $\delta_{CP}$  that allows for CP violation. The PMNS mixing matrix is commonly parameterised as:

$$U_D = \begin{pmatrix} 1 & 0 & 0 \\ 0 & c_{23} & s_{23} \\ 0 & -s_{23} & c_{23} \end{pmatrix} \begin{pmatrix} c_{13} & 0 & s_{13}e^{-i\delta_{CP}} \\ 0 & 1 & 0 \\ -s_{13}e^{-i\delta_{CP}} & 0 & c_{13} \end{pmatrix} \begin{pmatrix} c_{12} & s_{12} & 0 \\ -s_{12} & c_{12} & 0 \\ 0 & 0 & 1 \end{pmatrix} \quad (1.13)$$

$$= \begin{pmatrix} c_{12}c_{13} & s_{12}c_{13} & s_{13}e^{-i\delta_{CP}} \\ -s_{12}c_{23} - c_{12}s_{23}s_{13}e^{-i\delta_{CP}} & c_{12}c_{23} - s_{12}s_{23}s_{13}e^{-i\delta_{CP}} & s_{23}c_{13} \\ s_{12}c_{23} - c_{12}c_{23}s_{13}e^{-i\delta_{CP}} & -c_{12}s_{23} - s_{12}c_{23}s_{13}e^{-i\delta_{CP}} & c_{23}c_{13} \end{pmatrix}$$

where  $c_{ij} \equiv \cos \theta_{ij}$  and  $s_{ij} \equiv \sin \theta_{ij}$ . As will be seen in section A.2, neutrinos can be described as Dirac or Majorana particles. In the case that neutrinos are Majorana particles, it is not possible to rephase Majorana fields, as the Majorana mass term is not left invariant under the rephasing of the fields. This leads to extra Majorana phases  $\phi_1$  and  $\phi_2$ . The Majorana mixing matrix is related to the Dirac version in eqn. 1.13 as  $U_M = U_D P_M$ , where  $P_M = \text{diag}(1, e^{i\phi_1}, e^{i\phi_2})$ . That is, in the case that neutrinos are Dirac fermions, phases  $\phi_1$  and  $\phi_2$  are both zero and  $P_M = I$ . These Majorana phases do not produce any observable effect in the measurement of neutrino oscillations [34].

### 1.2.1 CP violation

Due to the existence of complex phase  $\delta_{CP}$ , particle-antiparticle symmetry is violated. The measurable difference due to CP violation can be expressed as the difference in transition probabilities for particles and antiparticles:

$$\Delta P_{\alpha\beta} \equiv P_{\alpha\beta} - P_{\bar{\alpha}\bar{\beta}} \quad (1.14)$$

The transition probability for antineutrinos  $P_{\bar{\alpha}\bar{\beta}}$  is calculated in the same manner as equation 1.10, except the mixing matrix is complex conjugated.  $\Delta P_{\alpha\beta}$  is therefore:

$$\begin{aligned} \Delta P_{\alpha\beta}(L, E) &\approx \sum_{j,k} U_{\alpha j}^* U_{\beta j} U_{\alpha k} U_{\beta k}^* \exp[-i \frac{\Delta m_{jk}^2 L}{2E}] - \sum_{j,k} U_{\alpha j} U_{\beta j}^* U_{\alpha k}^* U_{\beta k} \exp[-i \frac{\Delta m_{jk}^2 L}{2E}] \\ &= \sum_{j \neq k} (U_{\alpha j}^* U_{\beta j} U_{\alpha k} U_{\beta k}^* - U_{\alpha j} U_{\beta j}^* U_{\alpha k}^* U_{\beta k}) \exp[-i \frac{\Delta m_{jk}^2 L}{2E}] \\ &= 2i \sum_{j \neq k} \text{Im}(U_{\alpha j}^* U_{\beta j} U_{\alpha k} U_{\beta k}^*) \exp[-i \frac{\Delta m_{jk}^2 L}{2E}] \end{aligned} \quad (1.15)$$

It can be seen that for a survival measurement oscillation experiment where  $\alpha = \beta$ , then  $\Delta P_{\alpha\beta}(L, E) = 0$ , meaning the oscillation process conserves time symmetry (T) (where initial and final states are exchanged). Assuming CPT symmetry, CP is therefore conserved also, meaning the oscillation process is identical for particles and antiparticles. Eqn. 1.10 was applied in the reactor antineutrino analysis presented in this work.

The quantity in the final line is generally parameterised from the leptonic mixing matrix  $U$  as:

$$J \equiv \text{Im}(U_{\alpha j}^* U_{\beta j} U_{\alpha k} U_{\beta k}^*) = \pm c_{12} s_{12} c_{23} s_{23} c_{13}^2 s_{13} \sin \delta_{CP} \quad (1.16)$$

$J$  is known as the Jarlskog invariant. Its value is only non-zero if all 3 mixing angles are also non-zero.

### 1.2.2 Two Neutrino Example

For the purposes of demonstration it is useful to consider the case that where there are only 2 flavours of neutrino (which can still effectively describe experimental results in certain energy regimes). In the 2-flavour case, for example considering only  $e$  and  $\mu$ , the unitary matrix  $U$  is replaced with a  $2 \times 2$  matrix. Applying the previously discussed constraints on  $U$  yields a single real parameter  $\theta$ . It can be seen that complex phase parameter  $\delta_{CP}$  is a consequence of having 3 neutrino flavours, not appearing for the case of 2 neutrinos. The  $2 \times 2$  version of  $U$  can be parameterised as:

$$U = \begin{pmatrix} \cos(\theta) & \sin(\theta) \\ -\sin(\theta) & \cos(\theta) \end{pmatrix} \quad (1.17)$$

The flavour transition probability in equation 1.10 becomes:

$$P_{e\mu}^{2-\text{flav}}(L, E) = \sin^2(2\theta) \sin^2\left(\frac{\Delta m^2 L}{4E}\right) \quad (1.18)$$

## 1.3 Oscillation in Matter

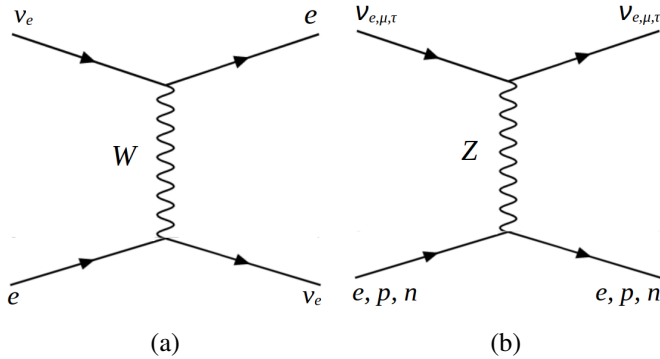


Figure 1.1: Neutrino interactions with matter mediated by the (a) charged current interaction (b) neutral current interaction (with electrons, protons and neutrons).

For neutrinos propagating through matter (e.g. propagating through the Earth, Sun) one must account for interactions with the matter on their journey until their eventual detection. Neutrinos can interact without any momentum transfer with electrons, protons and neutrons through CC and NC interactions. Feynman diagrams summarising these

interactions are shown in figure 1.1. These interactions are both contained in the weak interaction Lagrangian shown in eqn. 1.2. For energies  $E \ll M_W$ , the interaction can be described using the effective Hamiltonian in Fermi's theory of  $\beta$  decay. For the CC interaction, the Hamiltonian can be written as [35]:

$$\mathcal{H}_{\text{eff}}^{CC} = \frac{G_F}{\sqrt{2}} [\bar{\nu}_e \gamma^\mu (1 - \gamma^5) \nu_e] [\bar{e} \gamma^\mu (1 - \gamma^5) e] \quad (1.19)$$

Considering the electrons which neutrinos can interact with in matter as being static, the Hamiltonian used to describe neutrinos' propagation through matter is calculated using the expectation of the electron field  $e$ :

$$\begin{aligned} \mathcal{H}_{\text{eff}}^{CC} &= \frac{G_F}{\sqrt{2}} [\bar{\nu}_e \gamma^\mu (1 - \gamma^5) \nu_e] \langle [\bar{e} \gamma^\mu (1 - \gamma^5) e] \rangle \\ &= \frac{G_F}{\sqrt{2}} [\bar{\nu}_e \gamma^\mu (1 - \gamma^5) \nu_e] \int d^3 p_e f(\mathbf{p}) \frac{1}{2} \sum_s \langle e(\mathbf{p}, s) | \bar{e} \gamma^\mu (1 - \gamma^5) e | e(\mathbf{p}, s) \rangle, \end{aligned} \quad (1.20)$$

summing over electron spins  $s$  and momentum  $\mathbf{p}$ , where  $f(\mathbf{p})$  is the electron momentum distribution normalised to the electron number density:  $\int d^3 p f(\mathbf{p}) = n_e$

The calculation eventually yields:

$$\mathcal{H}_{\text{eff}}^{CC} = V_{CC} \bar{\nu}_e L \gamma^0 \nu_e L, \quad (1.21)$$

where  $V_{CC}$  is the charged current potential:

$$V_{CC} \equiv \sqrt{2} G_F n_e. \quad (1.22)$$

A similar calculation yields the NC potential experienced by a propagating neutrino due to interactions with electrons, protons and neutrons. The contributions due to protons and electrons cancel, leaving the NC potential in terms of the neutron density:

$$V_{NC} \equiv -\frac{1}{\sqrt{2}} G_F n_n \quad (1.23)$$

Armed with the interaction potentials, the impact to neutrino oscillation can be seen in

the calculation of the transition probability by recalling eqn. 1.9:

$$P_{\alpha\beta}(L) = \sum_{j,k} U_{\alpha j}^* U_{\beta j} U_{\alpha k} U_{\beta k}^* \exp[i(\phi_j - \phi_k)] \delta(E_j - E_k) \quad (1.24)$$

The phase  $\phi_j \equiv p_j L$  in the case of vacuum oscillations was previously well-defined by the masses of the neutrinos, whereas in the case of matter interactions, potentials  $V_{CC}$  and  $V_{NC}$  must now be accounted for. The momentum eigenstates can be calculated, assuming  $V \ll H$  as:

$$p \equiv \sqrt{(H - V)^2 - M^2} \approx H - \frac{M^2}{2H} - V \quad (1.25)$$

For the sake of simplicity, the 2-flavour approximation is used onward for demonstration.

Contributions impacting all neutrino flavours equally, i.e. proportional to the identity matrix, do not change the oscillation probability. The interaction potential  $V$  can therefore be written only in terms of the CC component, involving  $\nu_e$  interaction:

$$V \equiv \begin{pmatrix} V_{CC}/2 & 0 \\ 0 & -V_{CC}/2 \end{pmatrix} \quad (1.26)$$

Assuming that  $E$  is equal for all momentum eigenstates:  $H \rightarrow E$ . The momentum eigenstates can be calculated from the diagonalisation of

$$\begin{aligned} & -\frac{\Delta m^2}{4E} \begin{pmatrix} \cos \theta & \sin \theta \\ -\sin \theta & \cos \theta \end{pmatrix} \begin{pmatrix} -\cos \theta & \sin \theta \\ \sin \theta & \cos \theta \end{pmatrix} - \begin{pmatrix} V_{CC}/2 & 0 \\ 0 & -V_{CC}/2 \end{pmatrix} \\ &= \begin{pmatrix} -\frac{\Delta m^2}{4E} \cos 2\theta + V_{CC}/2 & \frac{\Delta m^2}{4E} \sin 2\theta \\ \frac{\Delta m^2}{4E} \sin 2\theta & \frac{\Delta m^2}{4E} \cos 2\theta - V_{CC}/2 \end{pmatrix} \end{aligned} \quad (1.27)$$

The diagonalisation of the  $H$  (subtracting contributions proportional to the identity matrix) allows the oscillation probability to be written in the same form as the 2-flavour oscillation probability in a vacuum, in eqn. 1.18. This can be done by defining  $\Delta m_{\text{eff}}$

and  $\theta_{\text{eff}}$  such that:

$$\begin{aligned} & - \begin{pmatrix} \cos \theta_{\text{eff}} & -\sin \theta_{\text{eff}} \\ \sin \theta_{\text{eff}} & \cos \theta_{\text{eff}} \end{pmatrix} \begin{pmatrix} -\frac{\Delta m^2}{4E} \cos 2\theta + V_{CC} & \frac{\Delta m^2}{4E} \sin 2\theta \\ \frac{\Delta m^2}{4E} \sin 2\theta & \frac{\Delta m^2}{4E} \cos 2\theta \end{pmatrix} \begin{pmatrix} \cos \theta_{\text{eff}} & \sin \theta_{\text{eff}} \\ -\sin \theta_{\text{eff}} & \cos \theta_{\text{eff}} \end{pmatrix} \\ & = \begin{pmatrix} -\frac{\Delta m_{\text{eff}}^2}{4E} & 0 \\ 0 & \frac{\Delta m_{\text{eff}}^2}{4E} \end{pmatrix}, \end{aligned} \quad (1.28)$$

where the effective mass difference along the diagonalised Hamiltonian is:

$$\Delta m_{\text{eff}}^2 = 2E \sqrt{\left( V_{CC} - \frac{\Delta m^2}{2E} \cos 2\theta \right)^2 + \left( \frac{\Delta m^2}{2E} \right)^2 \sin^2 2\theta}, \quad (1.29)$$

and the effective mixing angle which diagonalises the Hamiltonian in matter is

$$\sin 2\theta_{\text{eff}} = \frac{\frac{\Delta m^2}{2E} \sin 2\theta}{\sqrt{(V_{CC} - \frac{\Delta m^2}{2E} \cos 2\theta)^2 + \left( \frac{\Delta m^2}{2E} \right)^2 \sin^2 2\theta}} \quad (1.30)$$

Assuming the electron number density is constant along the path of propagation for a neutrino, equation 1.24 can be written in terms of the effective mass and mixing angles, in the same form as the vacuum form in eqn. 1.18.

$$P_{\alpha\beta}(L) \approx \left| \begin{pmatrix} \cos \theta_{\text{eff}} & \sin \theta_{\text{eff}} \\ -\sin \theta_{\text{eff}} & \cos \theta_{\text{eff}} \end{pmatrix} \begin{pmatrix} \exp[i\frac{\Delta m_{\text{eff}}^2 L}{4E}] & 0 \\ 0 & \exp[i\frac{\Delta m_{\text{eff}}^2 L}{4E}] \end{pmatrix} \begin{pmatrix} \cos \theta_{\text{eff}} & -\sin \theta_{\text{eff}} \\ \sin \theta_{\text{eff}} & \cos \theta_{\text{eff}} \end{pmatrix}_{\alpha\beta} \right|^2 \quad (1.31)$$

The consequence of matter interactions has drastic consequences for the observed effective mixing angle in eqn. 1.30. The Mikheyev-Smirnov-Wolfenstein (MSW) resonance condition occurs when  $\sin 2\theta_{\text{eff}}$  is maximal, irrespective of the vacuum mixing angle value  $\theta$  [36]. Resonance occurs when the electron number density reaches the value of:

$$V_{CC} = \sqrt{2}G_F n_e = \frac{\Delta m^2}{2E} \cos 2\theta \quad (1.32)$$

Figure 1.2 demonstrates the 2-flavour value of  $\sin 2\theta_{\text{eff}}$  for various values of vacuum

mixing angle  $\theta$ , against neutrino energy. The resonance at  $\sim 10\text{GeV}$ , for all values of  $\theta$ , correspond to energies accessible in modern neutrino beam experiments. For the reactor antineutrino analysis presented later in this work, it can be seen for low energy neutrinos (reactor and geo-antineutrinos having energies  $\mathcal{O}(\text{MeV})$ ),  $\sin 2\theta_{\text{eff}} \approx \sin 2\theta$ . Matter interactions were expected to play a negligible role in the SNO+ antineutrino analysis. A calculation of the effect matter interactions have on geoneutrino oscillation measurements is discussed in section 6.3.1.

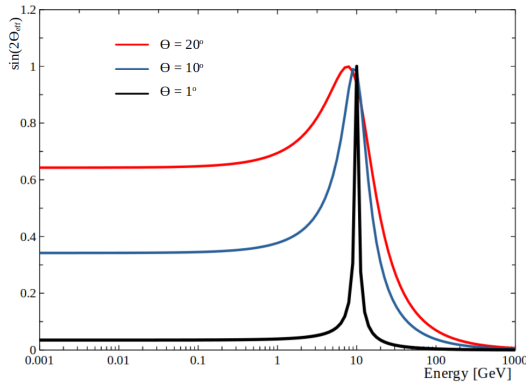


Figure 1.2: Demonstration of the MSW resonance, showing the effective mixing angle against neutrino energy for various values of the vacuum mixing angle. The average upper mantle mass density of  $\sim 3 \text{ g/cm}^3$  was assumed, with  $\Delta m^2 = 2.5 \times 10^{-3} \text{ eV}^2$ .

Matter effects can provide a handle on the sign and magnitudes of neutrino mixing parameters, not accessible in vacuum oscillation measurements. The positive value of interaction potential  $V_{CC}$  for neutrinos, constricts the sign of  $\Delta m^2$ , depending on mixing angle  $\theta$ . Solar neutrinos are impacted by matter interactions as they propagate outwards from the core (where  $\nu_e$  are produced). Matter interactions have also allowed for investigations of the differences between neutrinos and antineutrinos, where the sign of  $V_{CC}$  is reversed for antineutrinos. These experimental measurements have shed light on the sign and orderings of the neutrino masses, discussed in the upcoming sections.

## 1.4 Neutrino Oscillation Experiments

A variety of natural and manufactured neutrino sources, each producing neutrinos over various energy scales, can be detected over various propagation distances (baselines) in order to extract and measure each of theorised neutrino mixing parameters. Experiments

also vary in the manner of the oscillation measurement, whether a survival probability is measured  $P_{\alpha \rightarrow \alpha}$  (disappearance) or the experiment allows for the measurement of flavour transitions  $P_{\alpha \rightarrow \beta}$  (appearance). The next section discusses the current uncertainty in the mass orderings of the 3 neutrino states, named the ‘mass hierarchy’.

### 1.4.1 Mass Hierarchy Uncertainty

The oscillation probability in eqn. 1.10 shows that vacuum oscillation measurements are only sensitive to the absolute magnitude of the mass differences between the neutrino mass states. However, solar neutrino oscillation measurements are impacted by matter interactions and have clarified the sign of  $\Delta m_{21}^2$  as positive, while the sign of  $\Delta m_{31}^2$  has not yet conclusively been measured at the time of writing this thesis.

Figure 1.3 demonstrates the two possible neutrino mass hierarchies due to the unknown sign of  $\Delta m_{31}^2$ . The figure labels  $\Delta m_{32}^2$  and  $\Delta m_{21}^2$  as the atmospheric and the solar mass differences. The next section introduces various neutrino oscillation experiment types, and the parameters to which they are sensitive.

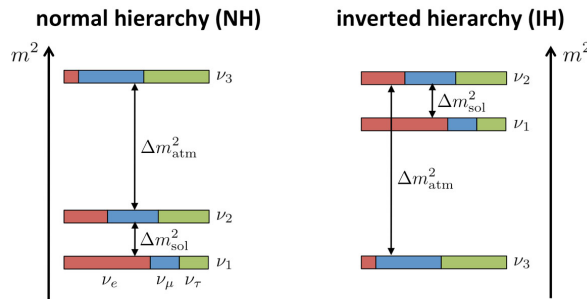


Figure 1.3: Sketch demonstrating the two possible neutrino mass hierarchies. The coloured regions represent the relative proportions each neutrino flavour eigenstates making up each mass eigenstate (the uncertainties in  $\delta_{CP}$  are not shown here, the colour bands only represent approximate flavour proportions). Plot was taken from [37].

### 1.4.2 Experimentally Accessing Mixing Matrix Components

Depending on the approximations allowed for the baseline and energies measured in a given neutrino oscillation experiment, a 2-neutrino picture can provide a meaningful description of the physics and highlight the dominant mixing parameters for which each

experiment type is most sensitive.

#### 1.4.2.1 Solar Oscillations

Considering the PMNS matrix in eqn. 1.13, its complexity can be reduced by the assumption that the value of  $\theta_{13}$  has been measured as very small and can be approximated as zero. Solar fusion reactions in the core provide a source of pure electron neutrinos (and electron antineutrinos due to interactions with the solar magnetic field [38]). Solar neutrinos do not have sufficiently large energies to produce muons upon interaction, therefore solar oscillation experiments aim to measure the disappearance  $\nu_e$  to extract mixing parameters. Defining a new basis of neutrino flavours in terms of the non-electron neutrino flavours  $\nu_\mu, \nu_\tau$ :

$$\begin{pmatrix} \nu_x \\ \nu_y \end{pmatrix} \equiv \begin{pmatrix} c_{23} & -s_{23} \\ s_{23} & c_{23} \end{pmatrix} \begin{pmatrix} \nu_\mu \\ \nu_\tau \end{pmatrix} \quad (1.33)$$

Combining the new basis with the  $\theta_{13} \approx 0$  approximated mixing matrix, yields a mixing matrix describing mixing between  $\nu_e$  and non-electron flavour  $\nu_x$ , dependent only on mixing and  $\theta_{12}$ , moving the mixing to a 2 neutrino flavour picture:

$$\begin{pmatrix} \nu_e \\ \nu_x \\ \nu_y \end{pmatrix} = \begin{pmatrix} c_{12} & s_{12} & 0 \\ -s_{12} & c_{12} & 0 \\ 0 & 0 & 1 \end{pmatrix} \begin{pmatrix} \nu_1 \\ \nu_2 \\ \nu_3 \end{pmatrix} \quad (1.34)$$

It can be seen that solar experiments are dominantly sensitive to  $\Delta m_{21}^2$  and  $\theta_{12}$  (although there is still some sensitivity to  $\theta_{13}$ ).

#### 1.4.2.2 Atmospheric/Accelerator Oscillations

Measurement of higher energy neutrinos allows access to alternate portions of the mixing parameters. Referenced previously, atmospheric neutrinos are high energy neutrino produced in hadronic showers from cosmic ray interactions in the atmosphere. The neutrinos generated in these interactions are primarily in the range of 100 MeV to 10 GeV [39]. The pions produced in these interactions decay into muons, which subsequently yield  $\nu_e$ ,

$\nu_\mu$  and antiparticles:

$$\begin{aligned}\pi^- &\rightarrow \mu^- + \nu_\mu, \quad \pi^+ \rightarrow \mu^+ + \bar{\nu}_\mu \\ \mu^- &\rightarrow e^- + \nu_e, \quad \mu^+ \rightarrow e^+ + \bar{\nu}_e\end{aligned}\tag{1.35}$$

Beams of high energy neutrinos can also be produced artificially in accelerator facilities. High energy pion and muon production facilities can produce a well-controlled source of  $\nu_{e/\mu}$  and their antiparticles. The T2K experiment samples from a neutrino beam produced at the J-PARC proton beam facility, with neutrinos of around 600MeV reaching the Super-Kamiokande far-detector situated approximately 300km away from the beam [40]. The MINOS and NOvA experiments share the NuMI neutrino beam, situated at 735km and 810km from Fermilab, respectively [41][42].

It has been seen already from previous neutrino oscillation experiments that  $\Delta m_{21}^2 \ll \Delta m_{31}^2$ . Regarding again the transition probability matrix in eqn. 1.11, typical accelerator and atmospheric neutrinos energies and baselines comfortably satisfy  $2E \gg \Delta m_{21}^2 L$ , leading to the approximation  $\exp[-i\Delta m_{21}^2 L/2E] \approx 1$ . In doing so, matrix elements in  $U$  can be commuted past the diagonal matrix  $\text{diag}(1, 1, \exp[-i\Delta m_{31}^2 L/2E])$ , cancelling with  $U^\dagger$ . Applying  $\theta_{13} \approx 0$  again, the remaining transition probability depends only on mixing angle  $\theta_{23}$ :

$$P_{\alpha\beta}(L, E) \approx \left| \begin{pmatrix} 1 & 0 & 0 \\ 0 & c_{23} & s_{23} \\ 0 & -s_{23} & c_{23} \end{pmatrix} \begin{pmatrix} 1 & 0 & 0 \\ 0 & \exp[i\frac{\Delta m_{21}^2 L}{2E}] & 0 \\ 0 & 0 & \exp[i\frac{\Delta m_{31}^2 L}{2E}] \end{pmatrix} \begin{pmatrix} 1 & 0 & 0 \\ 0 & c_{23} & -s_{23} \\ 0 & s_{23} & c_{23} \end{pmatrix} \right|^2 \tag{1.36}$$

The 2 flavour picture highlights the dominant sensitivity of atmospheric and long baseline accelerator survival measurements to mixing angle  $\theta_{23}$ .

As mentioned, high energy neutrino beams travelling through the Earth's crust may experience the MSW resonance. Beyond the 2 flavour demonstration, atmospheric and accelerator experiments also have sensitivity to the sign and magnitude of  $\Delta m_{32}^2$  and  $\theta_{13}$ . Beam experiments that can produce  $\nu_\mu$  and  $\bar{\nu}_\mu$  can also access  $\delta_{CP}$ . The T2K and NOvA experiments have made measurements of  $\delta_{CP}$ , where the preferred values from

each measurement currently shows tension. The next generation of long baseline accelerator neutrino experiments, Hyper-K and DUNE, are expected to measure CP-violation conclusively [43][44].

### 1.4.2.3 Reactor Oscillations

Nuclear reactors emit large flux of antineutrinos due to the fission reactions occurring in their cores, discussed in detail in chapter 5. Reactors provide a fixed-distance source of antineutrinos with a well-known energy spectrum and flux.

Expanding the 3 neutrino vacuum transition probability in eqn. 1.10, considering electron neutrino survival  $\bar{\nu}_e \rightarrow \bar{\nu}_e$ :

$$P_{\bar{\nu}_e \rightarrow \bar{\nu}_e}(L, E) = 1 - \cos^4 \sin^2(2\theta_{12}) \sin^2\left(\frac{\Delta m_{21}^2 L}{4E}\right) - \sin^2(2\theta_{13}) [\sin^2(\theta_{12}) \sin^2\left(\frac{\Delta m_{32}^2 L}{4E}\right) + \cos^2(\theta_{12}) \sin^2\left(\frac{\Delta m_{31}^2 L}{4E}\right)] \quad (1.37)$$

The factors proportional to  $L/E$  are often written in terms of units typical of reactor experiment baselines:  $\frac{\Delta m_{ij}^2 L}{4E} = \frac{1267 \Delta m_{ij}^2 [eV^2] L [km]}{E [MeV]}$ .

Using current global PDG measured values for mixing angles, summarised in table 5.3, figure 1.4 shows the survival probability calculated versus reactor baseline distance, applying eqn. 1.37. Survival probabilities at each distance have been weighted according to the expected measurable antineutrino energy spectrum from a PWR type nuclear reactor (see chapter 5). Measurable antineutrinos from reactor cores range in energy approximately 1.8 – 10 MeV. Reactor experiments are separated into two categories depending on the reactor-detector baselines. Marked in figure 1.4 are the points of optimal baselines for short and medium baseline experiments.

**Short Baseline Reactor Experiments** Short baseline reactor experiments are optimal for the measurement of small mixing angle  $\theta_{13}$ . For reactor energies, at short distances  $\mathcal{O}(\text{km})$ , applying the approximation  $\Delta m_{21}^2 L / 4E \ll 1$  to eqn. 1.37 yields a survival

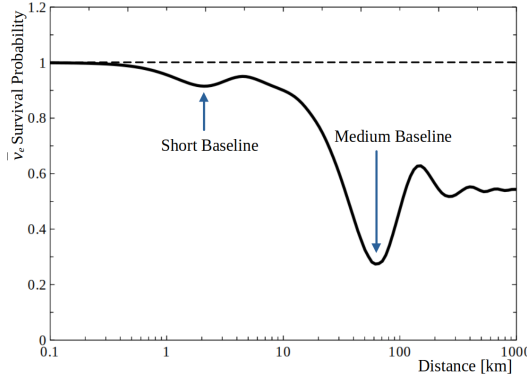


Figure 1.4: Plot of the survival probability using equation 1.37 where the survival probability at each distance was integrated over the expected measurable reactor antineutrino energy spectrum of a PHWR type nuclear reactor (figure 5.4)

predominantly dependent on  $\theta_{13}$ :

$$P_{\bar{\nu}_e \rightarrow \bar{\nu}_e}(L, E) \rightarrow 1 - \sin^2(2\theta_{13})\sin^2(\theta_{12})\sin^2\left(\frac{\Delta m_{ee}^2 L}{4E}\right) \quad (1.38)$$

where  $\Delta m_{ee}^2 = \cos^2(\theta_{12})\Delta m_{21}^2 + \sin^2(\theta_{12})\Delta m_{32}^2$ . The mixing parameters are extracted experimentally by fitting the  $L/E$  distribution measured in data. Figure 1.4 points to the optimal baseline to observe neutrino oscillations dominated by the value of  $\theta_{13}$ . Experiments such as Daya Bay, RENO and Double Chooz have made measurements of this parameter and all occupy the 1–2 km baseline region [45][46][47].

**Medium Baseline Reactor Experiments** Medium Baseline Reactor are more proficient than their small baseline counterparts in the extraction of  $\Delta m_{21}^2$ , with typically smaller sensitivities to  $\theta_{12}$  and  $\theta_{13}$ . This thesis focuses on the measurement of  $\Delta m_{21}^2$  and to a limited extent  $\theta_{12}$  in the SNO+ detector, measuring reactor antineutrinos.

Figure 1.5 displays the  $\bar{\nu}_e$  survival probability against reactor antineutrino energy, for a fixed baseline distance of 240km (the distance between SNO+ and the nearest nuclear reactor). Slow and fast sinusoidal variations are visible in the probability against energy, where the slow component is dictated by the value of small mass difference  $\Delta m_{21}^2$  and fast component decided by the larger  $\Delta m_{32}^2$  (and the assumed mass hierarchy). The small, fast variations in the survival probability cannot be resolved by the current generation of medium baseline reactor experiments. The JUNO experiment aims to measure these

components and resolve the neutrino mass hierarchy problem. JUNO plans to have an energy resolution of at least 3% at 1MeV to achieve this [48]. Figure 1.6 displays the expected JUNO reactor antineutrino energy spectrum, showing the unoscillated signal, with the oscillated spectra assuming NO and IO. The JUNO experiment is being built with a baseline of 53 km to a pair of nuclear reactors, placing it in the optimal region for medium baseline measurements, as seen in figure 1.4.

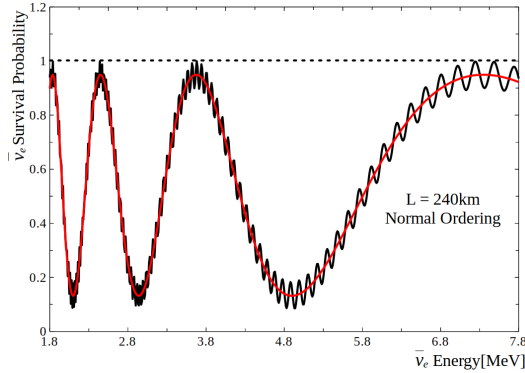


Figure 1.5: Antineutrino survival probability vs energy, assuming a baseline of 240km. The black line represents eqn. 1.37, while the red reflects the approximated version in eqn. 1.39

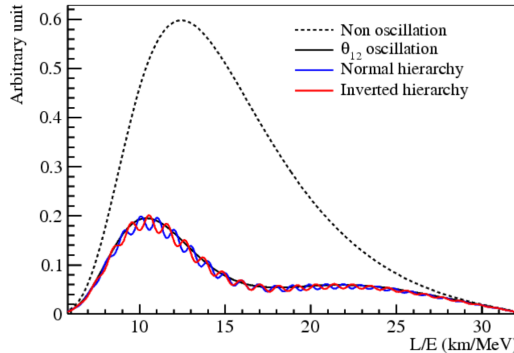


Figure 1.6: The expected antineutrino energy spectrum at JUNO, showing the unoscillated signal, along with oscillated signals for NO and IO. Plot taken from [49]

#### 1.4.2.4 Current Measurements of $\Delta m_{21}^2$

Returning to current generation of reactor experiments, the current world-leading measurement of  $\Delta m_{21}^2$  was made by the KamLAND experiment, which had a flux-weighted average reactor baseline of  $\sim 180$  km [50]. Neutrino beam experiments such as T2K, Minos/Minos+, and NO $\nu$ A have placed constraints on the oscillation parameters  $\Delta m_{32}^2$  and  $\theta_{23}$ , with T2K and NO $\nu$ A also making the only measurements at present of  $\delta_{CP}$ . Equa-

tion 1.36 presented the sensitivity that neutrino beam experiments (to a smaller degree) also have to  $\Delta m_{21}^2$ . The uncertainty in the current measurement of  $\Delta m_{21}^2$  subsequently impacts the interpretation of neutrino beam results, making its precise measurement particularly relevant. The following section discusses the precise measurement of  $\Delta m_{21}^2$  made previously by the KamLAND experiment. At the time of writing, there has not been another measurement of  $\Delta m_{21}^2$  since the KamLAND experiment and the occurrence of the 2011 Tōhoku earthquake in Japan, causing the shutdown of the majority of Japanese nuclear reactors. Solar neutrino measurements by SNO and Super-K have also made smaller contributions to the  $\Delta m_{21}^2$  global value, with larger associated uncertainties. The combined SNO and Super-K solar result slightly disfavours the KamLAND measured value of  $\Delta m_{21}^2$  by  $\sim 1.4\sigma$ . It will be seen in the next section, that the antineutrino signal at SNO+ originates predominantly from 3 nuclear reactors 240–250 km from the detector. This provides an ideal opportunity for an independent measurement of  $\Delta m_{21}^2$  in a medium baseline reactor experiment.

### 1.4.3 The KamLAND and SNO+ Reactor Antineutrino Analyses

The measurement reactor antineutrinos to extract neutrino oscillation parameter  $\Delta m_{21}^2$  at SNO+ is presented in this work. The manner of the analysis is strongly comparable to the current world-leading measurement of  $\Delta m_{21}^2$ , made by the KamLAND experiment, following their first report of reactor antineutrino oscillation in 2004 [51]. The KamLAND detector is, similar to SNO+, a kilotonne-scale liquid scintillator detector, but equipped with approximately 1900 photomultiplier tubes, versus the 9400 for SNO+. The value of  $\Delta m_{21}^2$  can be extracted by measuring the energy spectrum of reactor antineutrinos, the subject of chapter 7. For current experiments, such as SNO+, the variations in survival probability due to terms containing  $\Delta m_{3l}^2$  can be averaged over, to approximate eqn. 1.37:

$$\begin{aligned} P_{\bar{\nu}_e \rightarrow \bar{\nu}_e}(L, E) &\approx 1 - \frac{1}{2}\sin^2(2\theta_{13}) - \cos^4(\theta_{13})\sin^2(2\theta_{12})\sin^2\left(\frac{\Delta m_{21}^2 L}{4E}\right) \\ &= \sin^4(\theta_{13}) + \cos^4(\theta_{13}) - \cos^4(\theta_{13})\sin^2(2\theta_{12})\sin^2\left(\frac{\Delta m_{21}^2 L}{4E}\right) \end{aligned} \quad (1.39)$$

Figure 1.7 displays the measured energy spectrum of reactor antineutrinos arriving at the KamLAND detector, where the expected signal + background spectrum including neutrino oscillations are represented by the blue lines, in agreement with the data shown in black. The expected spectral shape without neutrino oscillation is also included, shown in dashed black. From these spectra, KamLAND made measurements of  $\Delta m_{21}^2$  and  $\theta_{12}$ :

$$\begin{aligned}\Delta m_{21}^2 &= 7.58^{+0.14}_{-0.13}(\text{stat})^{+0.15}_{-0.15}(\text{sys}) \\ \tan^2 \theta_{12} &= 0.56^{+0.10}_{-0.07}(\text{stat})^{+0.10}_{-0.06}(\text{sys})\end{aligned}\quad (1.40)$$

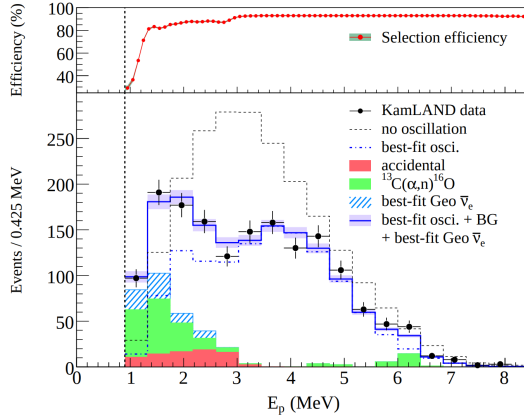


Figure 1.7: The oscillated reactor antineutrino energy spectrum measured at KamLAND, take from [52].

Compared to the KamLAND experiment, the number of nearby active reactors near SNO+ is much smaller. The three nearest reactors to SNO+ are the Bruce, Pickering and Darlington nuclear reactors, located at a distance of approximately 240, 340 and 350km, respectively. These reactors make up  $\sim 60\%$  of the total reactor antineutrino signal at SNO+. Although there are fewer contributing reactors compared to when the KamLAND experiment, the Canadian reactors are conveniently located close to one another, such that a strong, distinct oscillation signal may be measured at SNO+. Figure 1.8 shows the locations of nuclear reactors that were expected to contribute antineutrino events at the SNO+ detector for the antineutrino analysis presented in this work. World reactors are expected to produce  $\sim 200$  measurable antineutrino events per year (unoscillated), potentially interacting with any of the  $\sim 10^{32}$  free protons in the full SNO+ scintillator volume. Chapter 5 discusses the calculation of the oscillated reactor antineutrino spec-

trum, while chapter 6 examines the measurement of the antineutrino energy spectrum in the SNO+ detector, allowing for the extraction of oscillation parameters.

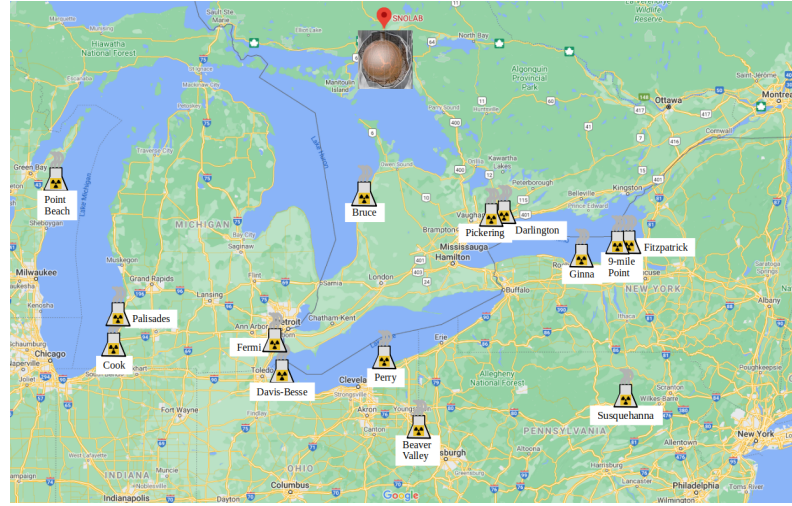


Figure 1.8: Active nuclear reactors within 700km of SNO+ (2020). Map image taken from *Google Maps*, 2021.

The observation of neutrino oscillation indicates the existence of neutrino mass. Appendix A examines the nature of the neutrino mass mechanism, where they may be described as Dirac or Majorana particles. These discussions lead to the main goal of the SNO+ experiment, a search for neutrino-less double beta decay ( $0\nu\beta\beta$ ), connected to background measurements presented in chapter 4 and appendix B.

## 2 | The SNO+ Experiment

This chapter introduces the SNO+ detector and describes the past, current and future phases of the experiment. Also discussed are the principles of detection in each experimental phase and the hardware and software used to extract and compile interesting physics data.

### 2.1 The SNO+ Detector

The SNO+ experiment employs the use of a large liquid scintillator detector located in (the middle of nowhere) Sudbury, Ontario, Canada. The detector itself is located in a cavern in SNOLAB, a class-2000 cleanroom lab facility<sup>1</sup>, at a depth of 2km in Creighton Mine - a currently active copper mine (figure 2.1(b)). The huge mass of rock overhead ( $5890 \pm 94$  meter water equivalent (m.w.e.)) allows for the experiment, a very low muon flux ( $0.27 \mu/\text{m}^2/\text{day}$ ) [54]. This, along with the stringent levels of cleanliness of the lab allows the detector to achieve very low levels of background radiation [55]. Chapter 6 outlines the impact muons can have in the reactor antineutrino analysis.

The SNO+ detector takes mostly after its namesake, the SNO experiment, which was a Cherenkov detector operating with 1 kilotonne of heavy water as its target volume [56]. A majority of the hardware was reused following the approval of the SNO+ experiment, but there were notably a number of upgrades carried out on the original SNO detector's data acquisition system [57]. The detector has undergone, and will go through, a number transition stages towards its eventual goal of searching for  $0\nu\beta\beta$  in the Te-loaded liquid scintillator phase of the experiment (appendix A).

Figure 2.1(a) shows a comparison of the measured muon flux for a number of underground laboratories. Borexino in the Laboratori Nazionali del Gran Sasso, KamLAND in the Kamioka Observatory and JUNO in the Jinping Laboratory, are kilotonne-scale neutrino detectors referenced throughout this work.

---

<sup>1</sup>where a class-1000 cleanroom has a maximum number of  $10^6$  particles ( $> 0.1 \mu\text{m}$  in size) per cubic metre [53]. Ordinary room air is approximately class-1,000,000.

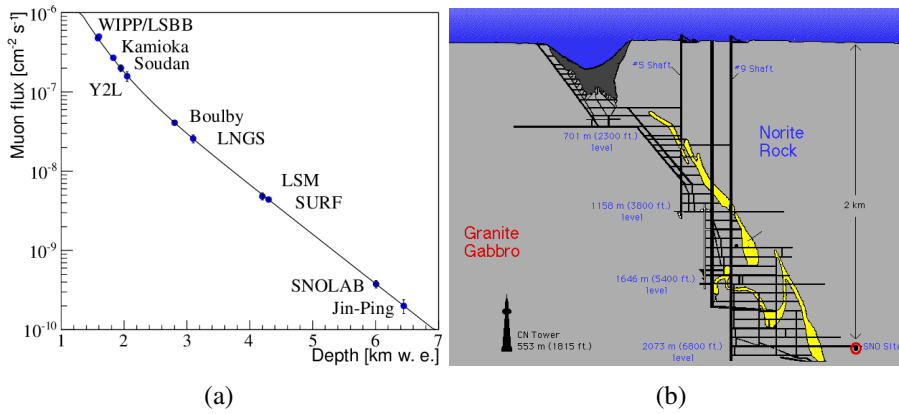


Figure 2.1: (a) Measured Muon flux against its depth for various experiments. Plot taken from [58] (b) Schematic showing SNOLAB’s location in Creighton Mine.

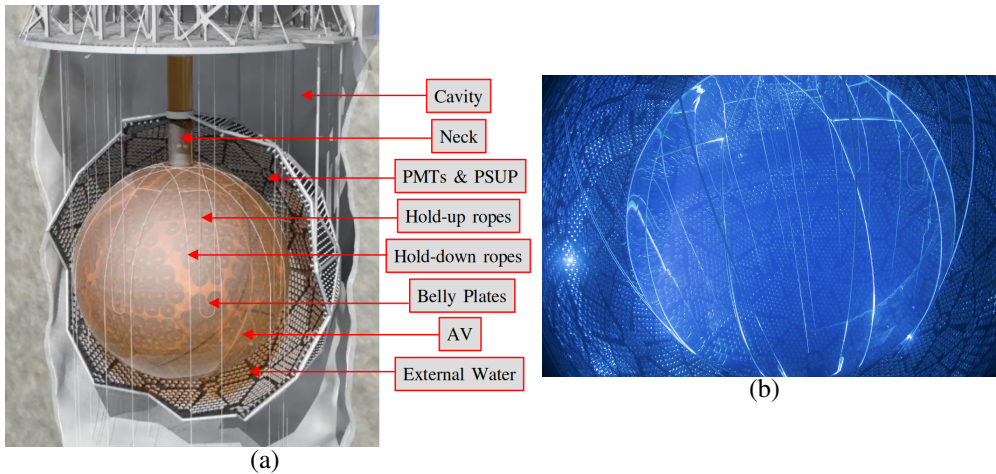


Figure 2.2: (a) Schematic of a cross-section of the SNO+ detector (b) Fish-eye lens view of the inside of the SNO+ Detector

The SNO+ detector has the highest photocathode coverage of any operational kilotonne-scale liquid scintillator or Cerenkov detector to date [59]. Coverage is defined by the fraction of  $4\pi$  solid angle from the centre of the Acrylic Vessel (AV) is watched by the photocathode surface on the photomultiplier tube (PMT) light detectors, where the coverage by photocathode surface is calculated to be 31%. Each PMT in the detector is surrounded by light concentrators, each in the shape of a Winston cone (figure 2.10(b)), to improve light collection [60]. These light concentrators increase the effective coverage to 59%. Accounting for the imperfect reflectivity of the reflective surfaces on the concentrators brings this down to 54% [59]. Furthermore, since these concentrators were installed in the original SNO experiment, the reflectors have degraded over time, and the

54% effective coverage represents more of an upper limit on the coverage. More detail on the PMT light detectors can be seen in section 2.5.

The centre of the SNO+ detector corresponds to the target volume, the liquid used for the detection of particle interactions. This liquid is contained within the **AV** - a spherical, transparent acrylic container 6m in radius, 5.5cm in thickness. Supporting the AV from above are tensylon ropes called the **hold-up ropes**, attached to the AV at the **belly-plates**. These are small regions of double-thickness acrylic on the horizon of the AV. As part of the upgrade from SNO to SNO+, the AV was also fitted with another set of **hold-down ropes**, to account for the change in buoyancy of the AV when water contained within was exchanged with less-dense liquid scintillator. At the top of the AV is the **neck**, a 6.8m tall cylindrical extension to the AV also constructed from acrylic, through which the detection medium is passed into the AV. The deck is the area directly above the detector where detector operators can access for maintenance and detector calibration. Further out from the AV is the PMT support structure (**PSUP**) upon which approximately 9400 inward-facing PMTs are affixed at an average radius of 8.4m from the centre of AV. Also attached to the outside of the PSUP are 91 outward-looking (**OWL**) PMTs, which are used in the identification of energetic cosmic muons entering the detector. 7kt of purified water fills the region between the AV and the PSUP, shielding the detection medium from the intrinsic radioactivity contained within the PMTs.

Chapter 9 explores a proposed alternative design for the next generation of large-scale scintillator detectors.

Apart from the primary physics goal of searching for the  $0\nu\beta\beta$  decay, the size, high PMT coverage and low background rate of SNO+ detector allows for a wide range of physics to be explored. This includes the measurement of solar neutrinos [55], supernovae neutrinos [61], exotic physics searches [62], along with the subject of this thesis, the measurement of reactor antineutrinos originating from the nuclear reactors surrounding SNO+. The next section summarises each of the experimental phases the SNO+ detector.

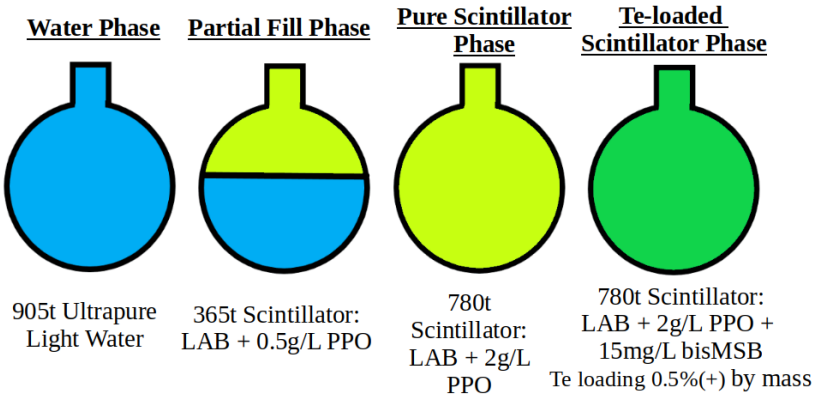


Figure 2.3: Summary of the various phases of the SNO+ experiment. Results presented in this work include the water and partial fill phases.

## 2.2 SNO+ Experimental Phases

The different stages of the the SNO+ experiment are defined by the target medium contained within the spherical AV (see figure 2.3). The period of time over which the work presented here was carried out, spanned over the water phase as well as the partial fill phase.

**Water Phase** Following the upgrade from SNO, the detector was first filled with 905t of ultra-clean light water, reaching a very low contamination level of  $4.2 \times 10^{-15} \text{ g}_{\text{U}}/\text{g}_{\text{H}_2\text{O}}$  and  $3 \times 10^{-16} \text{ g}_{\text{Th}}/\text{g}_{\text{H}_2\text{O}}$ . After an extended period of data-taking in the water phase, the contamination present in the detector was measured to a high degree of precision, where the measurements made could be used going forward into the following phases of the experiment. Amidst these very low background levels, a nucleon decay search and a solar neutrino measurement were carried out [62][55]. Appendix B presents a background analysis carried out in the water phase, measuring the radiation emitted by the hold-down and hold-up ropes in the SNO+ detector.

**Pure Scintillator Phase (+ Partial Fill Phase)** The second SNO+ phase involved replacing the light water with liquid scintillator. The SNO+ experiment was impacted (as was the rest of the world) by the Covid-19 pandemic, where the scintillator fill was interrupted at the beginning of 2020, leaving 365 of the total 780 tonnes of scintillator in detector for an extended period. The immiscibility of water and the liquid scintillator

lead to the formation of a water-scintillator interface. The two liquid system configuration constituted an unexpected experimental phase with stable detector conditions, over which physics analyses were carried out. Chapters 4 and 7 both involve analyses carried out over the partial fill phase. Figure 2.4 shows photos taken during the partial fill period, where the liquid interface has been highlighted with a white line and arrow (where the less-dense scintillator is floating above the water). The interface level was located at a z-position of 0.75m for the duration of this period (where  $(x,y,z) = (0,0,0)$  was defined by the centre of the AV sphere).

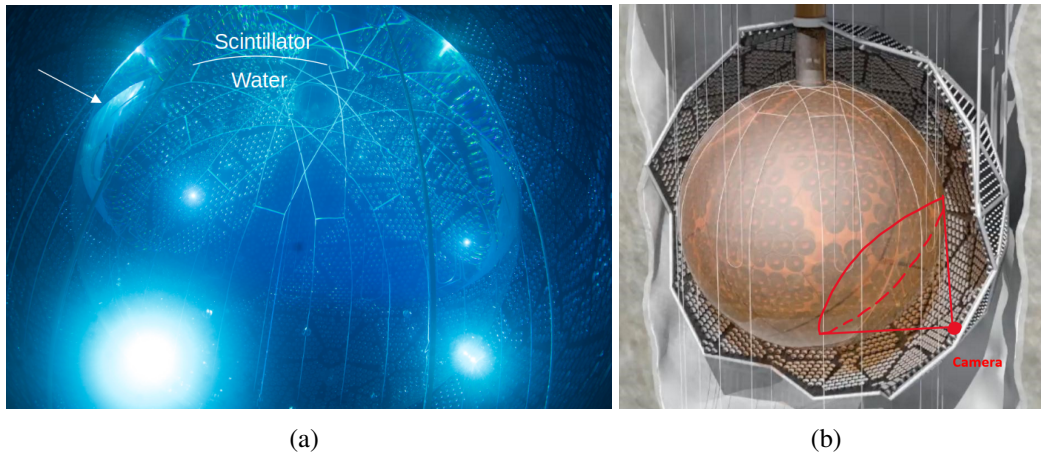


Figure 2.4: (a) Fish-eye photo of the SNO+ water-scintillator interface during the partial fill phase. (b) Approximate position of the camera used in (a).

The partial fill phase had 365t of scintillator, and a scintillator makeup of LAB + 0.5g/L PPO (discussed in section 2.3.2.1). At the time of writing this work, the scintillator fill has been completed, with 780t of scintillator added into the AV. There will be a period of time spent in the pure scintillator phase to allow for detector stabilisation, calibration and background measurements, in preparation for the Te-loaded phase. PPO has been added in batches to increase the PPO concentration in the filled detector towards the target concentration of 2g/L.

**Te-loaded Scintillator Phase** Following the pure scintillator phase, the third phase will involve the loading of  $^{130}\text{Te}$  to the scintillator where the search for  $0\nu\beta\beta$  will begin.

The following section outlines the mechanisms by which the water and scintillator media produce detectable light. Chapter 3 discusses event reconstruction in each medium.

## 2.3 Optics

This next section outlines the physical processes that allows for the detection of MeV-scale radiation in the SNO+ detector over the water and scintillation phases respectively. Energetic charged particles (e.g. an electron scattered by a neutrino) can deposit energy in the target medium at the centre of the SNO+ detector. This energy is converted to optical photons which then propagate out to the PMTs, where they can be detected.

### 2.3.1 Water Phase - Cherenkov Radiation

An energetic, charged particle travelling through a dielectric medium can emit Cherenkov radiation if it is travelling at a speed faster than the speed of light within that medium. An energetic charged particle passing by water molecules, which are polar in nature, causes them to align towards the direction of the charge, polarising the medium. When the charged particle has passed sufficiently far beyond a given section of polarised molecules, they will revert to their original orientations, emitting radiation during the de-polarisation process due to the dipoles oscillating. The threshold speed is dictated by the speed of the medium's response to the passing particle through depolarisation. Polarisation occurs for both slow-moving and above Cherenkov-critical speed charged particles. The sketch in figure 2.5 shows a slow and fast moving particle passing by polar molecules. For a slow moving particle, the net polarisation for dipoles pointing towards the charged particle amounts to zero due to the their spherically symmetrical distribution. For a fast moving charge, due to the finite response time of the dipoles, the dipoles point towards the quickly moving charge. At this instant there is no longer a spherical symmetry in the dipole distribution, yielding a net polarisation over the region in the wake of the fast-moving charged particle.

The angle between the trajectory of the emitted Cherenkov photons and the trajectory of the energy depositing superluminal charged particle is:

$$\cos(\theta)(\lambda) = \frac{1}{n(\lambda)\beta}, \quad (2.1)$$

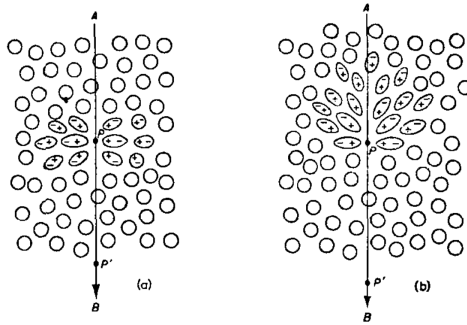


Figure 2.5: Sketch demonstrating the polarisation of a molar medium for a (a) slow (b) fast charged particle. Figure taken from [63].

where  $n(\lambda)$  is the refractive index of the detection medium and  $\beta$  is the speed of the charged particle. In the ultra relativistic limit where  $\beta \rightarrow 1$ , the Cherenkov angle approaches  $41.4^\circ$  in water, which has a refractive index of 1.33. This is reflected in the simulation of Cherenkov radiation in the SNO+ detector, seen in figure 3.3.

As the energetic particle emits Cherenkov radiation, it loses energy and slows down until it is travelling below the threshold speed. The amount of Cherenkov light an energetic particle gives off is described by the classical Frank and Tamm formula [63]. The number of photons emitted per unit length can be written as:

$$\frac{dN_\gamma}{dx} = 2\pi\alpha z^2 \int 1 - \frac{1}{n^2(\lambda)\beta^2} \frac{d\lambda}{\lambda^2}, \quad (2.2)$$

where  $\alpha$  is the fine structure constant,  $z$  is the charge number of the energy depositing charged particle. Visible is the wavelength dependence of the number of photons emitted, in the form of  $\lambda^{-2}$  (demonstrating the blue glow often seen in photographs of nuclear reactors cores). Integrating over the particle's full track length in Monte Carlo (MC) simulation, the total number of photons per MeV of incident particle can be calculated.

### 2.3.2 Liquid Scintillator Phases - Scintillation

The manner by which light is emitted in organic liquid scintillator is primarily through the mechanisms of fluorescence and phosphorescence. An energetic particle passing by the scintillator molecules making up the liquid scintillator, may excite electrons in the scintillator molecule, which then emit photons upon the de-excitation of the molecule.

The two scintillation categories, fluorescence and phosphorescence, are distinguished by the time scale on which these excited states decay and emit radiation. The liquid scintillators typically used in neutrino experiments, generally measure fluorescence and phosphorescence occurring on the scales of ns to  $\mu$ s and ms to s respectively [64].

Scintillation may occur in an organic molecule due to the excitation of its valence electrons. Organic scintillator molecules used in liquid scintillator detectors contain aromatic rings<sup>2</sup>. In an aromatic ring, atoms are bonded together cyclically, through the overlap of p-orbitals for adjacent atom in the chain.

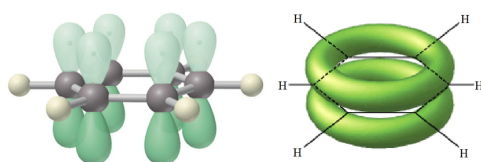


Figure 2.6: Sketch of a benzene ring and the delocalised pi-bonds not used in C-C and C-H bonding. Diagrams taken from [65].

In the case of benzene, the molecule's planar geometry of 6 bonded carbons is due to the formation of  $3\text{sp}^2$  orbitals by the  $n = 2$  shell electrons. 3 electrons in their  $\text{sp}^2$  hybridized orbitals each take part in  $\sigma$  bond, bonding to its 2 adjacent carbon neighbours in the ring along with a hydrogen atom, yielding the  $120^\circ$  bond angles in the ring's plane. The last remaining  $n = 2$  electron in carbon occupies a left over  $p_z$  orbital where the z-axis is perpendicular to the plane that the ring lies in [66]. The carbon atoms each have a remaining unbonded z-oriented p-orbital, which overlap in space above and below the ring, as shown in figure 2.6. This overlap creates a region of delocalised electrons which gives benzene its aromaticity. The benzene structure yields an energy level structure for the delocalised electrons with energy transitions favourable for optical light emission.

Excitement of these valence electrons may occur by elastic scattering or ionisation followed by recombination, to a variety of excited singlet states ( $s = 0$ ). Excitement from ground states to triplet states ( $s = 1$ ) is strongly reduced due to spin selection rules [67]. Scintillators can be characterised by a quantum yield, the probability of scintillation light emission following its excitation. It is possible, through the overlap of excited energy

<sup>2</sup>a benzene ring in the case of linear alkylbenzene, used in the SNO+ scintillator cocktail

level and the vibrational excited states of the ground state, that a scintillator molecule de-excites without light emission, leading to a non-unitary quantum yield.

Phosphorescence (or delayed fluorescence) occurs when the excited electron occupies and de-excites from the excited triplet state ( $s = 1$ ), labelled  $T_1$  in figure 2.7. An electron may reach this either through an inter-system crossing from a higher energy singlet state, or more commonly, ionisation and recombination into a triplet state. Triplet states are stable against decay to the ground singlet state, since the scintillating molecule must go through a ‘forbidden’ spin conversion to produce unpaired electrons. These spin selection rules yield longer lifetimes for the triplet states, corresponding to phosphorescence.

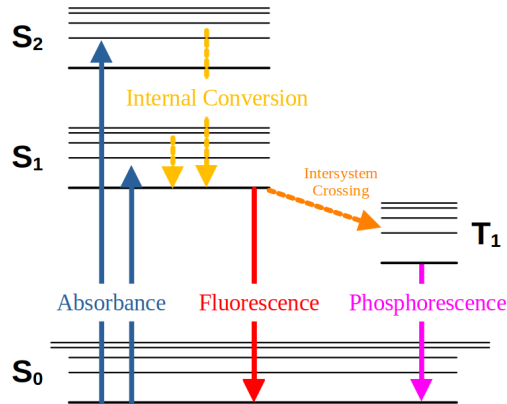


Figure 2.7: Sketch of the energy levels for  $\pi$  electrons in an organic scintillator molecule. S and T denote singlet and triplet states and the lowercase index represents the energy level.

The light yield for scintillator was simulated in RAT (section 2.8) using the empirically formed Birk’s law [68]:

$$\frac{dL}{dx} = S \frac{\frac{dE}{dx}}{1 + k_B \frac{dE}{dx}}, \quad (2.3)$$

where  $dL/dx$  is the emitted photon number per unit track length.  $S$  is the scintillator light yield constant,  $dE/dx$  is the particle’s energy loss per track length,  $k_B$  is Birk’s constant defined for the given scintillating material.

### 2.3.2.1 SNO+ Scintillator cocktail

**LAB** Linear Alykyl Benzene (LAB) was chosen as the solvent for the SNO+ scintillator cocktail. LAB was selected due to its high light yield, good  $\alpha$  and  $\beta$  particle discrimination and can reach very high levels of purity. LAB also has good compatibility with

acrylic and is a safe compound [69]. The low cost of LAB was also a critical consideration, important in all kt-scale neutrino experiments. Figure 2.8 shows the LAB and PPO molecular structures. As indicated in the figure, LAB chains can exist as a variety of lengths, the SNO+ LAB chain lengths composition was measured in [70].

For a scintillation photon propagating in the scintillator, the absorption length dictates how far it may travel before being reabsorbed by the medium itself. For large-scale scintillator experiments, the impacts that scintillation light reabsorption have on light yield and scintillator emission times must be accounted for. Extra fluors can be added to the scintillator in order to counteract these effects.

**PPO** SNO+ will employ a primary fluor in the form of 2,5-Diphenyloxazole (PPO), at an expected concentration of 2g/L. When a LAB molecule becomes excited, the purpose of the fluor is to allow energy to transfer (according to a transfer efficiency) from LAB to PPO, before the fluorescence occurs for the LAB molecule. These energy transfers are dominantly non-radiative in nature. The fluorescence and absorption spectra for the PPO fluor is shown in figure 2.9.

**BisMSB (Te-loaded Scintillator phase)** Secondary fluors, 1,4-bis(2-methylstyryl) benzene (bisMSB) may also be added to further improve the light yield. PMTs can efficiently detect photons of a finite range of wavelengths, as shown for the SNO+ tubes in figure 2.12(a). It can be beneficial to add a high quantum efficiency secondary fluor, which acts as a wavelength-shifter, such that there is improved overlap of the emitted scintillation light wavelengths and PMT efficiency. Figure 2.9 shows the emission spectra of PPO, bisMSB including the PMT efficiency curve. It can be seen the the bis-MSB emission spectrum has better overlap with the PMT efficiency, compared to PPO emission.

Energy may be absorbed by either LAB, PPO or bisMSB, where the assumed absorption probabilities used in RAT simulations are shown in figure 2.9. In the simulation of the SNO+ cocktail, LAB was assumed to have a transfer efficiency to PPO of 75% at a concentration of 2g/L. The PPO quantum yield was assumed to be 80%, yielding a total efficiency for absorption by LAB and emission by PPO of 60%. BisMSB can likewise absorb and reemit, with a quantum yield of 96% [71]. Updated measurements of quantum

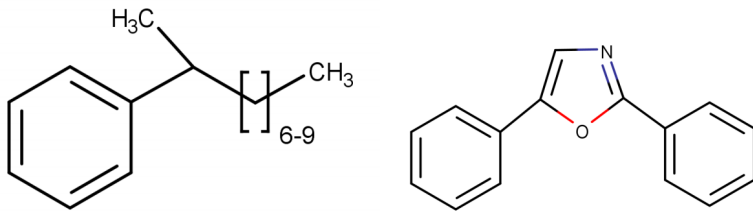


Figure 2.8: Molecular structure of LAB (left) and PPO (right). Drawings taken from the SNO+ scintillator cocktail publication [69]

and transfer efficiencies can be seen in Ref. [69].

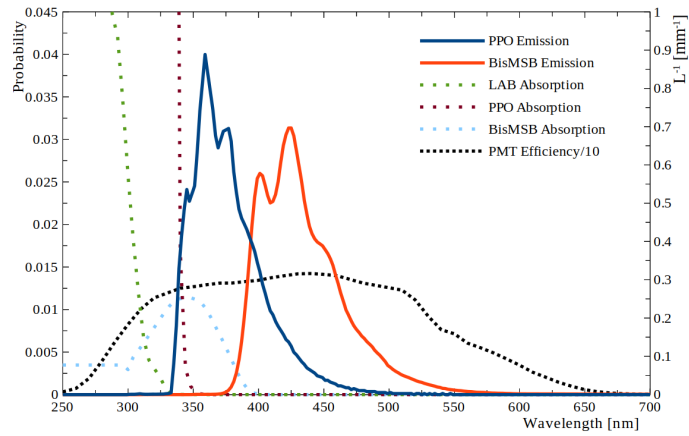


Figure 2.9: Absorption and Emission spectra for the LAB, PPO and bisMSB components in the SNO+ scintillator cocktail. The left y-axis shows probability of emission, the right y-axis corresponds to the sparsed dotted graphs showing absorption in units of  $\text{mm}^{-1}$ . The black fine dotted line shows the r1408 Hamamatsu PMT measured total detection efficiency (divided by 10 to fit on the graph) [72][69].

### 2.3.2.2 Scintillation Time Emission Profile

As discussed previously, the scintillation emission times of the SNO+ cocktail are characterised by short and long decay times: fluorescence and phosphorescence. The added fluors typically have emission times akin to fluorescence, on the order of ns also. The majority of scintillation light for a scintillator and fluor mixture is emitted by way of non-radiative transfer from the scintillator to the fluor. The total emission time spectrum shape therefore is highly dependent on the concentration of fluors added. Fast emission times are necessary for the reconstruction of energy, position and event type to a high degree of resolution.

Chapter 3 details the reconstruction of position and energy using time residual distributions. Chapters 8 and 9 discuss the impact scintillation times have on particle identification and position reconstruction. The modelling and measurement of these scintillation emission times are discussed further in chapter 4, where an in-situ measurement of these timing parameters was made in the partial fill phase using tagged BiPo214 events.

### 2.3.2.3 Scintillator Quenching

While radiation in the form of protons, neutrons,  $\alpha$ ,  $\beta$  and  $\gamma$  particles are all commonly produced in the SNO+ detector, the primary particle assumed to be the cause of detector triggering, are  $\beta$  particles. For example a  $\gamma$  particle produced in the detector will Compton scatter many electrons along its path, where the scattered electrons produce the detectable scintillation (and Cherenkov) light. Protons,  $\beta$ s and  $\alpha$ s are all charged and therefore can produce scintillation light when sufficiently energetic. The interactions in the scintillator due to these particles however yield different scintillator emission times and light yield due to their contrasting mass and resulting ionisation ability [73]. Chapter 4 contains in-situ measurements of the scintillator light yield and timing quenching due to  $\alpha$  particles compared to  $\beta$ s. Further discussions of particle identification using the scintillator's response to different particles is described further in section 8.2.2.

Introduced up to this point have been the different mechanisms of detection for each medium. Each medium also presents a number of advantages and disadvantages when compared to one another. Chapter 3 also compares the water and scintillator phases in terms of event reconstruction.

## 2.4 Differences Between Water and Scintillator

At the start of SNO+, the emptied SNO detector spent a long period of time exposed to air following the end of its operation. Filling the detector with water inside and out of the AV reduced the pressure exerted on its delicate structure. The water fill phase also allowed for the extraction of contamination embedded in the detector's components. The water phase also allowed for an independent characterisation of the PMTs' responses (following a long period without use), along with measurements of the backgrounds levels within the

detector prior to the addition of scintillator. Many of these water phase measurements will be repeated in the scintillation phase, allowing for comparison across phases.

**Contamination** One of the primary reasons to use scintillator instead of water to search for the rare  $0\nu\beta\beta$  decay is the contamination level of the medium itself. Since water is a polar medium, it is difficult to purify from radio-impurities compared to its non-polar scintillator counterpart. It is of critical importance in the  $0\nu\beta\beta$  analysis to minimise background rates, leaving scintillator as a prime candidate for SNO+ and its main physics goal.

**Direction** One significant advantage water has over the liquid scintillators used in current large scale experiments, is the ability to measure direction. It is possible to reconstruct the direction of an event using the direction of the Cherenkov radiation cone. Direction reconstruction allows for the identification of neutrinos with fixed source positions e.g. solar neutrinos (as was done previously in SNO), supernovae, reactor geoneutrinos. Directionality is also beneficial for background reduction and event type identification (e.g. identifying the two  $\beta$ s emitted back-to-back in a  $0\nu\beta\beta$  decay). There is currently a great deal of active research into scintillator cocktails and light collectors that allow for both high light yield and direction reconstruction.

**Light Yield** The critical difference between the two media are the light levels emitted. In giving up directionality in scintillation, it gives much higher light emission per unit deposited energy. The increased number of triggered PMTs in an event allows for much more precise position and energy reconstruction.

### 2.4.1 Addition of Te

The chosen organic liquid scintillator, for all its advantages, presented challenges in terms of the loading of  $^{130}\text{Te}$ . The isotope was added in the form of telluric acid. Inorganic compounds generally do not mix with organic liquids, prompting the development of a novel loading technique by the SNO+ collaboration. The synthesis of tellurium butane-diol (TeBD) was required in order to form a stable mixture of the Tellurium with the

scintillator [74][75].

The addition of TeBD to the scintillator cocktail does not impact significantly the absorption or scattering. TeBD addition however quenches the scintillation mechanism in the cocktail, leading to decreased light emission. Measurements of this decreased light yield in the SNO+ cocktail were made in Ref. [75]. The mixing method employed yielded mixtures with long-term stability and also allowed the scintillator to retain its high light yield, optical clarity and radiopurity. Apart from light yield changes, the addition of  $^{130}\text{Te}$  will increase the overall background rate in the detector, predominantly in the form of  $2\nu\beta\beta$  decays.

## 2.5 PMTs

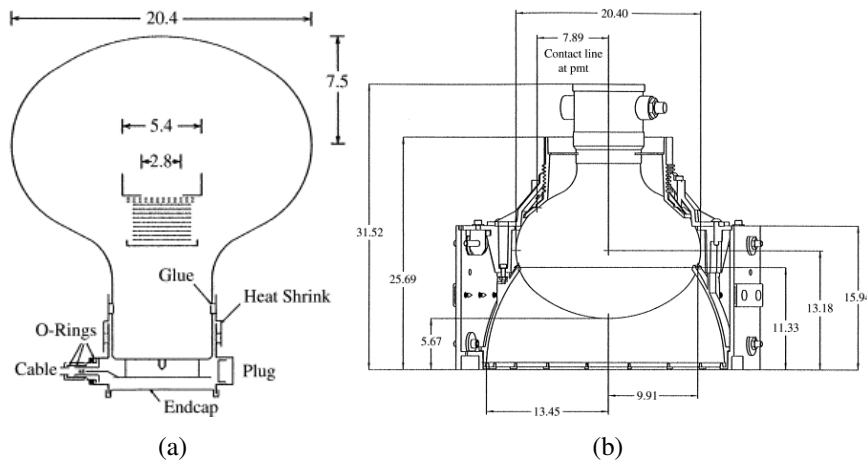


Figure 2.10: Schematics of the r1408 Hamamatsu Photomultiplier Tube (measurements are in units of cm).

The SNO+ detector is equipped with approximately 9400 r1408 Hamamatsu PMTs, each 8" in diameter, of dimensions shown in figure 2.10(a). When a photon arrives at the photocathode - the metallic film coating the glass of the tube, an electron (photoelectron) may become freed from the metal via the photoelectric effect [76]. A high voltage of  $\sim 2000\text{V}$  is applied across the photocathode and the anode in the base of the PMT. The field due to this voltage accelerates the photoelectron (p.e.) to the bottom of the PMT. Also contained in the base are many dynode layers, on which secondary electron emission may occur. When the accelerated p.e.s strike a dynode, secondary electrons are subsequently created

on each dynode, which are accelerated towards the next dynode in the series, creating an avalanche of electrons. The PMT therefore acts to amplify the signal due to the original photon(s). This final bulk of electrons arriving from the final dynode have a net charge, providing the signal that indicates a photon landed on the PMT photocathode. A PMT is said to ‘trigger’, when the charge collected over a chosen time period, passes a defined threshold. This PMT threshold is essentially decided by the dark noise rate (figure 2.12(b)).

In order to increase the effective light capture area, each inward-facing PMT is surrounded by a truncated Winston Cone as seen in figure 2.10(b). This light reflecting structure reflects light back into the photocathode. These reflections effectively fill in the gaps between PMTs, capturing the light which otherwise would have gone undetected.

**Timing** Optimal for good energy and position reconstruction, are fast PMTs. A fast PMT is one that produced a very narrow distribution of times between p.e. creation at the photocathode and the PMT triggering. This spread in transit times is quantified by a transit time spread (TTS). Figure 2.11 shows measurements of the transit times for the SNO+ tubes. Apparent in the figure is the prominent peak, with a TTS standard deviation of 1.5ns. A sub-dominant feature, is the pre-pulsing peak at -18ns, which is produced by photons bypassing the photocathode and directly producing p.e. on the dynodes. A late-pulsing peak can also be seen also 12ns. This is due to p.e.s scattering off the first dynode, travelling against the electric field direction, and eventually returning to the dynode stack, producing a later signal [77].

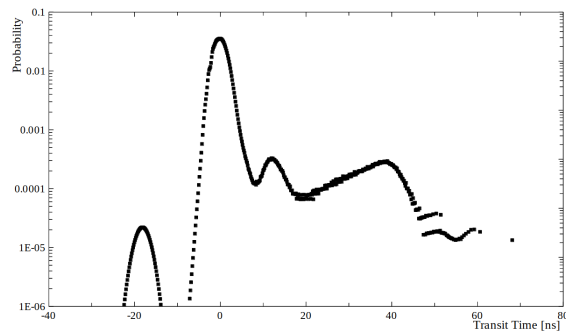


Figure 2.11: The measured r1408 Hamamatsu PMT transit time distribution.

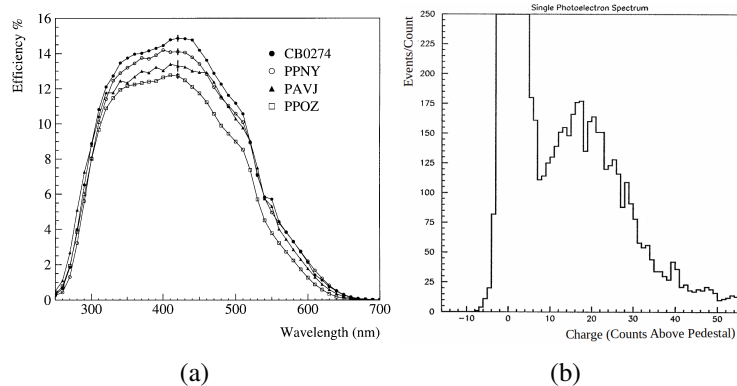


Figure 2.12: (a) r1408 Hamamatsu PMTs’ measured efficiency from Ref. [72] (b) The p.e. charge spectrum from Ref. [59].

**Efficiency** Figure 2.12(a) shows the total measured efficiency of the r1408 Hamamatsu PMT, as the product of the quantum efficiency<sup>3</sup> and the collection efficiency<sup>4</sup>.

**Charge** Figure 2.12(b) shows the single p.e. charge spectrum measured in-situ in SNO [59]. The peak centred around 0 charge extending beyond the graph represents the ‘dark rate’, the rate at which a PMT triggers due to the voltage across it without exposure to light. This dark rate is approximately 500Hz under typical detector conditions. The PMT trigger threshold is set at approximately 9 counts above pedestal, as seen in figure 2.12(b).

## 2.6 Data Acquisition System

In order to save only ‘interesting’ physics data, the data acquisition system (DAQ) is responsible for the grouping of multiple coincident PMT triggers, which occurs when energy is deposited in the target medium.

Hit PMTs provide an output analogue signal when triggered, which is sent through its associated electronics ‘channel’. When the combined PMT analogue signals surpass a threshold, the global trigger (GT) is activated, causing the charge and time from all triggered channels to be recorded as data.

Each of the roughly 9400 channels in SNO+ are divided across and managed by 19 crates,

<sup>3</sup>The probability of a p.e. being produced on the photocathode by a photon of a certain wavelength.

<sup>4</sup>The efficiency in a p.e. produced at the cathode incurring the avalanche of secondary electrons on the PMT’s dynodes

each containing 512 channels. In each crate, are 16 interface cards (PMTIC), which have 4 paddle cards each. Each paddle card is connected to 8 channels, yielding 32 PMTs connected to each paddle card. These PMTICs, collect and forward the signals of each connected channel to the readout system, as well as providing the high voltage required by each PMT to operate. PMTICs control the high voltage sent to each paddle card, but not each PMT individually.

Front end cards (FEC) are attached to each PMTIC in the crate, each receiving the signals from 8 channels. The responsibility of the FEC are to integrate PMT signals passed onto it. Each time a channel crosses its trigger threshold, a hit is recorded, a time-to-amplitude-converter (TAC) is started on the channel's CMOS chip, and the signal is integrated over 3 paths for the global triggers: high gain with short integration time interval (QHS), high gain with long integration (QHL) and low gain with short integration (QHX). The short and long integration time intervals are 60 and 390ns respectively. Upon a channel triggering, also produced for the GT, are square wave pulse 100ns in width (N100) and 20ns (N20), which can be used in global triggering such that each PMT contributes equally in amplitude. The N100 signal is the primary global trigger used in SNO+. The TAC is stopped if a global trigger arrives (to be discussed shortly), with the time following the trigger and the charge being saved to the channel's CMOS chip. If a global trigger does not arrive the TAC resets automatically after 410ns.

### 2.6.1 Global Triggers

The global trigger acts upon the sum of the signals from each triggered channel. The 4 types of signal sums are, the aforementioned N100 (the primary detector trigger), N20, ESUM Hi and ESUM Lo (analogue signals with high and low amplifications applied respectively). In each PMT crate, a crate trigger card (CTC) performs the summing of the channel signals for that crate. These summed signals are passed on to the Timing Rack, which contains 7 Analogue Master Trigger Cards (MTC/A+, upgraded versions of the MTC/A used in SNO) which sum up channel signals from all over the detector. Each of the 7 MTC/A+ are assigned to the 4 trigger signal types, with the remaining used to receive trigger signals from the OWL PMTs. Upon the summation of each channel's

contribution, using the primary N100 trigger as an example, a GT is declared when the threshold for coincident channel triggers within the 100ns time window is reached. Each MTC/A+ has 3 discriminators, triggering on the summed signals. Upon the firing of one of these discriminators, the signal is passed on to the Digital Master Trigger Card (MTC/D). The MTC/D checks against the trigger type, depending on which trigger types are flagged in, then sends a signal to the CTC of every crate when the global trigger is fired, according to its 50MHz clock. The time window for a given triggered event in the detector is 400ns long. Following a triggered event, there is a 420ns dead time in which the global trigger cannot fire, effectively defining the trigger window for an event recorded in the SNO+ detector.

### 2.6.2 Instrumentals

While the detector is primed to detect the small energy depositions of MeV-scale particles, the detector can also be triggered due to emissions/interference produced by the PMTs and associated electronics, and by human disturbances to the detector. An example of a common instrumental event is known as a ‘flasher’. Static discharges in a PMT under high voltage in the detector leads to the emission of light in the detector, triggering an event. Similar ‘non-physics’ events are removed with ‘data-cleaning’ algorithms, described in chapter 3.

### 2.6.3 Detector Runs

Saved physics data is generally separated into hour-long segments called runs. Each run has its own distinct run number and detector information for the run. This information generally consists the run type (e.g. physics data collection, calibration, maintenance), along with any activity occurring for that run (e.g. people working on deck can cause detector interference). Also saved for each run are the detector conditions (e.g. PMT status), such that simulations can accurately recreate detector response on a per-run basis.

## 2.7 Detector Calibration

This section outlines the main calibration sources used in the water phase of the SNO+ experiment. Calibration sources are required for reliable data-simulation comparison and in turn, accurate position and energy reconstruction. The deployment of well-understood optical and radioactive sources, allows for the measurement of radiation propagation throughout the detector, along with the PMT response and electronics timing measurements. Optical sources emit light of known wavelengths, such that the response of each PMT and associated electronics can be measured. Optical sources also allow for the measurement of wavelength-dependent propagation distances of light in the detection medium, as described in the next section. Radiation sources, described in the following section, produce MeV-scale radiation at known positions such that the detector's energy scaling (the number of PMT triggered hits per MeV of deposited energy in the detection medium) around the detector can be measured.

The scintillator data presented in this thesis was limited to the partial fill phase, during which source deployment was confined to the external water only (to avoid contamination of the scintillator). Chapter 4 discusses the calibration of the scintillator without the use of deployable calibration sources, instead using the BiPo214 coincidence background radiation, found throughout the detector.

### 2.7.1 Optical Calibration

Optical calibration sources are required for the measurement of the optical properties of the various mediums, such that the propagation of light throughout the detector is well understood and accurately reflected in simulation. Optical sources also allow for the measurement of the PMTs' response to the well understood light sources.

#### 2.7.1.1 Laserball

Used since the days of the SNO experiment, the laserball is an optical calibration source which emits light isotropically in the detector [78], where the wavelength spectrum emitted can be customised. The source is suspended within the detector volume, where

the device itself consists of an 11cm diameter quartz sphere. The device is filled with hollow glass spheres suspended in silicone gel, connected by an umbilical optical fibre through which light is injected into it. Various laser dyes can control the emitted wavelength spectrum. Shining light at a known injection time and known wavelengths in the detector allows for the calibration of each of the PMTs' response with respect to timing (discriminator time walk, cable delays) and charge (discriminator thresholds, single p.e. response)[59]. Calibration ropes within the detector allow the source to be moved throughout the detector. Various photon propagation lengths can be created over various source positions, allowing for the absorption length of the detector medium to be measured as a function of wavelength.

### 2.7.1.2 ELLIE Systems

The Embedded LED/Laser Light Injection Entity (ELLIE) systems consist of inward-pointing LEDs embedded in the PSUP of the detector. The ELLIE system is divided into 3 different subsystems: the timing module (TELLIE), scattering module (SMELLIE) and attenuation module (AMELLIE). These systems allow for the calibration of the PMTs and light propagation in the detector medium, like the laserball, but avoids potential contamination of the central detector medium itself through any deployment of a source into the detector [79].

## 2.7.2 Radioactive Calibration Sources

In order to measure the light yield of the scintillator and the detector's energy scale, along with performance the position and energy fitters (chapter 3), radioactive sources are deployed into the detector, at known positions.

### 2.7.2.1 N16

The primary energy calibration source used over the SNO+ water phase, passed over from SNO, is  $^{16}\text{N}$  source. The  $\beta$ -decay of  $^{16}\text{N}$  of half-life of 7.13s, provide high energy  $\gamma$  particles, the majority of which are 6.13MeV in energy. The  $^{16}\text{N}$  are produced by way of neutron capture on oxygen atoms in the  $\text{CO}_2$  on deck, where the 14MeV neutrons

for capture are provided by a Deuterium-Tritium generator. Similar to the laserball, the source is lowered into the detector by an umbilical chord, through which electronics and the  $^{16}\text{N}$  passes. A PMT contained in the neck of the source is triggered by scintillation light produced in the  $\beta$ -decay, allowing a given decay to be tagged [80]

### 2.7.2.2 AmBe

The Americium-Beryllium (AmBe) calibration source allows for a calibration of neutrons.  $^{241}\text{Am}$  undergoes  $\alpha$ -decay, where the emitted  $\alpha$ s capture on the  $^9\text{Be}$  target, yielding a neutron and  $^{12}\text{C}$ . 60% of the time  $^{12}\text{C}$  is produced in an excited state, which produces a 4.4MeV  $\gamma$  upon its de-excitation. The AmBe source consists of a prompt 4.4MeV  $\gamma$  event and a delayed 2.2MeV event from the eventual capture of the neutron on a hydrogen in the detector, following neutron thermalisation. The AmBe source is therefore an ideal source for the antineutrino coincidence event ( $e^+ + n$ ). Chapter 6 discussed the extraction of reactor antineutrino events in the partial fill phase.

### 2.7.3 Cover Gas System

A huge priority in the SNO+ experiment is to minimise the amount of ingress radioimpurities into the detector. Chapter 4 discusses the measurement of the background radiation due to  $^{214}\text{Bi}$  and  $^{214}\text{Po}$  event pairs, daughter particles of  $^{222}\text{Rn}$  which is found in the air that enters the main detector volume, primarily through the neck. To combat against radon contamination, a cover gas system was installed. This supplies purified nitrogen gas at a rate of 5L/min into the empty region in the neck [79].

## 2.8 Event Simulation

The SNO+ experiment utilises a GEANT4-based simulation and analysis tool called RAT (Reactor Analysis Tool) that was written by Stan Seibert originally intended for the Braidswood experiment. The RAT simulation has been developed over the experiment's lifetime into a highly detailed software package [79]. The GEANT4 toolkit contains intricate simulation methods, optimised and verified against data [81]. RAT includes calculations for the scintillation and emission of Cerenkov photons as well as their propagation through-

out the detector, including reflection, refraction, absorption, transmission and scattering. All pertinent Standard Model electroweak and hadronic physics and standard radiation-matter interactions at the MeV energy scale are included. Also implemented are particle generators and packages for the emulation of radioactive decay, solar neutrinos, reactor antineutrinos and supernovae events. Simulation in RAT also includes in-depth simulation of the electronics along with PMT and DAQ response. Data tables containing the run-by-run information of detector conditions can also be implemented in simulation for improved accuracy in the recreation of the detector’s response.

# 3 | Event Reconstruction

Event reconstruction is the process of extracting key physics parameters from triggered events in the detector. This chapter summarises the primary methods used to reconstruct event parameters such as position, time, energy and direction (water phase). Analyses presented in this work were carried out over both the water and partial fill phase, therefore event reconstruction in both phases are discussed.

The basic concept behind event reconstruction is to consider patterns in the raw PMT hit times to calculate the position, time, energy and direction of the physics event causing the detector to trigger. MeV-scale electrons interact and deposit energy in water and liquid scintillator, coming to a stop over the distance of approximately a centimetre [82] [75], smaller than the resolution of any of the position fitters in the water and scintillator phases. Event reconstruction algorithms referenced in this work all assumed that the culprit of the detector trigger was an energetic electron and assumed point-like energy deposition in the detector medium. The detector's responses to the typical particles measured in the detector are discussed further in chapter 8.

## 3.1 Position and Time Fit

Reconstruction algorithms use PMT hit times and hit PMT position patterns to calculate the most probable position and time of the event. The underlying methods used for determination of position and time in both water and scintillator are essentially identical. PMT hit time and position information are both used in the creation of ‘time residuals’ distributions.

### 3.1.1 Time Residuals

Time residual distributions are used as the primary tool to summarise PMT hit patterns and times. For a given event and associated triggered PMTs, time residuals are defined

and calculated for each hit PMT as:

$$t_{res}(\vec{r}_{ev}) = t_{PMT} - t_{t.o.f.} - t_{ev}, \quad (3.1)$$

where  $t_{PMT}$  is the hit time of PMT,  $t_{t.o.f.}$  is the time of flight for a photon travelling from an event position  $\vec{r}_{ev}$  to the hit PMT and  $t_{ev}$  is the time of the reconstructed event. The time of flight from an event to a given hit PMT position is calculated assuming straight line paths within each medium, while accounting for the refraction effects of light passing across medium boundaries. The most typical light path in an event consists of a photon travelling from an event in the scintillator, travelling through the acrylic of the AV, through the external light water and ending its journey on a PMT. Figure 3.1 displays the different refractive indices (against wavelength) a photon may experience as it travels across the SNO+ detector. Accounting for the light speeds and paths of photons in each medium allows for a time of flight calculation:

$$t_{t.o.f.}(\vec{r}_{ev}, \vec{r}_{PMT}) = \frac{d_{w/s}}{c_{w/s}^{eff}} + \frac{d_{AV}}{c_{AV}^{eff}} + \frac{d_w}{c_w^{eff}}, \quad (3.2)$$

where  $d$  and  $c_{\text{eff}}$  are respectively the distances travelled and the effective light speeds of a photon in each of the internal water/scintillator, AV and external water medium. Figure 2.9 shows the emission spectra for the various scintillation components in the scintillator cocktail, with the PMT efficiency. The effective velocity was calculated using the refractive index at 400nm, the most probable detected photon wavelength for the SNO+ scintillator cocktail and PMTs.

### 3.1.2 Event Position and Time Reconstruction

Figure 3.2 presents a simple demonstration of how hypothesised event positions are compared using time residuals. The raw PMT hit times in a triggered event are decided by the times of flight of photons travelling to the PMTs, as well as the intrinsic scintillation de-excitation emission times (section 2.3.2.2). In subtracting the times of flight, assuming the correct event position is used, the resulting time residual effectively yields the hit time distribution for an event occurring at the centre of the detector, isolating the scintillator's

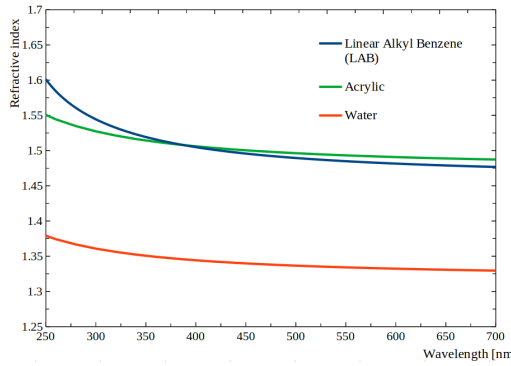


Figure 3.1: Plot displaying the refractive indices of light water, acrylic (making up the AV) and LAB, plotted against the wavelength of the photon propagating in the medium.

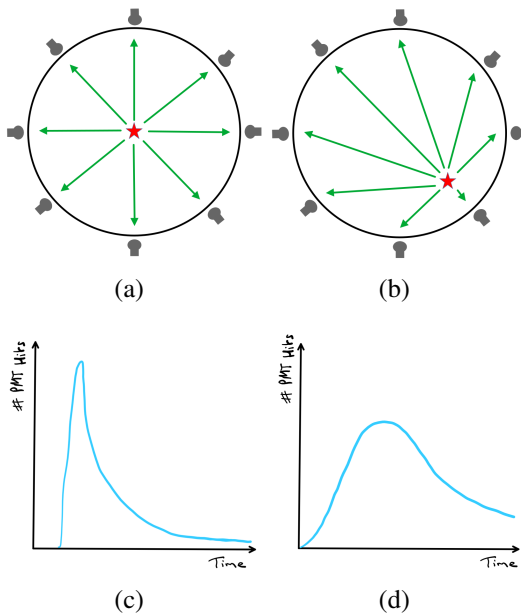


Figure 3.2: Sketches showing photon path lengths (green arrows) ending at PMTs, originating from events (red star) at (a) the centre of the detector (b) off-centre. (c) and (d) show drawings of the expected PMT hit time distribution shapes for the events in (a) and (b) respectively (without any time of flight subtractions).

emission time profile. Sketches (a) and (b) demonstrate the path lengths for light due to events at the centre, and some position off-centre respectively. Sketches (c) and (d) show the expected hit time distribution shapes for each event, without any time of flight subtractions applied. The off-centre events will have a wide range of short and long photon propagation times, yielding a wide hit time distribution. Subtracting the times of flight from the centre and off-centre events yields the narrow hit time distribution seen in plot (c), expected to have the same resulting time residual shape for both events. If the hypothesised position used in the time of flight calculations is incorrect, the calculation will

not yield the narrow scintillation emission spectrum, and instead produce a wide distribution, similar to that seen in (d). This leads to the basic principle used in reconstruction (for water and scintillator): the time residuals for a given event are calculated, varying the hypothesised event position  $\vec{r}_{ev}$  and time  $t_{ev}$ , until the time residual best matches the expected time residual at the centre of the detector. Formally, this is implemented in a likelihood fit. The likelihood, for a hypothesised event position and time at  $\vec{r}_{ev}$  and  $t_{ev}$ , given the collection of hit PMTs (of positions and times  $h_{\vec{x},t}$ ) in an event is calculated as:

$$\log \mathcal{L}(\vec{r}_{ev}, t_{ev} | h_{\vec{x},t}) = \sum_{i=0}^{N_{hits}} \log p(t_{res}^i(\vec{r}_{ev}^i, t_{ev}^i)), \quad (3.3)$$

where  $p(t_{res})$  is the probability density function (pdf) of the expected time residual distribution, generated in the simulation of many electron events. The most probable event position and time are the  $\vec{r}_{ev}$  and  $t_{ev}$  which maximise the likelihood, fitting the calculated time residual against the time residual pdf at the centre of the detector. Time residuals are predominantly dictated by the scintillator emission spectrum, but their shape is also affected by factors such as light propagation in the detector geometry, reconstructed position resolution and the time transit spectrum of the PMTs. Detector calibration sources are used to ensure the required agreement of simulated time residual pdfs and those measured in data. Chapter 4 discusses the calibration of scintillator emission times and light yield for the purposes of optimising position and energy reconstruction in the partial fill phase.

## 3.2 Direction (Water Phase)

Having measured the event's position in the detector, the direction of travel of the electron can be estimated from the hit PMT positions compared to the event position  $\vec{r}_{ev}$ :

$$\cos(\theta) = \vec{d} \cdot (\vec{r}_{pmt} - \vec{r}_{ev}) \quad (3.4)$$

The direction  $\cos(\theta)$  can be estimated through a likelihood fit using the pdf shown in figure 3.3. The distribution is peaked at  $41.4^\circ$ , corresponding to the previously shown

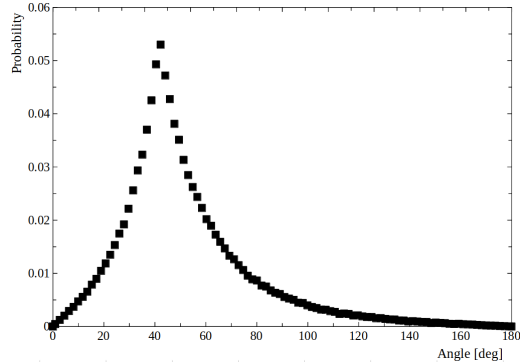


Figure 3.3: Pdf used in the likelihood fit of event direction in the water phase due to Cherenkov radiation.

Cherenkov angle in the ultra-relativistic limit in water.

At the time of writing, direction reconstruction in SNO+ has only been possible in the water phase. Cherenkov radiation still occurs for energetic particles in scintillator, but is generally obscured by the large scintillation light emission. The separation of Cherenkov and scintillation light due to MeV-scale radiation (while still retaining high light yields) is an active area of research. Prospects include liquid scintillators with slow scintillation emission times [83][84], water-based scintillators [85][86] and wavelength separators attached to PMTs [87]. Direction reconstruction in the SNO+ scintillator cocktail may also be possible for low concentrations of PPO [88].

### 3.3 Energy Fit

Energy reconstruction similarly applies the assumption that all events triggering the detector are due to electrons. Therefore, what is labelled as ‘reconstructed energy’ in this work is technically the electron equivalent reconstructed energy.

As introduced in chapter 2, energy reconstruction in both scintillator and water is essentially based on the total number of photons emitted by the detection medium due to the energy deposited into it by an energetic electron. The number of triggered PMTs in an event (nhits) is the primary parameter used to extract the number of photons emitted in the event. Energy reconstruction algorithms are used to account for the loss of any would-be hit PMTs. This loss of nhits (generally true for events at large radii) may arise

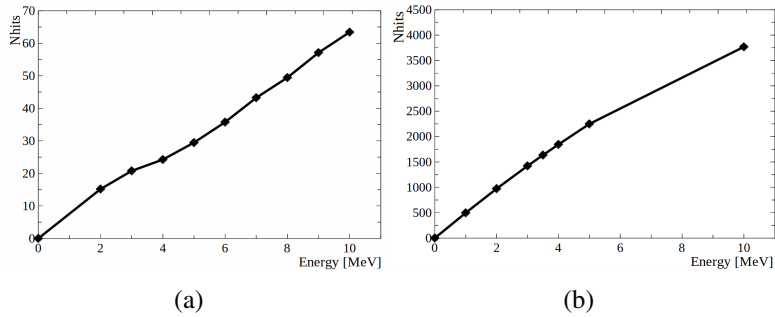


Figure 3.4: Plots of expected nhits versus electron energy, for electrons generated at the centre of the detector. (a) Water phase (b) Pure Scintillator phase.

due to: the detector geometry, PMT coverage, the optical absorption and scattering properties of the various detector media, the PMTs' quantum efficiency, angular response and dark noise rates. These calculations are all carried out in simulation, where the accuracy of the simulation is established by detector calibration.

Figure 3.4 shows plots of the expected nhits versus electron energy in the water and pure scintillator phases respectively, for events at the centre of the detector. The water nhits vs energy function in plot 3.4(a) was calculated from well-calibrated water phase data. The pure scintillator distribution was calculated in simulation, where the scintillator light yield properties were determined from tabletop measurements of the SNO+ scintillator cocktail [89] (discussed further in chapter 4). It can be seen that nhits scales approximately linearly with electron energy in both media. Nhits due to Cherenkov radiation deviates from linearity for low energy electrons. Deviation occurs in scintillator at higher energies, as hits start to saturate on the PMTs. The SNO+ tubes are not optimal in separating multiple photon hits on a single tube, multi-hits becoming increasingly frequent for events at large radii. Despite the sub-optimal PMTs, there are methods used to correct for multiple photon hits, such as the multi-hit correction [90][75].

## 3.4 Light Yield Across the Phases

The light yield in the SNO+ scintillator cocktail is almost 100 times that of water, emitted in all directions, producing more PMT hits, resulting in marked improvements in both reconstructed event position and energy resolutions. The maximum achievable energy

Table 3.1: Summary of the light yield measured in the water [91] and partial scintillator fill phases (chapter 4), with the expected light yields in the fully filled scintillator phases [75][89]. The light yields shown are for electrons at the centre of the detection medium ( $z = 2\text{m}$  in the partial fill case).

Phase	Light Yield (nhits/MeV)
Water	7.5
Partial Fill	330
Pure Scintillator	600
Te-loaded Scintillator	480

resolution of the SNO+ detector is decided by the Poisson limit:  $\sigma_E/E = 1/\sqrt{N(E)}$  where  $N(E)$  is the number of hit PMTs in an event due to an electron of energy  $E$ .  $\sigma_E$  is the standard deviation in the reconstructed energy. Apart from the improved resolution in reconstruction, the increased number of nhits per unit energy allows for much lower energy thresholds to be accessed in the scintillator phase.

The scintillator light yield is also dependent on the scintillator cocktail. Chapter 4 deals with the calibration of the scintillator in the partial fill phase which had a PPO concentration of 0.5g/L instead of the 2g/L concentration to be used in the final scintillator cocktail. The scintillator light yield is also quenched due to the loading of Te (section 2.4.1). Table 3.1 summarises the measured and expected light yields for the various detection media, from the water phase to the upcoming pure and Te-loaded scintillator phases.

## 3.5 Beyond Position and Energy

A number of other data analysis parameters were developed to assist in the isolation of signal from background events occurring in the SNO+ detector. The following section defines the parameters which were utilised in the data analyses that will be presented later in this work.

**ITR (Water)** The In Time Ratio (ITR) corresponds to the ratio of nhits with PMT time residual times between -2.5 and 5ns, to the total nhits. Cherenkov light yields very early hit times, where applying a minimum threshold ITR value can remove non-physics events in water, for example due to instrumentation, which would have low ITR.

**$\beta_{14}$  (Water)** This parameter was developed to distinguish between events with different levels of isotropy in the hit PMT pattern. Cherenkov radiation due to an energetic  $\beta$ -particle is strongly directional, while a 1MeV  $\gamma$ s can Compton scatter many electrons over its  $\sim$ 30cm propagation path in water, leading to more isotropic light emission. The parameter is calculated as:

$$\beta_{14} = \beta_1 + 4\beta_4 \quad (3.5)$$

where the first and forth Legendre polynomials are calculated using the cosine of the angle between all possible pairs of hit PMTs  $i$  and  $j$  [92].

$$\beta_k = \sum_i \sum_{j \neq i} P_k(\cos(\theta_{ij})) \quad (3.6)$$

**$\mathbf{u} \cdot \mathbf{r}$  (Water)** This is the product of the fitted direction with the fitted position of the event. It helps distinguish inward and outward facing events. For example  $\gamma$ s propagating from PMT glass to within the AV, are strongly skewed in negative  $\mathbf{u} \cdot \mathbf{r}$ , compared to radiation emitted isotropically originating from within the AV.

**Data Cleaning Masks** Referenced in chapter 2 are the instrumental effects which can cause the detector to trigger, providing contamination events. Data cleaning masks use low-level detector information such as PMT positions and hit times to remove these instrumental event, which are typically very distinct from physics events in their PMT hit patterns. Data cleaning masks generally provide sub-percent sacrifice of physics events.

# 4 | In-Situ Measurement of BiPo214 and Scintillator Calibration in the Partial Fill Phase

This chapter presents the measurement of BiPo214 coincident events in the partial fill phase for the purposes of a background level measurement, as well as a calibration of the scintillator’s properties.

**Background Rate Measurement** First, a measurement of the rate of BiPo214 events due to the supported  $^{222}\text{Rn}$  present in the scintillator was calculated. The aim of the measurement was to separate the  $^{222}\text{Rn}$  rate from the  $^{238}\text{U}$  chain content in the scintillator, from the  $^{222}\text{Rn}$  that had infiltrated the detector during the scintillator fill period. An approximate measurement was important such that if the contamination level was much larger than expectation, any contamination issues could be addressed before the detector was fully filled. The supported  $^{222}\text{Rn}$  rate measurement in the partial fill configuration was found to agree with the purity level expected and required for the upcoming  $0\nu\beta\beta$  search. More rigorous measurements are expected in the now fully filled detector.

**Scintillator Calibration** To minimise scintillator contamination ahead of the upcoming  $0\nu\beta\beta$  search in the Tellurium phase, no calibration sources were introduced inside the AV during the partial fill phase. In response to this, BiPo214 decays, occurring throughout the internal volume of the detector, provided the first calibration source for the scintillator cocktail optics (LAB + 0.5g/L PPO). The calibration with BiPo214 involved the tuning of scintillator’s response to  $\beta$  and  $\alpha$  particles separately, for the accurate simulation of scintillation light yield and scintillation emission times. These calibrations of the scintillator optics were required for all physics analyses carried out over the partial fill phase, and were found to greatly improve position and energy reconstruction.

## 4.1 BiPo214 Event Rates in the Partial Fill Phase

Minimising contamination in the detector is paramount for the vast majority of low energy neutrino experiments. Despite the concerted decontamination efforts made in these

experiments, some minimum amount of naturally occurring radioactive contamination is unavoidable throughout the detectors, originating from  $^{238}\text{U}$  and  $^{232}\text{Th}$  decay chains. For SNO+, understanding and minimising the rate of these contaminants is of the utmost importance for the eventual  $0\nu\beta\beta$  search (appendix A) and other physics analyses.

### 4.1.1 $^{238}\text{U}$ and $^{232}\text{Th}$ Decay Chains

Radioactive emission in the decay of certain daughter elements in the  $^{238}\text{U}$  and  $^{232}\text{Th}$  decay chains share event energies with those of the expected signal events in the  $0\nu\beta\beta$  analysis, impacting the search. Figure 4.1 shows simulations of the region of interest (R.O.I.) in energy, with expected  $0\nu\beta\beta$  signal shown in red. The R.O.I. is defined in the figure as  $-0.5\sigma - 1.5\sigma$  around the  $0\nu\beta\beta$  Q-value of 2.53 MeV, where  $\sigma$  is the detector's energy resolution expected in the Te-loaded scintillator phase. A great deal of time and effort has therefore been exerted over the experiment's lifetime to minimise the concentration of these impurities, through the purification of the liquid detection medium bulk itself (water and scintillator), along with all the components in the detector that can also provide contamination.

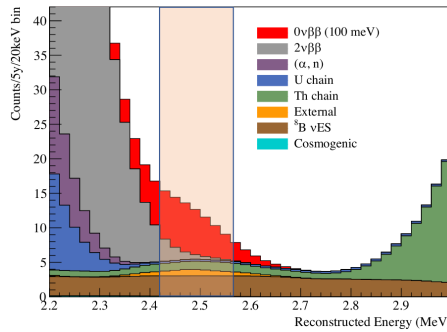
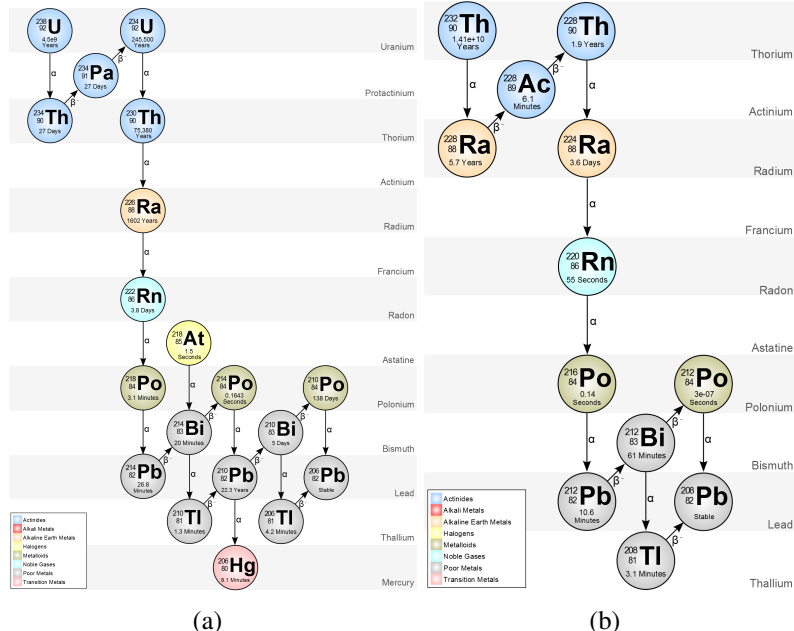
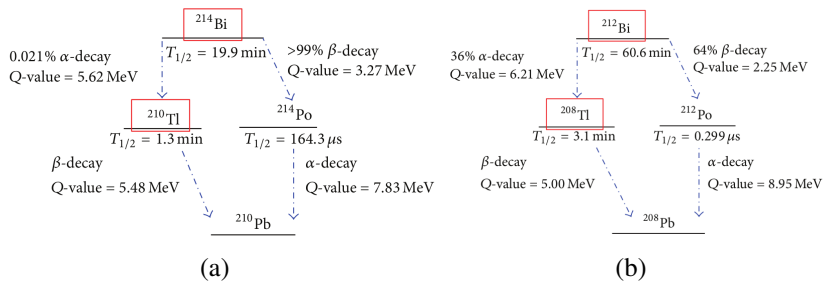


Figure 4.1: The simulated  $0\nu\beta\beta$  R.O.I., where backgrounds have been scaled to their expected rates, taken from [93].

Figure 4.2 shows the  $^{238}\text{U}$  and  $^{232}\text{Th}$  decay chains. Figure 4.3 provides a closer look at two particularly disruptive daughter elements in these decay chains,  $^{214}\text{Bi}$  and  $^{212}\text{Bi}$ , both emitting  $\beta$  and  $\gamma$  particles in  $\beta$  decays, occurring 99.979% and 64% of the time respectively. Each isotope's  $\beta$  decay energy spectrum have end-points of 3.27 and 2.25 MeV and are found in the  $^{238}\text{U}$  and  $^{232}\text{Th}$  decay chains, respectively.

The measurement of  $^{214}\text{Bi}$  can give insight into the supported  $^{222}\text{Rn}$  in the bulk of the


 Figure 4.2:  $^{238}\text{U}$  and  $^{232}\text{Th}$  decay chains. Plots taken from [94].

 Figure 4.3: A closer look at the  $^{214}\text{Bi}$  and  $^{212}\text{Bi}$  decay chains within the  $^{238}\text{U}$  and  $^{232}\text{Th}$  decay chains respectively. Red boxes highlight background decays of concern in the  $0\nu\beta\beta$  analysis. Plots taken from [95].

scintillator, an important background measurement in the campaign preparing for the Te-loaded scintillator phase. Appendix B similarly deals with the measurement of another background in the  $0\nu\beta\beta$  analysis, categorised as external  $\gamma$ s in figure 4.1.

Established now is the importance of having a maximally pure volume of scintillator. For the period over which the detector was being filled with scintillator, it was important to measure and frequently monitor the contamination levels of the scintillator, such that the addition of scintillator could be halted if the background levels became unexpectedly large.

### 4.1.2 Tagging BiPo214 during the Partial Fill Phase

Despite the troublesome nature of the  $^{212}\text{Bi}$  and  $^{214}\text{Bi}$  decays in the detector, their saving grace is the very short lifetimes of their Po daughters.  $^{214}\text{Po}$  and  $^{212}\text{Po}$  have decay lifetimes of 0.3 and 164.3 $\mu\text{s}$ , and Q-values of 7.8 and 8.95MeV respectively [96]. Due to the scintillation quenching for  $\alpha$ -particles, the scintillation light emitted is scaled down by a factor of  $\sim 12$  in the LAB + 0.5g/L PPO scintillator cocktail compared to an electron of equivalent energy. Despite the quenching, the energy was still well above the detector's detectable energy threshold in the partial fill phase.

The short Po lifetimes allowed for the use of a very powerful data analysis tool, allowing an analyser to search for the coincident Bi and Po events occurring close together in time and space. The distinct coincident signal allows for their straightforward removal in analyses in which they are a background. The coincidence tagging also allowed for a very pure sample of BiPo pairs to be extracted from the partial fill data, separated from the other background and instrumental events present in the detector, which are uncorrelated in time and position.

Tagging BiPo214 events was made more difficult during the filling stages of the detector due to PPO being added to the scintillator in large batches. This had the effect of producing, for periods of time during the fill, inhomogeneous PPO distributions and therefore varying light yields throughout the scintillator (the effects of PPO can be seen in section 2.3.2.1). PPO inhomogeneity was seen to last sometimes for weeks, until more scintillator was added, or cavity recirculation was activated, disturbing the system.

**Period of Stability - the Partial Fill Phase** With the onset of the Covid-19 pandemic around March 2020, the scintillator fill was halted with 365t of scintillator, with minimal access to SNOLAB allowed. Although this was obviously a large drawback to the experiment, it did provide an extended period of time of where the detector was stable. The previously added PPO had since become homogeneously concentrated throughout the detector, yielding homogeneous light yield around the detector.

### 4.1.2.1 Analysis Cuts

Table 4.1 summarises the analysis cuts originally optimised by J. Wang over the stabilised partial fill phase beginning in March 2020 [97]. Thanks to the distinct BiPo coincidence signal and large event energies considered, background events due to instrumentals were expected to be negligible. Regardless, a simple data-cleaning mask was applied to all events recorded in data. This mask was assumed to yield negligible signal sacrifice. The BiPo coincidence analysis cuts are similar to those used in the antineutrino analysis, discussed in chapter 6. The main measure of energy used to distinguish Bi and Po events was nhits. Energy reconstruction had not yet been optimised prior to the calibration work presented later in this chapter. It will be shown however that it was still possible to amass a very high purity collection of tagged BiPo214 events.

Table 4.1: Table summarising the cuts used to tag BiPo214 events in the partial fill phase. Unless specified, the same stated cuts were applied to both the prompt Bi and late Po events. Various, more strict positional cuts are also used throughout this chapter. For reference, the water-scintillator interface in this analysis was at  $z = 0.75\text{m}$ .

Parameter	Min	Max
Radius (m)	0	6
z-position (m)	0.85	6
Prompt Nhits	330	1050
Late Nhits	170	320
$\Delta t$ (ns)	4000	1e6
$\Delta r$ (m)	0	1
Position Fit Valid	True	True

### 4.1.2.2 BiPo214 Sample Purity - Accidentals Contamination

Figure 4.4 shows the nhits spectra for tagged  $^{214}\text{Bi}$  and  $^{214}\text{Po}$  events within the fiducial volume defined by  $z > 0.85\text{m}$  and  $r < 5.7\text{m}$ . Also shown are the time residuals for each (section 3.1.1), which represent the scintillator emission times the  $\beta$  and  $\alpha$  particles each decay emits respectively. Plot 4.4(c) of the time residuals demonstrates the observable difference in time residuals for  $\beta$  and  $\alpha$  particles in the LAB + 0.5g/L PPO scintillator cocktail. It is expected that the higher PPO concentration in the final scintillator cocktail (2g/L), will enhance  $\alpha$ - $\beta$  discrimination ability, as scintillator emission times are reduced [98].

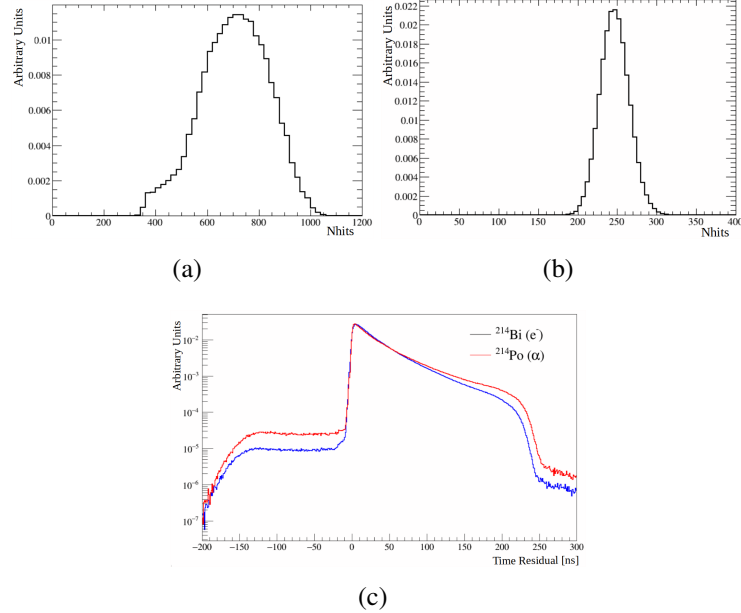


Figure 4.4: Plots of the nhits distributions found in Partial Fill data for tagged a)  $^{214}\text{Bi}$  and b)  $^{214}\text{Po}$ . c) shows the time residuals. BiPo214 events had positional cuts  $r < 5.7\text{m}$  and  $z > 0.85\text{m}$  applied, tagged from the 4th of April to the 12th of May 2020 (runs 257669-259063). These normalised time distributions show a noticeable difference in the background noise level for negative time residual times, which is likely due to light output for Po214 events is less than  $^{214}\text{Bi}$  relative to the base dark noise level.

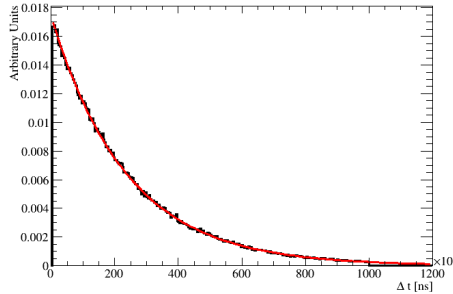


Figure 4.5: Normalised  $\Delta t$  distribution for tagged BiPo214 in  $r < 5.7\text{m}$  and  $z > 0.85\text{m}$ , tagged over runs 257669-259063. The red line depicts a fit using an exponential plus a constant.

Figure 4.5 shows the  $\Delta t$  distribution, the time between Bi and Po events for tagged BiPo214 event pairs within the volume defined by  $r < 5.7\text{m}$  and  $z > 0.85\text{m}$ . The contamination of random non-BiPo background event pairs, uncorrelated in time, that passed the BiPo214 coincidence cuts are known as accidentals. The accidental contamination was calculated by fitting the  $\Delta t$  distribution with the function  $A \exp(-t/\tau_{Po}) + C$ , where the normalisation factor  $A$ ,  $C$  and the  $^{214}\text{Po}$  decay time  $\tau_{Po}$  were allowed to float freely in the fit. Since accidental pairs are uncorrelated in time, their  $\Delta t$  distribution was expected to

be flat. The integral of the constant component  $C$  represents the number of accidentals in the sample. Fitting the distribution using Minuit's  $\chi^2$  option [99] yielded a decay time constant of  $235.9 \pm 0.9 \mu\text{s}$  where the uncertainty shown was the uncertainty in the fit, in agreement with the well-measured  $^{214}\text{Po}$  lifetime [100][96]. The fit value of the constant term demonstrated that there was very little accidental contamination of  $\mathcal{O}(10^{-3})\%$  in the sample of BiPo214 events tagged in the scintillator volume defined by  $r < 5.7\text{m}$  and  $z > 0.85\text{m}$ .

The following section describes the extraction of the supported  $^{222}\text{Rn}$  from the scintillator, using the very pure collection of tagged BiPo214 events.

## 4.2 Scintillator Supported Contamination Measurement in the Partial Fill

### 4.2.1 Separation from External $^{222}\text{Rn}$

The measurement of the  $^{222}\text{Rn}$  contamination supported from the scintillator itself relies on the separation of BiPo214 events due to the supported  $^{222}\text{Rn}$ , from ingress  $^{222}\text{Rn}$  that had infiltrated into the detector due to air exposure. Ingress  $^{222}\text{Rn}$  was generally seen each time a batch of scintillator was added to the detector. The cover gas system (chapter 2) was found to be adept in minimising the  $^{222}\text{Rn}$  pervading the scintillator volume from the deck, during and between scintillator fills. It will be shown however that small amounts of  $^{222}\text{Rn}$  still occasionally leaked in, through separate points of entry.

Separating of the two  $^{222}\text{Rn}$  contributions was possible during the extended period of the partial fill phase, where there were not large surges of ingress  $^{222}\text{Rn}$  with each fill. BiPo214 events due to supported  $^{222}\text{Rn}$  from the scintillator are in secular equilibrium [101]. These decays effectively occur at a constant rate against time, due to the extremely long lifetimes of the radioisotopes high up in the  $^{238}\text{U}$  decay chain. BiPo214 events originating from  $^{222}\text{Rn}$  ingress however are out of equilibrium, dependent on the 3.82 days half-life of  $^{222}\text{Rn}$  found in the air [102]. The separation of the long and short-lived sources of BiPo214 can be achieved by measuring the BiPo214 events over many days

of stable data, measuring the decay of  $^{222}\text{Rn}$ .

The rate per day of BiPo214 events was fitted with an exponential plus constant. The exponential term represents the BiPo214 rate from externally sourced  $^{222}\text{Rn}$ , which decays away with time. The constant term measures the supported BiPo214 events, supplied from parent isotopes higher up in the  $^{238}\text{U}$  decay chain:

$$\frac{dN}{dt} = A_{Rn} \exp(-t/\tau_{Rn}) + r_0 \quad (4.1)$$

where  $A_{Rn}$  is the normalisation rate and  $\tau_{Rn} = 3.82/\ln(2)$  days is the decay lifetime for the decaying  $^{222}\text{Rn}$ .  $r_0$  is the parameter of interest and represents the rate of BiPo214 events supported by the scintillator bulk itself. A likelihood fit was carried out using the Minuit fitting package.  $A_{Rn}$  and  $r_0$  were allowed to float freely and  $\tau_{Rn}$  was fixed to its expected value. This fit assumed that the period of data was stable and had no additional ingress  $^{222}\text{Rn}$  entering the detector over the data period measured. Due to this assumption, periods of data with even small amounts of  $^{222}\text{Rn}$  ingress during the measurement period, would effectively increase the fitted value of  $r_0$ , leading to the measurement of an apparent high concentration of long-lived contamination in the scintillator.

The next section first presents a fit of  $r_0$  during the partial fill period which yielded the lowest apparent concentration of  $^{222}\text{Rn}$  supported by the scintillator alone.

#### 4.2.2 Partial Fill Result

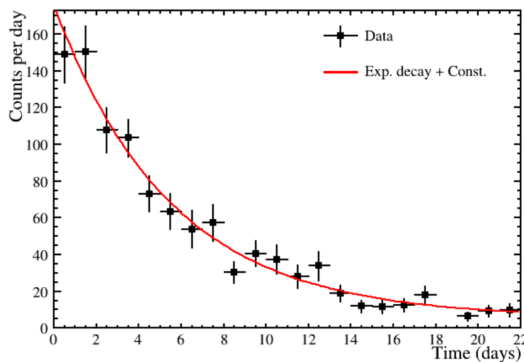


Figure 4.6: Rate per day of tagged BiPo214 events vs time, for events within a fiducial volume of  $r < 5.7\text{m}$  and  $2 < z < 4\text{m}$ . Shown in red is the fit function using eqn. 4.1. Data shown was taken from the 7<sup>th</sup> to the 25<sup>th</sup> July 2020.

The measurement of the supported BiPo214 rate was made using events tagged over a period with particularly stable detector conditions from the 7<sup>th</sup> to the 25<sup>th</sup> July 2020 (runs 260240-261078).

Figure 4.6 shows a plot of the BiPo214 rate per 24hrs over the stated time period, for events within a fiducial volume of  $r < 5.7\text{m}$  and  $2 < z < 4\text{m}$ . The rate was calculated accounting for the detector's livetime, the fraction of time per day the detector was actively recording data. The gap in data on day 18 was excluded as the detector spent less than 30% of the day recording data due to detector maintenance.

The fit yielded an  $r_0$  value of  $5.3 \pm 1.5$  events per day. The tagging efficiency for BiPo214 events occurring in the volume defined by  $r < 5.7\text{m}$  and  $2 < z < 4\text{m}$  compared to the total number of events occurring in the full scintillator spherical cap volume, defined by  $z > 0.75\text{m}$  and  $r < 6\text{m}$ , was calculated in MC simulations to be 31.3%. This rate was converted to a scintillator contamination level, expressed in terms of an equivalent mass of  $^{238}\text{U}$  per mass of scintillator:

$$C_{gU/g} = \frac{r_0 \tau_{238U}}{x_{eff}} \cdot \frac{m_{238U}}{N_A M_{scint}} \quad (4.2)$$

where  $\tau_{238U}$  is the  $^{238}\text{U}$  lifetime ( $= 6.44 \times 10^9$  years),  $x_{eff}$  is the BiPo214 tagging efficiency,  $m_{238U}$  is the atomic mass of a  $^{238}\text{U}$  atom,  $N_A$  is Avogadro's number and  $M_{scint}$  is the total mass of the scintillator contained within the AV. The partial fill phase contained a total 365t of scintillator in the detector, where 10t of this was contained in the neck of the detector, outside of the AV, thus  $M_{scint} = 355\text{t}$ .

The  $^{238}\text{U}$  concentration  $C_{gU/g}$  was calculated using the fit result shown in figure 4.6 as  $4.5 \pm 1.3 \times 10^{-17} \text{ g}_{\text{U}}/\text{g}_{\text{LAB}}$ , where the uncertainty shown is the uncertainty of the likelihood fit of  $r_0$ , carried out in Minuit[99]. Extra sources of uncertainty not considered here are discussed in the conclusion of this section. The measurement places it in the order of magnitude purity level required for the Te-loaded phase and what has been achieved in other liquid scintillator experiments such as Borexino and KamLAND [103][51].

### 4.2.3 Rn Leaking: Evolution in Time and Space

Shown was the contamination level calculation for a short period of 22 days of stable data, using a small volume of the scintillator away from the top of the AV and water-scintillator interface. The partial fill phase extended from the 21<sup>st</sup> March to the 24<sup>th</sup> of October 2020, where the rate of BiPo214 decays was not constant.

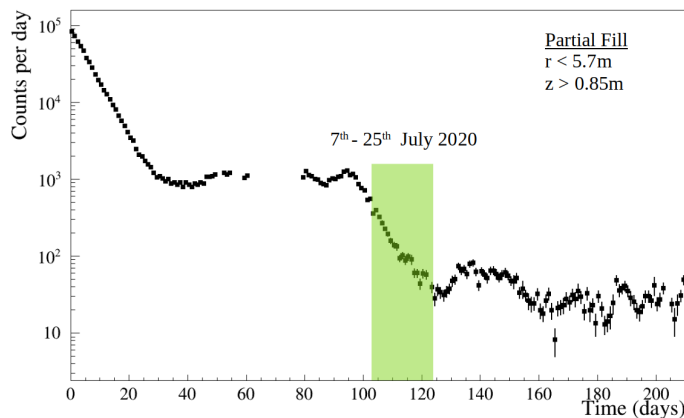


Figure 4.7: The rate of BiPo214 events per day against time, beginning on the 21<sup>st</sup> March 2020 in the partial fill phase, for events within a fiducial volume of  $r < 5.7\text{m}$  and  $z > 0.85\text{m}$ . Vertical error bars reflect statistical uncertainty.

Figure 4.7 displays the BiPo214 rate per day over the partial fill phase, for events within  $r < 5.7\text{m}$  and  $z > 0.85\text{m}$ , beginning on the 21<sup>st</sup> March 2020. The powerful BiPo214 coincidence analysis cuts, allowed for a minimal need of data-cleaning for their extraction from data. It was only required that a run had a minimum runtime of 30 minutes (avoiding potentially problematic data recorded during or shortly after periods of detector maintenance). The multiple-day gap in data beginning at day 60 coincides with the period of time that the detector was switched off for maintenance purposes, from the 23<sup>rd</sup> of May to the 10<sup>th</sup> of June 2020.

Apparent in the figure are the variations in BiPo214 rate with time. Shortly after the last scintillator fill period in March, it can be seen in the early days of the data that the BiPo214 rate decayed away with the  $^{222}\text{Rn}$  lifetime, until the BiPo214 rate reached a plateau at roughly day 30. This period with an approximately constant BiPo214 rate continued until the 26<sup>th</sup> of June (day 94) where the rate began to fall and the decay of  $^{222}\text{Rn}$  in the detector was seen again. Prior to day 94, it was believed that there was a

small rate of  $^{222}\text{Rn}$  leaking into the detector, at a rate in equilibrium with the decaying  $^{222}\text{Rn}$ , leading to the constant BiPo214 rate seen.

Searching for the source of the Rn infiltrating the detector was the target for an assembled group of SNO+ collaborators. The team had the rather scrupulous task of searching for possible leaks for all possible points of contacts the AV had with the deck, on which operations are carried out [104]. The team’s assessments ultimately lead to a number of upgrades. One noteworthy detector change occurring on the 25<sup>th</sup> of June (day 94) was the switching off of the detector’s bubbler systems. The bubbler system is a series of downward facing tubes that are used to measure the liquid level, using periodic expulsion of N<sub>2</sub> gas. The decrease seen in the BiPo214 rate following the disablement of the bubblers caused it to be the lead suspect. Assays of the N<sub>2</sub> gas in the dewer used to supply the bubblers, were found to have much lower Rn contamination compared to the air in the detector cavity ( $\mathcal{O}(10^{-5})$  Rn concentration in comparison [105]). However, the connections and tubing connecting the dewer to the bubblers were suspected to allow Rn diffusion into the system. Since then there have been upgrades to o-rings, including a replacement of the plastic piping with stainless steel versions [105].

Following the halt of the Rn leakage, the second period of falling BiPo214 rates provided an extended period over which the concentration of  $^{222}\text{Rn}$  supported by the scintillator could be measured. The green box highlights the period over which the minimal value of  $C_{gU/g}$  was measured, shown previously in figure 4.6.

It can be seen following this measurement period, that the BiPo214 rate subsequently increased and continued to fluctuate around an approximately constant rate. Over this period, there was a number of runs with externally deployed calibration sources, along with work carried out on the deck, suspected to have caused small increases in Rn. Following the restart of scintillator fill, beyond any data shown here, BiPo214 rates again increased as more scintillator was added.

#### 4.2.3.1 Motivation for Positional Cuts

The chosen z-position cuts, were used to find the most stable region of scintillator, with the lowest number of BiPo214 decays per unit volume. The cover gas system greatly

reduced  $^{222}\text{Rn}$  ingress when the scintillator was not being filled, but there were still small amounts of  $^{222}\text{Rn}$  being fed into the top of the detector. These impacted the measurement of  $r_0$ , where the fit assumes no additional Rn enters the detector during the fit time period. The  $z < 4\text{m}$  cut was applied to avoid this region.

An added complexity to the measurement, was the movement of contamination within the scintillator volume, evolving with time. As contamination was fed into the detector from the top, regions with high BiPo214 rates at the top of the detector were found to migrate to lower z-positions with time. This movement of contamination was found following periods with increased BiPo214 rates, likely due to contamination from the neck of the AV. Pockets of scintillator with high BiPo214 rates were found to fall from the top of the AV to the bottom, over the order of days [106]. The ‘fall’ of contamination was also seen for  $^{210}\text{Po}$  [107].

The Rn that had previously migrated from the top of the scintillator to the bottom, was found to persist longer than the scintillator at the middle and top. Due to the stratification, the chosen z-position cuts  $2 < z < 4\text{m}$  yielded a lower measurement of  $r_0$  compared to when the entire scintillator bulk was considered (where Rn rates were higher at the top and bottom of the scintillator). These stratified regions in BiPo214 rates were found to eventually dissipate with time.

#### 4.2.4 BiPo214 Rate Measurement Conclusion

Not included in the presented contamination measurement are uncertainties in the total scintillator mass, accounting for inhomogeneous regions of contamination in the scintillator and uncertainties in the BiPo214 tagging efficiency. These uncertainties were not accounted for, but are not necessarily negligible.

The purpose however of this measurement was to provide an order of magnitude measurement of the bulk scintillator contamination during the temporary partial fill period, such that if the contamination level was much larger than expectation, contamination issues could be addressed before the detector was fully filled.

The approximate measurement showed a supported contamination  $\mathcal{O}(10^{-17})gU/g$  which

meets the expected  $^{238}\text{U}$  decay chain contamination levels on-target for the  $0\nu\beta\beta$  [95]. More scrupulous measurements of the scintillator contamination under more stable conditions, accounting fully for all systematic uncertainties, will be made in the completely filled and calibrated scintillator detector.

It has been shown that BiPo214 coincidence event rates allowed for the key calculation of the overall  $^{238}\text{U}$  decay chain contamination level. The next section describes a first calibration of the scintillator cocktail’s optical properties, using the high purity sample of BiPo214 events distributed throughout the detector, collected over partial fill.

### 4.3 Scintillation Emission Calibration with BiPo214

Shown in chapter 3 was the use of time residual distributions to reconstruct event position and subsequently energy. The method relied upon the simulation of scintillator emission to create time residual pdfs (section 3.1.2), against which PMT hit times in data were fit. It was necessary therefore that the simulations used to generate the expected time residual pdfs needed in reconstruction, accurately reflected the time residuals seen in data. Ensuring position and energy reconstruction matching in data and simulation was undoubtedly important for any of the data analyses carried out over the SNO+ partial fill phase. Calibration of the scintillator emission times was required in order to achieve this.

Despite having no calibration sources introduced into the detector during partial fill, BiPo214 events distributed throughout the detector provided an opportune first calibration source of  $\alpha$ s ( $^{214}\text{Po}$  decay) and  $\beta$ s ( $^{214}\text{Bi}$  decay). Using the tagged BiPo214 events, it was possible to measure directly in data the scintillator’s response to  $\alpha$  and  $\beta$  particles separately, seen in the time residuals of  $^{214}\text{Po}$  and  $^{214}\text{Bi}$  events. Simulations were tuned such that the distributions in data and simulation agreed. Prior to this first calibration, simulations assumed scintillator optical parameters measured in benchtop experiments.

Unless stated otherwise, the BiPo214 data used in the following sections for the calibration of the scintillator properties was taken from the 4<sup>th</sup> of April to the 5<sup>th</sup> of May 2020 (runs 257669-259063).

### 4.3.1 Scintillator Emission Prior to Calibration with BiPo214

Benchtop measurements of the SNO+ scintillator cocktail were made prior to the partial fill scintillator phase [108][109]. The scintillation emission time model employed in RAT is made up of a sum of exponentials, assuming a scintillator rise time parameter, with a number of short and long decay time components [108]. The model parameterising the pdf for the emission times of scintillation photons emitted from a scintillator molecule was described in RAT as:

$$f(t) = \sum_{i=0} N_i \frac{e^{-\frac{t}{\tau_i}} - e^{-\frac{t}{\tau_{rise}}}}{\tau_i - \tau_{rise}} \quad (4.3)$$

where  $\tau_i$  and  $N_i$  are the decay constant and the relative contribution of the  $i^{th}$  exponential decaying component in the sum.  $\tau_{rise}$  is the rise time of the emitted scintillation light. Table 4.2 summarises model parameters used for the LAB + 0.5g/L PPO cocktail, derived from the benchtop scintillator timing fits [110].

Table 4.2: Table summarising the time constants measured in benchtop measurements for the LAB + 0.5g/L PPO cocktail in [110]

Benchtop Measurements - Scintillation Time Parameters							
Particle	$\tau_1$ [ns]	$\tau_2$ [ns]	$\tau_3$ [ns]	$A_1$	$A_2$	$A_3$	$\tau_{rise}$ [ns]
$\beta$	7.19	24.81	269.87	0.553	0.331	0.116	0.8
$\alpha$	6.56	23.82	224.19	0.574	0.311	0.115	0.8

Plots 4.8(a) and 4.8(c) show comparisons of the time residuals calculated using partial fill data with simulation for  $^{214}\text{Bi}$  and  $^{214}\text{Po}$  events. Apparent is the large discrepancy in the measured and expected time residuals when the benchtop measured emission times were assumed. In order for reconstruction to agree in data and simulation, the aim was to provide improved agreement between data and simulation times residuals by altering the scintillator emission times in simulation.

The method used to identify more appropriate optical parameters was an uncomplicated approach: BiPo214 events were repeatedly simulated, under the same detector conditions for the same runs used in data and were compared to the time residuals distributions measured in data, tuning the emission times until acceptable agreement was achieved.

### 4.3.1.1 Assumed Other Optical Parameters

The scintillator emission times of interest are the leading dictator of time residual distributions, but are not the sole factors which decide their shape. Required in the calculation of time residuals is the event trigger time, the reconstructed event position and the time of flight for a photon from the event position to a given PMT (section 3.1.1). There are a number of factors (secondary to emission times) which can affect the time residual shape.

The following factors were not expected to significantly impact the time distribution shape, but are summarised for completeness. Those other factors used in simulation (and in time of flight calculations) in the various SNO+ mediums were: photon absorption lengths, refractive indices and Rayleigh scattering lengths. Specific to the scintillator are factors such as reemission probability for LAB+PPO (the probability a photon absorbed by the scintillator is reemitted) and the reemission time decay time constant. Each of these factors are implemented in simulations in the form of a wavelength-dependent function. The optical factors for the non-scintillator media i.e. the external water and AV, had been previously measured in external laserball scans in the water phase of the experiment, so were still valid in the partial fill phase, summarised by A.S. Inácio in [111]. Calibration of the PMTs' timing and charge response, which affects position reconstruction were also measured in these water phase laserball scans.

Assumptions were also made for the LAB + 0.5g/L PPO scintillator cocktail in partial fill, as some benchtop measurements were only carried out for the LAB + 2g/L PPO solution:

- Absorption lengths: the absorption lengths for photons in LAB and PPO were linearly scaled with PPO concentration with respect to measurements made with 2g/L PPO concentration [89][112].
- The remission probability [71] along with the associated reemission times in LAB+PPO [108] were assumed to be constant with PPO concentration.

Having stated the assumed non-emission time optical parameters, the next section summarises the scintillation emission times which resulted in the best agreement with data.

### 4.3.2 Results of Scintillator Emission Time Tuning

The tuning of the scintillation emission time parameters alone was not expected to perfectly correct the time residual shape disagreement seen in data and simulation, since all the other optical parameters which also affect time residual shape had not yet been measured in-situ. The main aim however was to provide much improved data-MC agreement and in turn enhance position and energy reconstruction for the partial fill phase.

$^{214}\text{Bi}$  and  $^{214}\text{Po}$  events tagged in the region of  $z > 1.5\text{m}$  and  $r < 5\text{m}$  were chosen to compare data and MC and tune the emission time parameters. This region was chosen as to avoid the scintillator-water interface at  $z = 0.75\text{m}$ , as well as regions near the AV. Nonphysical reconstruction effects can occur for events very close to  $z = 0.75\text{m}$ , due to the position fitters incorrectly treating events originating in below the interface in the water as events occurring in the scintillator and vice-versa. It will be shown later however that these reconstruction effect produce small impact to the time residual distributions. For events with  $r \sim 5.4\text{m}$ , total internal reflection becomes an appreciable factor for light originating from within the AV due to the difference in refractive index of the scintillator and external water (figure 3.1). This generally leads to worse resolutions in reconstructed position and energy for events near the AV compared to events at smaller radii.

Table 4.3: Table summarising the updated scintillation time constants for the LAB + 0.5g/L PPO cocktail using BiPo214 events, yielding the improved time residual shape agreement in simulation and data.

In-situ Measurements with BiPo214 - Scintillation Time Parameters							
Particle	$\tau_1$ [ns]	$\tau_2$ [ns]	$\tau_3$ [ns]	$A_1$	$A_2$	$A_3$	$\tau_{\text{rise}}$ [ns]
$\beta$	13.5	23	98.5	0.55	0.335	0.115	0.8
$\alpha$	12.75	43	650	0.57	0.26	0.17	0.8

Figure 4.8 shows plots of time residuals calculated in data and simulation for (a) and (c): assuming emission times from benchtop measurements of LAB + 0.5g/L PPO, (b) and (d) used simulation where the emission time constants have been tuned to maximise the agreement in shape. The plots show a vast improvement in data-simulation shape agreement for the scintillator's response to  $\beta$  and  $\alpha$  particles, despite the lack of a dedicated calibration device.

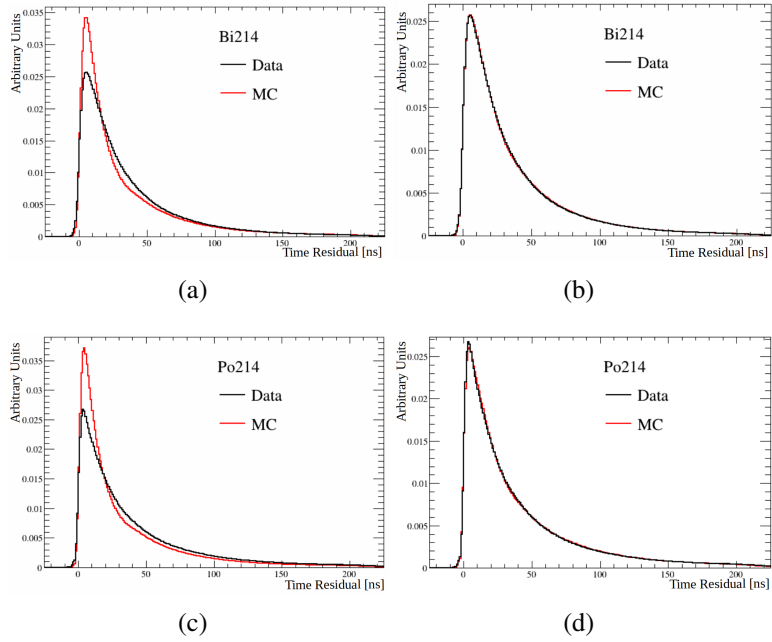


Figure 4.8: Plots of  $^{214}\text{Bi}$  ( $\beta$ ) and  $^{214}\text{Po}$  ( $\alpha$ ) time residuals applying positional cuts  $z > 1.5\text{m}$  and  $r < 5\text{m}$ , comparing data and simulation, before (a,c) and after (b,d) the tuning of scintillation emission time constants. Statistical uncertainty bars were found to be negligible.

### 4.3.3 Discrepancies Between In-Situ and Benchtop Measurements

Table 4.3 summarises the updated scintillation time constants that yielded the improved time residual agreement. It can be seen comparing with 4.2 that there is a large difference in the updated time constants (except for the rise time) compared to the previously assumed benchtop measured values. There are a number of possible reasons contributing to the discrepancies seen in-situ and the benchtop measurements:

It has been shown in other benchtop measurements [83], that instead of the 4 exponential sum used in RAT, simpler, alternate modelling of scintillation emission times which use a single decay constant (and rise time) can still accurately describe the emission times measured in the benchtop experiments. Large uncertainties were also seen in the fitted long decay constant values seen in the initial benchtop measurements in the 0.5g/L and 2g/L PPO concentration cocktails [110][109].

It also should be mentioned, the LAB + 0.5g/L PPO benchtop measurements saw faster emission times for  $\alpha$  particles compared to  $\beta$ s, an unexpected result due to the known quenching effects for the heavier  $\alpha$  particle. This was not seen in the in-situ measurement,

where figure 4.4(c) shows longer emission times for  $^{214}\text{Po}$  compared to  $^{214}\text{Bi}$ , as expected.

It has been shown in other scintillator studies that the measured scintillation decay times are inversely proportional to the PPO concentration in solutions of LAB + PPO [98]. It is expected therefore that the time constants calculated in both benchtop and the large scale in-situ measurements are liable to rapid variation for the low PPO concentration solution considered here.

It should also be noted that the cocktails used in the benchtop measurements were not sampled from the same batch of scintillator deposited in the detector.

To defend against incorrectly altering a timing constant to fit a discrepancy due to a localised defect in reconstruction or detector modelling, figures 4.9 and 4.10 display the data-simulation  $^{214}\text{Bi}$  time residuals for various small volume slices around the scintillator. It can be seen that the data-simulation agreement remains well-behaved throughout the detector's volume, with the largest of the small data-MC deviations seen in the volume directly above the water-scintillator interface. The following section explores the effect the updated emission times had on event reconstruction.

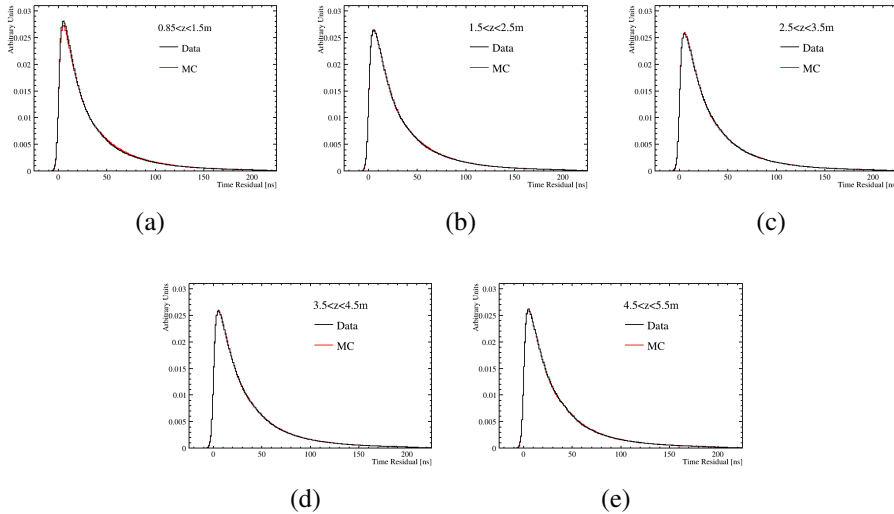


Figure 4.9: Plots of  $^{214}\text{Bi}$  time residuals, comparing data and simulation with updated emission time constants for various z-position cuts. All plots have a radial position cut of  $r < 5.5\text{m}$ .

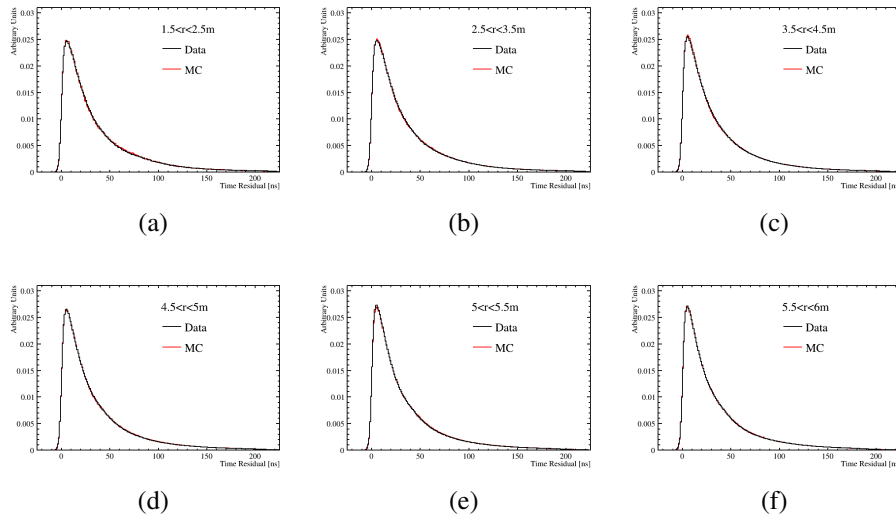


Figure 4.10: Plots of  $^{214}\text{Bi}$  time residuals, comparing data and simulation with updated emission time constants in table 4.3) for various radial cuts. All plots have a z-position cut of  $z > 1.5\text{m}$ .

## 4.4 Position Reconstruction Post-Calibration

Since position reconstruction is calculated using time residuals, it was important to measure any changes to it following the update to scintillation emission times. Deploying dedicated radioactive calibration devices in known positions within the detector, allows for a direct comparison of position reconstruction in simulation and data. Lacking this in the partial fill phase, BiPo214 events provided a calibration source for not only the  $\beta$  and  $\alpha$  scintillator timing, but also served to measure the position reconstruction resolution. The  $\beta$  particle emitted in the decay of  $^{214}\text{Bi}$  propagates a couple of centimetres in the scintillator [82]. Following the decay of  $^{214}\text{Bi}$ , the resulting  $^{214}\text{Po}$  propagates a negligible distance during its  $164\mu\text{s}$  half-life before it subsequently decays, where the emitted  $\alpha$  then propagates a negligible distance. Since the  $^{214}\text{Bi}$  prompt event occurs at the same position as the  $^{214}\text{Po}$  delayed event, the measured inter-event distance arises from the uncertainty in reconstructing the same position twice.

Figure 4.11 shows the distance between the reconstructed positions of  $^{214}\text{Bi}$  and  $^{214}\text{Po}$ , for event pairs tagged within  $r < 5.7\text{m}$ . The position of the peak is a measure of the position resolution<sup>1</sup>. Figure 4.12 shows again comparisons between data and the updated

<sup>1</sup>The measured inter-event distance arises from the uncertainty in reconstructing the same position twice. The peak represents  $\sqrt{2}$  times the resolution, assuming  $\beta$ s and  $\alpha$  events reconstruct with equal...

simulation, for x, y and z positions separately. The simulated position difference distributions were marginally narrower than those measured in data. The z-position distributions were also seen to be narrower than both the x- and y-position distributions, expected due to the smaller z-position phase space available in the approximately half-full detector. The mean of the z-position difference distribution in simulation was positioned +9mm compared to the data distribution.

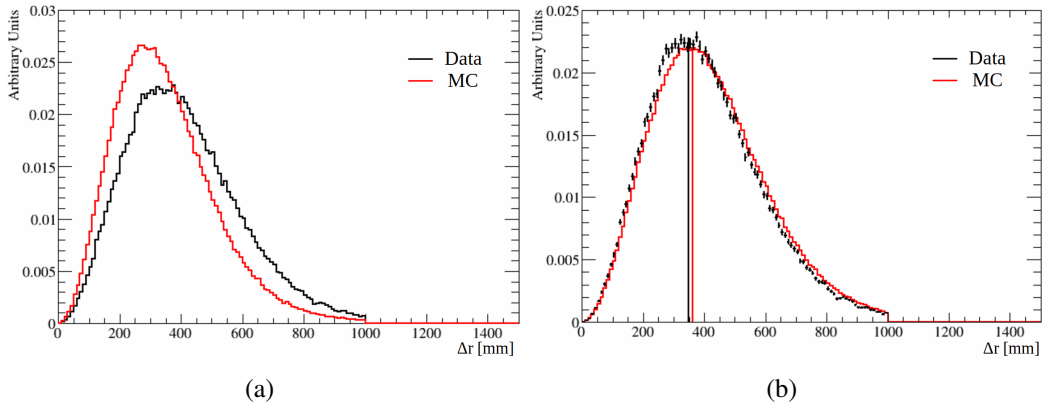


Figure 4.11: Plots of radial distances between  $^{214}\text{Bi}$  and  $^{214}\text{Po}$  events, using position reconstruction on simulated events assuming (a) benchtop measurements of scintillation emission time parameters (b) the updated scintillation emission time parameters shown in table 4.3. For (b) The vertical lines represent the peak positions for each distribution, while the error bars reflect statistical uncertainty. The BiPo214 events shown have positional cuts  $z > 0.85\text{m}$  and  $r < 5.7\text{m}$  applied. Visible is the  $\Delta r < 1\text{m}$  cut applied in the tagging of BiPo214.

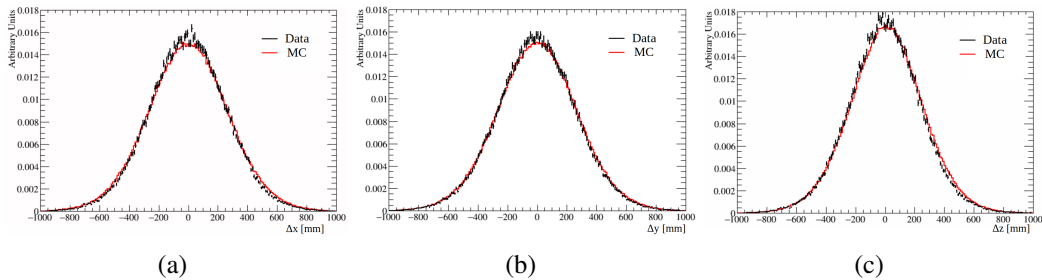


Figure 4.12: Plots of distances in x, y and z position between  $^{214}\text{Bi}$  and  $^{214}\text{Po}$  events, using simulated events with the updated scintillation emission time parameters shown in table 4.3. BiPo214 events have positional cuts  $z > 0.85\text{m}$  and  $r < 5.7\text{m}$  applied.

It can be seen that the Bi and Po radial distance distribution agreement for data and simulation was much improved following the updated time residual distributions required in the position reconstruction likelihood fit process. The difference in the peak positions (not necessarily true to due differing light yields).

tions was found to be 1cm, which yielded a negligible systematic uncertainty in position reconstruction for the partial fill antineutrino analysis, discussed further in section 7.2.

## 4.5 Calibration of Light Yield and $\alpha$ Quenching from BiPo214 events

The reactor antineutrino analysis is heavily reliant on the precise tagging of 2.2MeV neutron capture events. To achieve this, tagged BiPo214 events allowed for a simple calibration of the scintillator light yield. BiPo214 events were particularly useful for the neutron capture peak in the antineutrino analysis, since the  $^{214}\text{Bi}$   $\beta$  energy spectrum is centred around  $\sim$ 2.2MeV.

Scintillation light was calculated in simulation assuming Birks' Law in equation 2.3. Required were: the light yield constant  $S$  - the number of photons emitted per MeV of deposited energy and Birks' constant  $k_B$ . Also required for the light output due to  $\alpha$ -particles was the  $\alpha$ -quenching constant, which dictated the fraction of light output an  $\alpha$ -particle yields compared to an equal energy  $\beta$  [73][70].

The aforementioned benchtop experiments also included measurements of light yield,  $k_B$  and  $\alpha$ -quenching. As with the scintillation emission times, these measurements for the light yield parameters were previously assumed in simulations, but could be tuned by comparing tagged BiPo214 events in data and simulation.

The value of  $k_B$  plays a role in the total light yield, but unlike the light yield constant, dictates the energy dependence of the light yield. It was decided that  $k_B$  was assumed from the benchtop measurements, and the light yield constant alone would make up for any data-simulation disagreement in the  $\sim$ 1MeV wide  $^{214}\text{Bi}$  spectrum.

The optical parameters were calculated from BiPo214 events in the following order: The light yield constant was tuned such that data-simulation energy distributions agreed for  $^{214}\text{Bi}$  decays. Following the determination of the light yield constant by  $\beta$ -particles with  $^{214}\text{Bi}$ , any remaining discrepancy in  $^{214}\text{Po}$  data-simulation energy distributions was corrected for by calibrating the  $\alpha$ -quenching constant.

### 4.5.1 Results of Light Yield Parameter Tuning

Figure 4.14 shows  $^{214}\text{Bi}$  and  $^{214}\text{Po}$  nhits distributions assuming the benchtop measured light yield and  $\alpha$ -quenching constants. The scaling factor required agreement between data and simulation energy distributions was simply calculated as the ratio of the medians of each distribution in data and simulation. As was done in the scintillation emission time determination, the region defined by  $z > 1.5\text{m}$  and  $r < 5\text{m}$  was used for the tuning of parameters.

The nhits data/simulation median ratio was calculated as 1.081 for  $^{214}\text{Bi}$  and a ratio of 1.057 for  $^{214}\text{Po}$  (following the scaling of 1.081 applied to light yield constant). It can be seen from the plots and median ratios, that the benchtop experiment parameters underestimating the light yield for  $\beta$  particles, and overestimated the quenching due to  $\alpha$  particles in the SNO+ partial fill cocktail. Table 4.4 summarises the benchtop and updated values of these optical factors following their scaling.

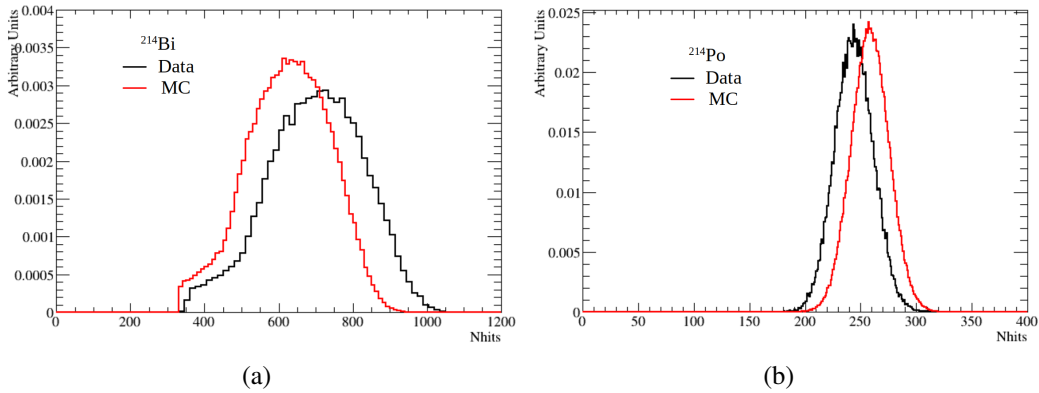


Figure 4.13: Plots of nhit distributions in data and simulation assuming the benchtop measured values of the light yield and  $\alpha$  quenching constants for (a)  $^{214}\text{Bi}$  (b)  $^{214}\text{Po}$ . Events have positional cuts  $z > 1.5\text{m}$  and  $r < 5\text{m}$  applied.

Table 4.4: Table summarising light yield and  $\alpha$  quenching constants measured in benchtop experiments and the in-situ BiPo214 calibration.

Parameter	Benchtop	From BiPo214
Light Yield [photons/MeV]	6190	6694
$\alpha$ -quenching	0.076	0.0803

Following the update to light emission parameters using the region defined by  $z > 1.5\text{m}$  and  $r < 5\text{m}$ , the agreement between data and simulation around the detector was investi-

gated. Plot 4.14 displays a graph of the data/simulation nhits median ratios for various small volume slices of  $^{214}\text{Bi}$  and  $^{214}\text{Po}$  events sampled from around the detector against radius and z-position. As expected the values of the data/simulation ratios are relatively homogeneous and close to unity within the region used to tune the light yield parameters. Moving away from the calibration region, the simulated nhits prediction is seen to decrease compared to that seen in data, the agreement worsening for positions approaching the AV. This was suspected to be due to the mismodelling of optical effects in simulation for light emitted near the AV. The data-simulation deviation in nhits can also be seen to a lesser extent for events near the scintillator-water interface, likely also due to inadequate modelling of the optical effects at the interface.

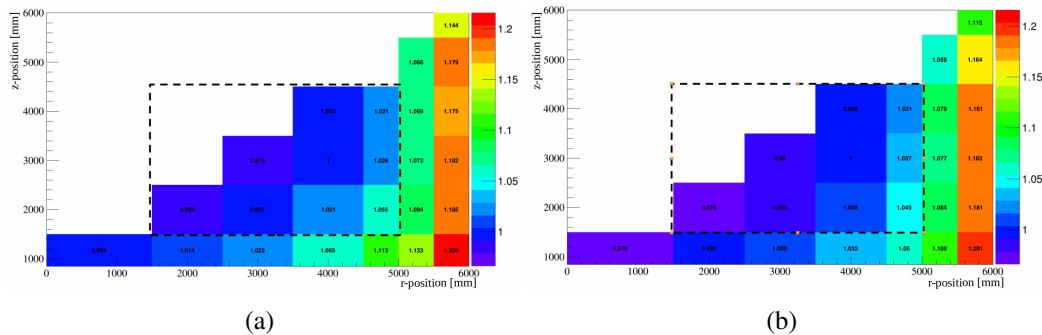


Figure 4.14: Plots of the data/simulation median nhits ratio vs position following the update to light yield parameters summarised in table 4.4. Black dashed boxes highlight the region in z and r-position used to select BiPo214 events to tune the parameters. (a)  $^{214}\text{Bi}$  (b)  $^{214}\text{Po}$ .

Following the updates to the values of the light yield constant and  $\alpha$ -quenching in table 4.4, the energy fitter was re-coordinated (pdfs remade in simulation with updated parameters) and BiPo214 events re-simulated. Figure 4.15 shows the reconstructed energy spectra of  $^{214}\text{Bi}$  and  $^{214}\text{Po}$  comparing data and simulation, this time using data taken over a much longer period, covering the majority of the partial fill phase, from 30<sup>th</sup> March to 26<sup>th</sup> of October 2020 (runs 257558-264716). Apparent following the light yield updates, is the good quality agreement in the spectral shapes. Small remaining discrepancies can be seen in the width of the  $^{214}\text{Po}$   $\alpha$  particle energy spectra in data and simulation. This could possibly be due to position reconstruction effects or some outstanding discrepancies in the light yield parameters which were either assumed from benchtop measurements, or the simplistic nature by which the light yield constant was scaled using the distributions'

median positions. In terms of the antineutrino analysis,  $\alpha$ -particles play a small role and so this remaining discrepancy was considered negligible.

The updated plots of energy reconstruction in figure 4.15 showed much improved agreement, but this was found to only be true for small radius events. Divergence at higher radii was likely due to the mismodelling of the optics approaching the AV. The next section discusses the calculation of a simple energy correction applied in the partial fill antineutrino analysis in order to counteract this divergence, and increase the fiducial volume which could be used.

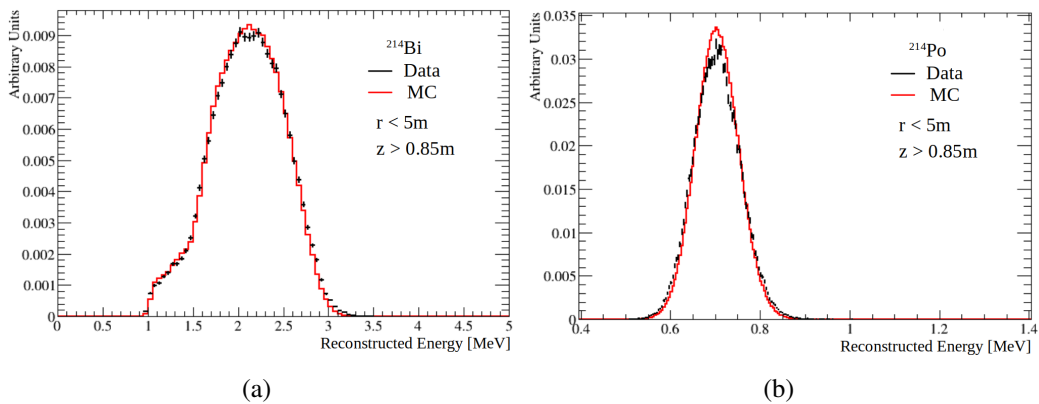


Figure 4.15: Reconstructed energy distributions in data and simulation following updates to the light yield parameters in table 4.4. (a)  $^{214}\text{Bi}$  (b)  $^{214}\text{Po}$ . Events have a positional cut of  $z > 0.85\text{m}$  and  $r < 5\text{m}$  applied.

### 4.5.2 Position Dependent Energy Corrections for the Reactor Antineutrino Analysis

Despite the good agreement between data and simulation for reconstructed energy at the centre of the scintillator volume, figure 4.14 highlighted the incomplete modelling of the optics approaching the AV. The water phase similarly saw larger discrepancies in the reconstruction of position and energy for events near the AV. It will be seen in chapter 6 that the antineutrino analysis relies heavily on the ability to tag narrowly around the 2.2MeV neutron capture peak. The analysis also benefits greatly from a large scintillator fiducial volume. In response to this, BiPo214 events were used again to calculate a simple energy correction factor, up to 5.7m in radius, to combat the impacts of mismodelled optics in the partially filled detector.

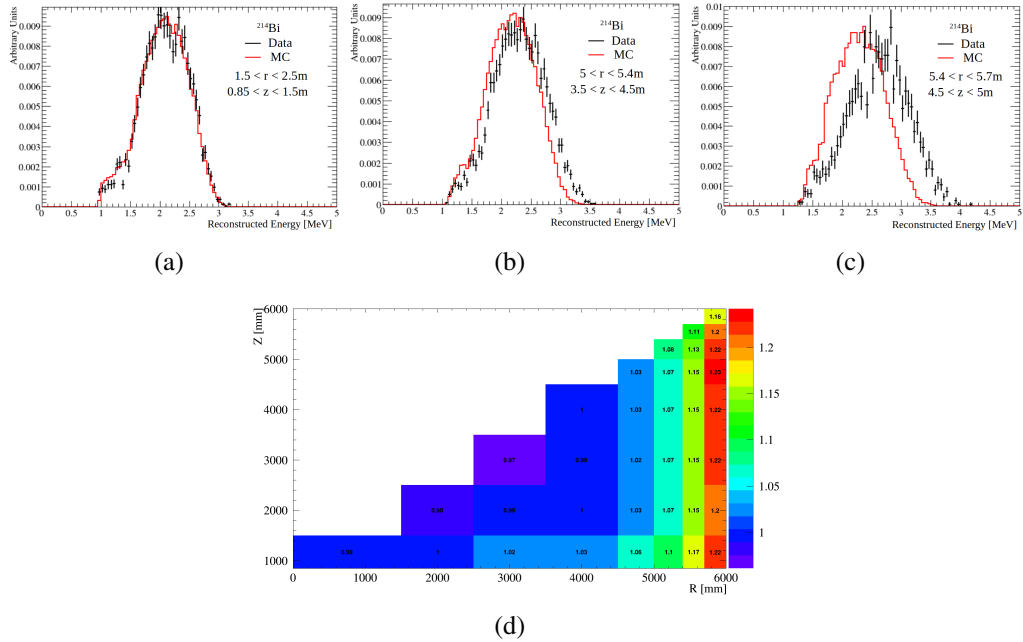


Figure 4.16: Plots (a)-(c) show data and simulation  $^{214}\text{Bi}$  reconstructed energy distributions, applying some selected positional cuts, prior to the application of any energy corrections. (d) Data/simulation  $^{214}\text{Bi}$  reconstructed energy median ratios, for various small volumes.

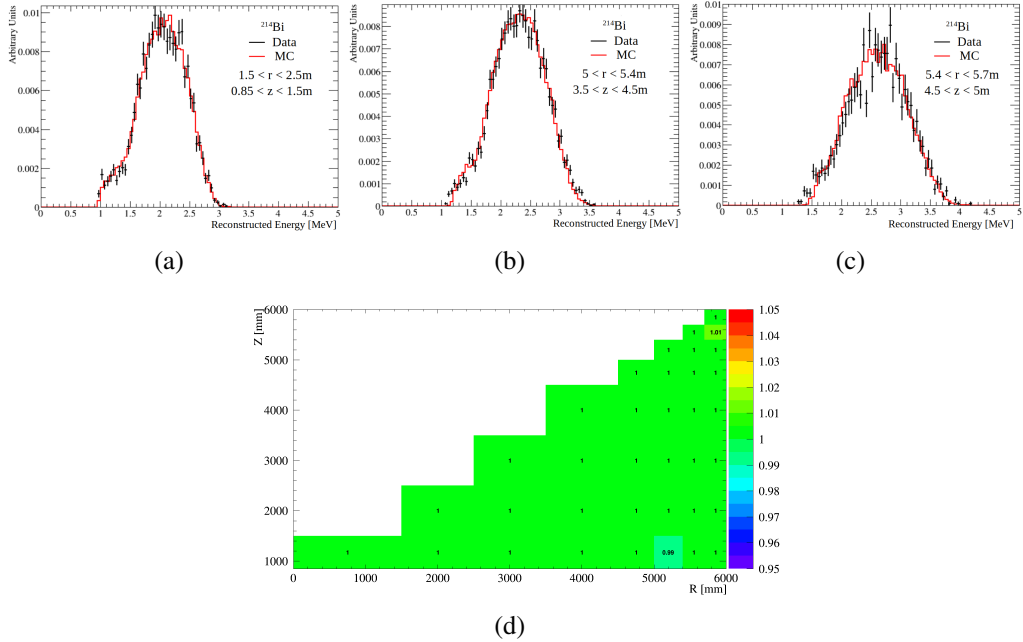


Figure 4.17: Plots (a)-(c) show data and simulation  $^{214}\text{Bi}$  reconstructed energy distributions following the position-dependent  $^{214}\text{Bi}$  energy scaling, applying some selected positional cuts. (d) Data/simulation  $^{214}\text{Bi}$  reconstructed energy median ratios, all showing approximately 1, as expected.

#### 4.5.2.1 Method

The chosen method, involved the calculation of scaling factors as a function of position in the scintillator and apply these to all reconstructed energies in simulation. Figure 4.16 shows the data/simulation reconstructed energy median ratios as a function of position, prior to any energy corrections, with example  $^{214}\text{Bi}$  energy distributions sampled from the discrete volumes. It can be seen clearly here that divergence occurs for events close to the AV. For the scaling of simulated event energies in the antineutrino analysis, the scaling factors (data/simulation  $^{214}\text{Bi}$  reconstructed energy median ratio) in each of the discrete volume slices defined by the z and r-position cuts in figure 4.16(d) were used. All simulated event energies were scaled by the factor in the small scintillator volume they fall in, such that simulation agreed with data.

The BiPo214 data and scaling factors presented in this section were calculated using the identical data run ranges used in the antineutrino analysis presented later, defined in section 6.1.

#### 4.5.2.2 Result of Energy Corrections

Figure 4.17(d) shows the results of the position dependent scaling corrections applied to simulation, yielding an expected data/simulation ratio of 1 in each scintillator slice (minor deviations from unity were primarily due to limited event statistics). Figure 4.18 shows the  $^{214}\text{Bi}$  and  $^{214}\text{Po}$  reconstructed energy spectra in data and simulation, following the use of energy scaling corrections, in the fiducial volume used in the reactor antineutrino analysis. It can be seen that the calculated position-dependent energy scaling factors allowed for excellent agreement over the fiducial volume. The ratios of the medians and the standard deviations ( $\sigma = \sqrt{\frac{\sum E_i - \mu}{N}}$ ) for the  $^{214}\text{Bi}$  spectra measured in data and simulation (figure 4.18) were found to be negligibly different to 1.

The scaling factors, calculated using the  $^{214}\text{Bi}$  spectrum, also yielded matching in the  $^{214}\text{Po}$  spectra in data and simulation. This was an indication that the energy correction factors were applicable to energies away from the  $^{214}\text{Bi}$  energies used to calculate them. This then demonstrated, to a limited extent, the validity of the desktop measurement of  $k_B$ , which dictates the energy dependence of the scintillation light yield. Although

BiPo214 events do not cover the entire range of antineutrino candidate energies (up to  $\sim 7\text{MeV}$ ), it was useful to test both  $^{214}\text{Bi}$  and  $^{214}\text{Po}$  energies, due to a lack of alternate-energy calibration sources in the partial fill.

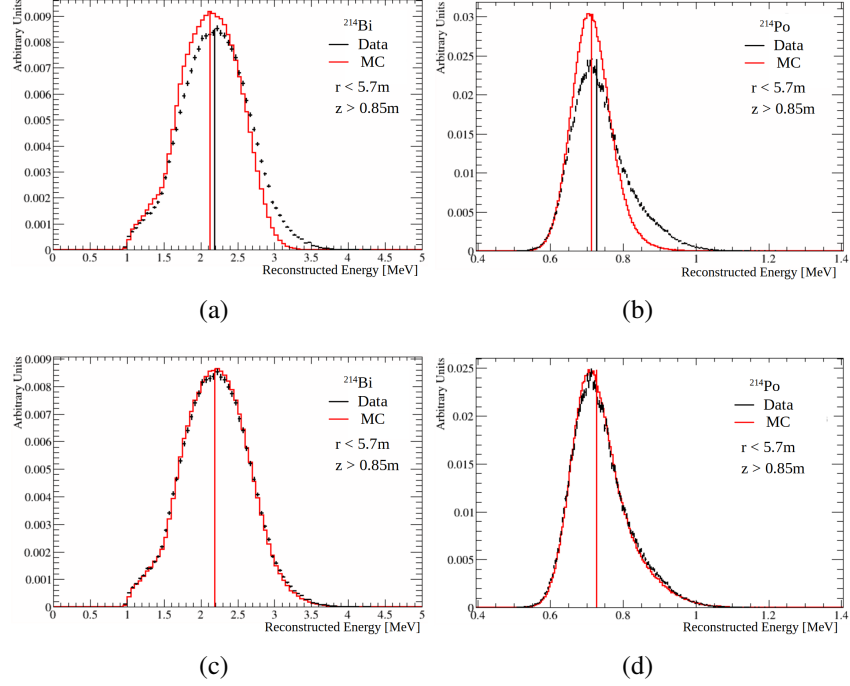


Figure 4.18: Results of energy correction scaling factors. (a) and (b) show  $^{214}\text{Bi}$  and  $^{214}\text{Po}$  energy spectra respectively in the entire antineutrino analysis fiducial volume, prior to energy corrections. The application of scaling factors show vast improvement in data and simulation agreement in (c) and (d). Vertical lines show the medians calculated for each distribution.

## 4.6 Conclusion

It has been shown that BiPo214 events provided a pragmatic calibration of a large number of scintillator properties in the transitional partial fill phase. Without any dedicated calibration sources deployed, the BiPo214 calibration produced competent data-simulation agreement for event position and energy reconstruction. The mismodelling of optics in simulation was seen to produce discrepancies in energy reconstruction for events approaching the AV. This was countered through position-dependent energy scaling correction factors, also calculated using  $^{214}\text{Bi}$  events. The scaling factors were found not only to work well for  $^{214}\text{Bi}$  events up to  $r < 5.7\text{m}$ , but could also be applied to lower energy  $^{214}\text{Po}$  events, yielding vastly improved data-simulation agreement. These calibrations

were certainly necessary for the reactor antineutrino analysis presented in this work, but also proved valuable for other SNO+ physics analyses and backgrounds measurements carried out during the partial fill phase.

**Calibration of scintillator timing (for  $\alpha$  and  $\beta$  particles)** It has been shown that emission time calibration has lead to a large improvement in time residual distribution shape, shown in figure 4.8. The use of BiPo214 events also had the advantage of being able to separately measure the scintillator's response of  $\alpha$  and  $\beta$  particles, allowing for their discrimination, to be used in other SNO+ partial fill analyses. The timing calibration has allowed for partial fill analyses to develop, such as: investigating event separation via pulse shape discrimination (PSD) [113] and scintillation-Cherenkov light separation in low concentration PPO using solar neutrinos [114].

**Improved position reconstruction** Following the timing updates, the BiPo214 events were then used to investigate the updated reconstruction, by measuring the distance between Bi and Po events in data and MC and comparing the distributions. Figure 4.11 showed the greatly improved consistency in the reconstruction of data and simulation in the partial fill phase, following the timing updates.

**Light yield calibration and improved energy reconstruction** The  $^{214}\text{Bi}$  energy spectrum, centred approximately around 2.2MeV, was favourable to calibrate with, for the efficient tagging of the 2.2MeV  $\gamma$ s produced in neutron capture events for the reactor antineutrino analysis. Figure 4.15 displayed the vastly improved data-simulation energy distribution agreement at the centre of the partial fill scintillator volume. Good scintillator stability was also seen over the partial fill period. The light yield parameters calculated using data taken from the 4th of April to the 12th of May 2020, still produced good data-simulation agreement for the extended dataset measured from 30<sup>th</sup> March to 26<sup>th</sup> of October 2020. Discrepancies due to optical mismodelling in the region of the AV were greatly reduced by energy correction factors, also calculated using BiPo214 events, as seen in figure 4.18 in the  $r < 5.7\text{m}$  antineutrino fiducial volume.

# 5 | Reactor Antineutrino Signal Calculation

This chapter summarises the calculations used for the prediction of the rate of measurable reactor electron antineutrino signal events in SNO+. The calculations essentially convert the published world nuclear reactor thermal powers and positions, to the expected detection rate. Neutrino oscillation parameters can then be extracted by the measurement of the antineutrino energy spectrum in data and comparing it in shape and rate with the calculated expectations. The chapter is divided into the different stages of the calculation: antineutrino emission, neutrino propagation followed by the cross-section of the interactions which allow for their detection. The total systematic uncertainties associated with the reactor signal will be introduced in section 7.2.2.1, referencing calculation steps in this chapter. It will be seen however that these uncertainties will be negligible compared to the large statistical variation in the data measured over the partial fill phase.

## 5.1 Antineutrino Emission in Nuclear Fission

Nuclear reactors produce electrical power through the carefully controlled fission of heavy isotopes within the cores of the reactors. To minimise the energy of a nucleus, neutron-rich heavy radioisotopes may fragment into neutron-rich daughter nuclei. These daughter nuclei subsequently beta-decay (to achieve stable nuclear configurations) emitting antineutrinos in the process. In total 6 neutrons on average are converted to protons per fission of radioactive nuclei fuelling most nuclear reactors [115]. This then corresponds to the emission of 6 antineutrinos per fission.

### 5.1.1 Nuclear Reactor Fuel

Nuclear reactors contain multiple radioisotopes as fuel for fission, where the relative amounts of these isotopes differ slightly depending on the reactor type. The four primary contributing radioisotopes used to fuel reactors are  $^{235}\text{U}$ ,  $^{238}\text{U}$ ,  $^{239}\text{Pu}$  and  $^{241}\text{Pu}$ . Long-lived fission fragments such as  $^{106}\text{Ru}$  and  $^{144}\text{Ce}$  can be found in nuclear reactor spent fuels, which also support antineutrino emission. Investigations by the Daya Bay collaborations have shown that including these fission fragments impact the expected antineu-

trino emission intensity on the sub-percent level [116]. These corrections were therefore excluded in RAT simulations. Similarly, [117] shows calculations of the antineutrino flux due to spent nuclear fuel waste (as a function of its age), but these fluxes also weren't included in the reactor analysis presented here, due to their negligible impact.

Required for the total antineutrino emission profile from a nuclear reactor core, are the individual radioisotope emission spectra and the relative contributions each radioisotope contributes to the total.

Each radioisotope's emission spectrum was calculated from the measurement of  $\beta$ -spectra associated with each fuel component's nuclear fission [118][119][120]. Models parameterising the emission spectra of each radioisotope have since been developed and compared against the measured fission data [121][122]. Each radioisotope's contribution to the total antineutrino emission spectrum have also been measured in a number short and medium baseline reactor experiments, such as Daya Bay [116] and KamLAND [51].

The uncertainties in the emission spectrum shape play a small role in the determination of  $\Delta m_{21}^2$ , while holding more significance in  $\theta_{13}$  measurements in short baseline reactor experiments [123].

The next section describes each isotope's unique antineutrino emission spectrum, as well as the model used to parameterise the total reactor emission spectrum.

### 5.1.1.1 Radioisotope Emission Spectra

The Huber and Schwetz parametrised model was used in RAT to describe the antineutrino emission spectra for each of the fuel radioisotopes fueling the reactor core [121]. The parameter models were calculated from beta decay spectra data for  $^{235}\text{U}$ ,  $^{239}\text{Pu}$  and  $^{241}\text{Pu}$ . The emission spectrum for  $^{238}\text{U}$  was also described using the same Huber and Schwetz model, but used theoretically calculated parameters based on an *ab initio* approach in [122]<sup>1</sup>. There is a  $\sim 10\%$  uncertainty in the predicted flux and a similar uncertainty in the  $^{238}\text{U}$  spectrum from these theoretical predictions. It isn't expected however that these uncertainties will play a significant role in the total reactor signal [123].

---

<sup>1</sup>More recent work which measured the  $\beta$ -spectra of the fission products of  $^{238}\text{U}$  has reduced the uncertainty in the expected antineutrino spectrum [124]

The antineutrino emission energy spectrum for a given isotope is described in the Huber and Schwetz model with an exponential 5th order polynomial. The number of antineutrinos emitted per fission per MeV is:

$$n(E_{\bar{\nu}}) = \exp\left(\sum_{i=1}^6 \alpha_i E_{\bar{\nu}}^{p-1}\right) \quad (5.1)$$

Table 5.1 summarises the coefficients used in the polynomial model used in RAT to describe the antineutrino emission spectra of each radioisotope. Figure 5.1 shows the expected antineutrino emission spectrum due to each of the four simulated radioisotopes.

Table 5.1: Summary of the coefficients for each reactor fuel isotope, used in equation 5.1

Isotope	$\alpha_1$	$\alpha_2$	$\alpha_3$	$\alpha_4$	$\alpha_5$	$\alpha_6$
$^{235}\text{U}$	4.367	-4.577	2.100	-0.5294	0.06186	-0.002777
$^{238}\text{U}$	0.4833	0.1927	-0.1283	-0.006762	0.002233	-0.0001536
$^{239}\text{Pu}$	4.757	-5.392	2.563	-0.6596	0.07820	-0.003536
$^{241}\text{Pu}$	2.990	-2.882	1.278	-0.3343	0.03905	-0.001754

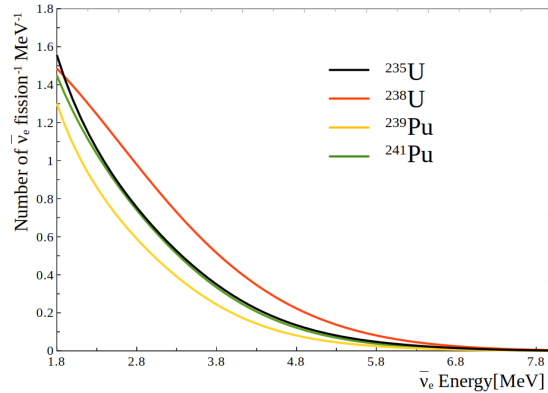


Figure 5.1: The antineutrino emission energy spectrum for each of the contributing isotopes found in nuclear reactor cores, calculated using equation 5.1.

### 5.1.1.2 Reactor Types - Fuel Composition

The relative compositions of these radioisotopes (deciding the total emission spectrum) are dictated by the type of nuclear reactor being considered. Reactors that were expected to contribute measurably to the antineutrino signal at SNO+ were placed in one of two reactor type categories: the pressurised water reactor (PWR) and the pressurised heavy water reactor (PHWR). Table 5.2 summarises the contribution each fissioning isotope

makes to the total antineutrino flux, for each reactor type. The PWR contributions have been adopted from measurements made by the KamLAND collaboration [51], confirmed by the Daya Bay measurement [116]. Private communications with Atomic Energy of Canada Limited (AECL) in 2013 provided the contributions specific to the Canadian PHWR reactor type. It has been demonstrated in simulation that the uncertainties associated with these relative contributions, yield negligible change to the expected signal [125].

Table 5.2: Table of each isotope’s fractional contribution to the total antineutrino flux for the PWR and PHWR reactor types.

Reactor Type	$^{235}\text{U}$	$^{238}\text{U}$	$^{239}\text{Pu}$	$^{241}\text{Pu}$
PHWR	0.52	0.05	0.42	0.01
PWR	0.568	0.078	0.297	0.057

### 5.1.2 Reactor Thermal Powers

Since the thermal energy emission per fission of each isotope is known [126], along with the corresponding antineutrino emission per isotope fission in table 5.1, a given reactor core’s thermal power ( $P_{th}$ ) can be converted to an instantaneous differential antineutrino emission intensity ( $\bar{\nu}_e$ s per unit energy per unit time) using:

$$\frac{d^2 N(E_{\bar{\nu}_e}, t)}{dE_{\bar{\nu}_e} dt} = \frac{P_{th}(t)}{f_i(t)e_i} \sum_{i=1}^{\text{isotopes}} f_i(t)n_i(E_{\bar{\nu}_e}, t), \quad (5.2)$$

where  $n_i(E)$  is the antineutrino emission per fission for the  $i^{th}$  isotope, shown in equation 5.1.  $e_i$  is the thermal energy released for the fission of the  $i^{th}$  isotope.  $f_i(t)$  is the fractional contribution the isotope has to the total fission rate occurring in the reactor.

Investigations carried out by the Daya Bay collaboration, comparing predictions by the Huber-Mueller (ILL-Vogel) model showed that a correction multiplicative factor of  $0.946 \pm 0.020$  ( $0.992 \pm 0.021$ ) was required for data of the measured the antineutrino emitted flux to agree with the emission model [116].

### 5.1.2.1 Time Variation

The current world-leading reactor antineutrino measurement of  $\Delta m_{21}^2$  made by the KamLAND experiment had reactor power output information with high granularity in time [52]. The KamLAND analysis incorporated a fit of the antineutrino flux variation against time, made possible due to the large reactor flux, yielded improved constraints on the antineutrino signal and backgrounds. Variation in signal is predominantly dictated when nuclear cores are switched on and off, a relatively common practice for the purposes of maintenance in reactors with multiple cores.

Due to the comparatively lower antineutrino flux at the SNO+ detector, the analysis presented in this work used a calculated flux integrated over time, where reactor power information is published on a yearly basis by the International Atomic Energy Agency (IAEA) [127][128]. The year averaged total thermal powers for reactors considered in the SNO+ reactor analysis are summarised in table C.1.

The Independent Electricity Systems Operator (IESO) provided an extra source of reactor activity for the three Canadian nuclear reactors Bruce, Darlington and Pickering (figure 5.5), reactors which provided the majority of the antineutrino flux at SNO+. The IESO publishes hourly the average electrical power produced by each reactor. This supplied up-to-date information on whether a reactor core was switched off, data that was otherwise unavailable in the IAEA source until the release of their annual publication. It was calculated that simulated reactor antineutrino events produced incorporating the IAEA and IESO sources, saw discrepancies in the expected flux of reactor antineutrinos at SNO+, on the level of 0.2% [129].

Armed with the expected intensity of antineutrinos emitted in given a reactor according to thermal power and fuel type and the number of free protons, the next step is to account for neutrino's propagation from each reactor's core to SNO+.

## 5.2 Neutrino Propagation

With the distance for each contributing nuclear reactor to the SNO+ detector known, a straightforward factor of  $(4\pi L^2)^{-1}$  was included for every reactor to account for the flux of neutrinos travelling from the reactor core to SNO+ (assuming neutrinos are emitted from each reactor core isotropically).

$$N_{\text{det}}(E_{\bar{\nu}}) = \sum_i^{\text{reactors}} \frac{N_i(E_{\bar{\nu}})}{4\pi L_i^2}. \quad (5.3)$$

To acknowledge neutrino oscillation, equation 1.39 was applied in simulation to the emitted electron antineutrinos which reached the SNO+ detector. These oscillations yielded the distortions in the prompt energy spectrum, from which neutrino oscillation parameters can be extracted. Referenced throughout this work, are the global PDG oscillation parameter values assumed in oscillation calculations. These parameters are summarised in table 5.3.

Having calculated the number of electron antineutrinos passing through the SNO+ detector, the next section involves the calculation of the inverse beta decay cross section, the interaction which produces a detectable event.

Table 5.3: Summary of the 2021 global PDG values for the oscillation values referenced throughout this work [130]

Global Oscillation Parameters 2021	
$\Delta m_{21}^2$	$7.53^{+0.18}_{-0.18} \times 10^{-5} \text{ eV}^2$
$\sin^2(\theta_{12})$	$0.307^{+0.013}_{-0.013}$
$\sin^2(\theta_{13})$	$2.20^{+0.07}_{-0.07} \times 10^{-2}$

## 5.3 Inverse Beta Decay

The method by which antineutrinos from reactors are measured is as old as the confirmed existence of neutrinos, when they were first measured in 1956 in the Cowan-Reines neutrino experiment [6]. The method used to tag antineutrino events relies on the distinct inverse beta decay (IBD) process. The detection of the colossal flux of antineutrinos

emitted by a nuclear reactor is offset by the tiny probability of interaction, quantified by the cross section, a Standard Model calculation.

### 5.3.1 The IBD Interaction Process in Liquid Scintillator

The IBD reaction involves the CC interaction of an antineutrino with a proton, producing a neutron and a positron:

$$\bar{\nu}_e + p \rightarrow e^+ + n \quad (5.4)$$

The minimum energy of an incoming antineutrino in the lab frame to produce a neutron and positron at rest is:

$$E_{\bar{\nu},\min}^{\text{IBD}} = \frac{(m_n + m_e)^2 - m_p^2}{2m_p} = 1.806 \text{ MeV} \quad (5.5)$$

The IBD interaction process occurring in a detector is represented in the sketch in figure 5.2. In liquid scintillator, the positron deposits its energy in the scintillator, emitting light, as it slows down over a distance of  $\sim 1\text{cm}$ , then very quickly annihilates with an electron in the detector, producing annihilation photons, which also deposit energy in the scintillator. A discussion of the event topology for IBD events compared to background events in the reactor antineutrino analysis, is discussed in chapter 6.

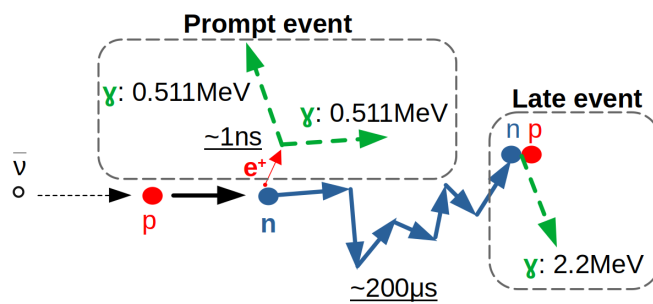


Figure 5.2: A sketch of the inverse beta decay interaction in liquid scintillator.

The neutron is created at the same point the positron is, but does not trigger the detector immediately. The neutron propagates in the lab frame on a random walk, thermalising via elastic collisions with protons in the detector yielding negligible scintillation light, until it is eventually captured by an indiscriminate proton in the detector. Neutron capture by a proton produces a deuteron ( $d$ ) alongside an easily detectable 2.2MeV photon:  $n + p \rightarrow$

$d + \gamma$ . The capture process has a half-life of  $\sim 200\mu\text{s}$ , occurring at a distance of  $\sim 30\text{cm}$  from the annihilation point of the positron. As mentioned in chapter 2 GEANT4 served to calculate the propagation of the positron, neutron and scintillation photons in simulation [81].

This characteristic time and position association of the prompt positron and delayed 2.2MeV neutron events provides an analyser with a powerful tool. Tagging the pairs of events yielded by IBD, separated by a distinct time and position difference between them, allows for very powerful mitigation of contamination from random background events constantly occurring in the detector, which are uncorrelated in time (chapter 6).

### 5.3.1.1 Positron Energy

Due to the large discrepancy in the mass of the neutron and positron, the neutron carries a very small amount of the incident antineutrino energy in the form of kinetic energy. This allows one to essentially directly measure the energy of the neutrino by determining the positron's energy.

Due to the  $\gamma$ s released in the annihilation of a positron with an electron (total energy equal to  $2m_e \sim 1.1\text{MeV}$ ), a positron emitted at the IBD threshold energy  $E_{\bar{\nu},\min}^{\text{IBD}}$  (eqn. 5.5), will still deposit energy well above the threshold measurable energy in scintillator at SNO+ (chapter 3). The energy deposited in the scintillator by the positron  $E_{\text{dep},e^+}$  can be approximately written in terms of the incident antineutrino's energy as:

$$E_{\text{dep},e^+} \approx KE_{\bar{\nu}_e} - m_n + m_p + m_e \approx KE_{\bar{\nu}_e} - 0.8\text{MeV}, \quad (5.6)$$

where it has been assumed that the neutron carries a negligible amount of kinetic energy due to its mass. Since the energy of the prompt positron event is proportional to the kinetic energy of the antineutrino, distortions due to oscillations in the measured positron spectrum produced in IBD are one-to-one to the energy spectrum of neutrinos passing through the SNO+ detector. Measuring  $\Delta m_{21}^2$  is therefore derived from the energy spectrum the prompt positron events for all tagged IBD positron-neutron pairs.

It should be noted that the simplified relationship between positron and antineutrino en-

ergies presented in eqn. 5.6 was for demonstration purposes only. Full 4-momentum conservation calculations were made in RAT simulations of reactor IBD events.

### 5.3.2 Inverse Beta Decay Cross Section

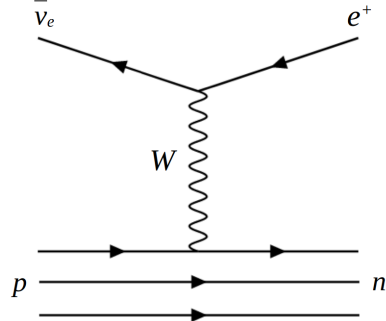


Figure 5.3: Tree level Feynman diagram of the IBD interaction.

Figure 5.3 shows the tree-level Feynman diagram of the IBD interaction. The IBD cross section used in the antineutrino analysis was calculated using [131]. Further descriptions of this calculation can be found in appendix D.

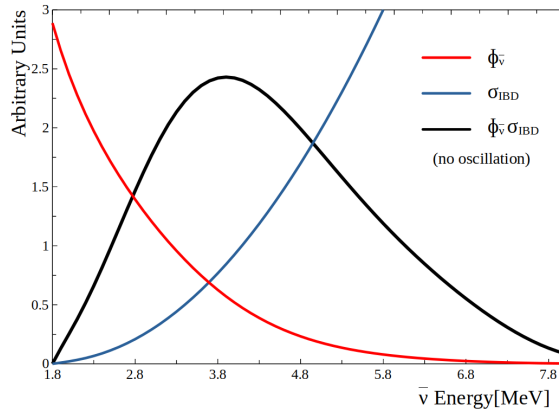


Figure 5.4: Distributions of the antineutrino emission spectrum (no oscillation) for a PHWR reactor (red), the IBD cross section (blue) and the product of the two (black). Each distribution has been scaled arbitrarily for the purposes of demonstration.

Figure 5.4 plots the shapes of the PHWR reactor emission spectrum alongside the IBD cross-section using equation D.8, as well as their product. The product reflects the expected energy spectrum an antineutrinos that can interact within the detector at SNO+ (no oscillation).

### 5.3.3 Target Protons in the Scintillator

Now established, is the rate of antineutrinos propagating from nuclear reactors, passing through the SNO+ detector and the probability of the IBD process occurring. Required next, is the number of target protons available in the SNO+ target volume available to found the IBD process on. The number of free protons was estimated using the measured number density of hydrogen atoms of the liquid scintillator. The calculation involved measurements of the LAB + PPO cocktail density and the proportions of the various LAB chain lengths (and thus hydrogen atom densities) making up the scintillator [69][70]. To account for variations in the detector cavity temperature, the measurements of the scintillator density were made against temperature. The SNO+ detector volume is kept on average at a temperature of  $14^\circ$ , where in the water phase, there was a temperature gradient seen from the top the bottom of the detector of approximately  $3^\circ\text{C}$  [132][133]. For the partial fill reactor analysis, with only 365t of scintillator in the top half of the detector, this gradient wasn't expected to be as large. Even with the assumption of a  $3^\circ\text{C}$  difference across the scintillator, a 0.4% uncertainty was calculated in the density. This was expected to impact to the antineutrino analysis negligibly.

The hydrogen number density was calculated to be  $6.30 \times 10^{28} \text{ m}^{-3}$ , calculated similarly to that of the carbon density in section 6.3.2.3. The volume of the scintillator contained in the AV in the partial fill phase was calculated to be  $382.7 \text{ m}^3$ , yielding a total of  $2.41 \times 10^{31}$  protons that IBD can be founded upon.

## 5.4 Expected Reconstructed Energy Spectrum

Table C.1 lists the nuclear reactors, thermal powers and distances for each reactor considered in the SNO+ reactor antineutrino analysis. Figure 5.5 demonstrates the expected reconstructed positron energy spectrum measurable at SNO+ due to oscillated reactor antineutrinos (and geoneutrinos), in the pure scintillator phase with 1 year of livetime. Shown in the figure are the unoscillated and oscillated signals (dotted and solid black respectively) calculated using equation 1.39 and current PDG global fit neutrino oscillation parameters [130]. The solid black oscillated signal is a stacked histogram, showing the

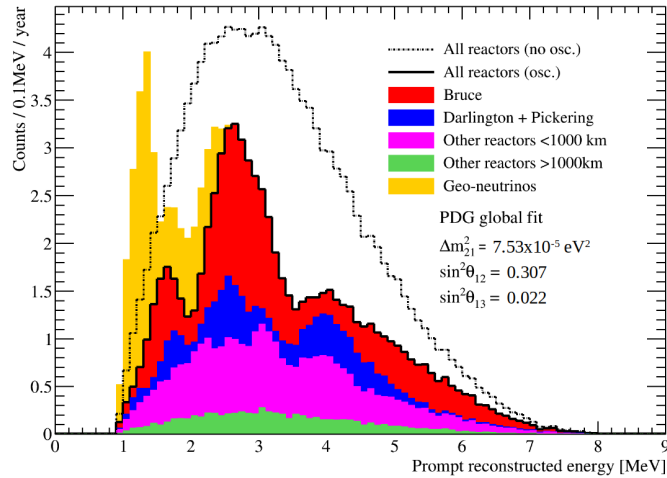


Figure 5.5: Stacked histograms demonstrating the expected reconstructed energy of positron events due to reactor and geoneutrino events, oscillated using eqn. 1.39 with oscillation parameters in table 5.3. Shown is a livetime of 1 year in the pure scintillator phase. A fiducial volume cut of  $r < 5\text{m}$  was applied to all simulated events.

separate contributions of the three nearest Canadian nuclear reactors Bruce, Darlington and Pickering, at distances of  $\sim 240$ ,  $340$  and  $350\text{km}$  respectively from SNO+, as well as combining the contributions of all reactors less than  $1000\text{km}$  away. The contributions of the 3 Canadian reactors combined yield  $\sim 60\%$  of the oscillated signal. Bruce, is the largest and nearest reactor to SNO+, contributing  $\sim 40\%$  of the oscillated signal. Chapter 7 discusses the analysis cuts applied to the simulated IBD events to isolate the positron energy spectrum shown.

In an ideal world, one could isolate the contribution of a single antineutrino source such as Bruce, and very precisely measure  $\Delta m_{21}^2$  from its distinct spectrum (or in the case of JUNO, place a detector equidistant to multiple reactors [48]). Despite the small number of nearby reactors, along with sub-optimal reactor distances for  $\Delta m_{21}^2$  extraction (chapter 1), the cluster of reactors all at  $\sim 240\text{km}$  from SNO+ still yields a distinct and substantial oscillated energy spectrum.

Shown now, are the calculations used to construct in simulation the expected antineutrino oscillated energy spectrum, against which data was compared to extract the neutrino mixing parameters. The next chapter details the data analysis techniques used to isolate the IBD events in data, as well as specifying the backgrounds present in the reactor antineutrino analysis.

# 6 | Reactor Antineutrino Signal Extraction

Signal extraction in this antineutrino analysis refers to the process of sifting through triggered event data and identifying the ‘prompt’ positron and the ‘late’ neutron capture event produced in IBD. This chapter summarises the data analysis methods and cuts used to extract the antineutrino signal in the partially filled SNO+ scintillator detector. Examined also are the sources of background events which can contaminate the reactor antineutrino analysis cuts, negatively impacting the sensitivity to oscillation parameters  $\Delta m_{21}^2$  and  $\theta_{12}$ .

## 6.1 Dataset and Livetime

Under ideal circumstances, the SNO+ detector would continuously record data throughout the year. Thanks to the 2<sup>nd</sup> law of thermodynamics, this isn’t the case. A detector run could be demoted as a good physics run for a variety of reasons:

- Failures in electronics (large numbers of inactive/overactive channels or abnormal trigger rates).
- Calibration or maintenance runs.
- Abnormal overall muon rates or OWL PMT detection efficiencies.
- Runs with excessive accidental background rates (section 6.3.3).
- Loss of power, earthquakes, lightning storms or blasting activity in the mine.
- Physics runs shorter than 30 minutes and the reason for ending early was not noted in the detector shift report by the detector operator.

Following the removal of runs which failed due to the above reasons, the data used in the partial fill antineutrino analysis was recorded from the 30<sup>th</sup> March to the 26<sup>th</sup> October 2020, runs 257558-264716, corresponding to a livetime of 127.80 days. Losses in livetime due to dead-time that may be induce by data-cleaning cuts which remove instrumental events, were assumed negligible. Simulation and data processing were carried out using RAT version 6.18.9.

## 6.2 Antineutrino Coincident Pair Event Selection

Introduced in the previous chapter was the distinct IBD interaction by which an incoming electron antineutrino can be detected. The correlation in position and time between the prompt positron event and the late neutron capture event accompanying the positron, allowed for the extraction of a very distinct signal from the high rate of triggered events occurring in the scintillator volume.

### 6.2.1 Position and Time Correlation

**Time Difference** The probability distribution for the neutron capture event following its random walk from its point of creation, can be written as:

$$P(t)dt = \frac{e^{-t/\tau}}{\tau}dt \quad (6.1)$$

where the capture occurs at time  $t$  after the prompt positron event (and the positron event is assumed to occur a negligible time following the neutron's creation). Time  $\tau$  represents the medium-dependent neutron capture constant for neutrons on  $^1\text{H}$  in the scintillator (the sub-percent capture of neutrons on  $^{12}\text{C}$  was neglected), which has been measured to be slightly larger than  $200\mu\text{s}$  in the KamLAND and Daya Bay scintillator cocktails [134][135]. Applying a maximum time difference threshold on event pairs provides a powerful handle on extracting IBD event pairs.

**Position Difference** The distance the thermalising neutron travels from its creation point can also be used. The position difference cut is second in influence compared to the time difference cut, for the reduction of uncorrelated random background events.

Figure 6.1 shows the reconstructed  $\Delta t$  and  $\Delta r$  distributions for reactor antineutrino events simulated in the partial fill phase, applying the analysis cuts summarised in table 6.1.

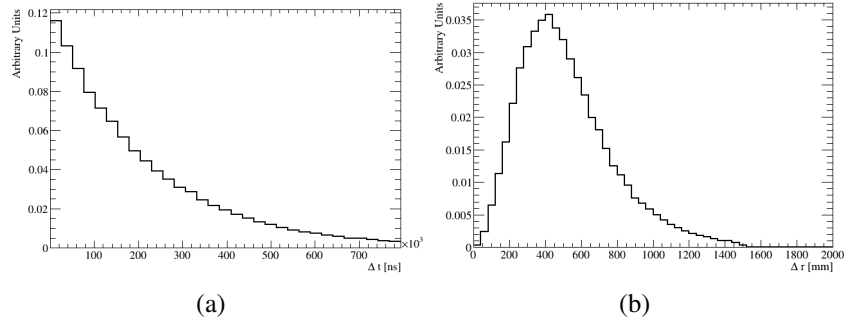


Figure 6.1:  $\Delta t$  and  $\Delta r$  distributions for reactor antineutrino events simulated in the partial fill phase.

### 6.2.2 Coincidence Pair Analysis Cuts

Apart from the time and position coincidence cuts, each candidate prompt and late event pairs were required to pass an assortment of other energy and position cuts summarised in table 6.1. For the late neutron capture event, narrow energy cuts around the prominent 2.2MeV peak, allowed for powerful reduction of random background events. The choice of cuts such as the muon follower veto and the multiplicity cuts will be discussed later in section 6.3.4, alongside the backgrounds they target. Thanks to the distinct IBD signal and large event energies considered, background events due to instrumentals were expected to be negligible. Regardless, a simple data-cleaning mask was applied to all events recorded in data. This mask was assumed to yield negligible signal sacrifice. For antineutrino events interacting in the fiducial volume defined by the positional cuts in table 6.1, the analysis signal efficiency was calculated in simulation as 78%. Accounting for the loss in livetime due to the muon veto cut, the total livetime of recorded data in this partial fill antineutrino analysis was 125.40 days.

#### 6.2.2.1 Correction Factors for Energy Cuts

Chapter 4 introduced the impact the mismodelling of optics approaching the AV had on reconstructed energy. It was observed for BiPo214, that event energies reconstructed in data near the AV were scaled higher compared to the same event reconstructed approximately within a 5m radius. This made placing narrow energy cuts surrounding the late 2.2MeV neutron capture peak more difficult, due to the peak's movement with position. To combat this, the scaling correction factors summarised in section 4.5.2, were applied

Table 6.1: Table of Partial Fill Analysis Cuts.

Parameter	Prompt Event	Late Event
Energy (MeV)	$0.9 < E < 8$	$1.85 < E < 2.4$
$\Delta t$		$400\text{ns} < \Delta t < 0.8\text{ms}$
$\Delta r$ (m)		$\Delta r < 1.5$
r (m)	$< 5.7$	$< 5.7$
z (m)	$> 0.85$	$> 0.85$
FitValid	True	True
Muon Veto veto all following pairs for 20s		$\text{nhits} > 3000$
Multiplicity	Remove events with: Energy $> 0.4\text{MeV}$ and $\Delta r < 2\text{m}$ between or 2ms after event pairs.	

to the energy threshold cuts. That is, energy scaling factors were applied to all simulated event energies such that data and simulation agreed, and then were also applied to the energy cut thresholds for both data and simulation, used to extract IBD events. This effectively narrowed the energy cuts needed to capture the neutron peak across all positions in the antineutrino fiducial volume, achieving a larger reduction of background events.

## 6.3 Backgrounds

The IBD event pairing technique provides powerful mitigation of contamination due to random uncorrelated background events. Conversely, backgrounds that yield correlated pairs of events within similar energy ranges, may also be tagged with the reactor antineutrino tag. This section introduces the various sources of background events considered in the antineutrino analysis, classified as either correlated and uncorrelated background events.

### 6.3.1 Correlated Background: Geoneutrinos

Reactor cores are not the sole source of MeV-scale antineutrinos. Antineutrinos are also emitted in the decay of naturally found radionuclides in the Earth's crust and mantle, generally due to  $^{40}\text{K}$ ,  $^{232}\text{Th}$ ,  $^{238}\text{U}$  and  $^{235}\text{U}$  [136]. These antineutrinos are typically named ‘geoneutrinos’, generating IBD events indistinguishable from those due to reactor an-

tineutrinos of the same energy. In terms of this analysis, the geoneutrinos produced in  $^{40}\text{K}$  and  $^{235}\text{U}$  decays do not yield an appreciable flux of antineutrinos above in the IBD energy threshold, so were therefore ignored. Previous measurements of geoneutrinos have been made previously by Borexino and KamLAND, both kilotonne-scale liquid scintillator experiments principally similar to SNO+. Currently, the total (and relative) amounts of the radioactive elements in the Earth’s mantle are not known to a high degree of precision. This is primarily due to lack of large-sample measurements of the geoneutrino flux to compare against [137][138].

The radionuclide content is known to vary across the Earth’s crust and mantle, where detection of geoneutrinos at SNO+ would be the first measurement in the Americas, with events originating primarily from the Archean Superior Craton and surrounding North American plate [139]. Samples measuring the local geology around SNO+ have been incorporated into the 3D models used to predict the flux of geoneutrinos reaching SNO+ [140]. As mentioned, there are large uncertainties associated with these models.

### 6.3.1.1 Expected Geoneutrino Flux

The models employed in RAT for the simulation of geoneutrinos at SNO+ were those referenced in [136]. The popular models used to describe the Earth’s contributing radioisotope composition, can be broken down into three overall categories, Low-Q, Mid-Q and High-Q. Each category is defined by the total predicted radiogenic heat emitted. Calculations provided by O. Šrámek using the Mid-Q model predict fluxes of  $34.1 \pm 5.0$  and  $9.5 \pm 0.8$  Terrestrial Neutrino Units (TNU) by the  $^{235}\text{U}$  and  $^{232}\text{Th}$  decay chains respectively at SNO+ [141], where a TNU is defined as one interaction in a year of fully efficient exposure to  $10^{32}$  free protons. Converting from TNU to the scintillator volume at SNO+, yields (assuming 100% antineutrino detection efficiency) 19.7 and 9.5 detectable geoneutrino interactions per year occurring within the full scintillator volume contained within in the AV (with similar calculations in chapter 5). The Low-Q and High-Q models respectively predict 17.2 and 24 events/year for Uranium and 4.7 and 7.6 events/year for Thorium.

While the measurement of geoneutrinos at SNO+ would be a great realization in itself,

their flux negatively impacts the extraction of the reactor antineutrino energy spectrum (due to their indistinguishability from reactor antineutrino IBD events), so were considered a background. The low flux and associated uncertainties due to Poisson fluctuations for geoneutrinos detectable at SNO+, makes distinguishing between the Low, Mid and High-Q models in the partial fill data impossible. The Mid-Q model was assumed for the analysis, where the associated large uncertainties played a small role in the sensitivity to  $\Delta m_{21}^2$ .

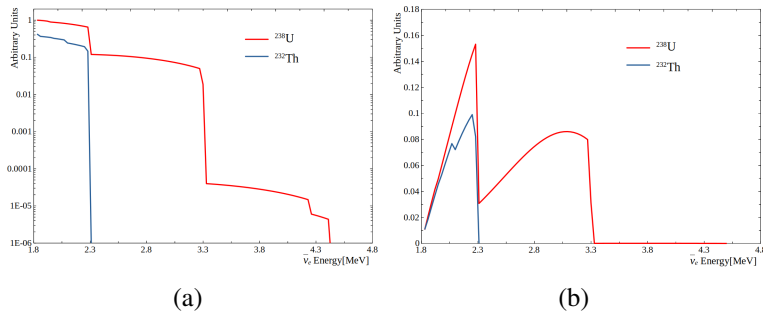


Figure 6.2: Predicted geoneutrino emission spectra shapes for the  $^{238}\text{U}$  and  $^{232}\text{Th}$  decay chains  
(a) Emission spectra shape for each source species [142], spectra were scaled to arbitrary units, but the relative normalisations agree with the Mid-Q model. (b) Product of the emission spectra in (a) with the IBD cross section in equation D.8.

Figure 6.2 shows the expected geoneutrino kinetic energy spectra from the  $^{238}\text{U}$  and  $^{232}\text{Th}$  decay chains above the IBD threshold energy (eqn. 5.5). In response to the limited statistics expected in partial fill and the geoneutrino model uncertainties, a single U+Th combined geoneutrino contribution has been used in all subsequent plots.

**Oscillation** Since geoneutrinos may also propagate long distances from the Earth's crust and mantle to SNO+, they can also undergo observable oscillation. Unlike reactor neutrinos, emitted from a localised point, the positions of geoneutrino sources are spread throughout the Earth's crust and mantle. The vacuum survival probability equation in 1.39 for reactor antineutrinos can be replaced with a probability averaged over hundreds of kilometres. This leads to a dependence only on mixing angles, i.e. no distortions in the energy spectrum shape due to  $\Delta m_{21}^2$ :

$$\langle P_{\bar{\nu}_e \rightarrow \bar{\nu}_e} \rangle \approx \sin^4 \theta_{13} + \cos^4 \theta_{13} [1 - \frac{1}{2} \sin^2 2\theta_{12}] \quad (6.2)$$

Figure 6.3 shows the partial fill Asimov dataset energy spectrum showing the expected rate of geoneutrinos alongside events due to reactor antineutrinos, passing the antineutrino coincidence cuts in table 6.1, oscillated at the PDG global oscillation parameters [143].

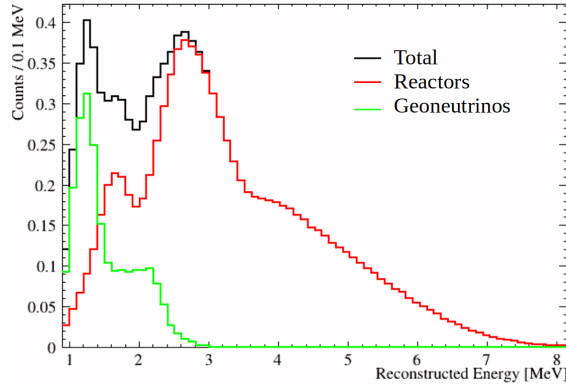


Figure 6.3: Asimov dataset of the reconstructed energy spectra for the partial fill dataset due to reactor antineutrinos and geoneutrinos, oscillated by the global oscillation parameters summarised by PDG [130].

**Note on Matter Effects** The vacuum oscillation probability has been assumed for this analysis. Introduced in chapter 1 were the impacts matter effects have to the neutrino survival probability, assuming a constant electron density experienced by the neutrino across its propagation. It is known however that the electron density varies as a function of radius throughout the Earth [144]. Calculations have been carried out for the KamLAND experiment, numerically solving the geoneutrino survival probability, accounting for matter effects and the added complexity of a varying electron density throughout the Earth [145]. It was found that for monoenergetic geoneutrinos propagating through the Earth, the impact to the survival probability for a geoneutrino propagating various distances through the Earth, differed from the distance averaged vacuum prediction by less than a percent [146], so was neglected in this analysis.

### 6.3.2 Correlated Background: $\alpha$ -n

A particularly threatening background to the reactor antineutrino spectral fit at SNO+, arises indirectly from the rate of energetic  $\alpha$  particles in the detector. The capture of  $\alpha$  particles by  $^{13}\text{C}$  atoms present in the detector can incur the interaction:  $\alpha + ^{13}\text{C} \rightarrow ^{16}\text{O}$

$\alpha + n$ , producing an IBD-like coincidence event in the detector.  $\alpha$  particles may also be captured by  $^{14/15}N$  and  $^{17/18}O$  yielding similar background events, but are ignored due to their negligible presence in the scintillator [70]. The term ‘ $\alpha$ -n’ in this work therefore refers specifically to the  $^{13}C(\alpha,n)^{16}O$  interaction.

The  $\alpha$ -n mimicry of the IBD interaction arises from the ejection of a neutron from the  $^{17}O$  atom following the  $\alpha$  capture. The energetic neutron thermalises and emits a 2.2MeV gamma upon its capture, just as in the IBD event. Discussed next, are the interaction pathways by which the  $\alpha$ -n interaction produce prompt events with the late neutron capture event.

### 6.3.2.1 $\alpha$ -n Prompt Energy Spectrum

Figure 6.4 shows a sketch of the three possible channels by which the  $\alpha$ -n interaction can produce coincidence pairs, as was simulated in RAT. The probability of each channel depends primarily upon the energy state the  $^{16}O$  is produced in.

1. Most commonly, a high energy neutron is emitted which elastically scatters multiple protons within the first  $\mathcal{O}(ns)$  of its random walk and eventual capture ( $\sim 200\mu s$  later) on a proton in the detector. GEANT4 predicted the thermalising neutron in  $\alpha$ -n to scatter on average 7 protons which subsequently produce measurable scintillation light in the SNO+ scintillator. The combined light emitted by these energetic scattered protons can pass the prompt event energy threshold, while the neutron capture provides the late event, just as the IBD interaction.
2. The high energy neutron may also inelastically scatter off a  $^{12}C$  nucleus, prompting its excitation and subsequent emission of a 4.4MeV  $\gamma$ , providing the prompt event.
3. Upon the  $\alpha$  particle capture, the  $^{16}O$  may be produced in one of two excited states. Upon the de-excitation of  $^{16}O$ , emitted are an  $e^+ + e^-$  pair of total energy 5.03MeV, or a 6.13MeV  $\gamma$ . In the simulation of the  $e^+ + e^-$  pair in RAT, it was assumed that each particle shared the total to each identically have a kinetic energy of 2.513MeV for simplicity. The annihilation of the positron with an electron in the scintillator yields annihilation gammas of total energy 1.02MeV, resulting in a total visible energy of 6.05MeV for the

prompt event.

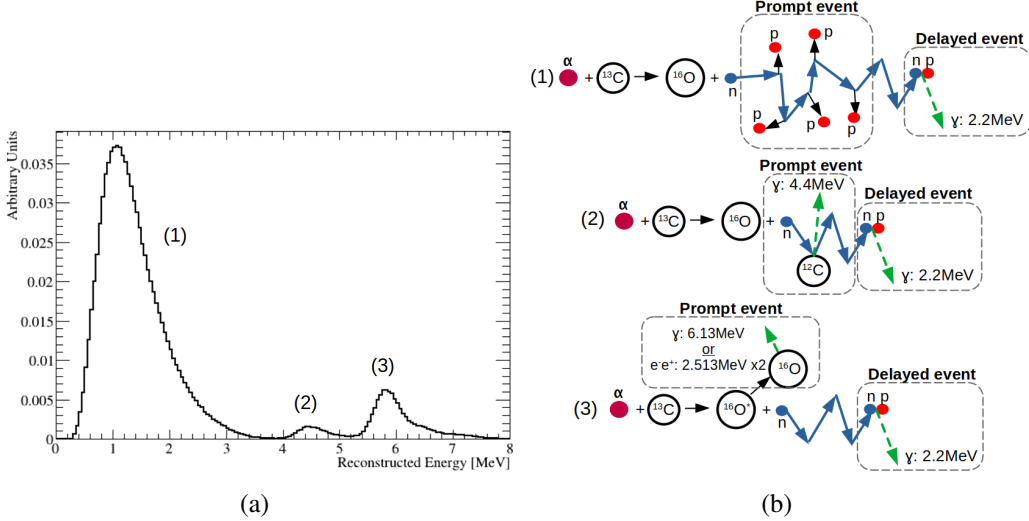


Figure 6.4: (a) Pdf generated in RAT of the expected measurable prompt event energy spectrum due to the  ${}^{13}\text{C}(\alpha,\text{n}){}^{16}\text{O}$  interaction. (b) Sketch of the three possible reaction pathways for the  $\alpha$ -n interaction.

Discussions of the calculations used to simulate the shape and rate of the  $\alpha$ -n interaction in RAT will follow shortly. Examined next, is the measurement of the rate of  $\alpha$  decays due to  ${}^{210}\text{Po}$  in detector over the partial fill phase, which sources the  $\alpha$ -n interaction in SNO+.

### 6.3.2.2 ${}^{210}\text{Po}$ Rate

Of all the  $\alpha$  particles produced in the detector  ${}^{210}\text{Po}$  decays are essentially the sole source of  $\alpha$  particles producing the  $\alpha$ -n interactions in SNO+.  ${}^{210}\text{Po}$  originates from the  ${}^{238}\text{U}$  decay chain, has a half-life of 138.4 days and emits  $\alpha$  particles at 5.304MeV [96].  ${}^{210}\text{Po}$  may also  $\alpha$  decay as  ${}^{210}\text{Po} \rightarrow {}^{206}\text{Po} + \alpha(4.517\text{MeV}) + \gamma(0.803\text{MeV})$ , 0.0012% of the time [147]. This decay branch was ignored in this partial fill analysis. Despite the quenching in  $\alpha$  scintillation during the partial fill phase (table 4.4), the reconstructed energy of the  ${}^{210}\text{Po}$   $\alpha$  was far above the threshold energy of the detector, allowing for an in-situ measurement of the  ${}^{210}\text{Po}$  rate, required for the calculation of the expected  $\alpha$ -n rate.

The rate of  ${}^{210}\text{Po}$  was measured in partial fill data by S. Riccetto, fitting the low energy peak centred around  $\sim 0.4\text{MeV}$  (the quenched energy peak produced by the 5.3MeV  ${}^{210}\text{Po}$   $\alpha$  particle). Figure 6.5 displays the fit method implemented, also fitting the underlying

$^{210}\text{Bi}$  contribution. A decay rate of 85Hz on average over the partial fill dataset, in a fiducial volume defined by  $r < 5.7\text{m}$  and  $z > 0.85\text{m}$ , with a >99% tagging efficiency. Extrapolating by volume to the full scintillator volume in partial fill, defined by  $r < 6\text{m}$  and  $z > 0.75\text{m}$ , a rate of 103.7Hz was estimated for  $^{210}\text{Po}$  for the antineutrino analysis.

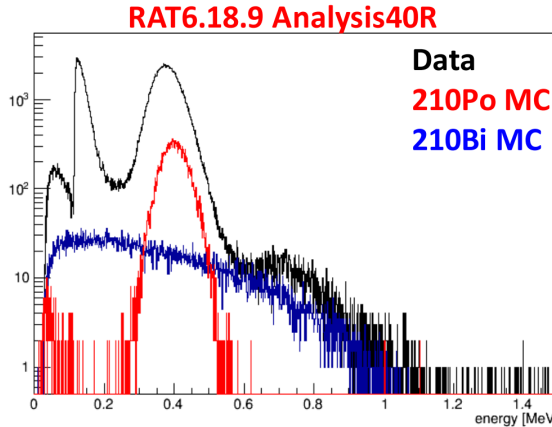


Figure 6.5: Low energy peak fit of the  $^{210}\text{Po}$  rate carried out by S. Riccetto, plot taken from [148].

### 6.3.2.3 $\alpha$ to $\alpha$ -n Conversion

Following the  $^{210}\text{Po}$  rate measurement, the next step in the  $\alpha$ -n rate prediction was the calculation of the  $\alpha$  to  $\alpha$ -n conversion fraction, through a calculation of the interaction cross section. The following calculations referenced here reflect studies of the  $\alpha$ -n interaction and ongoing measurements of its cross section since the 1950s [149]. There are still outstanding uncertainties in the cross section, branching ratios and emitted neutron energy spectra, where for some of these parameters there is ongoing debate.

To calculate the total yield of  $^{13}\text{C}$  ( $\alpha, \text{n}$ ) $^{16}\text{O}$  interactions for a given  $^{210}\text{Po}$   $\alpha$  decay rate, the conversion fraction to neutrons can be calculated as:

$$N = n_{^{13}\text{C}} \int_0^{E_\alpha} dE_\alpha \frac{\sigma(E_\alpha)}{dE_\alpha/dx}, \quad (6.3)$$

where the scintillator was treated as a thick target, assuming a mono-energetic  $\alpha$  particle slowed down in the scintillator according to the stopping power of the particle in the medium  $dE/dx$ . The number density of  $^{13}\text{C}$  is represented as  $n_{^{13}\text{C}}$ . Finally  $\sigma(E_\alpha)$  represents the  $\alpha$  capture cross section as a function of energy.

For the cross section, the JENDL/AN-2005 libraries were adopted for this analysis [150]. JENDL presents a calculation of the continuous  $\alpha$  capture cross section, based primarily on cross section measurements by K.K. Sekharan *et al.* (1967) [151] and J.K. Bair *et al.* (1973) [152]. Figure 6.6 shows the JENDL result for  $\alpha$  capture on  $^{13}\text{C}$  assumed in this analysis. Also shown are the direct measurements of the cross section, including the more recent Harissopoulos *et al.* [153] result, which is referenced throughout this work, but was not incorporated in the JENDL cross section used in this partial fill analysis.

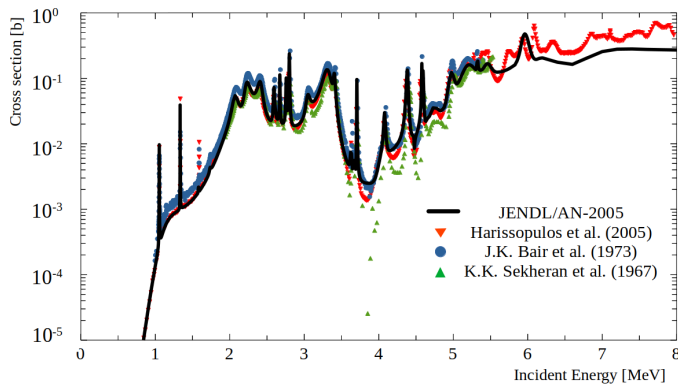


Figure 6.6:  $\alpha$  capture on  $^{13}\text{C}$  cross section against  $\alpha$  energy, showing in solid black, the calculated result from the JENDL/AN-2005 libraries [150]. Shown also are data points from direct measurements of the  $^{13}\text{C}$  cross section. These graphs were made using JANIS Web [154].

A numerical calculation of equation 6.3 for the Daya Bay liquid scintillator experiment was carried out assuming a  $^{210}\text{Po}$   $\alpha$  source. Using the shown capture cross section and GEANT4 .9 .2 simulations of the  $^{210}\text{Po}$   $\alpha$ 's propagation in the Daya Bay scintillator, taking stopping power factors from SRIM [155], a total neutron yield per  $^{210}\text{Po}$   $\alpha$  of  $5.8 \pm 0.4 \times 10^{-8}$  was found, where the uncertainty was predominantly decided by the cross section and its integration over the  $^{210}\text{Po}$   $\alpha$  path. This calculation was made for the Daya Bay Gd-loaded LAB liquid scintillator cocktail which was calculated to have a number density of  $^{13}\text{C}$  of  $3.85 \times 10^{20} \text{ cm}^{-3}$  (where the uncertainties in the density were small compared to the capture cross section). Rate uncertainties are discussed further in chapter 7.

The value for  $^{210}\text{Po}$   $\alpha$ -n conversion fraction assumed for SNO+, was taken from the aforementioned Daya Bay calculation, accounting for differences in the  $^{13}\text{C}$  content for the scintillator cocktail. Although SNO+ shares the same liquid scintillator compound as Daya Bay, scintillator chain lengths can vary markedly, so a separate measurement of the

carbon content needed to be accounted for. Previous measurements of the the SNO+ scintillator cocktail yielded an average elemental composition of  $H_{28.360}C_{17.195}N_{0.002}O_{0.002}$  in LAB + 2g/L PPO [70], along with a measured liquid scintillator density in partial fill of  $0.857\text{ g/cm}^3$ . These measurements yielded a moderately larger  $^{13}\text{C}$  number density (compared to the DayaBay liquid scintillator) of  $4.15 \times 10^{20}\text{ cm}^{-3}$ . Uncertainties in the measured density were on the level of 0.1%. For the partial fill scintillator (LAB + 0.5g/L PPO) the difference in  $^{13}\text{C}$  content due to the lower PPO concentration was considered negligible. Accounting for the larger measured  $^{13}\text{C}$  content in the SNO+ scintillator compared to the Daya Bay medium, the total  $^{210}\text{Po}$   $\alpha$  neutron conversion fraction was scaled up to  $6.2 \pm 0.4 \times 10^{-8}$  (assuming the same cross section dominated uncertainties in the Daya Bay result).

Assuming the  $^{210}\text{Po}$  rate measured in partial fill, and the  $\alpha$ -n yield rate calculated above, figure 6.7 depicts the Asimov dataset expectations for the partial fill dataset, applying the analysis cuts shown in table 6.1. Apparent immediately is the large amount of contamination due to  $\alpha$ -n in the partial fill phase. Their impact on the sensitivity to oscillation parameters will be demonstrated in chapter 8, followed by discussion of their removal in future SNO+ analyses.

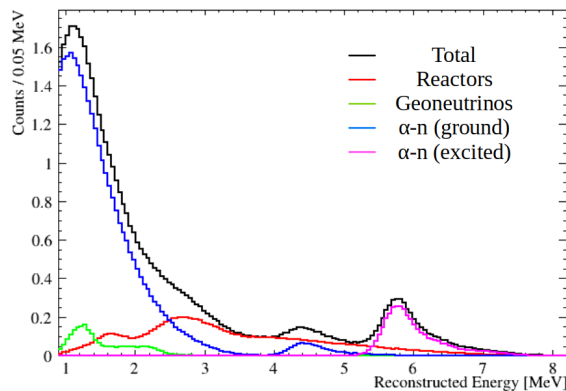


Figure 6.7: Asimov dataset of the reconstructed prompt event energy spectra for the partial fill dataset due to reactor antineutrinos, geoneutrinos and  $\alpha$ -n.

#### 6.3.2.4 $^{13}\text{C}(\alpha,n)^{16}\text{O}$ Spectrum Shape

While the total rate of the expected  $\alpha$ -n prompt energy spectrum is dictated by the total cross section in figure 6.4(a), there are a number of other factors apart from the cross

section which can impact the expected shape.

**$^{16}\text{O}$  Branching Ratios** The relative size of excited energy peak (3) to ground state peaks (1) and (2) in figure 6.4, depends upon the branching ratios of the first and second excited energy final states of  $^{16}\text{O}$ . The two  $^{16}\text{O}$  excited states form the single peak (3) in reconstructed energy. The 5.304MeV  $\alpha$  from  $^{210}\text{Po}$  only has sufficient energy to access the first two excited states of  $^{16}\text{O}$ , as summarised in table 6.2, alongside the branching ratios assumed in RAT simulations. There are currently large uncertainties on these excited state branching ratios<sup>1</sup>.

Table 6.2: Summary of the possible  $^{16}\text{O}$  states accessible following the  $^{13}\text{C}(\alpha, n)^{16}\text{O}$  interaction, following the  $\alpha$  decay of  $^{210}\text{Po}$  [150]

$^{16}\text{O}$ State	Threshold $E_\alpha$ (MeV)	Energy Level (MeV)	Decay Mode	Branching Ratio
Ground	0	0	-	90.8%
1 <sup>st</sup> Excited	5.014	6.049	$e^+ + e^-$	8%
2 <sup>nd</sup> Excited	5.119	6.13	$\gamma$	1.2%

**Neutron Energy Spectrum** Energetic neutrons are emitted at a wide range of energies by the ground state  $^{16}\text{O}$ . These spectra of these energetic neutrons dictate the prompt reconstructed energy spectrum due to the scattered protons in peak (1) of the  $\alpha$ -n prompt spectrum.

Figure 6.8 displays the assumed neutron energy spectrum used in the simulation of  $\alpha$ -n in RAT. The spectrum shown was created using the  $\alpha$ -n cross sections from JENDL and  $\alpha$  stopping powers for  $^{210}\text{Po}$   $\alpha$ s from SRIM, the same as those used for the total  $\alpha$ -n rate calculation in the previous section. The calculations adopted from JENDL also accounted for the neutron angular partial cross section distributions, typically parameterised by Legendre Polynomials [146].

For the expected magnitude of peak (2), any uncertainties in the inelastic neutron scatter

<sup>1</sup>Harissopoulos *et al.* presented a cross-section measurement with a 4% uncertainty, directly compared against deploying a dedicated  $\alpha$ -n source [147]. The source allowed for separation of the the two excited states (separately measuring the  $e^+$  annihilation peak). Good agreement was found at low energies, while a scaling factor of 0.6 was required for the 1<sup>st</sup> excited state [52]. Debate over the cross section uncertainties at higher energies is ongoing. It was noted in [156] that the Harissopoulos *et al.* result might be subject to overestimation for  $\alpha$  energies above 5MeV.

on  $^{12}\text{C}$ , as modelled in GEANT4, were again expected to be negligible due its small contribution overall.

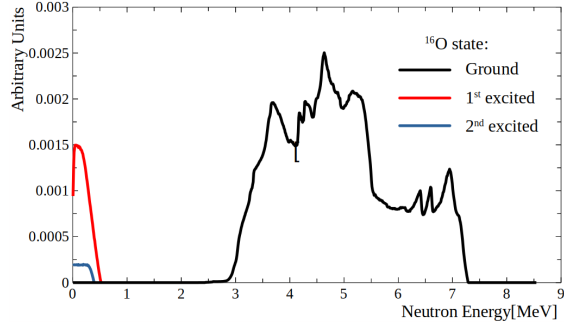


Figure 6.8: Neutron energy spectra for the  $^{210}\text{Po}$   $\alpha$ -sourced  $\alpha$ -n interaction [150] [155].

**Proton Scintillation Quenching. Peak (1)** The modelling of the subsequent energetic neutron interactions in the detector were calculated in GEANT4. The quenching of scintillation light for energetic protons was measured in dedicated neutron beam experiments carried out on samples of the SNO+ liquid scintillator, measuring  $k_B = 0.0093 \pm 0.0004 \text{ cm/MeV}$  for protons in LAB + 2g/L PPO [70].

Related to the calculation of the neutron energy spectrum above, it has been investigated by the Daya Bay and KamLAND experiments, the impact of simulating (also using GEANT4) the isotropic emission of energetic neutrons in  $\alpha$ -n interactions versus emission with an angular dependence [157][146]. It was found that the expected impact the angular dependence had to the prompt energy spectrum was small (primarily due to the fact that the energetic neutron scatters multiple times). In this statistics-limited analysis, isotropic emission of neutrons was assumed in the simulation of  $\alpha$ -n events in RAT.

### 6.3.2.5 Surface $\alpha$ -n events

The measurable reactor antineutrino flux would be maximised by including the entire scintillator volume within the AV. High rates of  $^{210}\text{Po}$  from the surface of the AV prevented the use of a maximal fiducial volume defined by  $r < 6\text{m}$  [158]. The fiducial volume of  $r < 5.7\text{m}$  was calculated in simulation to reduce the contamination of  $\alpha$ -n from the surface to negligible levels [159]. This allowed only  $^{210}\text{Po}$  measured in the scintillator bulk to be considered in the calculation of the expected total  $\alpha$ -n contamination.

### 6.3.3 Uncorrelated Background - Accidentals

As was seen in chapter 4 in the tagging of coincident BiPo214 events, the term ‘accidentals’ was used to describe the uncorrelated, random background events in the detector which pass the coincidence analysis cuts. For periods of data where there was a very high rate of background events, there was increased probability of two uncorrelated decays occurring close together in time and space, passing the antineutrino analysis cuts. The uncorrelated nature of the event pairs passing the coincidence cuts leads to the expectation of a flat distribution for the time between the event pairs ( $\Delta t$ ). The expected  $\Delta r$  distribution for accidental events is expected to approximately follow a  $(\Delta r)^3$  distribution (i.e. a random background event probability increases with the volume of the sphere defined by radius  $\Delta r$ ). The calculation of the expected accidentals contamination was calculated directly from the dataset, an advantage over the previously mentioned background calculations.

#### 6.3.3.1 Accidental Rate Contamination Calculations

**Antineutrino-like Event Rate Measurement** The primary method used to calculate the expected antineutrino contamination involved the rate of prompt-like and late-like events occurring in the detector, measured on a run-by-run basis. The total number of random accidental event pairs expected to pass the IBD coincidence cuts with time window  $\Delta t$ , calculated for a total search livetime  $T$  as:

$$N_{\text{acc}} = r_p \cdot r_l \cdot \Delta t \cdot T, \quad (6.4)$$

where  $r_p$  is the rate of single events that pass the prompt cuts individually in table 6.1. The calculation assumes a constant rate of uncorrelated background events over the run. In order to account for the  $\Delta r$  cut in the IBD tagging, all prompt-like and late-like events were paired at random, applying the  $\Delta r$  cut on the pair.  $r_l$  then was the rate of events which passed the late event analysis cuts, and also passed the  $\Delta r$  requirement with randomly paired prompt events. The calculated total accidental contamination for the entire partial fill antineutrino dataset was calculated as  $0.216 \pm 0.002$  events, showing statisti-

cal uncertainty. This small rate of expected accidental events was not included in the antineutrino likelihood analysis.

The accidental contamination rate dictated the choice of the 0.9MeV prompt event energy cut in table 6.1. A lower energy cut of 0.4MeV would have allowed for the entire  $\alpha$ -n spectrum in figure 6.4(a) to be measured and constrained. It was found however for this lower energy cut, the accidental contamination level increased to rates which could no longer be neglected.

**Extended  $\Delta t$  Window** An alternative calculation of the accidental contamination used for comparison, involved extending the  $\Delta t$  window in the IBD analysis cuts. Accidental event pairs uncorrelated in time were expected to have flat  $\Delta t$  distribution, so extending the window beyond the lifetimes of any correlated pairs would capture accidental pairs alone. The IBD cuts in table 6.1 were applied to data, with the  $\Delta t$  cut replaced with  $1 < \Delta t < 40.98\text{ms}$ , a window 50 times longer than the original cut. This yielded a total of 11 pairs and therefore an expected accidental contamination of 0.22 events, agreeing with the negligible result in the previous calculation.

### 6.3.3.2 BiPo214 Removal - Accidentals

It was shown in figure 4.7 that the rate of BiPo214 decays early on in the partial fill phase was large in the early portion of the phase, until eventually levelling out. BiPo214 events, although themselves correlated in time, are not expected to pass the IBD analysis cuts at an appreciable rate, since the delayed  $^{214}\text{Po}$  event ( $\sim 0.7\text{MeV}$ ) falls far below the late energy window. BiPo214 events however can produce antineutrino candidate event pairs at sufficiently high rates, as to contaminate the IBD selection in the form of accidental events. The prompt  $^{214}\text{Bi}$  event produces reconstructed energies which frequently pass the late neutron energy cut. Therefore, two independently decaying  $^{214}\text{Bi}$  events occurring close together in time and space could pass the IBD analysis cuts.

For this reason, BiPo214 events were tagged and removed from the dataset prior to the search of antineutrino events. Since BiPo214 pairs were not tagged at a 100% efficiency, a secondary check for the removal of BiPo214 pairs was also applied. For every tagged

antineutrino candidate pair, any  $^{214}\text{Po}$  event measured between the pair or after the late event (up to 2ms, covering many  $^{214}\text{Po}$  half-lives) demoted the antineutrino candidate pair to an accidental. The  $^{214}\text{Po}$  was defined as an event with reconstructed energy greater than 0.5MeV and reconstructed within 2m of either the prompt or late antineutrino candidate events, occurring after the prompt event. The tagging efficiency of the  $^{214}\text{Po}$  alone applying the above conditions was assumed to be 100% from simulation. It was found that this extra tag of the  $^{214}\text{Po}$  was not required, following the prior removal of tagged BiPo214 pairs. Repeating the accidental contamination when BiPo214 events were not first removed, yielded an expected contamination of 0.71 events across the partial fill dataset.

Plot 6.9 shows the energy spectrum of all prompt-like events, i.e. single events which pass only the prompt cuts in table 6.1, following the removal of BiPo214 pairs. These single prompt-like events form the energy distribution of the accidentals backgrounds, which was considered negligible in this analysis.

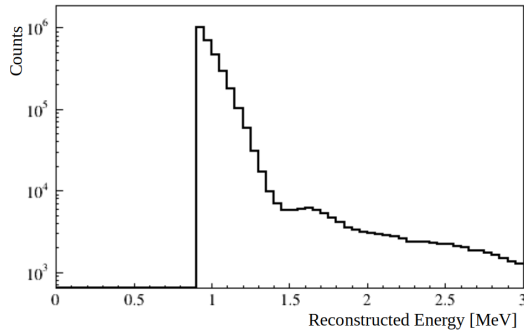


Figure 6.9: Energy distribution of all prompt-like events in the partial fill antineutrino dataset.

### 6.3.4 Atmospherics

#### 6.3.4.1 Atmospheric Neutrinos

As seen in chapter 1, highly energetic neutrinos created through cosmic ray interactions in the atmosphere can reach the SNO+ detector. These neutrinos span a wide range of energies, typically measured from 100MeV to 10GeV [39].

Atmospheric neutrinos can interact with nuclei in the detector,  $N$ , through NC and CC interactions as:  $\nu + N \rightarrow \nu + X$  and  $\nu + N \rightarrow l + X$ , producing new nuclei  $X$  and

leptons  $l$ . Atmospheric neutrinos can produce antineutrino candidate events by way of the production of multiple neutrons through the interactions with primarily  $^1\text{H}$ ,  $^{12}\text{C}$  and  $^{13}\text{C}$  in the scintillator. In the water phase, the much larger presence of oxygen yielded a non-negligible rate of expected contamination due to the decay of excited  $^{15}\text{O}$  produced through NC interactions. Calculations made for the water phase antineutrino analysis [133], were repeated in the partial fill phase to calculate the expected atmospheric neutrino contribution. The calculations were made using the GENIE neutrino Monte Carlo generator [160]. The GENIE calculations in scintillator showed a negligible number of contamination events were expected to pass the antineutrino analysis cuts [161].

The flux of MeV-scale  $\bar{\nu}_e$  reaching SNO+, originating directly from atmospheric interactions is many orders of magnitude below the flux of electron antineutrinos from reactor cores [162], and therefore was also ignored.

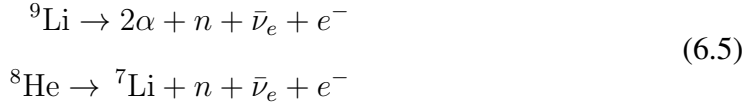
#### 6.3.4.2 Muon Induced Backgrounds

The rate of muons passing through the SNO+ detector is well understood, combining measurements made in the SNO+ water phase [163] with measurements made in the SNO detector [54]. The advantage SNO+ has over similar experiments is the depth at which it is situated (figure 2.1(a)). The resultant low muon flux (approximately 3 per hour) produces a large reduction in the expected rates of all cosmogenic-induced background events.

High energy cosmic-ray muons passing through or near the SNO+ detector also have the ability to produce antineutrino-like coincident events. Energetic muons can produce virtual photons which interact with nuclei (mainly  $^{12}\text{C}$  in the scintillator) producing neutrons and unstable isotopes [164]. The subsequent disintegration of the nuclei and emission of radiation due to the energetic muon is known as muon spallation. Below are descriptions of the antineutrino-like events muon interactions may produce, followed by the method used to remove them.

**Long-lived Muon Spallation Daughter Nuclei** The long-lived nuclei produced by muons (spallation daughters) can also emit neutrons upon their eventual decay [163].

The nuclei of concern in many antineutrino analyses are ones which may undergo  $\beta + n$  decay, mimicking an antineutrino IBD event pair.



Noteworthy spallation daughter nuclei are  ${}^9\text{Li}$  and  ${}^8\text{He}$ , decaying with Q-values of 13.6 and 10.7MeV, half-lives of 0.18 and 0.12 seconds, and having  $\beta + n$  branching fractions of 51% and 15% respectively. Muon follower events have been a careful subject of study for reactor and geo-antineutrino analyses carried out in Borexino and KamLAND [165][52]. The large number of other possible neutron-yielding spallation daughter nuclei (not expected to contaminate significantly this antineutrino analysis) can be seen in analyses carried out by KamLAND [164].

Another long-lived isotope carefully considered in the SNO+ water phase antineutrino analysis, was the muon-induced interaction  ${}^{18}\text{O}(n,n+p){}^{17}\text{N}$ . This interaction has been generally negligible in experiments with liquid scintillator, which typically do not contain significant amounts of oxygen. In SNO+ however, muons passing through the external water outside of the AV were considered. The  ${}^{17}\text{N}$  produced can decay via  $\beta + n$ . The decay lifetime is 4.173s [91], leading to the 20s muon veto cut in table 6.1, which covered  $\sim 5$  lifetimes of  ${}^{17}\text{N}$  decays, combined with the fiducial volume cut allowed for their contribution can be neglected.

**Muon Induced Neutrons** Interacting muons may produce multiple neutrons, where two neutrons capturing close together in space can mimic an antineutrino event.

**Muon Induced Fast Neutrons** The neutrons produced by muons may have sufficiently large energies such that, as in the  $\alpha$ -n process, can scatter protons in the detector, mimicking a prompt signal [164]. Fast neutrons can be produced by muons that propagate only through the external water in the detector, or surrounding rock in the cavity. These external muons are less easily tagged, than internally travelling muons. Externally produced fast neutrons may propagate into the scintillator, producing IBD-like events.

### 6.3.4.3 Removal of Atmospheric-Induced Antineutrino Candidates

The much reduced muon flux allowed for a straightforward veto of all data following a tagged muon event (table 6.1), without a significant loss of livetime.

**Muon Follower Data Veto** The long time window provided rejection of the spallation daughter decays and neutrons, ensuring they had already decayed/captured long before the search for antineutrinos was resumed. Muons passing through the scintillator produced very easily identifiable events with large nhits, and so were removed with an efficiency assumed to be negligibly different from 100%. Simulation studies supported the negligible impact of muons at SNO+, showing that the large nhit muon cut in table 6.1 was sufficient in reducing the muon follower event background to negligible levels [166].

The combination of a low muon rate, high muon tagging efficiency and the long muon veto time window, lead to the expectation of negligible levels of muon-induced backgrounds. This was expected, by a simple comparison with reactor and geoneutrino analyses carried out in similar detectors KamLAND [52] and Borexino [165]. Both experiments measured significantly higher rates of muons, with similar muon tagging efficiencies, while still measuring small rates of muon-induced backgrounds. A simple scaling approach of the background levels measured in both experiments also leads to negligible muon-induced contamination expected at SNO+.

**Multiplicity Cut** The multiplicity cut was already introduced in part, used to tag potential  $^{214}\text{Po}$  events following a tagged antineutrino candidate pair. The multiplicity cut involved a search for triggered events 2ms before, between and after the tagged antineutrino pair candidate. This allowed coincident pairs due to multiple neutrons (produced by muons or atmospheric neutrinos) to be removed. E.g. if one or more neutrons were tagged in the region of the prompt and late antineutrino candidate pair, the pair was removed. In the case that only two neutrons were produced by a muon or atmospheric neutrino, the multiplicity cut was less effective. To combat against the two neutron case, the multiplicity cut was defined as any reconstructed event greater than 0.4MeV, within 2m of the candidate pair, this allowed for the case of fast neutrons scattering protons. The multiplicity cut could remove a pair if scattered protons were measured in the region

of the pair. No antineutrino candidate pairs measured in this antineutrino analysis were found to fail the multiplicity cut, as expected.

Having outlined the expected backgrounds and their rates, the next section presents the antineutrino analysis cuts applied to the partial fill dataset, comparing simulation and data.

## 6.4 Measured Antineutrino Candidates in Partial Fill

Using the introduced calculations for reactor and antineutrino signal and background rates, Table 6.3 summarises the expected number of events to pass the analysis cuts (table 6.1) in the partial fill dataset, for the livetime defined in section 6.1. The uncertainties associated with each will be described in section 7.2.2.1.

Table 6.3: The expected reactor antineutrino signal and background rates.

Name	Expected Event Count
Reactors	9.4
Geoneutrinos	2.2
$\alpha$ -n	33.3

Applying the analysis cuts to partial fill data yielded a total of 44 candidate IBD pairs, in agreement with the  $44.8 \pm 6.7_{\text{stat}}$  pairs expected from simulation, summarised in table 6.3. Figure 6.10 displays the key distributions of all the antineutrino candidate pairs tagged in partial fill data alongside simulation for selected plots. The simulated distributions (apart from the prompt energy spectrum) were those of reactor antineutrino events applying the same analysis cuts, scaled to the expected 44.8 total events. The simulated prompt energy spectrum in figure 6.10(a) reflects simulation using the PDG global oscillation values, shown in table 5.3, with background normalisations assumed as the expected rates in table 6.3. It can also be seen that the measured late reconstructed energy,  $\Delta t$  and  $\Delta r$  distributions agree well with simulation. The  $\Delta t$  distribution was also fit using equation 6.1 using Minuit’s binned likelihood option, which yielded a decay time constant of  $220 \pm 30 \mu\text{s}$  where the uncertainty shown was the uncertainty in the fit. This was consistent with simulation and neutron lifetime measurements made in the scintillators of KamLAND and Borexino. While data and simulation showed good agreement in each

of the important IBD distributions, figure 6.10(e) shows an unexpected lack of events with small  $z$  and  $\rho$  position. The reason for this region not detecting any IBD events was not identified, although the limited event statistics lessens the significance of this discrepancy.

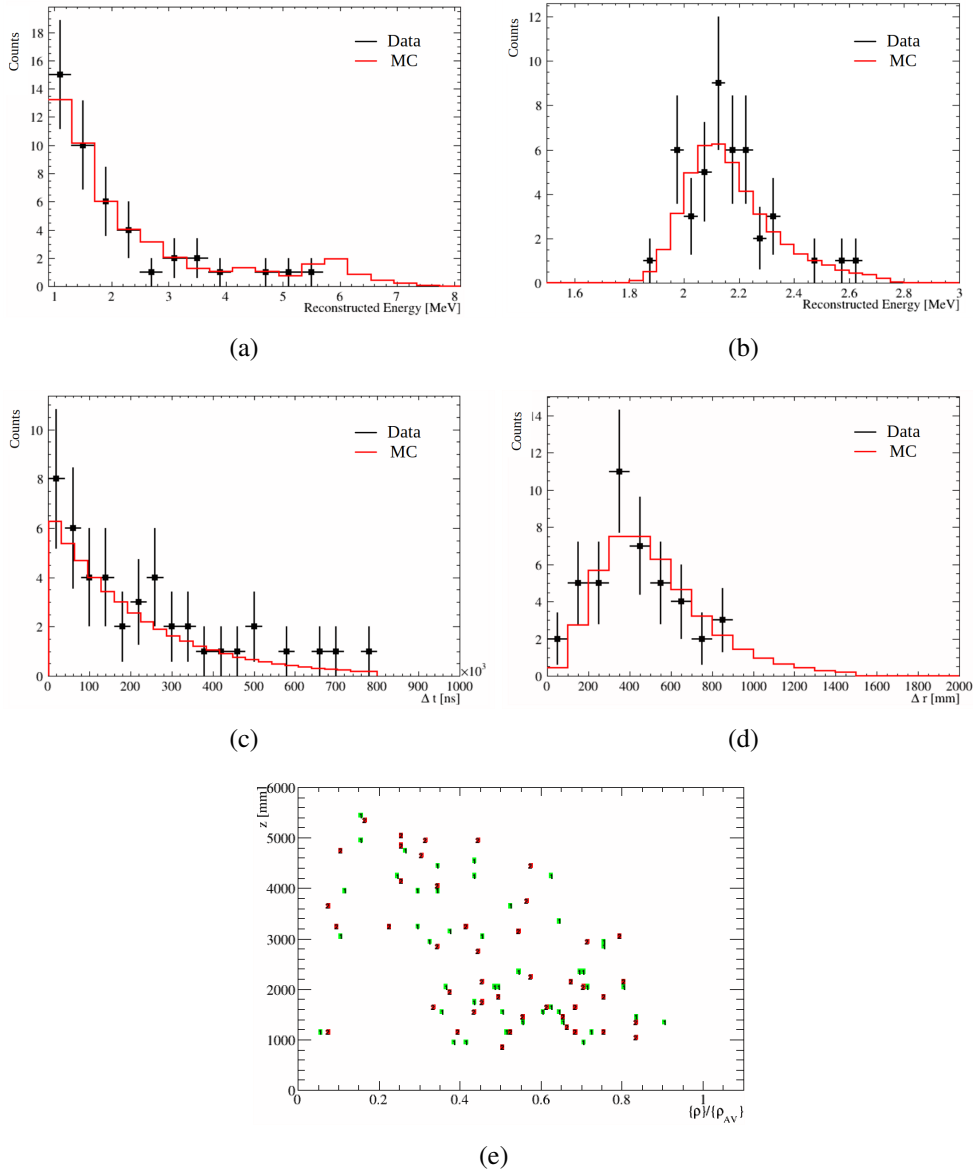


Figure 6.10: Coincident event distributions for the 44 event pairs measured in partial fill data. (a) Prompt reconstructed energy (MC oscillated using table 5.3 values) (b) Late reconstructed energy (c)  $\Delta t$  (d)  $\Delta r$  (e)  $z$  vs  $(x^2+y^2)^{1/2}$  position of event pairs (1 = prompt, 2 = late).

### 6.4.1 Conclusion

Following the calculation of expected signal and background rates in the antineutrino analysis, the application of the introduced analysis cuts to data and simulation yielded consistent distributions in terms of shape and normalisation. The next chapter involves the likelihood fit of the data prompt energy spectrum in figure 6.10(a), to extract neutrino oscillation parameters  $\Delta m_{21}^2$  and  $\theta_{12}$  along with the nuisance parameters.

# 7 | Results - Sensitivity Analysis

This chapter presents the spectral likelihood fit used to extract neutrino oscillation parameters from the measured IBD candidate prompt event energy spectrum. The following sections establish the analysis framework for the likelihood fit, including the management of backgrounds and systematics, followed by results of the fits. Due to the limited statistics, sensitivity to the oscillation parameters was limited in the partial fill phase. This antineutrino analysis will be repeated in the future scintillator phases, where chapter 8 demonstrates the experimental prospects of the fully filled SNO+ scintillator detector.

## 7.1 Energy Spectrum Likelihood Framework

The measurement of  $\Delta m_{21}^2$  stems from the characterisation of distortions in the measured prompt energy spectrum from reactor antineutrino events. The intention was to find the oscillation parameters which best represented the measured antineutrino energy spectrum in data (or from a Bayesian perspective, which parameter values are most likely true, considering the spectrum measured in data).

The C++-based likelihood calculation was adapted from OXO, a framework written originally by J. Dunger for the purposes of  $0\nu\beta\beta$  signal extraction at SNO+ [90]. The framework was created to efficiently manage the variety of C++ object classes used in the likelihood fit, such as pdfs, systematics effects, test statistics and optimisation algorithms.

### 7.1.1 Pdf Generation

Required for the likelihood fit, was the calculation of the expected rate and spectral shape for each nuclear reactor, as summarised in chapter 5. Pdfs were also included for each background source, as discussed in the previous chapter. The pdf of a specific reactor or background, represents the probability of measuring a tagged IBD event of a certain reconstructed energy, from that source.

### 7.1.1.1 Oscillating Reactor Reconstructed Energy Spectra

Oscillated energy spectra pdfs for each nuclear reactor were generated in simulation. Approximately  $5 \times 10^5$  IBD events were generated in simulation, where simulated antineutrino event pairs which passed analysis cuts were either kept or discarded, depending on the antineutrino kinetic energy and the propagation distance from the origin reactor (applying equation 1.39).

There were over 30 signal-contributing nuclear reactors within a 1000km radius of SNO+ accounted for in the partial fill analysis, each with their own distance, thermal power and reactor type, as summarised in table C.1. Each pdf reflected its own unique contribution to the expected measurable energy spectrum. Some of the larger reactor complexes have multiple nuclear reactor cores. These cores can be separated over a few kilometers from one another. This was neglected, where each reactor power plant was treated as a single reactor core, placing it at the thermal power-weighted average position of all the active cores for that plant.

**Far Away Reactors** There are many other nuclear reactors worldwide beyond this distance included in simulation, but due to their minimal contributions, a single pdf was used to represent their total flux (all assumed to be PWR-type reactors). The expected contribution of world reactors beyond 1000km to the total expected unoscillated signal at SNO+ was 9%. As was seen for geoneutrinos, since the sources of all reactors beyond 1000km are spread out over large distances, the distance-averaged survival probability in equation 6.2 was used to oscillate these events. In doing this, again, dependence in  $\Delta m_{21}^2$  was lost for these events.

The expected spectral shapes and event rates have now been established for each of the contributing reactors and backgrounds. The next section outlines the likelihood calculation, which combines all of the considered pdfs and fits each of their contributions in the energy spectrum measured in data.

### 7.1.2 Binned Likelihood Expression

A binned extended log likelihood was adopted for this reactor antineutrino analysis. Ignoring background events for the time being, the following expression is the likelihood calculated against the energy spectrum histogram measured in data with  $n_{\text{obs}}^j$  events in the  $j^{\text{th}}$  bin and  $N_{\text{bins}}$  bins in total. The first two terms in the expression below represent the binned extended log likelihood:

$$\log(\mathcal{L}(\vec{n}_{\text{obs}}|\vec{\theta})) = - \sum_{i=0}^{N_{\text{reac}}} N_i + \sum_{j=0}^{N_{\text{bins}}} n_{\text{obs}}^j \log\left(\sum_{i=0}^{N_{\text{reac}}} N_i P_i^j(\vec{\theta})\right) - \sum_{i=0}^{N_{\text{reac}}} \frac{(N_i - \widehat{N}_i)^2}{2\sigma^2}, \quad (7.1)$$

where the final term is a constraint term, described later. The log likelihood was calculated for the  $N_{\text{reac}}$  pdfs, where each pdf has a normalisation of  $N_i$  (i.e. the  $i^{\text{th}}$  reactor contributes  $N_i$  events to the total measured event count in data).  $P_i^j$  represents the content of  $j^{\text{th}}$  bin of the normalised pdf for the  $i^{\text{th}}$  reactor.  $\vec{\theta}$  represents the parameters of interest, the neutrino oscillation parameters, which dictate the shape of the oscillated reactor spectrum.

**Normalisation Parameters** The first two terms in equation 7.1 express the likelihood for some general  $N_{\text{reac}}$  reactor contributions. As seen in chapter 5, each reactor's calculated contribution has an uncertainty associated with it. These expected rates and uncertainties were used to constrain the total number of events in the data expected from a single reactor. The third term in the expression above represents a constraint in the form of a Gaussian, applied to each of the reactor contributions. The expected contribution for reactor  $i$  is represented by  $\widehat{N}_i$ .  $\sigma$  represents the standard deviation uncertainty in the expected reactor normalisation  $\widehat{N}_i$ . These normalisation constraints essentially act as Bayesian priors on each reactor's expected contribution [167].

It should be noted, that the binned likelihood calculation using fine histogram binning (0.05 MeV bins), yields the same results as a continuous likelihood expression. A binned likelihood method was chosen mainly for convenience.

**Neutrino Oscillation Parameters** The oscillation parameters  $\vec{\theta}$  impact both the shape and normalisation of the total energy spectrum through spectral distortions due to neutrino oscillation.

**Systematic Uncertainty Nuisance Parameters** Other parameters that can also distort pdf normalisations and shapes, are the systematic uncertainty parameters. This analysis relies on comparison of data and expectation using simulations. These parameters represent the uncertainties in key reconstructed parameters, which can affect the size and shape of the energy spectrum measured in data. Energy scaling and resolution are examples of systematic uncertainties considered in this analysis.

These parameters can be added to the likelihood expression in equation 7.1 in the form of nuisance parameters  $\vec{\lambda}$ . These nuisance parameters are measurable in-situ, and like the normalisation parameters, can be constrained. To do this, another term was added, also in the form of a Gaussian constraint term:

$$\log(\mathcal{L}(\vec{n}_{\text{obs}}|\vec{\theta}, \vec{\lambda})) = - \sum_{i=0}^{N_{\text{reac}}} N_i + \sum_{j=0}^{N_{\text{bins}}} n_{\text{obs}}^j \log\left(\sum_{i=0}^{N_{\text{reac}}} N_i P_i^j(\vec{\theta}, \vec{\lambda})\right) - \sum_{i=0}^{N_{\text{reac}}} \frac{(N_i - \widehat{N}_i)^2}{2\sigma_{N_i}^2} - \sum_{k=0}^{N_{\text{nuis}}} \frac{(\lambda_k - \widehat{\lambda}_k)^2}{2\sigma_{\lambda_k}^2}, \quad (7.2)$$

where  $\widehat{\lambda}_k$  represents the independently measured value of the nuisance parameters and  $\sigma_{\lambda_k}^2$  represents the respective uncertainties in those measurements.

The reactor normalisations could also be considered as systematic nuisance parameters, as they represent uncertainties in reactor flux (but have been separated here for demonstration purposes). For the inclusion of backgrounds, their pdfs were essentially treated as reactor pdfs, except for their non-dependence on oscillation parameters  $\vec{\theta}$ . Their normalisation parameters  $N$  and respective constraints  $\sigma_N$  were treated identically to reactor pdfs.

### 7.1.2.1 Pdf Distortion: Systematic Uncertainties

This section involves the addition of the fittable nuisance parameters in the likelihood fit.

**Energy Scale and Resolution** For the measurement of an energy spectrum, uncertainties in the reconstructed energy had to be considered. These to leading order, were characterised by energy scale and resolution. Energy scaling uncertainties play a significant role in the sensitivity to  $\Delta m_{21}^2$ . This oscillation parameter essentially dictates the positions of the peaks and troughs in the measured oscillated reactor energy spectrum. However, uncertainties in energy scaling leads to ambiguity in the measured positions of these spectral peaks and troughs, and a subsequently diminished sensitivity to  $\Delta m_{21}^2$ . Figure 7.1 shows an example of energy scaling and smearing applied to the expected reactor antineutrino signal.

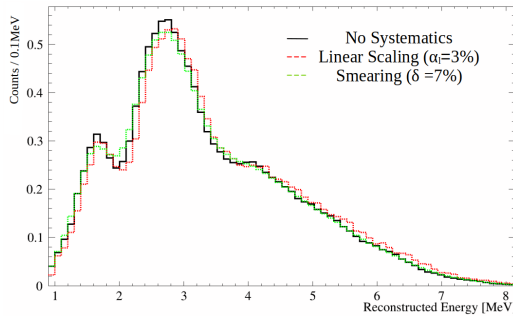


Figure 7.1: The reactor antineutrino signal spectrum in the partial fill analysis, applying linear energy scaling and energy smearing due to uncertainties in energy reconstruction.

Pdfs in the spectral fit analysis were constructed in the form of 1D histograms (with probability  $P(b_i)$  of measuring an event in the  $i^{th}$  energy bin), systematics were therefore constructed and applied to each pdf in the form of distortion matrices:

$$P(b_i)' = M_{ij} P(b_j) \quad (7.3)$$

The energy scaling uncertainties were represented by diagonal matrices  $M$  and could be placed in two categories: linear or non-linear. Linear scaling was quantified simply by  $\alpha_l$ , applied as a constant multiplicative factor on reconstructed energy  $E$  for all pdfs. Non-linear energy scalings could also be quantified by a scaling function ( $\alpha_{nl}$ ), dependent on  $E$ , which quantified the scintillator's non-linear response uncertainties at different energies, as will be seen in chapter 8.

Uncertainty in the energy resolution was accounted for by a convolution of each pdf with a normal distribution. This smearing of reconstructed energies was quantified by

a smearing factor  $\delta$ , used to calculate the standard deviation of the normal distribution convolved with each pdf. The distortions in the energy spectra pdfs for energy scaling and energy resolution were respectively applied as:

$$\begin{aligned} P(E') &= P(\alpha_{l/nl} \cdot E) \\ P(E') &= \int dE P(E) \mathcal{N}(E' - E, \sigma_{E'}), \text{ where } \sigma_{E'} = \sqrt{E'} \delta \end{aligned} \quad (7.4)$$

As each pdf is dependent on reconstructed energy  $E$ , all systematic matrix transformations were applied identically to all pdfs considered in a given likelihood fit. It will be seen that specific systematic distortions could also be applied to selected pdfs, when required.

**Position Resolution** Uncertainties in reconstructed position were expected to alter the spectral shape negligibly and instead impact the normalisation parameters. Uncertainties in the resolution affected the total number of events expected to fall in and out of the analysis fiducial volume. These uncertainties were contained in the total normalisation uncertainty factor  $\sigma_{N_i}$  in equation 7.2.

In the spectral fit, parameters  $\alpha_{l/nl}$  and  $\delta$  were added alongside the reactor and background normalisation factors  $N_i$ , to a parameter list. These parameters were then handled by an optimiser, to calculate the parameters which maximise the likelihood 7.2, as described in the next section.

### 7.1.3 Test Statistic - Profile Likelihood Calculation

Outlined now is the likelihood calculation made for a given dataset and assumed nuisance and oscillation parameters. The considered parameter values which maximised the likelihood value in equation 7.2 were used to estimate the most probable values of these parameters, given the data. The OXO code framework contained a number of options for optimising/sampling a given likelihood space (e.g. GridSearch, Markov Chain Monte Carlo). The ROOT Minuit optimiser was used in this analysis.

Apparent in the introduction of this likelihood expression used, was the large number of

parameters. Instead of finding all of  $\hat{\vec{\theta}}, \hat{\vec{\lambda}}$  that maximises  $\log(\mathcal{L}(\vec{n}_{\text{obs}} | \vec{\theta}, \vec{\lambda}))$ , one may carry out a 2-step calculation. It was advantageous to first maximise  $\log(\mathcal{L})$  w.r.t. nuisance parameters  $\vec{\lambda}$ , such that the test statistic was mapped out over a phase space containing only the oscillation parameters of interest. To measure the parameters  $\Delta m_{21}^2$  and  $\theta_{12}$  and the uncertainty in that measurement, a 2D phase space of these oscillation parameters was constructed. At each point, with specific values of  $\Delta m_{21}^2$  and  $\theta_{12}$ , all other non-oscillation parameters were fit for, such that the likelihood was maximised in equation 7.2. The survival probability in eqn. 1.39 is only weakly dependent on  $\theta_{13}$  so was treated as constant in all likelihood fits in this work, assuming the global PDG value in table 5.3.

Filling out the oscillation parameter phase space and maximising log likelihood at each point, gave an indication of which oscillation parameters best fit the data. The uncertainty in the parameters of interest was formally expressed in the form of test statistic.

### 7.1.3.1 Wilks' Theorem

In order to compare the viability of different oscillation parameters in the considered phase space (where each set of oscillation parameters represents a ‘model’), sensitivity confidence intervals were constructed using likelihood ratios  $\Delta \log(\mathcal{L})$ . The approach to this measurement was guided by the Neyman-Pearson lemma which states, when carrying out a hypothesis test between two simple hypotheses, there is no test more powerful than the likelihood ratio test [168].

For the oscillation parameter measurement, a profile likelihood ratio was used. The log likelihood ratio  $\Delta \log(\mathcal{L})$  compares the maximal log likelihood value, with respect to  $\vec{\theta}$  and  $\vec{\lambda}$  with the all other  $\log(\mathcal{L})$  in the  $\vec{\theta}$  phase space, which were maximised w.r.t.  $\vec{\lambda}$ . The  $\vec{\theta}$  value with maximum  $\hat{\mathcal{L}}$  in the phase space was denoted as  $\hat{\vec{\theta}}$  such that  $\Delta \log(\mathcal{L})$  is written as:

$$\Delta \log(\mathcal{L}) = \log \left( \frac{\mathcal{L}(\hat{\vec{\theta}}, \hat{\vec{\lambda}})}{\mathcal{L}(\vec{\theta}, \hat{\vec{\lambda}})} \right) \quad (7.5)$$

Wilks’ theorem states that, in the large sampling limit, the likelihood ratio test statistic  $2 \Delta \log(\mathcal{L})$  is distributed as  $\chi_p^2$  where  $p$  denotes the degrees of freedom, equal to the dimension of  $\vec{\theta}$  [167]. It can be shown that this profile ratio of likelihoods, obeys Wilks’

Theorem [169][170].

## 7.2 Systematics

Due to the limited number of reactor signal events expected in the dataset, sensitivity in the partial fill phase to oscillation parameters  $\Delta m_{21}^2$  and  $\theta_{12}$  was expected to be considerably limited. The scarce number of signal events also led to a decreased influence of systematic uncertainties, since Poisson fluctuations principally dictated the overall uncertainties in the likelihood fit. Regardless, the leading order systematic uncertainties were calculated. This antineutrino analysis is expected to be repeated in the future scintillator phases of the SNO+ experiment. Chapter 8 discusses the impact each systematic has on the sensitivity to  $\Delta m_{21}^2$ , calculated in the Te-loaded phase of the experiment, assuming various data-taking livetimes.

### 7.2.1 Calculation of Energy Scaling and Smearing Systematics

Of the systematics, uncertainties in energy reconstruction carry the largest impact on the sensitivity to  $\Delta m_{21}^2$ . Chapter 4 discussed in detail the use of BiPo214 to calibrate the energy reconstruction. Figure 4.18 showed negligible differences in the  $^{214}\text{Bi}$  energy spectrum measured in data and simulation following the application of position-dependent energy correction factors. This agreement was also found to be uniform across the whole antineutrino fiducial volume, as seen in figure 4.17(d). Not seen in the figures referenced, are the data-simulation discrepancies due to the time evolution of detector conditions, discussed next.

Figure 7.2 displays the evolution of energy reconstruction with time. The plots again show  $^{214}\text{Bi}$  energy spectra measured in the data and simulation used in figure 4.18, but dividing the dataset into four subsets (each of livetime  $\sim 32$  days). It can be seen data-simulation disagreement increased with time over the partial fill phase. Also visible, is the decreasing overall rate of BiPo214 decays with time over the analysis period.

It was seen in chapter 4, that a short period of time early in the partial fill phase was used to calibrate the scintillator optics, from the 4th of April to the 12th of May 2020.

Although good levels of PPO mixing had been measured in April [171], it is likely that the PPO mixing was not yet maximally homogenous during the period used to calibrate scintillator optics. Further infusion of PPO throughout the scintillator volume following this calibration period, likely sourced the discrepancies seen in the overall energy scaling for the  $r < 5.7\text{m}$  volume. The calibration period also had the highest rate of BiPo214 events, causing the discrepancies arising at the end of the partial fill to be obscured when the entire partial fill data was considered in figure 4.18.

Although BiPo214 statistics became more limited in the datasets shown in figures 7.2(c) and 7.2(d), which had the largest data-simulation discrepancies, statistical uncertainties in the calculated median and standard deviation were  $< 3\%$  and so were ignored for the determination of data/simulation ratios quoted in figure 7.2.

**Note on positrons vs  $\beta$ s** Without a positron calibration source, calibration using  $\beta$ s from  $^{214}\text{Bi}$  events was applied to reactor IBD positron events. While reconstruction may differ between  $\beta$ s and the  $\gamma$ s produced in positron annihilation, the modelling of  $\gamma$ s in liquid scintillator was assumed to be accurate in GEANT4. Any inaccuracies in this modelling should also yield negligible systematic uncertainties, as energy and position reconstruction in simulation and data, both rely on the same GEANT4 modelling.

## 7.2.2 Summary of Likelihood Nuisance Parameters

Table 7.1 summarises the systematic uncertainties in reconstructed energy and position, calculated using BiPo214. The impact these systematic uncertainties had to the reactor analysis cut efficiency was calculated in simulation. The positions and energies of simulated reactor antineutrino events were scaled and smeared by the presented uncertainties, where the tagging efficiency was recalculated and compared to the efficiency without any systematics applied.

**Energy** It has been demonstrated that energy reconstructions discrepancies in data and simulation arose principally due to variations in time. Discrepancies in the median ratios shown in figure 7.2 for the four datasets were used to calculate a total systematic uncertainty in energy scaling. To isolate the uncertainties in energy resolution, the simulated

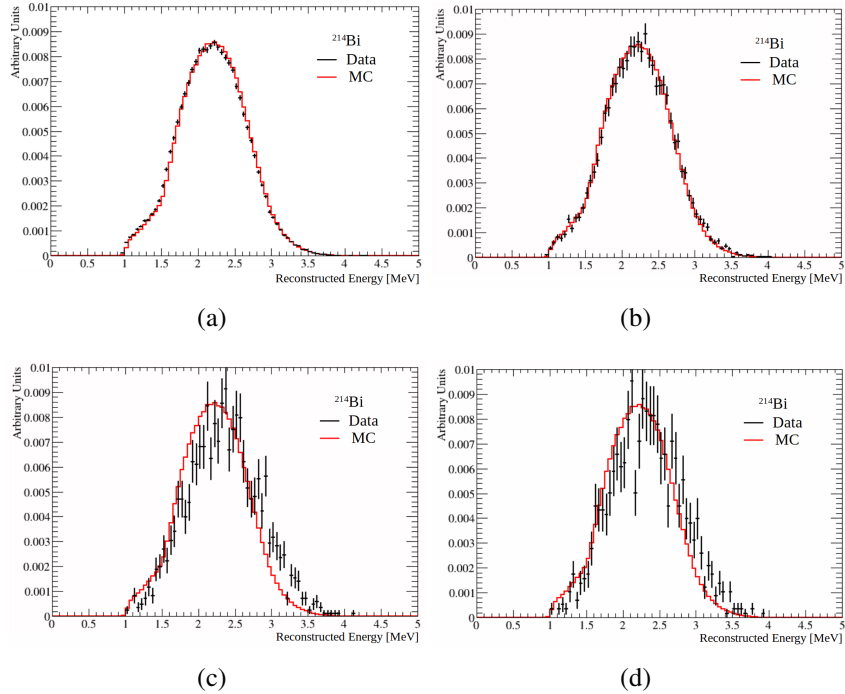


Figure 7.2:  $^{214}\text{Bi}$  reconstructed energy spectra measured in data and simulation, divided into four datasets each of livetime 31.95 days (ordered chronologically). The data/simulation ratios of the median ( $\tilde{E}$ ) and standard deviation ( $\sigma_E$ ) for the energy distributions were calculated as  $(\tilde{E}_{\text{data}}/\tilde{E}_{\text{mc}}, \sigma_{E,\text{data}}/\sigma_{E,\text{mc}})$ : (a) (0.99, 1.002) (b) (1.01, 1.012) (c) (1.06, 1.09) (d) (1.05, 1.07).

$^{214}\text{Bi}$  spectra in each time range were first scaled by data/simulation median ratios, then the resulting remaining ratios in the standard deviations were used to calculate uncertainties in energy resolution. Table 7.1 shows the averaged, absolute deviation from unity for: energy scaling represented by the median ( $\alpha_l = (\tilde{E}_{\text{data}}/\tilde{E}_{\text{mc}})$ ) and energy smearing represented by the standard deviation of the distribution ( $\delta = \frac{\sigma_{E,\text{data}}}{\sigma_{E,\text{mc}}}$ ). Changes to the tagging efficiency in table 7.1 were calculated by scaling event energies in simulation by  $E \rightarrow \alpha_l \cdot E$  and smearing energies using a Gaussian distribution as  $E \rightarrow \mathcal{N}(E, \sigma_E)$ . Losses in the signal efficiency were primarily due to late event energies being pushed outside of the narrow neutron energy window.

**Position** The BiPo214  $\Delta r$  distribution in figure 4.11(b) was used as a measure of the reconstructed position resolution uncertainty between data and simulation. A minor data-simulation discrepancy was seen, where positions were reconstructed with a marginally finer resolution in simulation compared to data. The position shift uncertainty of 5cm was not derived from BiPo214 and was instead assumed to demonstrate its impact to the

reactor antineutrino analysis. Event positions in simulation were smeared for each  $x$ ,  $y$  and  $z$  as  $x \rightarrow \mathcal{N}(x, \sigma_x)$  and shifted using  $x \rightarrow x + \Delta$ . A similar treatment used for the calculation of energy reconstruction systematics was repeated, measuring the BiPo214  $\Delta r$  distribution as a function of time. No significant evolution in the agreement between simulation and data was found. Table 7.1 displays the small impact the systematic uncertainties in position and energy reconstruction had on the expected reactor flux.

Table 7.1: Summary of the assumed systematic uncertainty values in the partial fill antineutrino analysis and their impact to the reactor antineutrino tagging efficiency.

Uncertainty	Value	Change to Efficiency
Energy Scaling ( $\alpha_l$ -1)	3.3%	-1%
Energy Smearing ( $\delta$ )	3%	-0.4%
Position Smearing ( $\sigma_{x,y,z}$ )	1cm	-0.02%
Position Shift ( $\Delta$ )	5cm	-0.2%

### 7.2.2.1 Nuisance Parameter Summary

Table 7.2 summarises the final systematic nuisance parameters used in the likelihood fits of the prompt energy spectrum. Described below are the sources of uncertainty for the reactor signal and sources of background.

**Reactors** The normalisation uncertainty used for each reactor pdf was assumed from calculations carried out in the water phase antineutrino analysis [91][133]. The total uncertainty value was primarily dictated by combined uncertainties in the modelled reactor flux, along with contributions from reactor core thermal powers, flux factors implemented from Daya Bay measurements [116] and reactor fuel fission fractions. The total uncertainty assumed for each reactor pdf normalisation was 3%. Sources of uncertainties that were assumed to play a negligible role have been referenced previously, including proton density, the MSW effect, spent nuclear fuel, non-equilibrium isotopes in nuclear reactor cores and the IBD cross-section.

**Geoneutrinos** The geoneutrino normalisation uncertainty was assumed to be 100% in the fit due to the large uncertainties in the models used to predict their flux. A single combined contribution for U and Th chains was also assumed due to the limited geoneutrino

event rate expected.

**$\alpha$ -n** The  $\alpha$ -n spectrum was split into two pdfs, where peaks (1) and (2) were separated from peak (3) in figure 6.4(a). This was done in response to known uncertainties in the  $^{16}\text{O}$  excited states. The expected  $\alpha$ -n rate was calculated from the calculation made for the Daya Bay experiment which yielded a normalisation uncertainty of 7% for the ground states of  $^{16}\text{O}$ . This rate employed the use of the JENDL/AN-2005 calculation, where it was seen in figure 6.6 that there were disagreements with direct cross-section measurements. In a response to these disagreements, a normalisation uncertainty of 30% was assumed for the  $\alpha$ -n ground state contributions. A 100% uncertainty was assumed for peak (3). In order to incorporate uncertainties in the expected light yield due to protons, an extra linear energy scaling parameters was added. This scaling factor acted only on the proton recoil contribution in peak (1), separate from the energy scaling term  $\alpha$  applied to all other pdfs. The proton energy scaling factor uncertainty was assumed from neutron beam measurements of proton light yield quenching for the SNO+ scintillator cocktail [70].

The normalisation uncertainties shown in table 7.2 show the source-specific uncertainties, combined in quadrature with the uncertainties in the signal efficiency shown table 7.1 (which were applied to all signal and background sources passing the IBD analysis cuts). Thresholds for which the nuisance parameters in the likelihood fit sample from were limited to  $\pm 3\sigma$  around their expected values, where the initial value for the fit optimiser was randomly chosen uniformly from this  $\pm 3\sigma$  range. The exception to this rule was for the shape nuisance parameters, where energy scaling factors were limited to a  $\pm 2\sigma$  range (in order to avoid pdfs with zero probability bins) and the energy smearing value was limited to positive values due to an inability to ‘un-smear’ a distribution.

### 7.3 Likelihood Fitting Results

Figure 7.3 presents the results of the likelihood fit of the reactor antineutrino candidate energy spectrum measured in partial fill data, shown in figure 6.10(a). The plots show confidence level contours calculated using the profile likelihood ratio as described in sec-

Table 7.2: Standard deviation values representing systematic uncertainties for the constraint terms in eqn. 7.2, assumed in the likelihood spectral fit. Numbered peaks in the  $\alpha$ -n spectrum refer to figure 6.4(a).

Nuisance Parameter	Uncertainty Value
Normalisation	$\sigma_{N_i}/\widehat{N}_i$
Reactor Norm. Uncertainty	3.2%
Geoneutrino Norm. Uncertainty	100%
$\alpha$ -n Norm. Uncertainty (Combined peaks (1) and (2))	30%
$\alpha$ -n Norm. Uncertainty (Peak 3)	100%
Shape	$\sigma_{\lambda_k}/\widehat{\lambda}_k$
Energy Scaling ( $\alpha_l$ -1)	3.3%
Energy Smearing ( $\delta$ )	3%
$\alpha$ -n Proton Energy Scaling Uncertainty ( $\alpha_l^p$ -1) ( $\alpha$ -n peak (1) only)	3%

tion 7.1.3. Plot 7.3(a) reflects 2D frequentist limits in the phase space of  $\Delta m_{21}^2$  and  $\theta_{12}$  representing the sensitivity to both parameters. Apparent immediately is the impact low statistics had, where the  $1\sigma$  frequentist limit formed on  $\Delta m_{21}^2$  and  $\theta_{12}$  includes the majority of the considered phase space. Contours of 25%, 50% are shown for the purpose of demonstrating the shape of the likelihood space. There is more sensitivity to  $\Delta m_{21}^2$  compared to  $\theta_{12}$ , as expected. The leading constraints on  $\theta_{12}$  have been made from solar neutrino flux measurements, primarily by SNO and Super-Kamiokande [143]. Plot 7.3(b) shows the 1D slice of the likelihood space, at the global PDG value of  $\theta_{12}$  (table 5.3). The likelihood distribution favours primarily  $\Delta m_{21}^2$  values of  $8.8^{+1.1}_{-1.3} \times 10^{-5} \text{ eV}^2$  and  $12.6^{+1.6}_{-1.3} \times 10^{-5} \text{ eV}^2$ , where the confidence intervals are  $1\sigma$  frequentist limits extracted from the 1D likelihood space in figure 7.3(b). It can be seen that the 2021 global value of  $\Delta m_{21}^2$  is consistent within a  $1\sigma$  frequentist bound of the best-fit  $\Delta m_{21}^2$  value of  $8.8^{+1.1}_{-1.3} \times 10^{-5} \text{ eV}^2$ . Figure 7.3(c) demonstrates the good agreement between data and simulation in the prompt reconstructed energy spectrum at the best-fit value of  $\Delta m_{21}^2$  and the global pdg value for  $\theta_{12}$ . The best-fit point at  $\Delta m_{21}^2 = 8.8 \times 10^{-5} \text{ eV}^2$  was favoured compared to the likelihood fit of the prompt energy spectrum without neutrino oscillation by a frequentist confidence level of 93.6%.

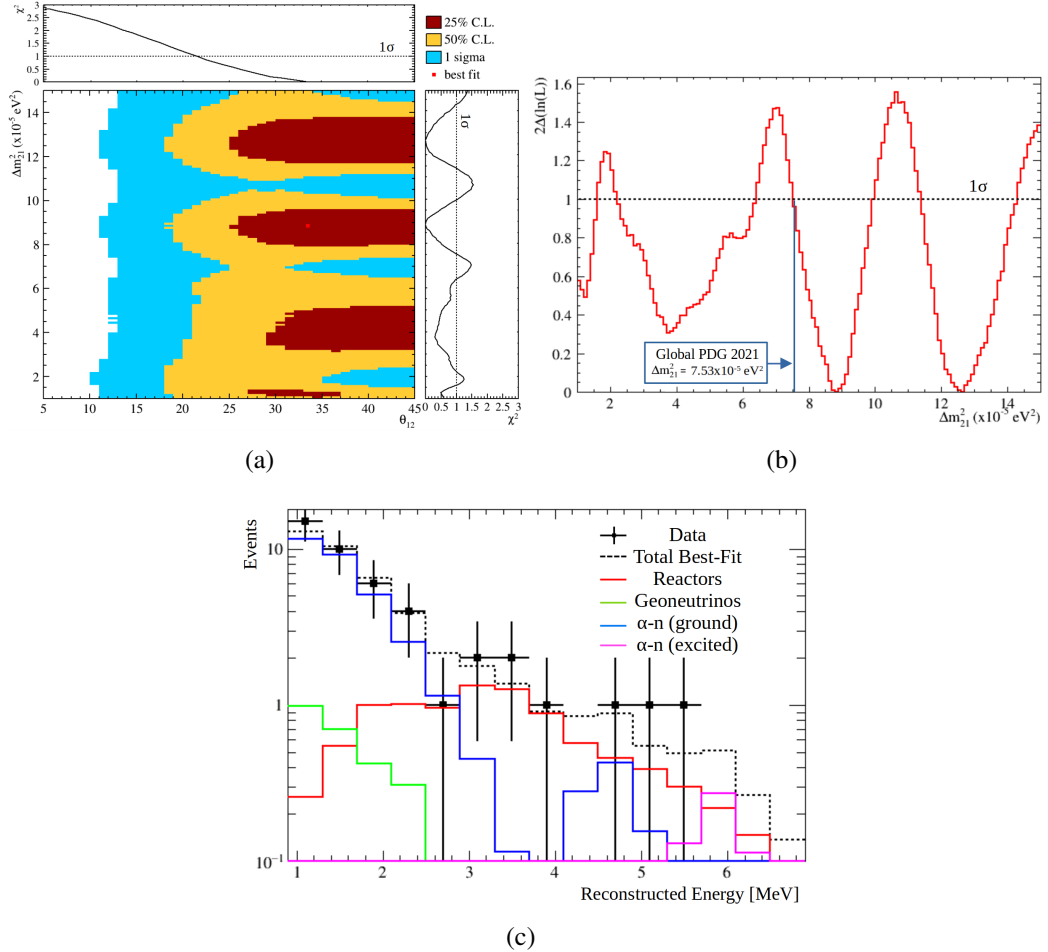


Figure 7.3: Profile likelihood in the space of  $\Delta m_{21}^2$  and  $\theta_{12}$ , fitting the energy spectrum in figure 6.10(a). (a) 2D phase space, showing frequentist confidence level contours. The red point marks the best fit point of  $\Delta m_{21}^2$  and the global PDG value of  $\theta_{12}$ . (b) The 1D likelihood space vs  $\Delta m_{21}^2$  assuming the global PDG value of  $\theta_{12}$ . (c) Prompt event energy spectrum showing data and simulated expectation, at the best-fit  $\Delta m_{21}^2$  value of  $8.8 \times 10^{-5}$  eV $^2$ .

The large statistical uncertainties in the partial fill analysis resulted in a minimal impact of the systematic uncertainties to the oscillation parameter sensitivity. The influence each systematic has on the oscillation parameter sensitivity will be discussed in chapter 8, fitting simulated data in the fully filled detector, assuming various detection lifetimes. It will be seen that for even comparatively large reactor signal statistics, the systematic uncertainties still bear a small influence on the sensitivity to  $\Delta m_{21}^2$  and  $\theta_{12}$ .

### 7.3.1 Bayesian vs Frequentist Confidence Intervals

Figure 7.4 displays the identical likelihood space in  $\Delta m_{21}^2$  and  $\theta_{12}$  in figure 7.3, where Bayesian contours have been plotted instead of the frequentist ones shown previously [172]. The contours represent the regions of the likelihood space that contain 25, 50 and 68% of the total integral under the entire likelihood distribution (in the chosen phase space). Shown also on the coloured z-axis, are the equivalent confidence level positions previously shown using the frequentist approach. It can be seen that the Bayesian approach yields comparatively narrower confidence intervals than those made using the frequentist procedure. The Bayesian likelihood distribution integration calculation accounts for the multiple favoured regions in the parameter phase space, while the frequentist approach does not. Also shown is a comparison of the 1D  $1\sigma$  confidence level calculated for each approach. While the overall significance of this statistics-limited oscillation measurement is left unchanged, the comparison of the two approaches serves to demonstrate the measurable differences in the confidence intervals that can occur when multiple parameters are favoured, a common occurrence in oscillation measurements.

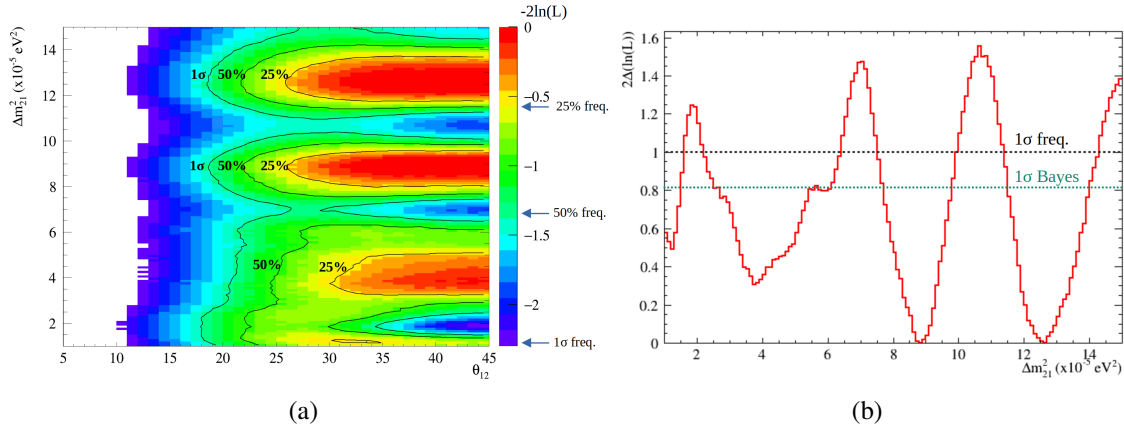


Figure 7.4: Profile likelihood in the space of  $\Delta m_{21}^2$  and  $\theta_{12}$ , where the labelled black contour lines reflect Bayesian confidence intervals. (a) 2D phase space, where frequentist confidence intervals are labelled on the z-axis (b) The 1D likelihood space in  $\Delta m_{21}^2$ .

### 7.3.2 Nuisance Parameters

Table 7.3 summarises the fitted nuisance parameters  $\hat{\lambda}$  at the best fit value for  $\Delta m_{21}^2$  in figure 7.3(b). It can be seen that the fitted background rates were close to expectation. It

will be shown in the following chapter that the partial fill measurement was very much below the statistics needed to make a measurement of geoneutrinos significantly inconsistent with zero geoneutrino counts. The limited statistics dominated the uncertainties in the spectral fit, causing the best-fit values of  $\alpha_l$  and  $\delta$  to be negligibly different from expectation. It was found, that the fitted values for  $\alpha_l$  and  $\delta$  were equal to the randomly chosen initial values given to the optimiser, yielding no difference to the likelihood shape space. Shown therefore, are their expected values. The largest deviation from expectation seen was seen in the proton recoil energy scaling factor, showing a 2% difference. This is potentially explained by the fact that the proton light yield was assumed from measurements in a neutron beam experiment, testing a scintillator cocktail with a higher PPO concentration: LAB + 2g/L PPO.

Table 7.3: Summary of the fit nuisance parameters for the best-fit  $\Delta m_{21}^2 = 8.8 \times 10^{-5} \text{ eV}^2$ . The constraints applied to each nuisance parameter were summarised in table 7.2.

Nuisance Parameter	Expected	Fit
$\alpha$ -n Normalisation	33.3	31.9
Geoneutrino Normalisation	2.2	2.5
Energy Scaling $\alpha_l$	1	1
Energy Smearing $\delta$	0	0
$\alpha$ -n Proton Energy Scaling Uncertainty $\alpha_l^p$ ( $\alpha$ -n peak 1 only)	1	1.02

### 7.3.3 Conclusion

As expected, the limited signal count in the short partial fill phase did not allow for a significant measurement of oscillation parameters  $\Delta m_{21}^2$  and  $\theta_{12}$ . While multiple values of  $\Delta m_{21}^2$  were favoured in the partial fill result, it was shown that signal and background expectations agreed well with observation and consistency was seen with the current global value of  $\Delta m_{21}^2$ . The partial fill result demonstrated understanding of the detector, the expected background and signal rates and the methods used to extract neutrino oscillation parameters. The experimental prospects of the continued antineutrino analysis in the fully filled detector are explored in the following chapter.

## 8 | Future Sensitivity and $\alpha$ -n Discrimination

The onset of the Covid-19 pandemic provided opportunity to make a measurement of the reactor antineutrino energy spectrum in the partially filled SNO+ scintillator detector. The short livetime, limited scintillator volume and changing detector conditions lead to a statistics-limited analysis, where precise limits could not be placed on  $\Delta m_{21}^2$  and  $\theta_{12}$ . Despite the limited nature of the measurement, the presented techniques and framework will allow for a straightforward repeat of the signal extraction and likelihood fit of future SNO+ scintillator data.

Presented in this chapter are the potential results of the reactor antineutrino analysis in the future scintillator phases. Assumptions, primarily derived from partial fill, of the  $\alpha$ -n background rate and systematics will be made, where their impact to sensitivity will also be shown. Also presented is a study of the separation of  $\alpha$ -n background events from the inverse beta decay (IBD) signal in the full scintillator phases, where  $\alpha$ -n removal would greatly aid in the sensitivity to  $\Delta m_{21}^2$ .

### 8.1 SNO+ Oscillation Sensitivity in Future Phases

The antineutrino analysis is expected to be continued over both the pure and Te-loaded scintillator phases, where the primary differences between the phases will be light yield and background rates. The decreased light levels (and therefore energy resolution) for the Te-loaded scintillator phase is not expected to be measurably influential to the spectral fit. A larger impact may emerge through increased overall background rates. Increases in the rates of accidentals and  $\alpha$ -n events are expected, due to the introduction of  $^{130}\text{Te}$  (yielding  $2\nu\beta\beta$  decays) and  $^{210}\text{Po}$  which will accompany the addition of TeBD into the detector.  $\alpha$ -n and IBD pulse shape discrimination techniques presented in this chapter are expected to assist in combating the impacts of these added contamination.

### 8.1.1 Asimov Dataset Generation

Simulations of the full SNO+ detector assumed the Te-loaded phase scintillator cocktail of: LAB + 2g/L PPO + 15mg/L bisMSB + TeDiol + DDA, with 0.5% loading of Te by mass and DDA added at a 0.5 molar concentration [90][69]. Figure 8.1 shows a binned Asimov dataset (where each bin is set to their expected value) for a livetime of 1 year. The same IBD analysis cuts used in partial fill in table 6.1 were applied, excluding the z-position cuts and energy corrections. The reactor and geoneutrino fluxes were also assumed from the calculations made for the partial fill phase. Table 8.1 shows the assumed signal and background events per year used in the datasets, reflecting expectation for both the pure and Te-loaded scintillator phases. At the time of writing, the  $^{210}\text{Po}$  rate per unit volume in the fully filled detector has been measured to be  $\sim 60\%$  of the rate measured in the partial fill phase [173]. This lower  $^{210}\text{Po}$  is reflected in the expected  $\alpha$ -n rate in table 8.1. The remaining nuisance parameter systematics such as energy scaling, proton-specific scaling and smearing systematics, were all reapplied from the partial fill phase, summarised in table 7.2.

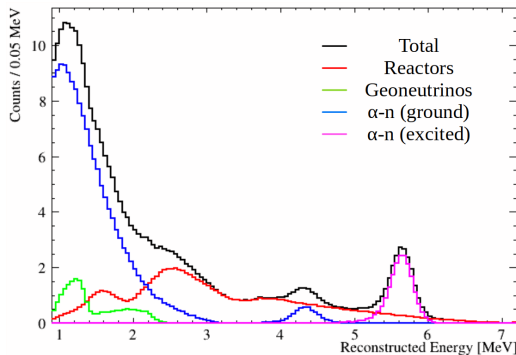


Figure 8.1: Asimov dataset of expected energy spectrum for 1 year in the Te-loaded scintillator phase, reflecting the signal and background rates in table 8.1.

Table 8.1: Expected signal and background counts for a livetime of 1 year in the Te-loaded scintillator phase, applying IBD analysis cuts in 6.1 (excluding the z-position cut). Global PDG oscillation parameter values were assumed. The two  $\alpha$ -n constraints were again applied to the ground and excited  $^{16}\text{O}$  states.

Name	Events	Normalisation Constraint
Reactors	83	3%
Geoneutrinos	19	100%
$\alpha$ -n	174	30,100%

### 8.1.2 Oscillation Parameter Sensitivity

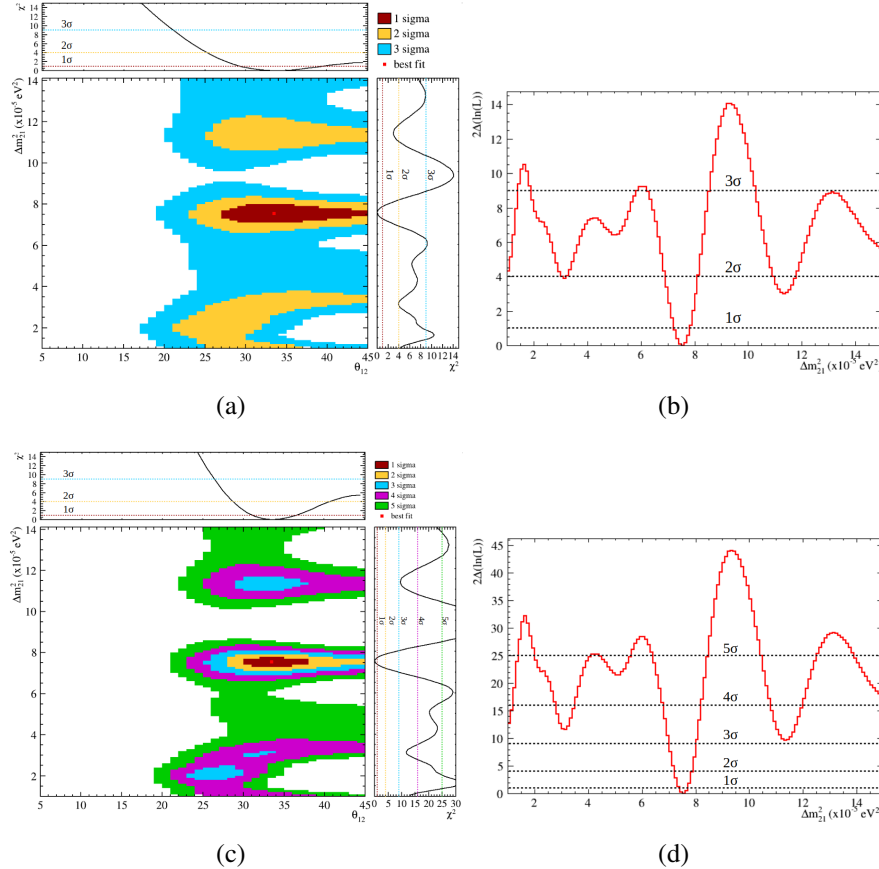


Figure 8.2: (a)  $\Delta m_{21}^2$  and  $\theta_{12}$  2D phase space, showing frequentist confidence limit contours. The red point marks the best fit point. (b) The 1D likelihood space from (a), at the PDG global value of  $\theta_{12}$ . (c,d) repeated for a 5 year livetime.

Figure 8.2 shows again plots of the profile likelihood space in  $\Delta m_{21}^2$  and  $\theta_{12}$ , carrying out a spectral fit of the Asimov dataset in figure 8.1, for 1 and 5 year lifetimes. The impact of the increased lifetime and fiducial volume in the full scintillator phases can be seen immediately when compared to the partial fill result. Also shown in the plots arranged along each axis, are 1D slices of the profile likelihood space, at best-fit value for the oscillation parameter on the opposite axis. Table 8.2 summarises the  $1\sigma$  frequentist limits on  $\Delta m_{21}^2$  for 1 to 10 year lifetimes, extracted from the 1D likelihood space, assuming the global PDG value for  $\theta_{12}$ . Plot 8.3 then shows these limits as a function of livetime. It can be seen that the function  $\sqrt{t}$  effectively describes the sensitivity against time, reflecting the dependency on the number of collected signal events. These extrapolations assume constant reactor activity in the upcoming years. Also shown therefore are bands which

approximate  $\sim 10\%$  deviations from the total expected number signal events, at a given livetime. These bands were simply calculated as  $\sqrt{N(1 \pm 0.1)}$  times the fitted function shown in black. Also shown are fit assuming strongly reduced  $\alpha$ -n rates, discussed further in section 8.2.4. The impacts that the assumed systematics have on the sensitivity to  $\Delta m_{21}^2$  will be demonstrated in the next section. Assuming the stated expectations however, it can be seen that the current global measurement precision of  $\Delta m_{21}^2$  can be surpassed within  $\sim 4$  years, while this can be reduced to 3 years if the  $\alpha$ -n contamination is reduced by a factor of 10. The current global value was primarily determined by the KamLAND reactor antineutrino measurement.

Table 8.2: Sensitivity to  $\Delta m_{21}^2$  in the Te-loaded scintillator phase for various livetimes. Shown for comparison is the global PDG  $\Delta m_{21}^2$  value, at the time of writing.

Livetime	Frequentist limits ( $1\sigma$ )
1 year	$7.53^{+0.36}_{-0.37} \times 10^{-5} \text{ eV}^2$
3 years	$7.53^{+0.21}_{-0.22} \times 10^{-5} \text{ eV}^2$
5 years	$7.53^{+0.17}_{-0.16} \times 10^{-5} \text{ eV}^2$
10 years	$7.53^{+0.12}_{-0.11} \times 10^{-5} \text{ eV}^2$
Global PDG :	$7.53^{+0.18}_{-0.18} \times 10^{-5} \text{ eV}^2$

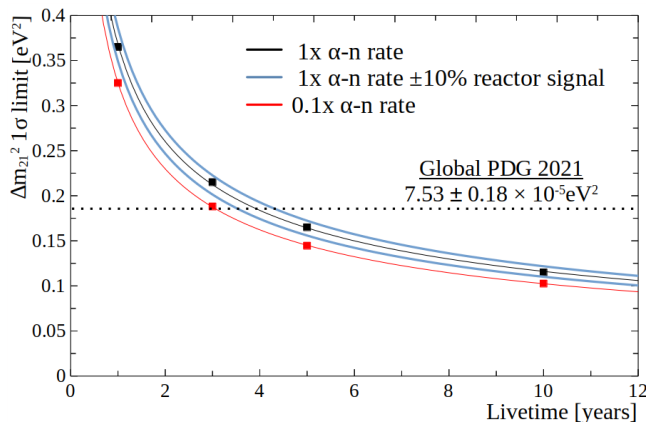


Figure 8.3: The livetime evolution of the 1D  $1\sigma$  sensitivity limits on  $\Delta m_{21}^2$  sensitivity shown in table 8.2. The solid line is the function  $A \times \sqrt{t}$ . The impacts due to the assumed  $\alpha$ -n rates and systematics are summarised in table 8.3. The light blue bands represent  $\pm 10\%$  differences in the measured reactor event statistics.

### 8.1.2.1 Assumed Backgrounds and Systematics

Assumptions were made about the  $\alpha$ -n rate used for the expected sensitivity to  $\Delta m_{21}^2$ . It has been mentioned that increased levels of  $^{210}\text{Po}$  are expected in the Te-loaded phase.

The next section however discusses  $\alpha$ -n removal through pulse shape discrimination in the future scintillator phases. Figure 8.4 displays the impact the assumed  $\alpha$ -n rate has on the achievable limits that can be set on  $\Delta m_{21}^2$ , for 5 years of livetime. The normalisation and energy systematics in these Asimov dataset fits were adopted from the partial fill, as summarised in table 7.2. Table 8.3 then compares both the impacts of  $\alpha$ -n rates along with the assumed systematic uncertainties may have on the sensitivity to  $\Delta m_{21}^2$ . Shown are the  $3\sigma$  frequentist limits calculated when fits are repeated applying the shown adjustments to the systematic uncertainty constraint values. The entry ‘Non-linear Energy Scale’ corresponds to a simplified representation of uncertainty in  $k_B$  in equation 2.3, which dictates the energy dependence of scintillation light yield. An extra energy-dependent scaling factor referenced in eqn. 7.4 was added to the fit in the form of  $\alpha_{nl}(E) = \frac{1+E \cdot k_B}{1+E \cdot k'_B}$ , where  $k_B$  is the constant used in simulation, while  $k'_B$  was fitted in the likelihood fits. It is demonstrated that the systematic uncertainties generally yield small changes to the sensitivity. It is clear however that that the minimisation of  $\alpha$ -n will be a priority for the antineutrino analysis in future scintillator phases, where  $\alpha$ -n separation is discussed in the next section. It should be noted that the expected accidental contamination and their impact to the sensitivity has not been calculated. The accidental contribution is generally calculated directly from data, as was seen in the partial fill. Those data, recorded over periods with high background rates, showed negligible accidental contamination. However, for the Te-loaded scintillator phase, the tail of the  $2\nu\beta\beta$  energy spectrum will overlap with the neutron energy window, increasing the likelihood of accidentals.

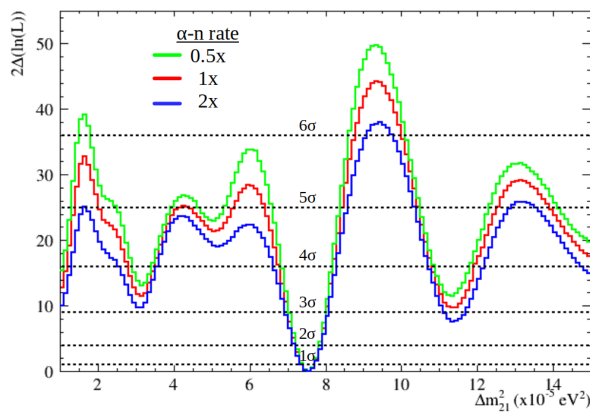


Figure 8.4: 1D slices of the 5 year lifetime profile likelihood space in figure 8.2(d), displaying the impact of the  $\alpha$ -n rate to  $\Delta m_{21}^2$  sensitivity.  $\alpha$ -n rates are expressed as a fraction of the rate in table 8.1.

Table 8.3: Sensitivity to  $\Delta m_{21}^2$  for various assumptions about background rates and systematics, fitting the 5 year Asimov dataset generated in the Te-loaded scintillator phase. Highlighted in black is the sensitivity for the previously assumed systematics and  $\alpha$ -n rate.

Background/Systematic	Frequentist limits ( $3\sigma$ )
<b><math>1 \times \alpha</math>-n rate</b>	<b><math>7.53^{+0.50}_{-0.54} \times 10^{-5} \text{ eV}^2</math></b>
Background Rate	
$0.5 \times \alpha$ -n rate	$7.53^{+0.47}_{-0.50} \times 10^{-5} \text{ eV}^2$
$2 \times \alpha$ -n rate	$7.53^{+0.54}_{-0.61} \times 10^{-5} \text{ eV}^2$
Improved Systematics	
$1 \alpha$ -n pdf 4% norm. constraint	$7.53^{+0.50}_{-0.53} \times 10^{-5} \text{ eV}^2$
No Energy Scale	$7.53^{+0.50}_{-0.53} \times 10^{-5} \text{ eV}^2$
No Energy Smear	$7.53^{+0.49}_{-0.54} \times 10^{-5} \text{ eV}^2$
Diminished Systematics	
Non-linear Energy Scale $\pm 10\%$	$7.53^{+0.50}_{-0.54} \times 10^{-5} \text{ eV}^2$
Reactor 6% norm. constraint	$7.53^{+0.51}_{-0.54} \times 10^{-5} \text{ eV}^2$
Energy Scale $\pm 5\%$	$7.53^{+0.50}_{-0.54} \times 10^{-5} \text{ eV}^2$
Energy Smear $\pm 5\%$	$7.53^{+0.50}_{-0.54} \times 10^{-5} \text{ eV}^2$

### 8.1.3 Geoneutrino Sensitivity

While geoneutrinos are a background in the reactor oscillation analysis, their measurement at SNO+ would be a first in the Americas. To extract the sensitivity to geoneutrinos, many individual datasets were generated, each reflecting the statistical fluctuations expected in the given livetime. Each dataset was fit, where the geoneutrino normalisation at the best-fit values for  $\Delta m_{21}^2$  was recorded. Figure 8.5(a) shows a histogram of the best-fit geoneutrino normalisations for 500 individual dataset likelihood fits for 1 and 10 year livetimes. The means of the distribution can be seen to match the expected 19 geoneutrino events per year assumed in the Asimov dataset in figure 8.1. Normal distributions are shown, fit using Minuit's binned likelihood method. The standard deviation was calculated to be 8 and 52 geoneutrino events for the 1 and 10 year cases, respectively. As  $\alpha$ -n and reactor antineutrino events share in the geoneutrino energy spectrum region, the spread in fit normalisations is larger than the statistical deviation expected for a pure measurement of geoneutrinos. As was seen for  $\Delta m_{21}^2$ , the measured geoneutrino sensitivity scales with the square root of the number of events collected. It is expected for 1 year in the Te-loaded scintillator phase,  $1\sigma$  bounds inconsistent with zero counts may be

formed, while it would take 10 years to form  $3\sigma$  bounds.

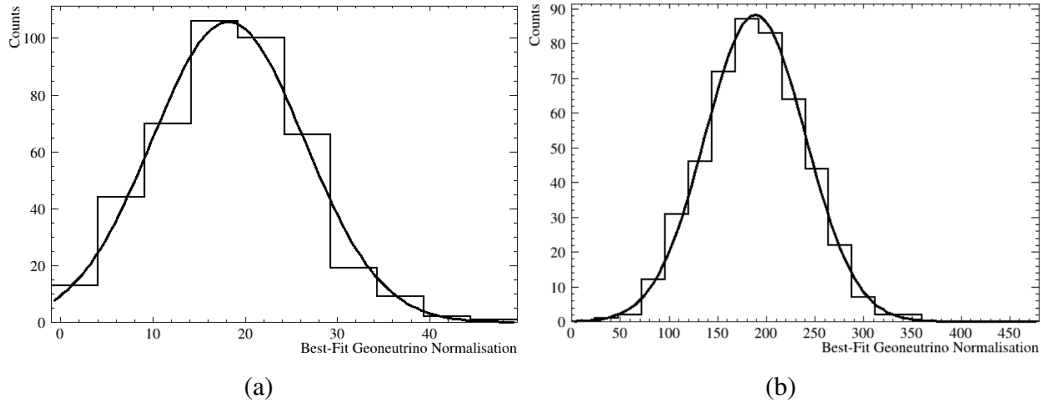


Figure 8.5: Histogram of the best fit geoneutrino normalisations for 500 Te-loaded scintillator datasets (1 year) each reflecting statistical fluctuations.

## 8.2 $\alpha$ -n Event Classification

The need to diminish  $\alpha$ -n events has been established for the continuation of the antineutrino analysis into the future scintillator phases. Visible in figure 8.1, is the low energy proton recoil contribution in  $\alpha$ -n which conceals the low end of the reactor antineutrino energy spectrum. Figure 8.4 demonstrated the significant sensitivity to  $\Delta m_{21}^2$  that can be gained from relinquishing background events from this low energy region.

This section presents pulse-shape-discrimination (PSD) techniques that may be used in future scintillator phases to allow for the removal of  $\alpha$ -n proton recoil events. Discussed are the origins of time residual shapes for each event type, along with comparisons between the likelihood and Fisher discriminant methods, which can be used to characterise each event type. The discrimination ability for PSD will be presented in the frame of the partial fill scintillator, implementing the current in-situ scintillation timing measurements calculated in chapter 4. Without a dedicated measurement of the proton scintillation timing, these PSD techniques were not used in the partial fill analysis. The following partial fill calculations primarily serve to demonstrate the what may be possible in the future scintillator phases (and future liquid scintillator experiments).

### 8.2.1 Pulse Shape Discrimination - Time Residuals

Chapters 2 and 3 discussed the scintillator energy deposition for different particles, namely for  $\beta$ s and  $\gamma$ s. When an energetic particle travels through the detector's medium (scintillator or water), it slows down as it deposits its kinetic energy. For two particles of equivalent energy, the distance and time over which this energy is deposited depends upon the particle's energy, mass and charge. These characteristics also dictate the scintillation emission times yielded for a particular particle type. Particles with sparse energy depositions and/or slow emission times incur wider PMT hit time residual distributions (section 3.1.1). As such, the time residual distribution for a given event in the detector can be used to characterise the particle that triggered the detector.

PSD techniques have been developed extensively for the upcoming  $0\nu\beta\beta$  search in SNO+. It has been seen that signal  $0\nu\beta\beta$  events, which are more ‘point-like’ in their energy distribution, can be separated from background  $\gamma$  events of equivalent energy, which are comparatively more dispersed [75][90].

### 8.2.2 $\alpha$ -n Discrimination : Proton Recoils vs Positrons

The primary difference between events due to proton recoils from  $\alpha$ -n and the positron from IBD, is the nature of the energy deposition in the scintillator. The interactions for each event type yield differences in (1) the characteristic scintillation emission times and (2) the time over which energy is deposited in the scintillator.

The scintillation emission times for  $\beta$  and  $\alpha$  particles were measured in chapter 4. The increased ionisation power of the  $\alpha$  particle leads to comparatively lower light levels, where scintillation quenching acts more severely on the fast scintillation components. This leads to an overall increase of scintillation emission times, resulting in time residual distributions with measurably longer tails, as seen in figure 4.4(c). Higher PPO concentrations lead to faster overall emission times [98] and improved  $\alpha$ - $\beta$  discrimination [174].

While the time residuals for  $\alpha$  and  $\beta$  particles could be accurately simulated, at the time of writing, the scintillation emission times due to protons had not yet been measured for

the SNO+ cocktail. Protons due to their mass, have ionisation powers between that of  $\alpha$ s and  $\beta$ s. Simulations shown in this work, conservatively assumed that protons had the same emission times as  $\beta$  particles. Figure 8.6 shows time residuals calculated in partial fill simulations of prompt positron IBD events and proton recoil events due to  $\alpha$ -n. A measurable difference in time residual shape can be seen, despite the assumption of  $\beta$  emission times for protons.

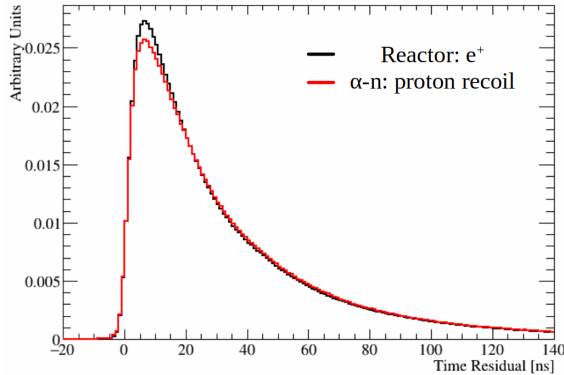


Figure 8.6: Time residual pdfs in partial fill for reactor IBD events and proton recoil due to  $\alpha$ -n. Reconstructed energy cuts  $0.9 < E < 3.2\text{MeV}$  were applied.

While an  $\alpha$  particle is involved in the  $\alpha$ -n reaction, the capture cross section in figure 6.6 shows the  $\alpha$  is captured at relatively high energies. This, combined with the quenched light emission for  $\alpha$  before capture, means the  $\alpha$  contributes comparatively little to the total scintillation light in an  $\alpha$ -n prompt event [175]. Recoiling protons therefore are the primary particles producing the difference seen in time residuals.

### 8.2.2.1 Origins of Differences in Simulated Time Residuals

Since the emission times for protons and  $\beta$ s were assumed the same in simulation, the speculation was that the underlying basic matter interactions, predicted by GEANT4 could be used to explain the apparent differences in time residuals. To do this, the simulated truth information of many simulated positrons due to IBD and recoiling protons in  $\alpha$ -n were generated. The following comparisons between reactor IBD and proton recoil events used a reconstructed prompt energy cut of  $0.9 < E < 3.2\text{MeV}$ . The position, time and deposited scintillator energy for each particle involved in each event were recorded:

**Reactor IBD** The positron, annihilation  $\gamma$ s, and the  $\beta$ s Compton scattered by the annihilation  $\gamma$ s.

**$\alpha$ -n** The high energy neutron and the multiple scattered protons.

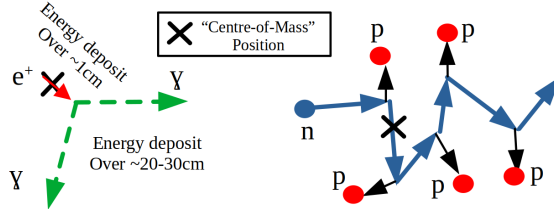


Figure 8.7: Sketch of energy deposition for IBD and  $\alpha$ -n events

To serve as a reference point for a given event, a ‘centre-of-mass’ (COM) in time and position was calculated. This was the position and creation time of every particle, weighted by each particle’s deposited energy into the scintillator:

$$\vec{r}_{\text{COM}} = \sum_{i=1}^n \frac{\vec{r}_i E_i^{\text{dep}}}{E_{\text{tot}}} \quad t_{\text{COM}} = \sum_{i=1}^n \frac{t_i E_i^{\text{dep}}}{E_{\text{tot}}}, \quad (8.1)$$

where  $n$  is the number of energy depositing particles in the event. Figure 8.7 shows a sketch of the COM and the expected differences in energy deposition for IBD and  $\alpha$ -n events. With the central point now defined in position and time for a given event, the spread in the energy deposition of all the particles involved in each event could be defined with respect to the COM point. Distances and times were again weighted by energy deposition.

$$\sigma_r = \sqrt{\frac{\sum \left( \frac{\vec{r}_i E_i^{\text{dep}}}{E_{\text{tot}}} - \vec{r}_{\text{COM}} \right)^2}{n-1}} \quad \sigma_t = \sqrt{\frac{\sum \left( \frac{t_i E_i^{\text{dep}}}{E_{\text{tot}}} - t_{\text{COM}} \right)^2}{n-1}}. \quad (8.2)$$

Figure 8.8 displays the event spreads in time and position by energy depositing particles for prompt  $\alpha$ -n proton recoil and reactor IBD positron events, calculated in GEANT4.

Regarding the position spreads in plot 8.8(b), the energy deposition by positrons in space is actually larger on average than for the recoiling protons. This is true especially for low energy positrons, as the annihilation  $\gamma$ s contribute a larger fraction of the total energy and Compton scatter electrons over 10–20cm. If one was to regard positional spread alone, a

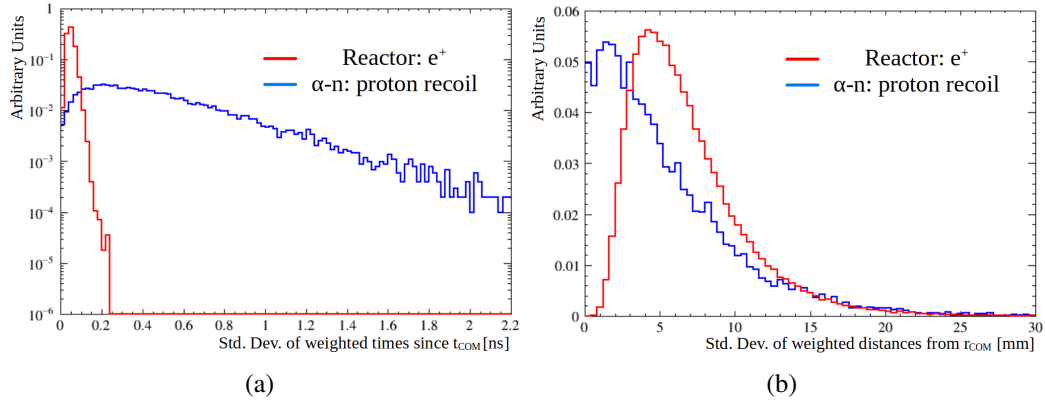


Figure 8.8: The standard deviations defined in equation 8.2, representing the spread of positron events in IBD and recoiling protons from  $\alpha$ -n. (a)  $\sigma_r$  (b)  $\sigma_t$ .

narrower time residual spectra would be expected for the proton recoil, in disagreement with what was seen in the simulated time residuals in figure 8.6.

Considering however the time spreads in plot 8.8(a), it can be seen that there is a much larger discrepancy in the spread of times over which energy is deposited in the scintillator. Although protons are recoiled over by neutrons over a smaller volume compared to IBD, the protons deposit energy over longer times compared to IBD events. The difference in time spreads is believed to be the dominant contributor to the broader time spectra in figure 8.6 for  $\alpha$ -n compared to IBD events, when equivalent emission times for  $\beta$ s and protons were assumed.

The upcoming section compares the ability to separate  $\alpha$ -n and IBD events using the likelihood and Fisher discriminant methods, demonstrated in the partial fill.

### 8.2.3 $\alpha$ -n/IBD Classifier: Likelihood and Fisher Discriminant

Calculations will be presented again using partial fill simulations, where proton and  $\beta$  scintillation times were treated as equivalent. Emphasis however is placed on the comparison of the separation powers between the likelihood and Fisher discriminant methods.

Time residual pdfs generated for IBD and  $\alpha$ -n event types, allow for the calculation of the most probable event classification, given the time residual measured in data. The calculation of a test-statistic can be used to discriminate and separate on an event-by-event basis,  $\alpha$ -n from IBD.

### 8.2.3.1 Likelihood Ratio

Time residual histograms were constructed for each event in data, with  $N$  bins, and  $n_i$  entries in the  $i^{\text{th}}$  bin. Given a hypothesised event type  $H$ , the probability of measuring a time residual in bin  $i$  is  $P(i|H)$ . The log likelihood test statistic  $\mathcal{T}$  for each event type was calculated as:

$$\mathcal{T} = \log \frac{\mathcal{L}_{\text{IBD}}}{\mathcal{L}_{\alpha n}} = \sum_{i=1}^N \log \frac{P(i|\text{IBD})^{n_i}}{P(i|\alpha n)^{n_i}} \quad (8.3)$$

Figure 8.9(a) displays normalised distributions of  $\mathcal{T}$  calculated for many simulated events of each event type in the partial fill detector. The separation between  $\mathcal{T}$  for the event types is seen to be small, as expected due to a lack proton scintillation emission times, compounded by the low PPO concentrations in the partial fill phase. ROC curves summarising the signal efficiency against a minimum threshold in  $\mathcal{T}$  is shown in figure 8.10.

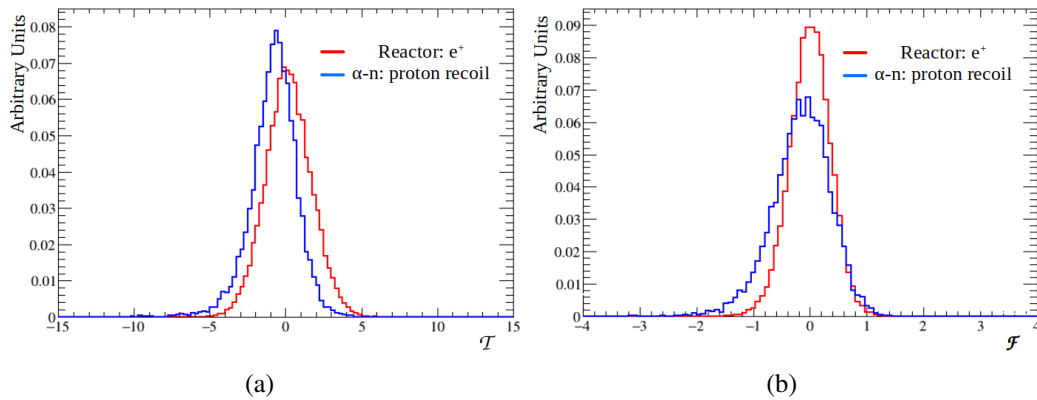


Figure 8.9: Test-statistics calculated for  $\alpha$ -n and IBD events, applying prompt energy cut  $0.9 < E < 3.2\text{MeV}$  (a) Log-likelihood difference  $\mathcal{T}$  in eqn. 8.3 (b) Fisher discriminant  $\mathcal{F}$  in eqn. 8.6.

### 8.2.3.2 Fisher Discriminant

The likelihood ratio calculated in equation 8.3 assumes all PMT hits were independent. This approximation is acceptable for the purposes of event position reconstruction in SNO+, which considers  $\beta$ s point-like in their energy deposition, emitting scintillation light isotropically.

It has been demonstrated however in figure 8.8(a), that proton recoil events due to  $\alpha$ -n can vary widely in the number of protons recoiled and the times of their energy depositions. The consequence of these event-by-event variations, can lead to correlations

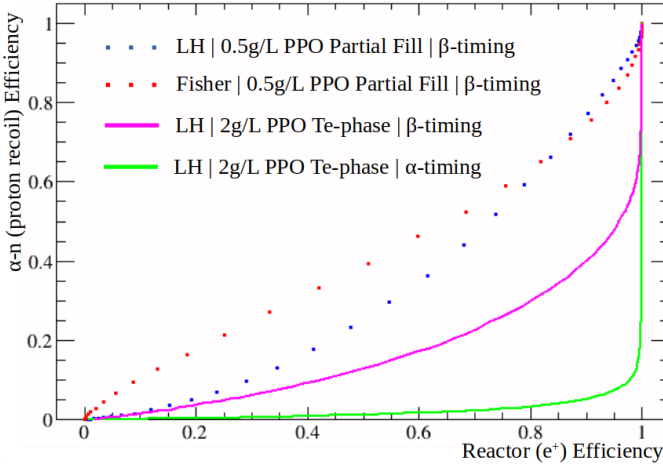


Figure 8.10: ROC curves applying analysis cut thresholds on  $\alpha$ -n and IBD events for likelihood ratio  $\mathcal{T}$  and Fisher discriminant  $\mathcal{F}$  in partial fill. Also shown are possible separation abilities in the Te-loaded scintillator phase, discussed in section 8.2.4.

between PMT hit times. An  $\alpha$ -n with many recoiling protons, emits more more late light, increasing the number of hit times around the time residual peak. Events involving only 1-2 energetic protons, scattered over a short period of time, are expected to produce a narrower distribution, where the event trigger threshold was reached more quickly.

The Fisher discriminant incorporates these correlations between the hit times. The efficacy of this discriminant has already been introduced for the purposes of  $0\nu\beta\beta$  background separation [90]. Covariance matrices describing the correlation between binned time residual pdf bins  $i$  and  $j$  was calculated for each event type as:

$$\Sigma_{ij} = \sum_{\mu=1}^{N_{\text{ev}}} \frac{(n_i - p_i)(n_j - p_j)}{N_{\text{ev}} - 1}, \quad (8.4)$$

where  $p_i$  reflected the contents of the time residual pdfs in the  $i^{\text{th}}$  bin and  $N_{\text{ev}}$  simulated events was summed over.  $n_i$  described the bin contents of the normalised time residual histogram constructed for a single event.

Armed with the time residual pdfs (with histogram entries  $\vec{p}$ ) and covariance matrices for each event type, the Fisher weighting vector was calculated:

$$\vec{w} = (\Sigma_{\text{IBD}} + \Sigma_{\alpha n})^{-1}(\vec{p}_{\text{IBD}} - \vec{p}_{\alpha n}). \quad (8.5)$$

This leads to the Fisher discriminant  $\mathcal{F}$ , calculable for single event with a normalised time residual histogram, contents given by  $\vec{n}$ :

$$\mathcal{F} = \vec{n} \cdot \vec{w}. \quad (8.6)$$

Figure 8.9(b) shows the separation for  $\alpha$ -n and IBD events and shows improvement over the likelihood method figure 8.10, by accounting for the event-by-event variation. The covariance matrix calculation shown was limited in time residual times from -10 to 40ns, for the purposes of practicality. The likelihood calculation however considered the entire time residual spectrum leading to it eventually outperforming the Fisher discriminant, seen in the ROC curves.

### 8.2.4 $\alpha$ -n and IBD Separation Prospects

Limited separation was seen in the partial fill case, where  $\beta$  timing was assumed for protons and PPO concentrations were low. Shown also in figure 8.10 is the likelihood signal efficiency for  $\alpha$ -n and IBD events, repeated in the Te-loaded scintillator phase. Presented are two assumptions, assuming proton scintillation emission times as equal to  $\beta$ s and  $\alpha$ s, expected to be an underestimation and overestimation of the true proton quenching, respectively. Apparent is the significant potential for the removal of proton recoil  $\alpha$ -n events when fast scintillation times are employed and the slower proton emission times are accounted for.

**$\beta$  Emission Times for Protons** Figure 8.8(a) demonstrated the difference in energy deposition time between low energy  $\alpha$ -n and IBD events, yielding the resulting differences in time residuals, even when  $\beta$  emission times were assumed for protons. Table 8.4 summarises the timing constants employed in the simulation of the Te-loaded scintillator with 2g/L PPO concentration. It can be seen that the final scintillator cocktail is expected to have significantly faster scintillation emission times compared to that measured in partial fill (table 4.3). The faster scintillation emission times allow for significant improvement of the separation using PSD. It should be noted for these simulation studies, that the in-situ measured scintillation emission times in partial fill data were found to be

considerably different to those measured in the tabletop experiments.

**$\alpha$  Emission Times for Protons** In the case where  $\alpha$  times are assumed, while this is an overestimation of the expected differences between  $\alpha$ -n and IBD time residual distributions, it is expected that the  $\alpha$  times reflect more closely the true proton emission time (since the proton and  $\alpha$  are closer in mass than a  $\beta$ ). The signal efficiency with  $\alpha$  times therefore serves as an upper limit on the possible improvement due to a dedicated proton timing measurement. It can be seen that the quenching of scintillation times is expected to yield a vast improvement on the ability to separate  $\alpha$ -n from IBD events due to their differences in energy deposition alone. A dedicated measurement of the proton scintillation emission timing in the SNO+ scintillator cocktail is expected to be made in the future.

The two cases serve to present the impact of faster scintillation emission times due to increased PPO concentration and subsequently the further discrimination possible when the slower emission times of protons compared to  $\beta$ s are accounted for.

Table 8.4: Scintillation time constants for eqn. 4.3 for the Te-loaded scintillator cocktail [176].

Scintillation Time Parameters assumed for Te-loaded Scintillator									
	$\tau_1$ [ns]	$\tau_2$ [ns]	$\tau_3$ [ns]	$\tau_4$ [ns]	$A_1$	$A_2$	$A_3$	$A_4$	$\tau_{\text{rise}}$ [ns]
$\beta$	3.7	10	52	500	0.72	0.23	0.02	0.03	0.8
$\alpha$	3.69	15.5	79.3	489	0.63	0.23	0.07	0.07	0.8

### 8.2.5 Conclusion

The prospects of the SNO+ reactor antineutrino analysis entering the future scintillation phases were presented for a number of timescales. Based upon assumptions of the signal and background rates from the partial fill, the measurement sensitivity to  $\Delta m_{21}^2$  was presented in table 8.2, where it is expected measurements comparable to that of KamLAND will be possible. It was also demonstrated in figure 8.4 that the reduction of the  $\alpha$ -n contamination can considerably improve sensitivity. This is expected to be possible through PSD methods.

It was then demonstrated in simulation, that there are measurable differences in IBD and

$\alpha$ -n time residuals, despite the assumption that protons and  $\beta$ s have the equivalent scintillation emission times. Calculations using GEANT4 indicated that the large differences in energy deposition for both event types in liquid scintillator, aids in their discrimination. It was shown that due to event-by-event variations in energy deposition for  $\alpha$ -n, a Fisher discriminant may be able to provide extra event separation beyond the likelihood method. PSD discrimination was not implemented in the antineutrino analysis due to a lack of proton scintillation time measurements. However, the expectation is that the future measurements of proton scintillation timing, combined with higher PPO concentrations, may allow very efficient removal of the notoriously uncompromising  $\alpha$ -n background events.

# 9 | Stratified LIquid Plane Scintillator - SLIPS Detector

This chapter discusses the novel design of a cheap large-scale liquid scintillator detector. The first half of this chapter introduces the construction of this next-generation detector, while the latter half presents performance tests which demonstrate the detector's capabilities, carried out in simulation.

## 9.1 Current Liquid Scintillator Detector Designs

Whether it be neutrino beam, neutrino telescope or multi-purpose large scale liquid scintillator experiments, the next generation of neutrino and rare decay experiments all reflect a clear trend in expanding detector sizes. The DUNE experiment expects 40kt of liquid argon fiducial mass across four time projection chamber modules [44], the JUNO experiment will operate with a target mass of 20kt of liquid scintillator [48], Hyper-K is a water Cerenkov detector with an anticipated fiducial mass of  $\sim$ 190kt [43] and IceCube-Gen2 intends to instrument  $\sim$ 10km<sup>3</sup> of ice [177].

The size evolution of liquid scintillator detectors are no exception to the trend. Daya Bay ( $8 \times 20\text{t}$ ), Borexino ( $\sim 300\text{t}$ ), SNO+ ( $\sim 1\text{kt}$ ), KamLAND ( $\sim 1\text{kt}$ ) and JUNO ( $\sim 20\text{kt}$ ) are some of the recent, current and future experiments which reflect the trend of the increase of scintillator target masses with time. Each experiment's structure is shown in figure 9.1. Also apparent across these current liquid scintillator detectors, is their similarity in design. Each detector requires a boundary separating the scintillation region from the PMTs due to the intrinsic radioactivity they contribute. This requirement generally adds complexity to construction. Separation is generally achieved using acrylic/nylon barriers, whose own radioactivity can also lead to substantial cuts to the fiducial detection volume for a number of low energy ( $\sim$ MeV) studies. Such barrier constructions become increasingly difficult and expensive for larger detector volumes. JUNO are pushing the boundaries of what might be achievable in the construction of their acrylic vessel, a transparent spherical structure  $\sim$ 35.4m in diameter and 12cm in thickness [178]. Visible

in figure 9.1(e) is the stainless steel structure required to support the large acrylic vessel.

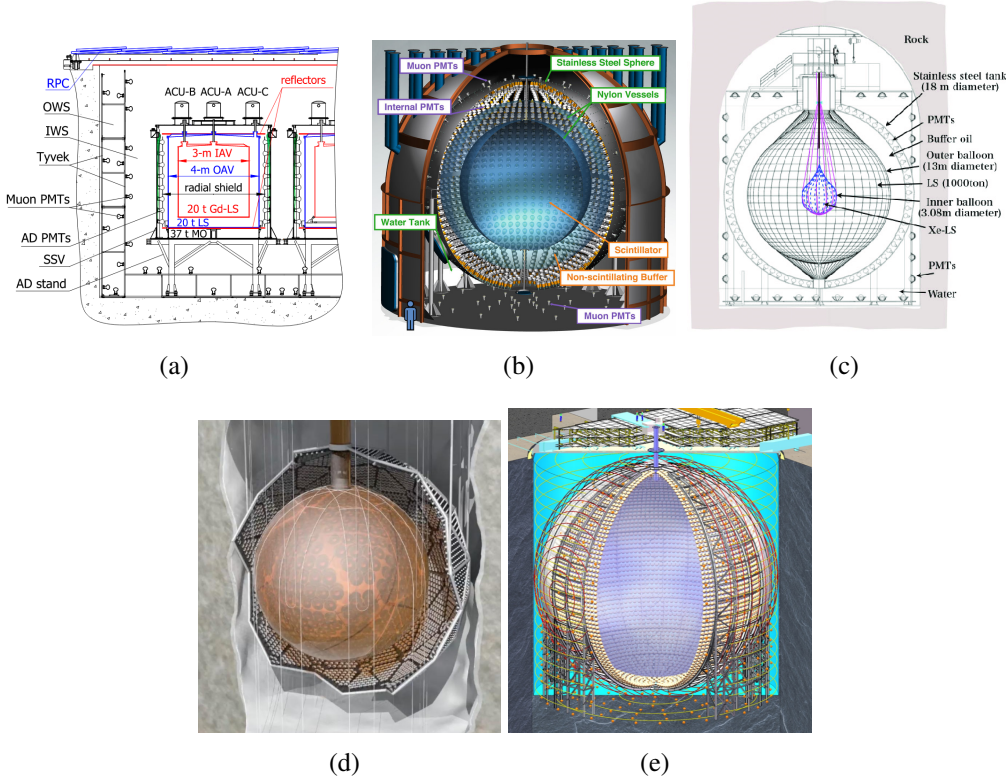


Figure 9.1: Designs of some recent, current and future scintillator detectors (a) DayaBay (b) Borexino (c) KamLAND (d) SNO+ (e) JUNO

The upcoming sections aim to detail an alternative design, which does away with the need for physical barriers to separate regions, all while aiming for a much cheaper and simpler construction.

## 9.2 SLIPS Detector Design

Figure 9.2 shows a 3D rendering of the Stratified LIquid Plane Scintillator (SLIPS) detector. The SLIPS concept is to do away with the physical barrier enclosing the purified liquid scintillator. PMTs are mounted on the bottom of a wide cavity submerged in a distillable, lipophobic liquid (e.g. various ethylene glycols), above which a less dense scintillator is layered. Thin and highly reflective surfaces, near the top and sides of the detector, efficiently reflect scintillation light down to the bottom PMT array. These reflective sheets also provide shielding from light emitted by radiation originating from

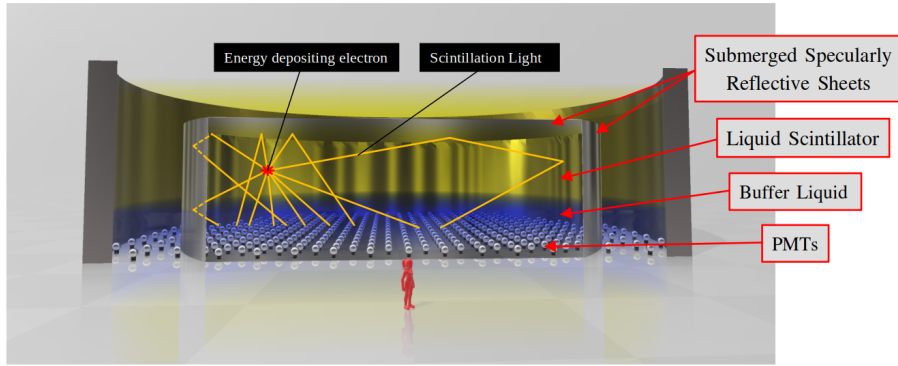


Figure 9.2: A 3D rendering of the ‘Pancake’ configuration. An example of a physics event is also shown, where the scintillation light paths are represented by orange lines. The PMT number density shown is less than that used in simulation tests.

the detector container and cavity. PMTs may also be placed in the region between the reflective surfaces and the container to serve as a muon veto.

Due to the long path lengths of scintillation light created by reflections, the detected light levels can become limited by the extinction length of photons in the scintillator. It is therefore advantageous for the detector height to be much less than the extinction length, leading to a short and wide detector configuration. Alternative detector shapes are explored later in the design, with the flat circular detector shown in figure 9.2 designated as the ‘Pancake’ configuration.

A large scale practical example of a stable two liquid system was the partially filled SNO+ detector. Figure 2.4 shows a photo taken from inside the SNO+ detector, taken during the partial fill phase. The scintillator-water interface is highlighted in the photo by a white arrow and line. The interface formed was found to be very stable over the partial fill period, which lasted approximately 6 months.

The next section describes the simulations carried out in GEANT4, for the purposes of testing the performance of the SLIPS detector.

### 9.3 Detector Simulation

For the purposes of testing, a cylindrical scintillator volume was chosen to be 10m tall and 25m in radius, as shown in figure 9.3. The centre of the cylindrical scintillator volume

was defined as the origin and the x-y plane was aligned with the plane of the PMTs. Alternative detector shapes and sizes are considered in section 9.5.

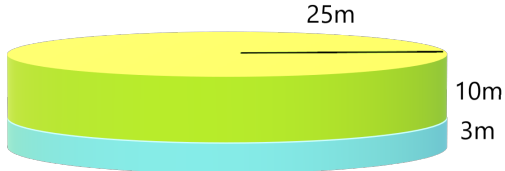


Figure 9.3: SLIPS detector inner scintillator dimensions used in simulations tests.

The calculation of the propagation of radiation in the SLIPS detector was carried out using a GEANT4 [81] based simulation. Standard MeV-scale electromagnetic and hadronic physics packages were included, along with the `GLG4Sim` package (also adopted in RAT) to generate energy deposition in the scintillator and the subsequent light emission and propagation. Data acquisition systems and electronics were also simulated, adapting the DAQ and PMT trigger logic code from RAT as outlined in chapter 2, using the N100 trigger as the global trigger for SLIPS.

### 9.3.1 PMTs

Two PMT types were simulated in the performance testing presented in this work. The primary PMT chosen for the multi-kilotonne detector, was the 20" r12860 PMT from Hamamatsu Photonics, while further studies later in the chapter were carried out using the 8" r5912-100 Hamamatsu model (section 9.4.3). The 20" PMTs were modeled in simulation using the specifications according to Ref. [179]. GEANT4 geometry models of the PMT's dimensions were created, attributing the measured quantum efficiency spectrum shown in figure 9.4(a) to the photocathode surface. Also included were, the measured single photoelectron (SPE) charge spectrum and the transit time spread (TTS). The charge spectrum was modelled simply as a Gaussian distribution, from which PMT hit charges were sampled for the triggering of PMTs and the global trigger. Table 9.1 summarises the key PMT parameters used to build and characterise each PMT type in simulation.

Channel discriminator thresholds were set to the typical SNO+ detector value of 9 ADC counts. Such that, for the r12860 PMT, a photon that produced a single p.e. on the pho-

Table 9.1: Key parameters assumed in the simulation of the two types of PMTs presented in this work.

Parameter	r12860 (20") [179]	r5912-100 (8") [77]
Peak to Valley Ratio	4.75	4.2
Transit Time Spread ( $\sigma$ )	1.3ns	0.87ns
Quantum efficiency (400nm)	31%	32%

tocathode would not trigger the PMT 3% of the time (4% for the r5912-100 PMT). The global trigger and channel threshold parameters that were optimised for the SNO+ experiment, are not necessarily optimal for the SLIPs detector and the 20" r12860 Hamamatsu PMTs. However, the work presented here considers event energies sufficiently beyond the trigger threshold such that DAQ trigger parameters did not play a significant role. A trigger gate event width of 400ns was also adapted from SNO+.

The PMTs were distributed in a hexagonal packing planar arrangement, with 54cm centre-to-centre between adjacent tubes. In all simulations the PMTs were placed such that the top of the photocathode cap was 2m below the scintillator-buffer interface, sufficiently distant from the interface to shield the scintillator from the PMT's intrinsic contamination.

### 9.3.2 Simulated Liquid Scintillator and Buffer Liquid

The detector's design principle requires the use of immiscible liquids with similar refractive indices. Since most organic scintillator solvents tend to be hydrophobic, these can therefore be paired with hydrophilic liquids, such as glycols, which tend to be less dense. This then more naturally leads to a design with scintillator on top and PMTs in a bottom buffer region.

The same scintillator cocktail employed by SNO+ was adopted for simulation testing: LAB + 2g/L PPO + 15mg/L bisMSB [69]. Figure 9.4(a) shows the absorption and emission spectra of the contributing components present in the cocktail, identical to figure 2.9, where the PMT quantum efficiency has been replaced with that of the r12860 20" PMT.

For the buffer solution, ethylene glycol was chosen as the candidate to pair with LAB in simulation. Ethylene glycol can be purified to high levels of purity through distillation

and has a similar refractive index to LAB in the wavelength region of interest, as shown in figure 9.4(b). Matching refractive indices in the buffer and scintillator liquids minimises the refraction effects for light crossing their interface, improving light detection efficiency and simplifying event reconstruction.

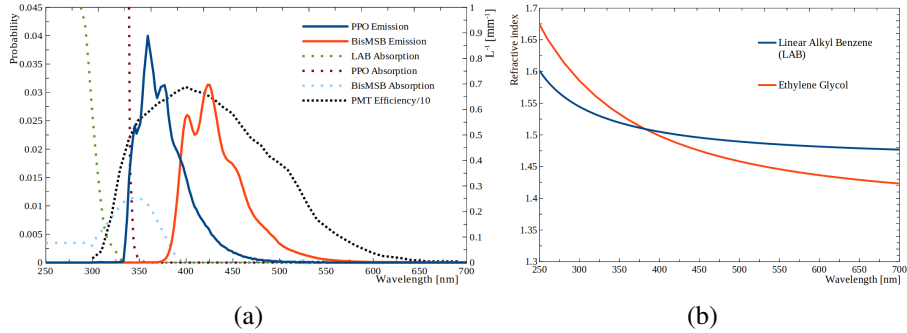


Figure 9.4: (a) The black dashed line shows the r12860 Hamamatsu PMT measured total detection efficiency (divided by 10 to fit on the graph), the other distributions are identical to those shown in figure 2.9 (b) The refractive index spectra for LAB and ethylene glycol [69][180].

## 9.4 Performance Testing in Simulation

With the detector simulation configuration now defined, this section presents the results for estimated light levels and position reconstruction.

### 9.4.1 Light Yield

Energy resolution is an important component in many relevant physics analyses. Previously mentioned analyses, such as the future  $0\nu\beta\beta$  search at SNO+ and the mass hierarchy measurement using reactor neutrinos at JUNO, require the best possible energy resolution to measure spectra and suppress backgrounds. Detectors used for nuclear reactor non-proliferation monitoring, which often aim to measure nuclear reactor neutrino fluxes, have a reduced demand for high quality energy resolution, since the IBD coincidence tag for antineutrinos strongly reduces background contamination and the emphasis tends to be on the flux rather than details of spectral shape.

In liquid scintillator detectors, the energy resolution is essentially dictated by Poisson's fluctuations on the total number of hits recorded on PMTs in a physics event. The reflec-

tive sheets allow for the potentially economical collection of light, detected with PMTs only arranged at the bottom of the detector. Figure 9.5 shows the light level due to  $\beta$ s generated around the detector. The z-axis coloured axis represents the total number of p.e.s produced on PMT photocathode surfaces due to a 1MeV  $\beta$  as a function of event position within the scintillator volume in plot 9.5. It can be seen that a high detected light level is achievable in the SLIPS detector, with relatively homogeneous light collection around the detector. Table 9.2 shows key comparisons in projected light collection for the SLIPS detector with the Borexino, KamLAND and JUNO detectors. The JUNO experiment also 20kt in mass, will be equipped with  $\sim$ 20,000 large PMTs to achieve their energy resolution goal of 3% per MeV. This would be a world-leading accomplishment for a kilotonne-scale optical detector. It can be seen that the SLIPS detector could potentially achieve a comparable level of excellent light yield using approximately half the number of PMTs and a much simpler construction.

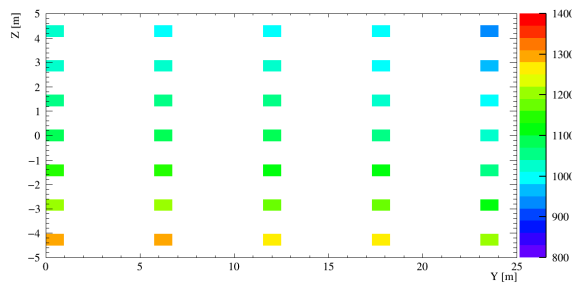


Figure 9.5: Light yield (total p.e.s per MeV) as a function of true  $\beta$ -particle position in the SLIPS detector, of dimensions shown in figure 9.3.

Table 9.2: Table summarising detector size, number of PMTs and the light yield for the Borexino, KamLAND and JUNO detectors compared to SLIPS.

	Borexino [181][182]	KamLAND [183][184]	JUNO [185][178]	SLIPS
Target Mass	300t	1kt	20kt	20kt
No. PMTs	2200	1900	$\sim$ 20,000	8000
Light Yield (p.e/MeV)	450	200	>1200	$\sim$ 1100

#### 9.4.2 Position Reconstruction

High quality position reconstruction is an important part of many physics analyses in order to achieve good signal-background separation. Event positions can be reconstructed

in a manner similar to that introduced in chapter 3, using PMT hit times and hit patterns. However, in the flat SLIPS detector, the reconstruction of vertical and horizontal event positions can be treated differently. The reconstruction of x and y positions can be more readily calculated since the PMT hit density shares the same plane, whereas the calculation z-position is complicated by a higher reliance on the timing of reflected light paths.

#### 9.4.2.1 Vertical Position Determination with PMT Hit Times

The calculation of z-positions using direct light arrival times is comparatively more challenging in a flat PMT configuration compared to a spherical arrangement of inward facing tubes. However a strong constraint on the z-position arises from the time differences between direct and reflected scintillation light. Figure 9.6 shows triggered PMT hit times vs PMT  $\rho$  (radius in x-y plane) for many  $\beta$  events generated at an assortment z-positions.

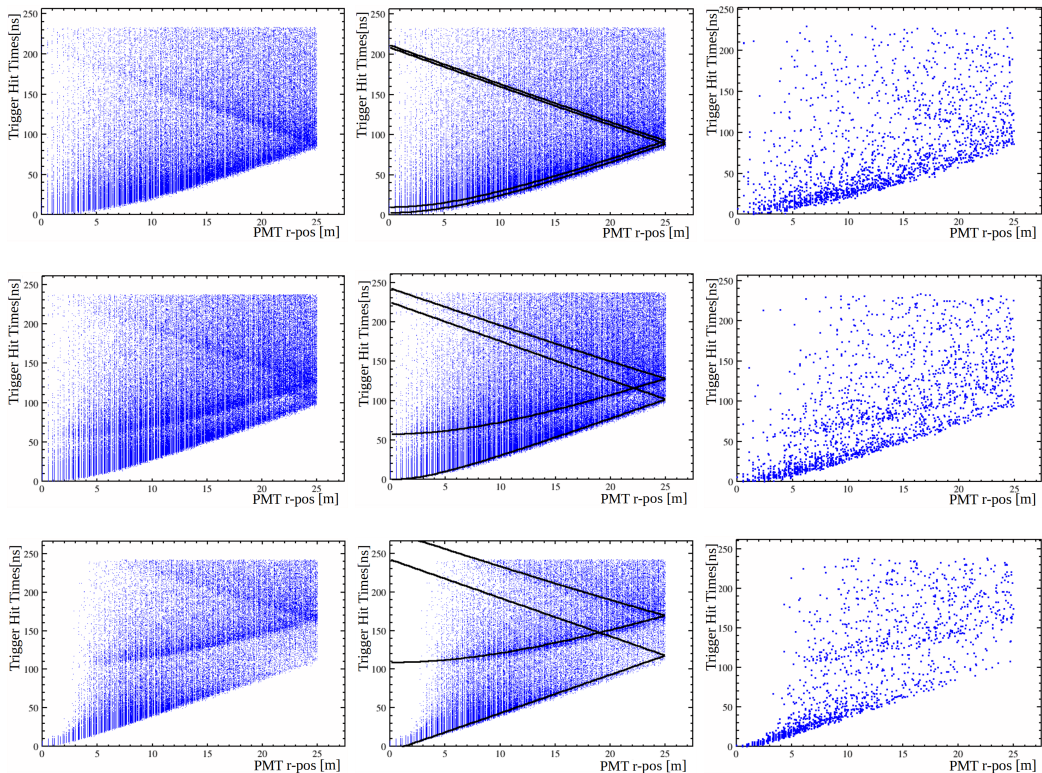


Figure 9.6: PMT hit times vs PMT radial position  $\rho$ . Top row:  $z_{ev} = +4.5\text{m}$ , middle row:  $z_{ev} = 0\text{m}$ , bottom row:  $z_{ev} = -4.5\text{m}$ . Left column: Many  $\beta$  events, middle column: Analytical calculation of the direct and reflected light wavefronts, right column: an example, single 3MeV  $\beta$  event.

The black lines overlaying the hit times in the second column indicate time of flight cal-

culations for direct and reflected light paths of photons travelling in the SLIPS detector, from an event to a given PMT position. Calculations assumed straight line paths and an effective refractive index (between that of LAB and ethylene glycol). Direct light paths are shown in the figures, as well as reflected light paths with: a single reflection on the ceiling, single reflection on the side walls, double reflections on the ceiling and sides walls. The right-most column of plots demonstrate that the direct and reflected wavefronts are clearly visible on an event-by-event basis. Wavefront separation becomes more difficult for events approaching the reflective sheets, as demonstrated in the top row of plots.

Late scintillation emission times produce the hit times seen to lag behind the wavefront regions, where the SNO+ scintillator cocktail of LAB + 2g/L PPO scintillator was assumed to have a leading time decay constant of 4.8ns [69]. It will be shown in section 9.4.3, that using faster a scintillator cocktail (either by increasing PPO concentrations or using alternative scintillators) and/or faster PMTs aids in the reconstruction of event positions. Direct and reflected wavefronts are more easily distinguished for scintillators with fast scintillation emission times, which yield narrow distributions in PMT hit times.

**Likelihood Fit of PMT Hit Times** For a demonstration of z-position resolution, a likelihood fit was carried out, based on triggered PMT hit times and PMT positions. In order to compare PMT hit times a global event trigger time was calculated. It was found that the mean of the first 50 PMT hit times, yielded a standard deviation of  $\sim 0.3\text{ns}$  in the trigger times calculated for many events. This trigger time was subtracted from all PMT trigger times in the following plots. Figure 9.7(b) shows a pdf generated from PMT trigger times vs PMT radial position. Pdfs were generated by simulating many 3MeV  $\beta$  events and creating pdfs at z-position intervals separated by 2.5cm.

The reconstructed z-position for an event was taken as the z-position of the pdf that maximised the likelihood for that event's PMT hit time distribution. The binned extended likelihood expression can be written as:

$$\log(\mathcal{L}(\vec{n}_{\text{hits}}(t)|\vec{r}, E)) = \sum_{i=0}^{N_{\text{bins}}^{\rho}} \sum_{j=0}^{N_{\text{bins}}^t} n_{ij} \log(\nu_{ij}(\vec{r}, E)) - \nu_{ij}(\vec{r}, E), \quad (9.1)$$

where  $n_{ij}$  is the number of PMT hits measured in the bin  $(i, j)$  defining PMT position and hit time,  $\nu_{ij}$  represents the expected number of hits for that bin for a  $\beta$  with event position  $\vec{r}$  and energy  $E$ . In order to account for fluctuations in the previously described event trigger calculation, the trigger time in each fit was allowed to freely float up to  $\pm 0.3\text{ns}$  around the estimated event time.

Figure 9.7(b) shows the PMT hit time distribution for an example 3MeV event, as well as the fit results for 500 3MeV  $\beta$  events, all generated at the origin. The standard deviation of the best fit z-positions was found to be 8cm, similar to the position resolution of 9cm expected in the SNO+ scintillator phase [90].

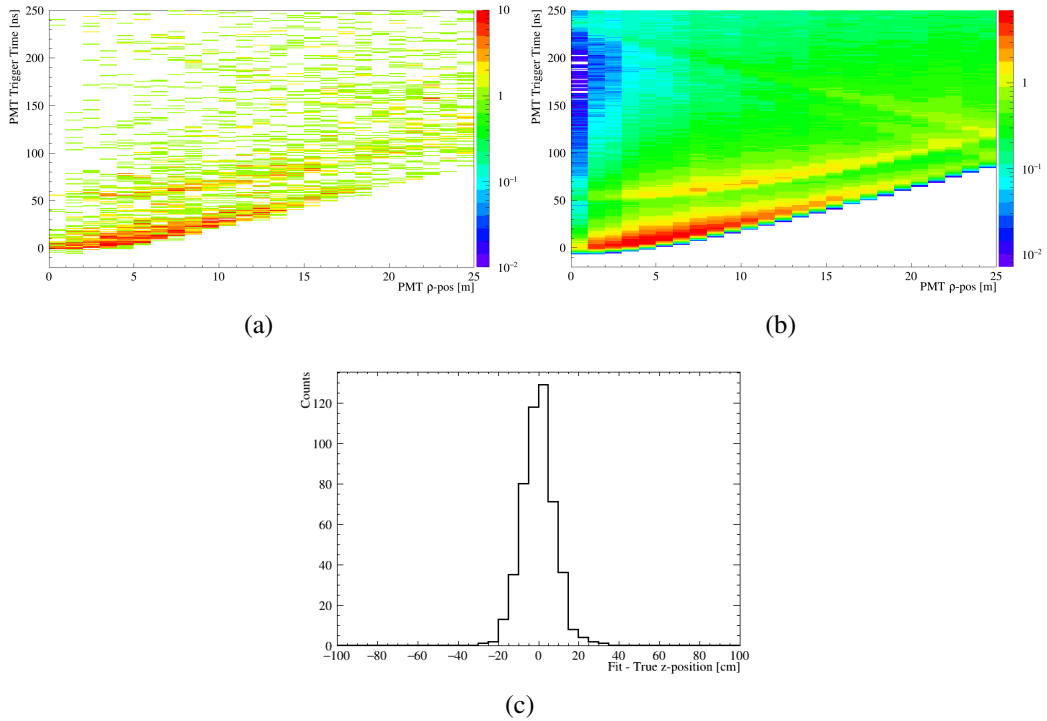


Figure 9.7: (a) PMT trigger times vs PMT position for an example 3MeV  $\beta$  event generated at the origin. (b) Pdf generated from many 3MeV  $\beta$  events at the origin (c) Likelihood fit results of the calculated z-position for 500 single 3MeV  $\beta$  events. The standard deviation of the histogram is 8cm.

It can be seen that, despite using fewer PMTs placed in single plane arrangement, the SLIPS detector can yield similar position resolutions to current and future large-scale scintillator detector designs. Section 9.4.3 investigates the impact that fast scintillators and fast PMTs can have on position resolution. The next section demonstrates the reconstruction of x,y and z positions based only on PMT hit densities, without the use of PMT

hit times.

#### 9.4.2.2 Reconstruction using PMT Hit Densities

**Horizontal Position Determination** Figure 9.8 shows PMT hit density plots for many  $\beta$  events generated in a SLIPS detector, with the same dimensions shown in figure 9.3. These plots serve to demonstrate that the x and y event positions can be determined from the PMT hit distributions alone, even without the use of PMT hit times. Having an ability to determine position using hit densities alone is of benefit for the use of scintillators with slow emission times for Cherenkov separation [83], where position reconstruction via timing is poorer compared to fast scintillators.

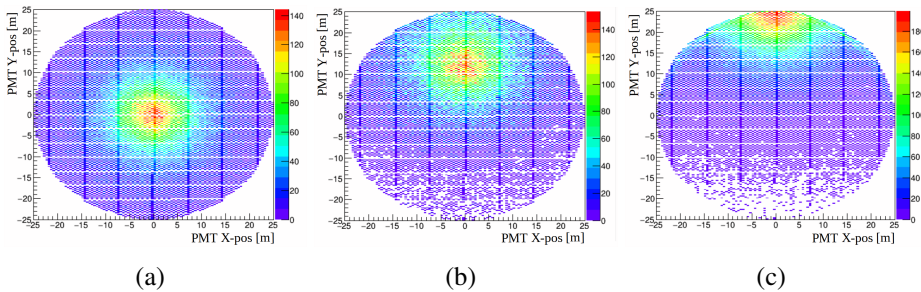


Figure 9.8: PMT hit density vs x,y position made with many  $\beta$  events in the Pancake SLIPS detector.  $\beta$  events were generated at (a) (0,0,0) (b) (0,12,0)m (c) (0,24.5,0)m. The z-axis reflects arbitrary units.

Again, a likelihood fit was carried out, fitting PMT hit density histograms using triggered PMT hits occurring within a 400ns time window. Pdfs of PMT hits vs PMT position were generated with many 3MeV  $\beta$  events. Each pdf was generated at various horizontal displacements separated by 5cm, all with z-positions at the centre of the scintillator. PMT hit density distributions for single 3MeV events were each generated at (0,0,0) and were fit using these pdfs. The best fit horizontal position was the pdf that maximised the binned extended likelihood, again using equation 9.1, but instead summing over x and y-position bins. In this case  $\vec{n}_{\text{hits}}$  is the observed number of triggered PMT hits in the binned histogram in PMT positions.  $n_{ij}$  is the number of in the  $(i, j)$  PMT position bin and  $\nu_{ij}$  represents the expected number of hits for that bin, for the pdf constructed from many  $\beta$ s of energy E and position  $\vec{r}$ .

The likelihood fit of 500 3MeV  $\beta$  events yielded a fit resolution in the  $\rho$  direction of

18cm, which is notably smaller than both the PMT width and separations (51 and 54cm respectively). Smaller and more dense PMT arrangements are expected to improve this. While the inclusion of the PMT hit times in the calculation of horizontal event positions would improve the resolution, the density calculation served to demonstrate the capabilities of a detector of this size equipped with slow scintillator.

**Vertical Position Determination** The same approach used in the horizontal position determination can also also be applied to the vertical position. As expected, the planar geometry of the PMTs yields worse position resolution using the hit density approach in z compared to x and y.

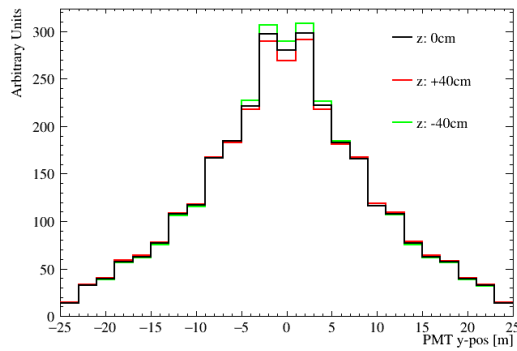


Figure 9.9: Pdf of PMT hit density vs PMT y-position for 3MeV  $\beta$  events, for  $\beta$ s generated at z-positions separated by 40cm ( $x = y = 0$ ).

The same likelihood fit of hits vs PMT position for hits occurring within a 400ns event window was repeated. Pdfs of the expected PMT hit density distributions were generated for z-positions separated by 5cm, at  $x=y=0$ . Figure 9.9 shows representative expected hit density distributions versus PMT y-position (shown in one dimension for clarity). The three pdfs show the expected density distributions for 3MeV  $\beta$  events, each separated by 40cm in z-position. The likelihood fits of 500 3MeV events generated at the scintillator centre yielded a standard deviation of 37cm in the distribution of best-fit horizontal positions. The use of timing information is therefore important along this axis, as expected.

### 9.4.3 Faster Scintillators & Faster PMTs

Figure 9.6 shows the calculable wavefront positions and shapes that allow for the reconstruction of event position. The resolution of the these wavefronts can be improved by

decreasing the spread in PMT hit times. Two methods to achieve this involve using faster PMTs and/or a scintillator cocktail with faster scintillation emission times.

For illustration, figure 9.10 shows side-by-side plots of wavefront hit time distributions using both faster PMTs as well as faster scintillator emission times, compared to the original SLIPS setup outlined in the introduction. The 20" r12860 Hamamatsu tubes were replaced with the faster 8" r5912-100 Hamamatsu model, with PMT's TTS specified in table 9.1. These PMTs were placed in a hexagonal close packing configuration as before with adjacent PMTs spaced by 20.82cm centre-to-centre (0.5cm glass-to-glass). A total of  $\sim 50,000$  PMTs were used in the 25m radius Pancake configuration SLIPS detector. The LAB+PPO+bisMSB scintillator cocktail was also altered in simulation such that the leading exponential decay constant for scintillation emission times was changed from 4.8ns to 3ns (achievable through PPO addition [98]).

The side by side comparison shows a noticeable improvement in the wavefront separation. Repeating the time-based likelihood fit on this faster configuration, it was found that z-position resolution was improved from 8cm to 5cm for 3MeV  $\beta$  events.

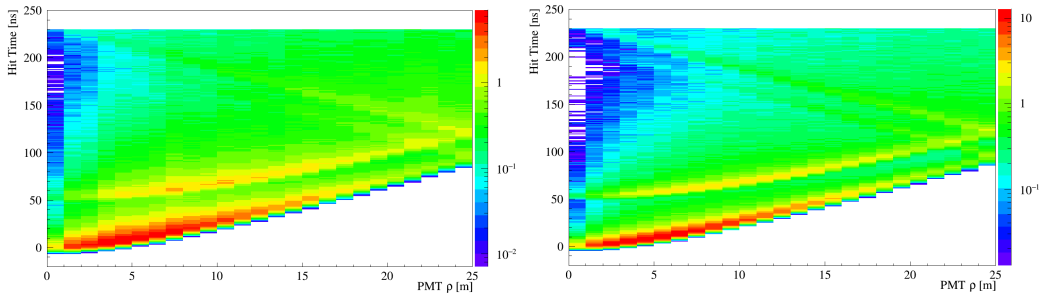


Figure 9.10: Demonstration of the increased resolution of the direct and reflected wavefronts when faster PMTs and scintillators are used (a) 20" r12860 Hamamatsu PMTs (1.3ns TTS) and a 4.8ns leading scintillator emission time constant (b) 8" r5912-100 Hamamatsu PMTs (0.87ns TTS) and a 3ns leading scintillator emission time constant.

#### 9.4.4 Light Collecting Concentrators

In order to increase the light collection and avoid the cost of installing additional PMTs, the SNO detector employed light concentrators [60], shown in figure 2.10(b). Generally, the light-detecting photocathode surface does not cover the full width of the PMT itself. Even for very densely packed spherical PMTs, this leaves insensitive regions between

PMTs, which reduces the effective photocathode coverage of the detector.

The difference between the planar SLIPS detector and the common spherical design, are the angles of incidence at which the arriving scintillation light lands on the PMTs. For spherical detectors, the majority of light arrives at the PMTs perpendicular to the PMT faces. As seen in figure 9.2, a much higher proportion of the scintillation light in SLIPS arrives at the bottom of the detector at steep angles of incidence.

Concentrators are highly efficient in light collection up to a calculable maximum acceptance angle [186]. In a SLIPS configuration, a large angular acceptance is required, limiting the achievable concentration factor. Their inclusion might still achieve some useful improvement to the expected photocathode coverage.

To investigate the impact that cone style concentrators could have in the SLIPS detector, short light concentrators were modelled in simulation. Figure 9.11 shows the shape of the reflectors used in simulation surrounding each PMT (assuming the 8" r5912-100 PMT). The PMTs were arranged, as before, in a hexagonal close packing arrangement, with a nearest glass-to-glass distance of 0.5cm. To allow for the packed arrangement of PMTs the concentrators were truncated. The concentrator base width was made equal to the 9.51cm photocathode radius of the r5912-100 model. Simulations assumed a 90% specular reflection efficiency for the concentrator surface.

Figure 9.12 shows pdfs of PMT hit times vs PMT position with 8" PMTs, with and without concentrators. It can be seen that the concentrators increase the light yield for small  $\rho$  (PMTs directly below the event), while the wavefronts become less intense at larger  $\rho$ . This is predominantly due the steep angles of incidence light arriving at distant PMTs, where there is an increased probability of reflecting back up into the scintillator. The Pancake SLIPS detector equipped with 8" PMTs, saw a light yield increase from 1180 to 1290 p.e./MeV when concentrators were added. The z-position resolution was found to change negligibly from 5cm with and without the Winston cones.

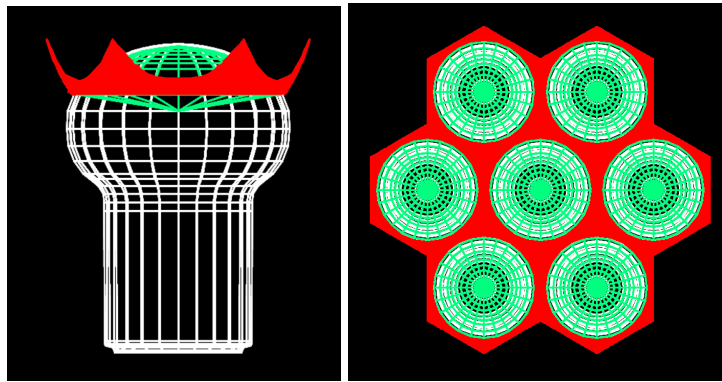


Figure 9.11: HepRep renderings [187] of the concentrators tested in simulations of the SLIPS detector. (a) Side-on view of a single 8" r5912-100 PMT [77], showing the photocathode (green) and truncated Winston cone (red). (b) Top-down view of a few hexagonally packed PMTs with concentrators masking the regions of the PMT which do not contain a photocathode surface.

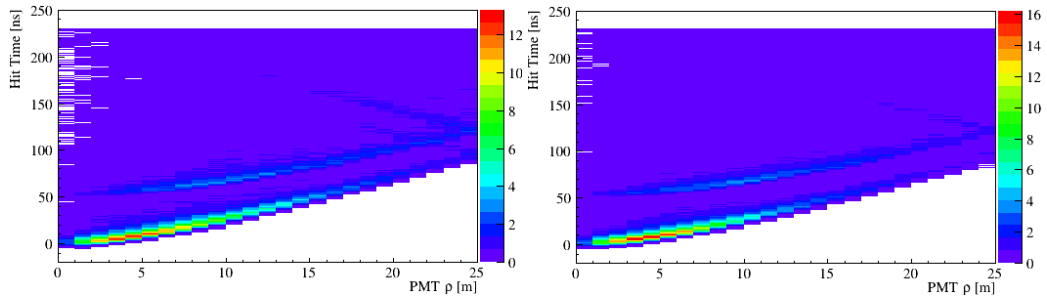


Figure 9.12: Pdfs of PMT hit times vs PMT position for the Pancake SLIPS detector, equipped with fast 8" PMTs and fast 3ns scintillator (a) No light concentrators (b) with light concentrators.

## 9.5 Alternative SLIPS Detector Shape

The aim of the SLIPS design is to provide a relatively low-cost, large-scale detector of simple construction. It is common for low energy neutrino experiments to be placed in deep underground tunnels originally excavated for the mining of geological materials (e.g. SNO+ in Creighton Mine). An alternative SLIPS detector shape to consider therefore, is a narrow and long cuboid shape, which conforms to typical tunnel dimensions. Figure 9.13 displays example dimensions of the Cuboid SLIPS configuration, containing roughly 20kt of scintillator.

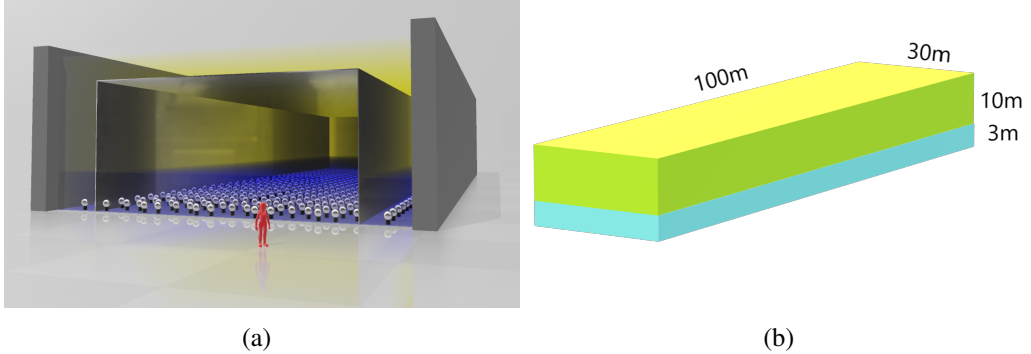


Figure 9.13: Cuboid configuration of the SLIPS Detector (a) 3D rendering of the detector (b) Detector inner scintillator dimensions used in simulations test

### 9.5.1 Cuboid Detector Minimum Width

Position resolution calculations were previously shown for the Pancake detector. While the Cuboid configuration could potentially allow for a simpler and cheaper construction, the narrowness of the detector can worsen position reconstruction due to the increased number of reflections, as well as increasing the radioactive backgrounds from the cavity rock.

Figure 9.14 displays again direct and reflected wavefronts, comparing the Pancake and Cuboid configurations. The dimensions of each type are shown in figures 9.3 and 9.13, where the Cuboid detector's width was varied. For the purposes of demonstration, the wavefronts have again been plotted as PMT hit times vs radial position  $\rho$ . The plots serve to illustrate the negative impact reflections have on position reconstruction. Visible in plot 9.14(e) for the Pancake 25m radius detector, are the prominent direct and reflected wavefronts, along with reflections on side walls. For the Cuboid configuration in plots 9.14 (b)-(d), the wavefronts become more spread out and overlap one another as the width of the detector decreases. This is due to the high degree of wall reflections in the narrow detector, effectively smearing the PMT hit times.

## 9.6 Conclusion

The SLIPS design presents a highly scalable and simply constructed liquid scintillator detector. SLIPS' no-barrier design avoids the difficult construction of large transparent

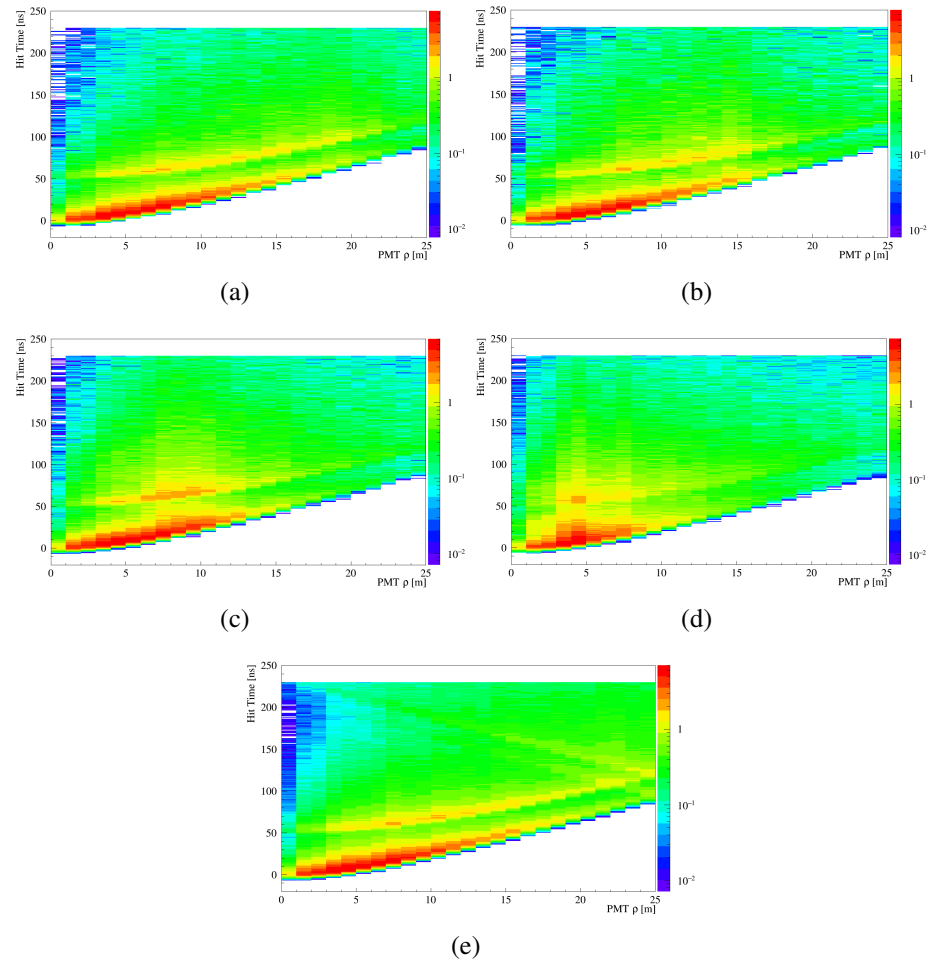


Figure 9.14: Plots of PMT hit times vs position, generated from many 3MeV events at the centre of the detector for. Plots (a)-(d) are for the Cuboid configuration, of length 100m and width (a) 40m (b) 30m (c) 20m (d) 10m. Plot (e) again shows the Pancake configuration of diameter 50m

barriers, as well as reducing the background contamination from boundary layers. It has also been shown that the use of reflective sheets yield highly efficient light collection with good position resolution, using far fewer PMTs than those employed in traditional spherical detectors.

## 10 | Conclusion

This thesis presented a first measurement of neutrino oscillation in reactor antineutrinos arriving at the SNO+ detector. The analysis was complicated by a half-full scintillator-water detector configuration, large  $\alpha$ -n rates, a lack of calibration sources and evolving scintillator light levels. BiPo214 events provided a practical calibration source for the scintillation emission times and light yield for  $\alpha$  and  $\beta$  particles. These parameters were found to differ significantly from those seen in tabletop measurements, but vastly improved the agreement between data and simulation in position and energy reconstruction. The reduced exposure to reactor antineutrinos in the partial fill phase lead to limited sensitivity to  $\Delta m_{21}^2$ . A total of  $45 \pm 6.7_{\text{stat}}$  candidate events were expected (9.5 of which were signal reactor antineutrinos), where 44 events were measured in data. Two values of  $\Delta m_{21}^2$  were favoured, at  $8.8_{-1.3}^{+1.1}$  and  $12.6_{-1.3}^{+1.6} \times 10^{-5}$  eV $^2$ , where the smaller best-fit value of  $\Delta m_{21}^2$  was consistent with the current global PDG value of  $7.53 \pm 0.18 \times 10^{-5}$  eV $^2$ , within a  $1\sigma$  frequentist confidence interval. This result demonstrated good understanding of the detector and the expected background and signal rates. The prospects of the continued antineutrino analysis over future scintillator phases were then presented. Simulations showed that a precise measurement of  $\Delta m_{21}^2$  may be possible, where the current global uncertainty can be surpassed within a 3-5 year livetime in the Te-loaded scintillator phase, depending primarily on  $\alpha$ -n levels. Highly efficient  $\alpha$ -n removal may be possible using PSD methods, where a calibration of the proton scintillation emission times is expected to be made for the SNO+ scintillator.

Background measurements were also performed in both water and scintillator phases, where the results are expected to contribute in future SNO+ analyses. A novel method was used to extract the radiation from the SNO+ ropes (appendix B), measuring the background rate as  $0.27 \pm 0.02_{\text{stat}} \pm 0.13_{\text{sys}}$  times the rate from previous ex-situ measurements. BiPo214 rates were used to measure the supported concentration of  $^{222}\text{Rn}$ , from the  $^{238}\text{U}$  chain, in the scintillator, finding the concentration to be  $4.5 \pm 1.3 \times 10^{-17} \text{g}_{\text{U}}/\text{g}_{\text{LAB}}$ .

Finally, the highly scalable and simply constructed ‘SLIPS’ liquid scintillator detector was presented. Simulation studies demonstrated that detector may be able to achieve highly efficient light collection with good position resolution, using far fewer PMTs than those employed in traditional spherical detectors.

## A | Neutrino Mass

### A.1 Neutrino Mass Scale

The magnitudes of the neutrino masses have not yet been measured, but is a very active area of research. Experiments such as KATRIN [188], Project8 [189], ECHO [190] and WITCH [191] probe the neutrino mass through precise measurements of the  $\beta$ -decay spectrum. KATRIN hold the current world-leading upper limit on the neutrino mass  $m_\nu < 0.8 \text{ eV}/c^2$  (90% CL) [192].

Indirect measurements placing limits on the magnitudes of neutrino masses have also been derived from cosmological observations, as the absolute value of the neutrino masses have consequences on the evolution of large scale structure in the universe [193]. The strongest constraint for the upper limit on the sum of the neutrino masses comes from measurements of the cosmic microwave background by the Planck satellite, combined with measurements of the baryon acoustic oscillation, placing an upper limit of  $\sum m_\nu < 0.16 \text{ eV}$  (95% CL) [194]. The stated upper limit depends on assumptions made about the number of neutrinos, their evolution over the lifetime of the universe and the cosmological model used to describe the matter evolution of the universe, where the Planck result has been shown to be the most robust cosmological measurement to date [195][196].

### A.2 Neutrino Mass

Upon the discovery of massive neutrinos, it is natural to ask the question of what mechanism is behind the neutrino mass. The experimental success the SM in describing massive fermions as Dirac particles, naturally leads to the addition of massive neutrinos in SM as Dirac particles also, yielding a number of consequences.

### A.2.1 Dirac Neutrinos

The field  $\psi$  is a solution to the Dirac equation, used to describe all massive fermions in the SM:

$$(i\partial_\mu \gamma^\mu - m)\psi = 0 \quad (\text{A.1})$$

The general solution  $\psi$  is a 4-component Dirac spinor. The Dirac spinor  $\psi$  can be broken down into its left and right-handed chiral components:

$$\begin{aligned} \psi &= \psi_L + \psi_R \\ i\partial_\mu \gamma^\mu \psi_L &= m\psi_R \\ i\partial_\mu \gamma^\mu \psi_R &= m\psi_L, \end{aligned} \quad (\text{A.2})$$

where  $\psi_L$  and  $\psi_R$  are Weyl 2-component spinors. The 4-component Dirac spinor can be viewed as made up of two left and right-handed Weyl spinors in eqn. A.2. Hermann Weyl originally proposed Weyl spinors, 2-component solutions to an alternative of the Dirac equation, to describe massless fermions [197]. Dirac had originally rejected idea though as they did not conserve parity [198] (later found to be a true non-conservation). SM massless neutrinos exist as Weyl spinors, solutions to the equations A.2 where  $m = 0$ .

The mass term for all massive fermions in the SM arises from the coupling of left and right-hand chiral components  $\psi_L$  and  $\psi_R$ . The general Dirac mass term in the SM Lagrangian for a fermionic field  $\psi$  can be written as:

$$\mathcal{L}_{\text{Dirac}} = -m_D(\overline{\psi}_R \psi_L + \overline{\psi}_L \psi_R) \quad (\text{A.3})$$

In the case of massless neutrinos, neutrinos exist in the SM only as left-handed Weyl spinors and antineutrinos as right-handed ones. Since only left-handed neutrinos and right-handed antineutrinos participate in weak interactions, the existence of the right-handed component of neutrino (and left-handed antineutrino) is unphysical and therefore not included in the SM.

Mass in the SM is generated in the coupling of left and right-handed fields. One can treat

neutrinos as all other massive fermions and introduce two not-yet-observed fields,  $\nu_R$  and  $\overline{\nu_L}$ . This addition of 2 degrees of freedom is known as the ‘minimally extended Standard Model’. It is still the case that only  $\nu_L$  and  $\overline{\nu_R}$  can participate in weak interactions, where the  $\nu_R$  and  $\overline{\nu_L}$  components do not couple to any of the SM gauge fields. This leaves  $\nu_R$  and  $\overline{\nu_L}$  known as ‘sterile’ fields.

Treating neutrinos as SM fermions that couple to the Higgs field, the mass obtained in the Higgs-lepton Yukawa Lagrangian is:

$$m_i^\nu = \frac{y_i^\nu v}{\sqrt{2}} \quad (\text{A.4})$$

where  $v$  is the Higgs’ vacuum expectation value (VEV) and  $y_i^\nu$  are the Yukawa coupling constants [10]. The Yukawa constants quantify the coupling each fermion has to the Higgs field, yielding the mass observed in experiment for each of the known charged leptons and quarks.

It has been shown in the assumption that neutrinos are Dirac particles, there is a need to introduce two extra degrees of freedom in the form of a right-handed component of the neutrino field and left-handed antineutrino, for each neutrino generation ( $e, \mu, \tau$ ) [10]. Aside from the addition of unobserved fields, another motivation for an alternate description of neutrino masses arises from the observation that neutrino masses are at least 6 orders of magnitude smaller than any other fermion masses in the SM. The Yukawa coupling constant description in eqn. A.4 does not provide any indication for the reason neutrino couplings are so much smaller, suggesting an alternative mass mechanism for neutrinos. It should be noted however, the origin of the Yukawa coupling values for all other quarks and leptons are also left unexplained by the SM.

### A.2.2 Majorana Neutrinos

Ettore Majorana investigated the possibility of generating neutrino mass, while retaining only the two degrees of freedom observed in weak interactions of left-handed neutrinos and right-handed antineutrinos. Majorana proposed in 1937, that since fermion mass is generated in the coupling of left and right-handed fields, as seen in the Dirac mass

term in eqn. A.3, if the right handed neutrino field  $\nu_R$  is replaced with the antiparticle of the left-handed neutrino  $\nu_L$ , mass can be generated for neutrinos [199]. This avoided the requirement of two extra degrees of freedom due to the introduction of right-handed neutrinos  $\nu_R$  and left-handed antineutrinos  $\overline{\nu}_L$ .

The antiparticle of a left-handed particle is a right handed field. The charge conjugation operator can be defined as  $\psi \rightarrow \psi^c \equiv -\mathcal{C}\overline{\psi}^T \equiv -i\gamma^2\gamma^0\overline{\psi}^T = -i\gamma^2\psi^*$ . It can be shown this yields  $\psi^c$  with opposite chirality to  $\psi$  [10]. The Majorana condition stated:

$$\psi_R \equiv (\psi_L)^c \quad (\text{A.5})$$

The neutral neutrino field serves as an ideal Majorana particle candidate, as the only known neutral fermionic field. Assuming this equivalence for any other charged fermionic field (of charge  $q$ ), would lead to charge violation ( $q \rightarrow -q$ ).

Applying the Majorana condition to the Dirac mass term in equation A.3, yields the Majorana mass term for neutrinos:

$$\mathcal{L}_{\text{Majorana}} = -m_D(\overline{\nu}_R\nu_L + \overline{\nu}_L\nu_R) = \frac{1}{2}m_M((\overline{\nu}_L)^c\nu_L + \overline{\nu}_L(\nu_L)^c) \quad (\text{A.6})$$

This removes the coupling between left/right-handed active/sterile neutrinos (and right/left-handed active/sterile antineutrinos) in the Dirac mass term. The Majorana neutrino mass term instead abolishes the separation between particle and antiparticle, coupling the two as the left and right-handed chiral components, as required in the mass term.

The Majorana mass term however has consequences in  $SU(3)_C \times SU(2)_L \times U(1)_Y$  gauge invariance required in the SM. The left-handed Majorana mass term (which carries weak hypercharge  $\pm 2$ ) does not conserve  $SU(2)$  symmetry. The Majorana mass term also has consequences in the conservation of lepton number. The SM attaches lepton number of (-)1 to (anti)neutrinos, which is assumed to be conserved in the weak interaction. The Majorana mass term  $(\overline{\nu}_L)^c\nu_L$  yields a lepton number change of  $\pm 2$ . Total lepton number appears to be a conserved quantity, however lepton flavour number has been seen to be violated in neutrino oscillations. Lepton non-conservation searches can be made in particle collider experiments [200]. Mu2e sets out to investigate the non-conservation of

lepton flavour in the neutrino-less decay of  $\mu^- \rightarrow e^- + \gamma$  [201].

It is understood that the SM is not the final answer. Theories at higher energies may be able to explain the origin and differences between charged leptons and quarks also. One example of a Beyond Standard Model (BSM) theory, the lowest dimensional solution addressing the SU(2) non-conservation issue in the left-handed Majorana mass term can be written as [10]:

$$\mathcal{L}_5 = \frac{1}{2} \frac{g}{\mathcal{M}} (L_L^T \tau_2 \Phi) C^\dagger (\Phi^T \tau_2 L_L) + \text{h.c.}, \quad (\text{A.7})$$

where  $\mathcal{M}$  is a constant representing the energy at which the new physics generates the term,  $\tau$  are the Pauli matrices and  $L_L$  is the SM SU(2) lepton doublet and  $\Phi$  is the Higgs doublet. This mass term is classified as an effective theory as it has an energy dimension of 5, where renormalisable SM terms have dimension up to 4.

As mentioned, the Dirac description requires a sterile right-handed neutrino field, a singlet in all SM gauge transformations. The right-handed Majorana mass term therefore does not violate any SM invariance laws, as seen next in the Dirac-Majorana combined picture.

### A.2.3 Dirac-Majorana Mixing

Instead of considering the Dirac and Majorana spinors separately, it is possible to consider their relation in combination. A combined total mass term can be written as the sum of the Dirac mass, coupling the left and right-handed fields, along with Majorana mass terms for the left and right-handed fields separately:

$$\begin{aligned} \mathcal{L}_{\text{mass}}^{D+M} &= \mathcal{L}_{\text{mass}}^D + \mathcal{L}_{\text{mass}}^L + \mathcal{L}_{\text{mass}}^R \\ &= -m_D \overline{\nu_R} \nu_L - \frac{1}{2} m_R \overline{(\nu_R)^c} \nu_R - \frac{1}{2} m_L \overline{(\nu_L)^c} \nu_L + \text{h.c.} \\ &= -\frac{1}{2} \overline{N_L^c} M N_L, \end{aligned} \quad (\text{A.8})$$

where in the final line, the left-handed neutrino fields were defined as:

$$N_L = \begin{pmatrix} \nu_L \\ (\nu_R)^c \end{pmatrix} = \begin{pmatrix} \nu_L \\ \mathcal{C} \overline{\nu_R}^T \end{pmatrix} \quad (\text{A.9})$$

This leads to the definition of mass matrix  $M$ :

$$M = \begin{pmatrix} m_L & m_D \\ m_D & m_R \end{pmatrix} \quad (\text{A.10})$$

Due to  $M$  not being diagonal, chiral fields  $\nu_L$  and  $\nu_R$  do not have definite masses. It is possible to diagonalise mass matrix  $M$  through a unitary transformation where chiral left-handed massive neutrino fields  $n_L$  are defined:

$$\begin{aligned} N_L &= Un_L \\ n_L &= \begin{pmatrix} \nu_{1L} \\ \nu_{2L} \end{pmatrix} \\ U^T M U &= \begin{pmatrix} m_1 & 0 \\ 0 & m_2 \end{pmatrix} \end{aligned} \quad (\text{A.11})$$

In doing so, the Dirac-Majorana mass term can be written concisely as:

$$\mathcal{L}^{D+M} = \frac{1}{2} \sum_{i=1,2} m_i \overline{(\nu_{iL})^c} \nu_{iL} + \text{h.c.} = \frac{1}{2} \sum_{i=1,2} m_i \overline{\nu}_i \nu_{iL} \quad (\text{A.12})$$

where the massive neutrino field has been defined as:

$$\nu_i = \nu_{iL} + \nu_{iL}^c = \nu_{iL} + \mathcal{C} \overline{\nu}_{iL}^T \quad (\text{A.13})$$

The combined Dirac-Majorana mass has been written simply as Majorana mass term assuming a non-zero Majorana mass (where gauge invariance does not prevent a Majorana mass term for  $\nu_R$ ). The result is that if neutrinos have non-zero Majorana mass, they are Majorana particles, despite any Dirac mass terms. The left-handed fields are represented by  $\nu_L$  and  $(\nu_R)^c$  for a neutrino generation in the flavour basis, where  $\nu_L$  participates in weak interactions and  $(\nu_R)^c$  is sterile. Due to the mixing of these sterile and active neutrinos, oscillations between these neutrinos is expected to be possible [10].

### A.2.3.1 The Seesaw Mechanism

As mentioned, the Dirac mass term is SU(2) invariant, while the Majorana mass term for left-handed neutrinos is not allowed by the SM for this reason. The right-handed sterile neutrino however is a singlet in the SM gauge theory  $SU(3)_C \times SU(2)_L \times U(1)_Y$ .

One reason for the popularity of Majorana neutrinos in many BSM theories, is that they can provide explanation for the tiny neutrino mass compared to the other massive fermions. Assuming the case where the left-handed Majorana neutrino mass is zero, to be consistent with the SM SU(2) invariance, the eigenvalues of  $M$  in eqn. A.10 are:

$$m_{1,2} = \frac{m_R}{2} \mp \sqrt{\frac{m_R^2}{4} + m_D^2} \quad (\text{A.14})$$

For the case  $m_R \gg m_D$ , one of the Majorana masses becomes very small  $m_1 \approx m_D^2/m_R$  and the other Majorana mass approaches  $m_R$ . The light Majorana mass eigenstate can then be written, from eqn. A.11 as:

$$\nu_{1L} \approx \nu_L + \frac{m_D}{m_R} (\nu_R)^c \quad (\text{A.15})$$

i.e. approximately equal to the SM neutrino. The assumed limits of  $m_R$  and  $m_D$  and Majorana masses provides explanation to the observed neutrino mass. As mentioned the neutrino mass is many orders of magnitude smaller in mass than its fellow massive fermions, charged leptons and quarks. One can assume  $m_D$  is of a similar order to these particles, i.e. not larger than the electroweak scale of order of 100 GeV. The Dirac mass terms describing their mass obeys the SM gauge symmetries. The Majorana mass  $m_R$  however, describes the mass of the sterile neutrino  $\nu_R$ , a singlet to all of the SM symmetries. It is therefore plausible due to the lack of a requirement that it obey SM gauge transformations, that  $m_R$  is generated by physics at energies far beyond the SM. Assuming,  $m_R$  is at the scale of grand unifying theories  $10^{15}$ GeV (GUT-scale), yields a Majorana neutrino mass  $m_1$  of a few keV, below the current upper limits of the neutrino masses we observe [192].

## A.3 Neutrino-less Double Beta Decay

The current consensus most-viable method to measure if neutrinos are Majorana particles, is by the observation of the rare neutrino-less double beta decay ( $0\nu\beta\beta$ ).

### A.3.1 Double Beta Decay

The search for the possible rare  $0\nu\beta\beta$  decay relies on the occurrence of the double beta decay, also a rare event.  $\beta$ -decay is the reduction of a nucleus' energy through the conversion of a neutron to a proton, summarised as  $(Z, A) \rightarrow (Z \pm 1, A) + e^\mp + \bar{\nu}^\pm$ . For a selection of nuclei, double beta decay ( $2\nu\beta\beta$ ) may occur, simultaneously undergoing two  $\beta$  decays i.e.  $(Z, A) \rightarrow (Z \pm 2, A) + 2e^\mp + 2\bar{\nu}^\pm$ . In these selected nuclei, the  $2\nu\beta\beta$  decay lowers the nucleus energy further compared to the single  $\beta$  decay, as demonstrated in figure A.1.  $^{130}\text{Te}$  was chosen as the isotope to provide double beta decays in the SNO+ detector. Considered in the choice of  $^{130}\text{Te}$ , were properties such as the decay Q-value (the background events present at this energy), the  $2\nu\beta\beta$  lifetime (dictating the background rate) and cost.

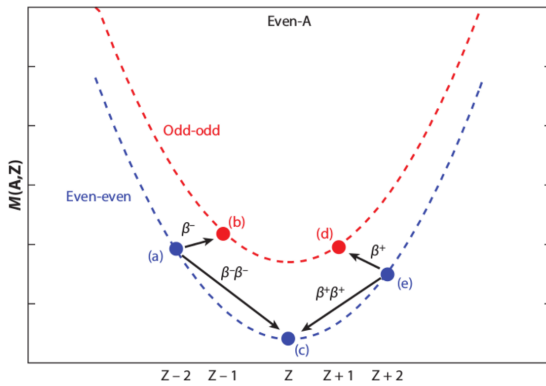


Figure A.1: Expected nucleus energy for various possible single  $\beta$  and  $\beta\beta$  transitions. Dotted lines show nucleus energy for odd-odd and even-even numbered protons and neutrons. The points show example nuclei, where the given even-even nucleus achieves energy reduction for the  $\beta\beta$  and not the  $\beta$  decay. Plot taken from [202].

The simplest BSM description of the possible  $0\nu\beta\beta$  decay is shown in figure A.2. There are many possible BSM mechanisms which can yield the  $0\nu\beta\beta$ , but regardless of the mechanism, the black box theorem states that an observation of  $0\nu\beta\beta$  indicates that neutrinos are Majorana particles [203]. An observation of  $0\nu\beta\beta$ , a lepton number violating

process, would indicate new physics beyond the SM.

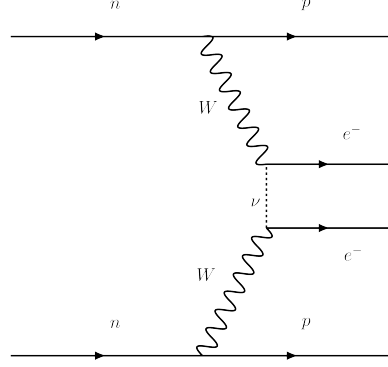


Figure A.2:  $0\nu\beta\beta$  Feynman Diagram showing the exchange of a light Majorana neutrino.

The rate of  $0\nu\beta\beta$  decays can be calculated for the particle physics process in figure A.2, as well as from nuclear physics modelling. The half-life for  $0\nu\beta\beta$  assuming light Majorana neutrino exchange can be written as:

$$(\tau_{1/2}^{0\nu\beta\beta})^{-1} = g_A^4 G_{0\nu} |M_{0\nu}|^2 \frac{m_{\beta\beta}}{m_e^2}, \quad (\text{A.16})$$

where  $M_{0\nu}$  is the nuclear matrix element,  $G_{0\nu}$  is a phase space factor and  $m_{\beta\beta}$  is the effective Majorana for electron neutrinos given as  $m_{\beta\beta} = \sum_{i=0}^3 U_{ei} m_i$ .

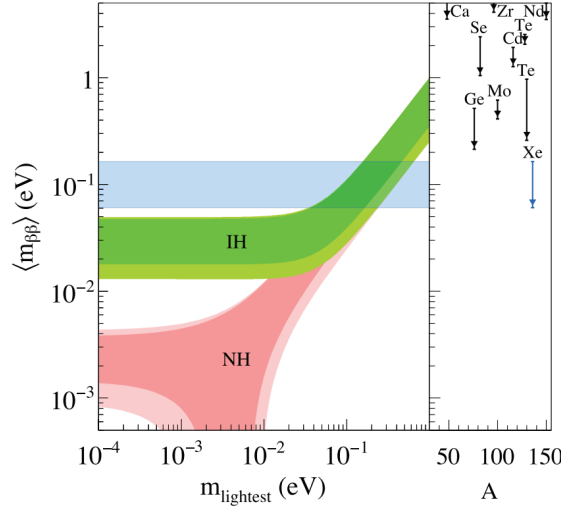


Figure A.3: The effective Majorana mass against the mass of the lightest neutrino, showing the phase space for normal hierarchy (NH) and the inverted hierarchy (IH). The blue band shows the best limits on  $m_{\beta\beta}$  up to 2016, from the KamLAND-Zen experiment [204]. Plot taken from [205].

Significant uncertainties in the predicted  $0\nu\beta\beta$  rate arise from the difficult calculation

of nuclear matrix element  $M_{0\nu}$ . There are a number of models that cover wide range of value, leading to differences of a factor of 2 or more [206]. Uncertainties also arise from assumed absolute magnitude of the neutrino masses (or the minimum neutrino mass), along with Majorana phases  $\phi_{1/2}$  [207]. The remaining uncertainty in the hierarchy of the neutrino masses plays large a role in  $m_{\beta\beta}$ . Figure A.3 summarises the significant impact the neutrino mass orderings, where the IO hierarchy is favourable for the measurement of an appreciable rate of  $0\nu\beta\beta$  events.

Figure A.4 demonstrates the measurement of a  $0\nu\beta\beta$  rate. The major background to the signal  $0\nu\beta\beta$  events is the dominant process of  $2\nu\beta\beta$ . The signal rare process is extracted by measuring the energy spectrum of the combined energy of the 2 electrons in the double beta decay process. Should neutrinos be emitted in the decay, a continuous range of combined electron energies will be measured as the undetected neutrinos carry away portions of the energy. In the case however that no neutrinos are emitted, a narrow peak of the combined electron energies centred around the isotope's Q-value.

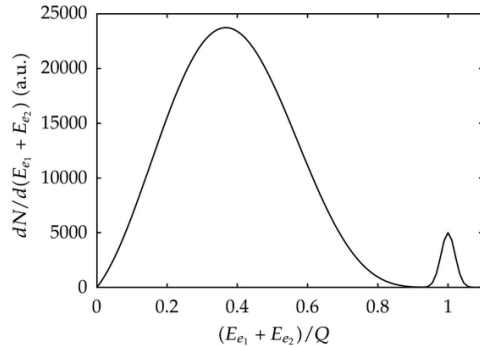


Figure A.4: Sketch of the two electron energy sum spectrum, normalised to the decaying isotope Q-value. A 5% energy resolution was assumed. Plot taken from [208].

## B | Measurement of the SNO+ Ropes Background in the Water Phase

This chapter outlines results of a background analysis carried out in the water phase, measuring the radiation due to  $^{208}\text{Tl}$  and  $^{214}\text{Bi}$  decays occurring in the SNO+ ropes. The novel method used took advantage of positional symmetries to isolate and measure the background rate specifically originating from the ropes in the SNO+ detector.

Comprehensive measurements of the backgrounds present in the SNO+ detector were carried out over 2017-18, which were used in a nucleon decay search and a measurement of solar neutrinos [62][55]. Following another extended period of water data-taking, ending eventually in 2019, the solar, nucleon decay and background measurement analyses were repeated.

Section 4.1.1 introduced the importance of measuring and understanding the various backgrounds which fall into the  $0\nu\beta\beta$  region of interest centred around the Q-value of 2.53MeV. Backgrounds were separated into two categories: internals and externals, where external backgrounds originate from all detector components not including the target medium within the AV. The water phase of the SNO+ experiment allowed for the opportunity to measure the various external background rates. The measurements are expected to carry over into the scintillator phases of the experiment, as the rates of most external backgrounds are not expected to change upon the introduction of scintillator within the AV.

One background of concern arise from externally sourced  $\gamma$ s that can propagate and reach within the  $0\nu\beta\beta$  fiducial volume. For example in the  $\beta$  decay of  $^{208}\text{Tl}$ , a daughter of the  $^{232}\text{Th}$  decay chain, emits a 2.6MeV gamma in 100% of the decays. A  $\beta$  is also emitted (with Q-value 4.99MeV), which for  $^{208}\text{Tl}$  external to the AV, does not propagate through the acrylic. Only the 2.6MeV  $\gamma$  therefore, with its extended absorption length in water and scintillator may reach the centre of the AV. Light and energy loss for  $\gamma$  arriving from outside the AV pushes the reconstructed electron-equivalent energy down slightly to the 2.5MeV range, landing in the  $0\nu\beta\beta$  ROI.

## B.1 Background Events Originating from the Ropes

The main contributing external sources of contamination are the AV itself, the ropes surrounding the AV, the external water and the PMTs, all of which are contaminated with the aforementioned  $^{208}\text{Tl}$ , along with  $^{214}\text{Bi}$  which can also contribute lower energy  $\gamma$ s. Due to the poor event reconstruction in the region near/beyond the AV, it is difficult to separately measure in-situ each background source's contribution of background events.

This chapter introduces a novel method which can measure the contribution of the SNO+ ropes, separately from the AV and external water, all of which are located in the same region of the detector. Prior to this analysis, the AV and rope background contributions were measured as a single overall background rate [62][55]. Their combination also relied upon ex-situ measurements of detector components prior to their installation into the detector. Introducing individual measurements of each external components allows a better constraint on each of the external backgrounds sources in various water and scintillator physics analyses.

Results will be shown for data taken over a long period background water with particularly low background levels. The dataset was made up of runs between and including runs 200004 to 206391 (24<sup>th</sup> October 2018 to 25<sup>th</sup> May 2019), totalling  $193.33 \pm 0.07$  days of recorded physics data [209]. Overall internal and external backgrounds were reduced greatly for this period due to the installation of the cover gas system [79].

The simulations used in this analysis were produced using RAT v6.17.6, produced under the detector conditions for the runs taken in data. The data and MC simulated data was processed with RAT v6.18.3.

Independent analyses over the same dataset, measuring the rate of internal and external backgrounds were carried out by I. Lam and T. Zummo respectively. Care was taken such that the fiducial volumes used in these analyses didn't cross over with the region used for the ropes analysis. The next section introduces the method used to isolate rope background events from the AV, internal and external water.

## B.2 Method to Isolate Rope Events

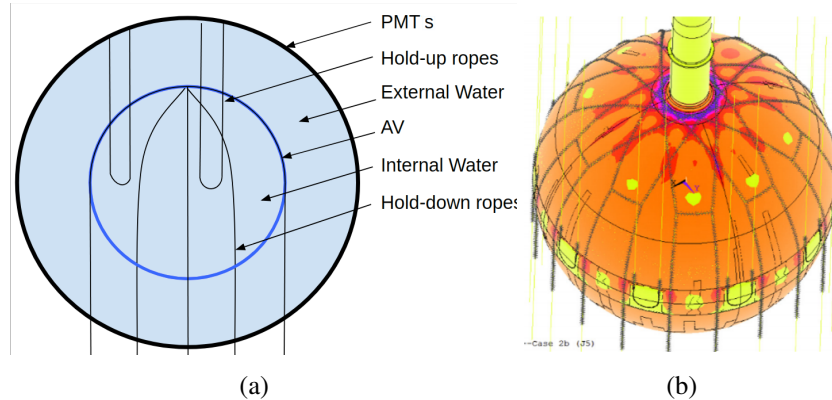


Figure B.1: Drawings of the SNO+ detector with ropes (a)View of the components of the SNO+ Detector relevant in this chapter (b) Closer look at the AV, Hold-down (black) and Hold-up (yellow) ropes. Colour variation across the AV in this diagram reflects strain on the material, the reader should not take this colour variation to play any significant role in this analysis.

The main background source emanating from the hold-down (Hd) and hold-up (Hu) ropes is due to the  $\beta$  decay of  $^{208}\text{Tl}$ .  $^{208}\text{Tl}$  can also found in internal water, AV and the external water, however the ropes provide a particularly high rate, and are also in quite close proximity to the expected fiducial volume within the AV. The belly plates can be found at the equator of the AV, which are thicker regions of the AV, where the Hu ropes attach. These are shown in yellow in figure B.1.

$^{214}\text{Bi}$  is another radioactive element found in the ropes and throughout the detector. It may undergo  $\beta$  decay emitting low energy 1.7MeV  $\gamma$ 's ( $^{214}\text{Bi}$  can also emit  $>2.2\text{MeV}$   $\gamma$ 's in  $\sim 7\%$  of decays), but due to their smaller contribution, cuts were chosen generally to capture  $^{208}\text{Tl}$  events.

$^{208}\text{Tl}$  and  $^{214}\text{Bi}$  can be found throughout the detector. In these following sections, comparisons were made between data and backgrounds generated at their expected rates in simulation. These expected background sources and rates assumed in simulations (prior to the results of this analysis) are summarised in table B.1.

Table B.1: Table summarising the expected decay rates (events per year) occurring in each background source [210]

Background Source	$^{208}\text{Tl}$	$^{214}\text{Bi}$
Hold-down ropes	$1.84 \times 10^6$	$3.22 \times 10^6$
Hold-up ropes	$2.28 \times 10^5$	$3.99 \times 10^5$
Internal water	$1.46 \times 10^5$	$1.24 \times 10^7$
AV	$1.5 \times 10^6$	$1.28 \times 10^7$
External water	$1.96 \times 10^6$	$4.62 \times 10^7$

### B.2.1 Positional and Energy Cuts

Table B.2 summarises the analysis cuts applied to data used isolate rope events in the detector, while the sketch in figure B.2 shows the positional cuts applied with respect to the Hd ropes. Care was taken specifically with the radial cuts, as to not cross over with analyses on the internal and external background rates [91].

**Energy Cuts** Excluding the energy and z-position cut, the thresholds shown in table B.2 have been applied in all following plots of data and simulations shown in this chapter. Figure B.11 shows the simulated reconstructed energy spectrum for  $^{208}\text{Tl}$  and  $^{214}\text{Bi}$  events in the ropes. It can be seen that the chosen energy cuts capture the tail of the energy distribution, predominantly due to  $\gamma$ s from  $^{208}\text{Tl}$ . Lower energy cuts were excluded due to the contamination and instrumental effects arising for low energy events, approaching the detector trigger threshold in the water phase. For the repeated solar, nucleon decay and background analyses carried out in the 2018-19 data, a blinding scheme was applied to the dataset. A maximum energy cut of 5MeV was enforced on all water to minimise the biasing of results.

Only events with  $\vec{u} \cdot \vec{r} > 0$  were allowed in order to avoid background contamination originating from the PMTs themselves. The events originating from the PMTs have been studied separately to this analysis [55][91] and were found to produce events with strongly inward pointing events, towards the centre of the AV (negative  $\vec{u} \cdot \vec{r}$ ).

The motivation for the  $\vec{u} \cdot \vec{r}$  cut used is displayed in figure B.3. The plots demonstrate  $\vec{u} \cdot \vec{r}$  distribution shapes (applying all cuts in table B.2 except for  $\vec{u} \cdot \vec{r} > 0$ ) applied to water data and simulations. The data was taken over 23 days of water data in October-November

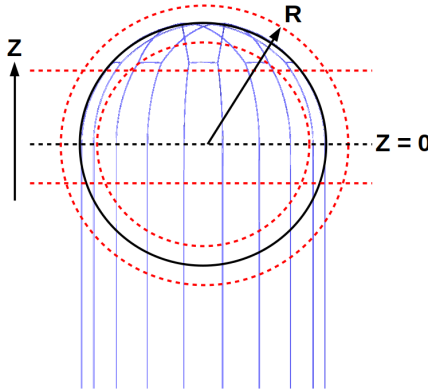


Figure B.2: Sketched side-on view of AV (black) and Hd ropes (blue). The black horizontal dashed line indicates the z-level of AV’s equator. Horizontal and circular red dashed lines indicate the z and r cuts respectively, taken from table B.2

Table B.2: Summary of analysis cuts and masks applied to data and simulation.

Parameter	Min	Max
r (m)	5.7	6.3
z (m)	-1.5	3.5
Energy (MeV)	3.1	5
ITR	0.55	-
$\beta_{14}$	-0.12	0.95
$\vec{u} \cdot \vec{r}$	0	-
waterFit	True	
FitValid	True	
Data cleaning mask (runs 200220-200386)	0xDB0000007FFE	
Data cleaning mask (all other runs)	0xFB0000017FFE	

2018 (runs 200004 to 207718) and MC simulated data of  $^{208}\text{Tl}$  events generated in the ropes (where the rate is arbitrarily large). Immediately noticeable when comparing these data, is the large number of inward facing, negative  $\vec{u} \cdot \vec{r}$  events in data, suggesting large contamination by PMTs, backgrounds originating from the PSUP region.

As mentioned, the PMTs backgrounds have been studied extensively and are known to produce events with events with negative  $\vec{u} \cdot \vec{r}$ . Taking only positive  $\vec{u} \cdot \vec{r}$  events minimised PMT contamination and doesn’t largely affect rope event signal efficiency (the majority of which have positive  $\vec{u} \cdot \vec{r}$ ).

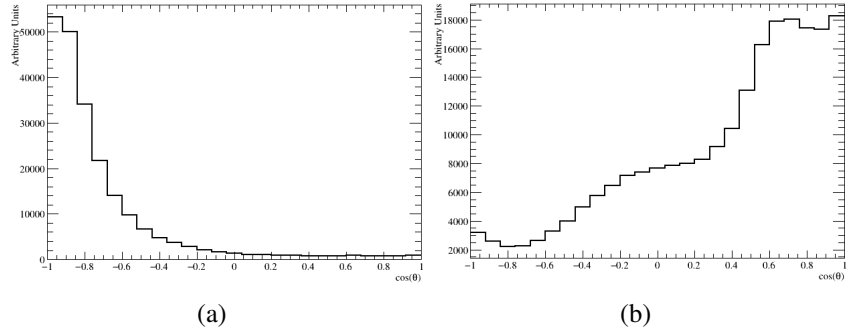


Figure B.3:  $\vec{u} \cdot \vec{r}$  distributions with all cuts applied except for  $\vec{u} \cdot \vec{r} > 0$  for (a) data (b) simulated data of  $^{208}\text{Tl}$  events generated in the Hd ropes.

**Expected Rope Positions** There are 20 Hold-down ropes around the AV, with each adjacent rope expected to be separated by  $18^\circ$  in azimuthal angle  $\phi$  (figure B.4). Hu ropes can be found in between every second pair of Hd ropes. Although Hu ropes are made of the same material as the Hd ropes, their expected rates are about an order of magnitude lower than for the Hd ropes, due to the Hu ropes being thinner. The parent radionuclides in the U and Th chains have sufficiently long half-lives, that the relative ages of the Hd and Hu ropes (the Hd ropes being installed more recently) weren't expected to factor into their relative background rates.

Due to their close proximity, in this analysis the Hd and Hu ropes are generally treated as one entity, where it was their combined contribution that was measured.

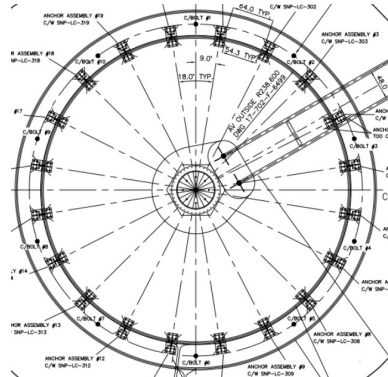


Figure B.4: Top-down view of AV with Hd ropes positions marked with X's, adjacent ropes are separated by  $18^\circ$  in angle  $\phi$ . The labels shown in the diagram are of no significance to this analysis.

**Peaks in azimuthal angle  $\phi$  due to ropes** Figure B.5 demonstrates histograms of azimuthal angle  $\phi$  from reconstructed position, simulating  $^{208}\text{Tl}$  and  $^{214}\text{Bi}$  events in only

the ropes. Peaks can be found occurring at the expected positions of the ropes which are marked in red, every  $18^\circ$ .

While these peaks are visible in  $\phi$  at the expected rope positions, when actual data is considered these small peaks due to the ropes become heavily obscured by the other high rate backgrounds in the shared region, originating from the AV, internal and external water.

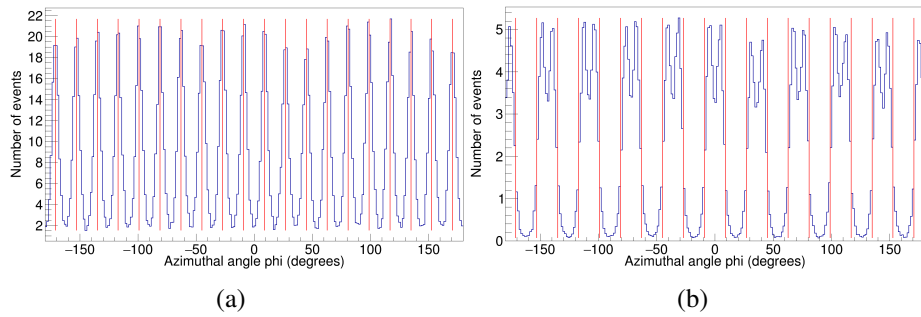


Figure B.5: Histograms (blue) of  $\phi$  using reconstructed events generated in simulation, applying cuts in table B.2. Histograms were scaled to a livetime of 22 days at the expected rope rates in table B.1. (a) Hd ropes only (b) Hu ropes only. Hu ropes are located between every second pair of ropes (see figure B.1), so peaks due to Hu ropes can be found in between Hd rope expected positions marked in red. No error bars shown here for clarity.

## B.2.2 The Stacking Method

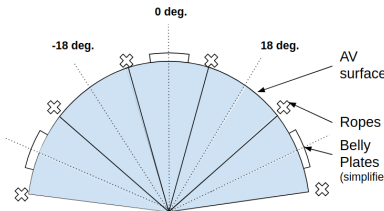


Figure B.6: A simplified, not-to-scale top-down view of a portion of the detector around the equator of the AV. The Hd rope positions marked with X's, while the belly plates represented by white boxes on the surface of the AV (in reality their shape is more complex).

In order to isolate the peaks formed due to the ropes from the rest of the backgrounds, the "stacking" method was introduced. Referring to figure B.4, ropes are expected to be found every  $18^\circ$  (Hd rope at  $9, 27, 45^\circ$  etc.). In order to take advantage of the rope's unique symmetry, events found in  $18^\circ$  segments were summed together. Instead of plotting in  $\phi$  from  $-180$  to  $180^\circ$ , events were plotted in the range  $0$  to  $18^\circ$  (with a peak

expected the centre due to the rope at  $9^\circ$ ). Every event found in all other  $18^\circ$  segments, was shifted to the 0 to  $18^\circ$  segment (figure B.6 can be used for reference).

A total summed peak was expected, centred around  $9^\circ$ , made up of events originating from all the ropes around the AV. The same simulations of the Hd and Hu ropes in figure B.5 was used to produce the histograms in figure B.7, both plots utilising the stacking method.

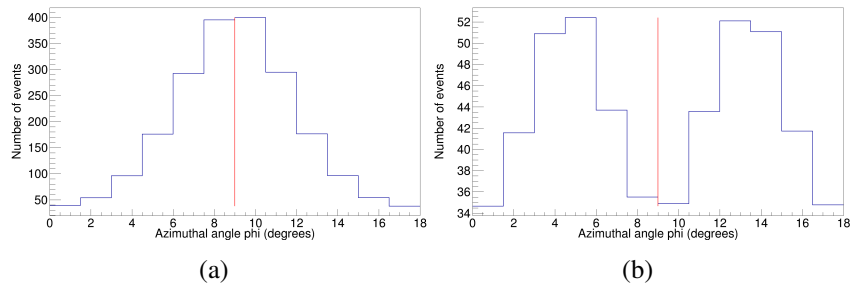


Figure B.7: Total summed peaks in  $\phi$  using MC simulated data, due to a) Hd ropes only b) Hu ropes only. Hd ropes expected position are marked in red. Histograms were scaled to a livetime of 22 days at the expected rope rates in table B.1.

Figure B.7(a) shows a single well-defined peak is formed, centred around  $9^\circ$  (marked in red), as expected for the Hd ropes. The contributions due to each set of ropes at their expected background rates combine together to form a slightly wider peak than that formed due to the Hd ropes alone.

### B.2.2.1 Approach to Non-rope Backgrounds

Of all the background sources in the region of the AV, it was expected that only the ropes have a clear positional symmetry in azimuthal angle  $\phi$ . Applying this stacking method to isotropic sources or in regions away from the ropes was expected to yield a flat distribution in  $\phi$ . It was expected then that applying the stacking method on all backgrounds in the region of the ropes, any peak seen in  $\phi$  was expected to be made up solely of events that originate from the ropes. Any events originating from non-rope background sources were expected to be found below the baseline on which the peak sits.

The number of events making up the peak formed in stacked  $\phi$  could then be compared in data and simulated data, generated at the expected background rates. The peak integral was calculated by removing all events below a baseline on which the peak sits (figure

B.8). The baseline was found by calculating an average bin height of the expected minimum bins, expected to be at  $0^\circ$  and  $18^\circ$ . Two bins were chosen on either side to calculate the baseline height, to allow for the statistical fluctuation of the underlying non-rope background flat distribution in  $\phi$ . The peak integral expression used was:

$$A_{\text{peak}} = X - \frac{n}{2} \left( \frac{M_1 + M_2}{2} + \frac{M_{N-1} + M_N}{2} \right), \quad (\text{B.1})$$

where  $N$  is the total number of bins across  $\phi$ ,  $n$  is the number of bins across which the integral is calculated,  $M_i$  is the number of events in bin  $i \in N$  and  $X$  is the sum of total events in  $n$  bins.

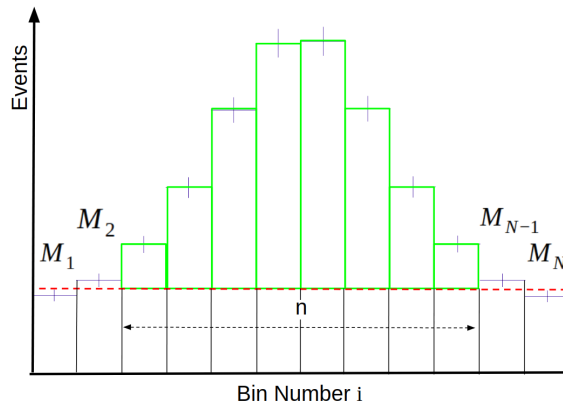


Figure B.8: Demonstration of the peak integral calculated using bins marked in green, with the baseline marked with a dashed red line. The baseline was calculated from bins labelled  $M_i$ .

Considering a general linear function of bin contents  $N_n f(N_n)$ , an approximation of the standard deviation of  $f(N_n)$  is:

$$\sigma_{f(N_n)} = \sqrt{\left(\frac{\partial f}{\partial N_1}\right)^2 \sigma(N_1)^2 + \left(\frac{\partial f}{\partial N_2}\right)^2 \sigma(N_2)^2 + \dots + \left(\frac{\partial f}{\partial N_n}\right)^2 \sigma(N_n)^2}. \quad (\text{B.2})$$

Inserting statistical uncertainty for each bin into the peak integral expression above, the peak integral standard deviation is:

$$\sigma_A = \sqrt{X - \left(\frac{n}{2}\right)^2 \left( \frac{M_1 + M_2}{2^2} + \frac{M_{N-1} + M_N}{2^2} \right)}. \quad (\text{B.3})$$

**Rope events contained in the peak** Figure B.9 demonstrates the ability to isolate rope events assuming nominal background rates. Plot B.9(a) shows a stacked peak in  $\phi$  for

simulated data of only Hd and Hu rope background decays, at expected rates over the stated livetime (section B.1). Plot B.9(b) shows  $^{208}\text{Tl}$  and  $^{214}\text{Bi}$  events in the internal water, AV and external water, generated alongside the Hd and Hu rope  $^{208}\text{Tl}$  and  $^{214}\text{Bi}$  events, all reflecting their expected rates. The peak integrals calculated for figures B.9(a) and B.9(b) were calculated as  $13670 \pm 154$  and  $13888 \pm 348$  respectively, showing agreement within statistical uncertainty (equation B.3). It can be seen in the comparison that the uncertainty of the peak shape increases as the number of non-rope events increases, as expected.

Figure B.9(c) shows simulations of the stacking method applied to rope and non-rope backgrounds, plotted together on the same plot. The baseline of each background source was subtracted away for the demonstration of each background's relative strength of symmetry in  $\phi$ . Notable also from this plot are the small, yet distinct contributions in stacked  $\phi$  of  $^{208}\text{Tl}$  and  $^{214}\text{Bi}$  events originating from the external water. The low background rates of the non-rope backgrounds allowed for minimal contamination of the rope signal. Despite this, their small impact to the rope peak was measured and accounted for in simulation, as discussed in the following section.

**Note on the External Water Symmetry** A small symmetry in  $\phi$  was observed for the external water. It was found that this symmetry was no longer observed in simulation when the reflectivity of the ropes was set to zero. Simulating the ropes with a highly reflective surface caused an excess of external water events located near the region of the ropes, to be reconstructed at the rope positions, due to these light reflections [91]. While the rope reflectivity assumed in simulation had only been measured ex-situ prior to their installation, the impact of the external water symmetry will be shown to be small (table B.4).

### B.2.3 Constraining the Non-rope Backgrounds

Measurements of the AV, internal and external water were carried out in order to constrain their contribution in the region of the ropes fiducial volume. Again, the constraints applied in this ropes analysis were made using measurements from regions outside of the

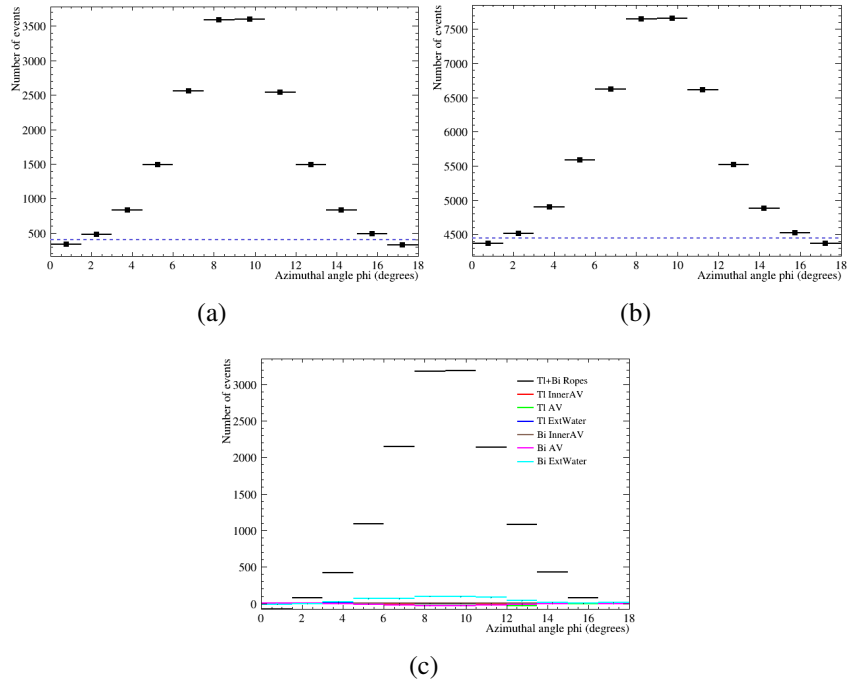


Figure B.9: Simulated Data, stacking in  $\phi$  of  $^{208}\text{Tl}$  and  $^{214}\text{Bi}$  events, applying a minimum energy cut of 3.1MeV, generated in (a) Hd and Hu ropes (b) internal water, AV, external water and Hd and Hu ropes. Error bars reflect statistical uncertainty. Plot (c) shows ropes and all the non-rope backgrounds, each of their contributions shown separately (baseline subtracted away for each source individually).

volumes used in the dedicated internal and external background analyses referenced previously in [55] and [62]. Impacts of the uncertainties in non-rope background rates were found to minimally impact the rope peak shape and integral, shown later in the chapter.

Table B.3 summarises the constraint factors applied to the expected rates summarised previously in table B.1. Each of the non-rope backgrounds constraints were treated/calculated as follows:

**Internal water** The data shown in this work was a period with very low background rates. Simulations in figure B.9(c) showed that events originating in the internal water contribute negligible symmetry to the stacked  $\phi$  plots. Due to the lack of impact, the internal water was assumed at the expected rate in table B.1, measured from earlier periods of data in the water phase.

**External water** The external water background contamination was measured through periodic sampling of the external water in ex-situ assays [79]. The contamination was calculated from the background counts measured in the sample due to  $^{222}\text{Rn}$  contamination in the sample. These measurements yielded larger uncertainties compared to the aforementioned in-situ external water analyses, but served as a practical, independent assessment and constraint for the ropes analysis. The assays yielded fraction-of-expectation factors 5.6% and 55% for  $^{208}\text{Tl}$  and  $^{214}\text{Bi}$  respectively in the external water.

**AV** The AV shares the same region in space as the ropes and contains significant levels of radioactivity (table B.1). In order to independently measure the AV background rates, a fiducial volume away from the ropes was considered, replacing the z-position cuts in table B.2 with  $-6 < z < -4\text{m}$ . In this region, only the internal, external water and the AV were expected to contribute. The AV's  $^{208}\text{Tl}$  and  $^{214}\text{Bi}$  contributions were calculated through a simple event count in the described region at the bottom of the detector, where the assumed internal and external water rates had the aforementioned constraints applied to them. The event count yielded a factor 75% of expectation for the total  $^{208}\text{Tl}$  and  $^{214}\text{Bi}$  due to the AV. It is known that the AV isn't completely featureless at the bottom of the detector (NCD anchors and the bubbler block are present for example), but these features were not expected to significantly impact the evaluation of the AV constraint, which in turn, only weakly impacts the rope rate evaluation.

Table B.3: Measured AV constraints, calculated using the independent constraints found in the internals and externals analyses.

	Fraction of nominal rate	
Background	$^{208}\text{Tl}$	$^{214}\text{Bi}$
Internal water	1x	1x
AV	0.75x	0.75x
External water	0.056x	0.55x

## B.2.4 Results

Figure B.13 shows plots of the stacking method applied to the data and simulated data, applying a minimum energy threshold of 3.1MeV. Simulations assumed the rates shown

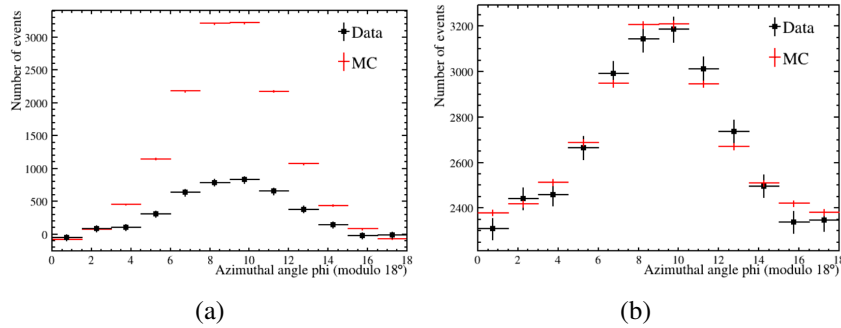


Figure B.10: Stacked  $\phi$  events for data and simulation, applying  $E_{\min}=3.1\text{MeV}$ , including the backgrounds and rates shown in table B.1 and constraints applied from table B.3. (a) Data and simulation with baselines subtracted, and (b) the simulated peak was placed at the data baseline, then scaled to the data peak integral.

in table B.1 and constraints applied from table B.3. The peak baseline for data and simulation were both calculated, where the simulated peak baseline was placed at the data baseline position in plot B.10(b). The peak integrals in data and MC were then calculated. It was found that the simulated peak integral was larger than that predicted in simulation. Plot B.10(a) shows the data and MC at expected background rates, while plot B.10(b) shows the simulated peak scaled to the data peak integral. It can be seen that the shape of the peaks agree well in the normalised case.

The shape agreement between data and simulation put a greater degree of confidence in that events in the peak were indeed made up of events originating from  $^{208}\text{Tl}$  and  $^{214}\text{Bi}$  decays in the region of the ropes.

The plots also highlight the difference in the peak integral value in simulation and data. At the  $E_{\min}$  cut for the plots shown in both figures ( $E_{\min} = 3.1\text{MeV}$ ), the peak integral from data was  $0.27 \pm 0.02_{\text{stat}}$  times that predicted in MC. This would suggest that the actual rope background rate is approximately 4 times lower than expectation, which were decided mainly by measurements carried out prior to the installation of the Hd ropes. The next section discusses the calculation of the systematic uncertainty in the presented rope contamination measurement.

## B.2.5 Calculation of Systematic Uncertainties

The sources of systematic uncertainty considered were:

- Energy scale and resolution uncertainties
- Positional reconstruction shift and resolution uncertainties
- $\beta_{14}$  shift uncertainty
- Directional  $\vec{u}.\vec{r}$  shift uncertainty
- Internal, external water and AV constraints

The impact of each of the above systematics was measured by shifting/smearing/scaling (the precise methods used upcoming) each parameter in simulated data, then measuring the resultant impact to the final relative rope peak integral compared to that seen in data. Table B.4 summarises the systematic types and values used in the rope contamination uncertainty calculation.

**Energy Scale and Resolution** Uncertainties in the energy scale were accounted for by linearly scaling all the reconstructed event energies with the upper and lower limits of the energy scale uncertainty. Following this, the rope contamination in data was recalculated.

To account for uncertainties in reconstructed energy resolution, events in simulated data were smeared using normal distribution of zero mean and standard deviation  $\sigma = \sigma_E * \sqrt{(1 + \delta)^2 - 1^2}$ , where  $\sigma_E = \sqrt{E}$  and  $\delta$  is the largest of the upper and lower uncertainties of the energy resolution. The uncertainty values used in this analysis were calculated using the  $^{16}\text{N}$  calibration, deployed both internally and external to the AV.

Energy scaling had the largest impact to the ropes analysis, as the energy cuts in the ropes analysis captured events in the tail of the  $^{208}\text{Tl}$  energy distribution. Its impact was heightened due to the energy blinding cut applied at 5MeV. Calculation of uncertainties in energy scale were carried out for both the internal water, away from the AV, as well as the external water, up to  $r = 7.5\text{m}$  [211]. Since the ropes region defined in table B.2, encompassed regions inside and out of the AV, conservatively, the energy scaling systematic values for the external water were assumed for all events passing the rope analysis cuts. The energy resolution uncertainty had far less impact on the measured result. Its value was assumed from previous energy calibrations for the AV region, carried out in water data prior to the data range shown in this work [91].

**Positional Shift and Resolution** Uncertainties in position reconstruction were dealt with in a similar fashion as energy. The ropes analysis was highly dependent on position resolution, the next largest systematic, as fine resolution was required for the separation events excesses surrounding rope positions. Events were smeared with a normal distribution of zero mean and standard deviation  $\sigma$ . For event position biases, simulated events were each shifted by a shift uncertainty. The ropes analysis relied heavily on periodic positioning of the ropes around the AV, so positional systematics were applied separately on each x, y and z coordinate. The uncertainties in position were again adapted from previously made calculations for the external water background analysis, as presented in Ref. [62] and [55]. The uncertainties calculated for the external water region was applied to all events in the ropes analysis.

**Directional Uncertainties** Uncertainties in the directionality of water events were also accounted for. This were implements in simple shifts of parameters  $\beta_{14}$  and  $\vec{u} \cdot \vec{r}$ . Again, these uncertainty shifts were adopted assuming the same values calculated for the external water background analysis, measuring water data recorded in 2017 and 2018.

**Constraint Uncertainties** The constraints determined in section B.2.3 were determined with large uncertainties associated with them. Regardless, the nature of the stacking method for rope event isolation was expected to be minimally impacted by these uncertainties. The determined rope result was recalculated, applying an uncertainty of  $\pm 100\%$  (i.e. zero or two times the constraints in table B.3) for the AV, internal and external water, without much impact seen.

Table B.4 summarises the change to the measured data/simulation fraction of expectation rope rate for each of the systematic uncertainties considered. Apparent are the dominating impacts that energy scaling and positional resolution have of the measured rope rate. Assuming independence between the considered reconstructed parameters, uncertainties were summed in quadrature for a total uncertainty in the measured rope rate. The data/simulation fraction of expectation for  $E_{\min}=3.1\text{MeV}$  was  $0.27 \pm 0.02_{\text{stat}} \pm 0.13_{\text{sys}}$ .

Table B.4: Summary of the systematics and the fractional change to the determined data/simulation measured rope rate. Applying  $E_{\min}=3.1\text{MeV}$ .

Systematic	Value	Change (%)
Energy Scaling	+9.4/-9.4%	-25.4/+30.2
Energy Smearing	0.145%	+0.3
x-pos smear	19.4cm	+12.9
y-pos smear	19.4cm	+12.9
z-pos smear	19.4cm	+12.8
x-pos shift	+12.1/-6cm	+3.2/-0.8
y-pos shift	+12.1/-6cm	+3.1/-1.0
z-pos shift	+12.1/-6cm	+1.1/-1.2
$\beta_{14}$ shift	+0.0042/-0.035	+0.3/0.1
$\vec{u} \cdot \vec{r}$ shift	+0.08/-0.13	+1.8/-5.4
AV constraint	+100%/-100%	+1.4/-1.5
Internal water constraint	+100%/-100%	-0.01/+0.01
External water constraint	+100%/-100%	-3.5/+3.4

### B.2.5.1 Further checks of stacking method in data

**Energy Analysis** Beyond the shape agreement in stacked  $\phi$  peak found in data and simulation, it was also possible through an energy analysis to test that the peak integral in data was truly capturing rope events. If the method was effective, regardless of the decay rate, the energy distribution of the events found in the stacked  $\phi$  peak of data taken should have reflected the same shape as the energy spectrum of  $^{208}\text{Tl}$  and  $^{214}\text{Bi}$  rope events generated in MC simulated data, shown in figure B.11.

It was not possible however to isolate rope events and plot their energy distribution, as they were measured as a surplus of events in  $\phi$  on top of a flat background distribution. An alternate approach was required. The stacking method assumed that the events contained within the peak in stacked  $\phi$  are indeed  $^{208}\text{Tl}$  and  $^{214}\text{Bi}$  events rope events. Assuming this, the stacked  $\phi$  peak integral should decrease in magnitude vs  $E_{\min}$  in the same manner that  $^{208}\text{Tl}$  and  $^{214}\text{Bi}$  rope events decrease in number vs  $E_{\min}$  in simulation. It was expected then that the data/simulation stacked  $\phi$  peak integral ratio would remain constant vs the minimum energy cut.

This assumption however relies on small systematic uncertainties in energy scaling between data and simulation, which is not necessarily the case (table B.4). Regardless, the

peak integral ratio as a function of  $E_{\min}$  is shown in figure B.12. It can be seen that a flat distribution of the data/simulation ratio vs  $E_{\min}$  is consistent within the combined statistical and systematic uncertainties, in the given energy range. A small trend can be seen within uncertainty of a larger overestimation of the rope rate in simulation can be seen at higher energies, this could be due to energy scaling uncertainties, or event contamination at lower energies. Allowing low energy events yields contamination from low energy radiation due to other nuclei in U and Th chains, along with non-physical instrumental events. Considering lower  $E_{\min}$  values, the ratio was found to increase. For example, applying a lower  $E_{\min}$  value of 2.5MeV yielded a data/simulation peak ratio of  $0.32 \pm 0.02_{\text{stat}}$  was measured, suggesting an influx of radiation from the ropes due to contaminants other than  $^{208}\text{Tl}$  and  $^{214}\text{Bi}$ , not considered in simulation. It was found that for higher values of  $E_{\min}$ , statistics for rope events became too limited. Figure B.13(g) shows the normalised stacked  $\phi$  plots in data and simulation (normalised to the data rate), it can be seen that clear peaks with good agreement in shape can be seen for all the considered  $E_{\min}$ .

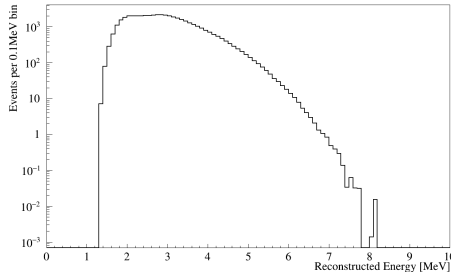


Figure B.11: Energy spectrum of  $^{208}\text{Tl}$  and  $^{214}\text{Bi}$  event generated in the Hd and Hu ropes, generated in simulation (normalised to their respective expected rates, table B.1).

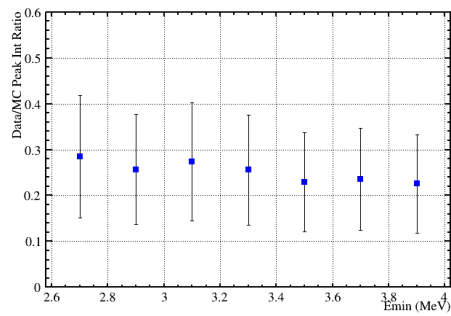


Figure B.12: Data/simulation peak integral ratio vs  $E_{\min}$ . The distribution appears consistent with the expected flat distribution within uncertainty. The expected rope contamination was  $\sim 3\text{-}4\times$  higher than what is measured in data for all the  $E_{\min}$  shown.

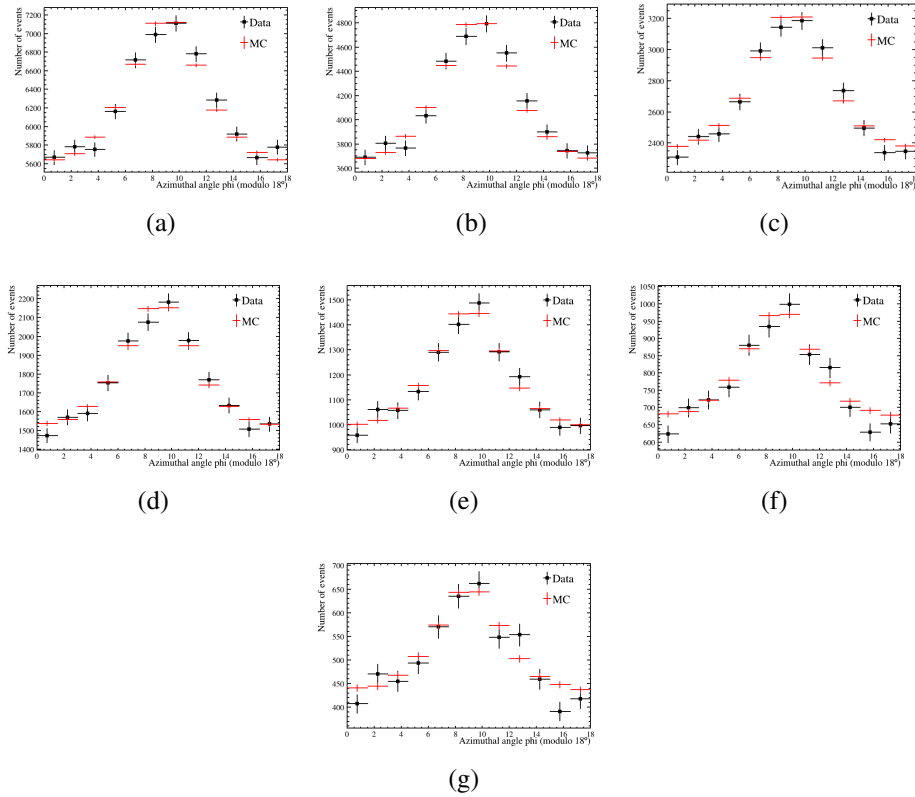


Figure B.13: Stacked  $\phi$  events for data and simulation, where the simulated peak was placed at the data baseline, then scaled to the data peak integral.  $E_{\min}$  for the plots are in order, sharing the same  $E_{\min}$  as those in figure B.12

**Regions Away from the Ropes** To test the method further, the same treatment of data was applied in regions of the detector away from where rope events contribute. The same region used to constrain the AV contribution,  $-6 < z < -4m$ , was used for this test. This region regards the bottom of the detector, void of the ropes and belly plates. One would therefore expect no prominent peak to be formed in stacked  $\phi$  here.

Figure B.14 shows stacked azimuthal angle plots calculated from data taken at the bottom of the detector. It can be seen that the stacking method applied in this region, does not yield a clear and distinct peak in  $\phi$ .

**Dividing the Detector into Segments** There was the possibility that a peak stacked  $\phi$  was instead made up some particularly high background rate localised region in the detector, producing an apparent rope signal in  $\phi$ . This peak when viewed as a total stacked  $\phi$  plot, summing all events around the whole detector, could easily be mistaken

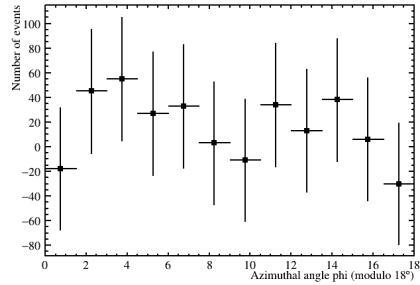


Figure B.14: Stacking in  $\phi$  for data, around the bottom hemisphere region of the detector applying positional cuts  $-6 < z < -4\text{m}$ .

as being rope events.

Another method used was splitting up stacked  $\phi$  plots into segments in quadrants of  $\phi$ . The expectation was that if the peak in stacked  $\phi$  is made up of rope background events, one would therefore expect approximately equal contributions from each of the ropes around the detector.

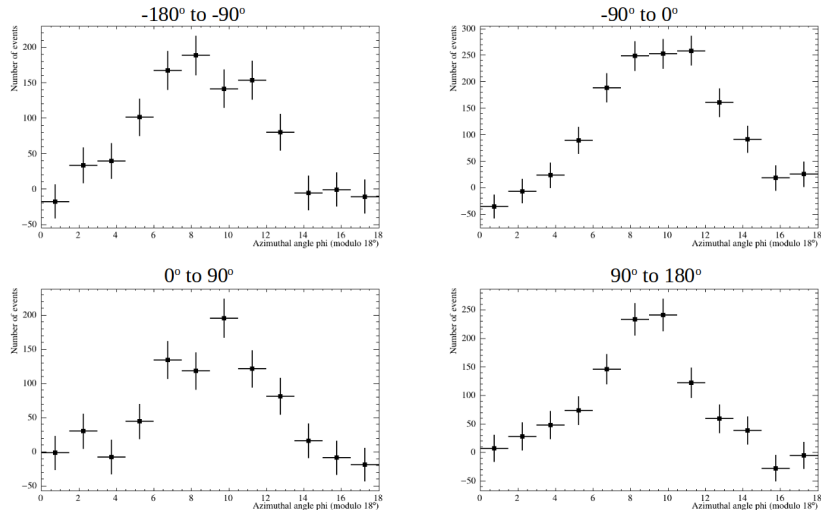


Figure B.15: Stacking in  $\phi$  again defined by cuts in table B.2,  $E_{\min} = 3.1\text{MeV}$ , where events are limited to  $90^\circ$  segments around the detector. The baseline was calculated and subtracted for each quadrant peak.

Figure B.15 shows stacked  $\phi$  plots, where stacking was limited to events within  $90^\circ$  quadrants. It can be seen that each  $\phi$  quadrant shows peaks of roughly equal sizes. This demonstrates that the events contained in the total stacked  $\phi$  peak, originate from positions isotropic around the detector, consistent for rope events.

### B.2.6 Conclusion

The stacking method and its effectiveness in isolating radiation from the ropes in SNO+ has now been demonstrated. The method allowed for an independent measurement of the ropes, without requiring input from the separate water analyses for the internal and external water. This allowed the measured rope rate to be used as a constraint on the ropes in those separate analyses, leading to an eventual comprehensive measure of the background rates from all the contributing components in SNO+ over the water phase. The in-situ measurement also revealed that there was an overestimation using the previously assumed rope rates, determined in ex-situ measurements prior to their installation in SNO+. The stacking method measured a rope rate was found to be  $0.27 \pm 0.02_{\text{stat}} \pm 0.13_{\text{sys}}$  times the rate previously assumed in table B.1. The updated measured rope rate will be used as constraints in updated the solar and nucleon decay analyses, which will regard the same water data as has been shown here. This measured rope rate will also be used as input rates for future physics analyses occurring in the pure and Te-loaded scintillator phases. This rope rate method has since been repeated in the partial scintillator phase, where due to the improved light yield, the low energy contributions from  $^{40}\text{K}$  in the ropes have become measurable. The  $^{40}\text{K}$  rate has been measured similarly as  $\sim 20\%$  of the expected rate, derived from the same ex-situ measurements on the ropes prior to their installation [212].

## C | Reactor Core Information

Table C.1: Summary of the thermal powers and distances for each of the nuclear reactors within a 1000km radius from SNO+. Information were taken from the publicised nuclear reactor information tables [127].

Reactor Name	Type	No. Cores	Avg. Core Thermal Power (MW)	Distance (km)
Bruce	PHWR	8	2232	240.8
Pickering	PHWR	6	1522	340.43
Darlington	PHWR	4	1810	349.17
Ginna	PWR	1	1806	469.5
Nine Mile Point	BWR	2	2747	500.03
Fitzpatrick	BWR	1	2620	500.6
Perry	BWR	1	3171	519.24
Fermi	BWR	1	3530	527.36
Point Beach	PWR	2	1744	552.26
Davis Besse	PWR	1	2819	562.53
Palisades	PWR	1	2499	615.01
Beaver Valley	PWR	2	2824	652.71
Cook	PWR	2	2842	657.77
Prairie Island	PWR	2	1682	682.8
Susquehanna	BWR	2	3763	722.69
Three Mile Island	PWR	1	1935	789.61
Dresden	BWR	2	2874	799.9
Byron	PWR	2	3637	807.78
Braidwood	PWR	2	3582	809.06
Indian Point	PWR	2	3025	819.86
Limerick	BWR	2	3429	829.28
LaSalle	BWR	2	3451	834.26
Peachbottom	BWR	2	3826	846.11
Quadcities	BWR	2	2869	898.24
Hope Creek	BWR	1	3281	904
Salem	PWR	2	3055	904.45
Seabrook	PWR	1	3647	910.05
Millstone	PWR	2	2926	923.41
Clinton	BWR	1	3134	932.84
Duane Arnold	BWR	1	1902	971.72
Calvert Cliffs	PWR	2	2704	973.8
North Anna	PWR	2	2718	974.73
Pilgrim	BWR	1	487	984.74
Monticello	BWR	1	1809	987.48

## D | IBD Cross Section

This appendix describes the IBD cross section used in the calculation of the expected reactor and geoneutrino signal at SNO+, referenced in chapter 5.

Figure 5.3 shows the tree-level Feynman diagram of the IBD interaction. The IBD matrix element for reactor antineutrinos (<10MeV) can be calculated within the Fermi theory:

$$\mathcal{M} = \frac{G_F \cos \theta_C}{\sqrt{2}} [\bar{v}_{\bar{\nu}_e} \gamma_\mu (1 - \gamma_5) v_e] [\bar{u}_n (V^\mu + A^\mu) u_p], \quad (\text{D.1})$$

where  $G_F$  is the Fermi coupling constant,  $\theta_C$  is the Cabibbo angle.  $\bar{v}_{\bar{\nu}_e}$ ,  $v_e$ ,  $\bar{u}_n$  and  $u_p$  are the Dirac spinors for the electron antineutrino, positron, neutron and proton respectively. The first square brackets represents the leptonic current and the second is the hadronic current, where  $V^\mu$  and  $A^\mu$  are the vector and axial-vector components parts of the hadronic weak interaction in the SM.

The IBD cross section used in the antineutrino analysis was calculated using Ref. [131] which treated nucleons as having infinite mass in the reactor energy regime:

$$\mathcal{M} = \frac{G_F \cos \theta_C}{\sqrt{2}} [\bar{v}_{\bar{\nu}_e} \gamma_\mu (1 - \gamma_5) v_e] [\bar{u}_n (\gamma^\mu f - \gamma^\mu \gamma^5 g - \frac{i f_2}{2M} \sigma^{\mu\nu} q_\nu) u_p]. \quad (\text{D.2})$$

The hadronic components were parameterised in terms of vector and axial vector coupling constants  $f = 1$  and  $g = 1.26$  respectively.  $f_2$  represents the anomalous nucleon isovector magnetic moment, taken to be 3.706. In this energy regime also, the coupling constants were assumed not to vary with momentum transfer  $q^2$ .

Defining the Mandelstam variables as:

$$\begin{aligned} s &= (p_{\bar{\nu}} + p_p)^2 = M_p^2 + 2M_p E_{\bar{\nu}} \\ t &= (p_{\bar{\nu}} - p_e)^2 = M_n^2 - M_p^2 - M_p(E_{\bar{\nu}} - E_e) \\ u &= (p_{\bar{\nu}} - p_n)^2 = M_p^2 + m_e^2 - 2M_p E_e. \end{aligned} \quad (\text{D.3})$$

The momentum transfer  $q^2$  can be written in terms of the positron and antineutrino energies, where  $\theta$  is the angle between the incoming antineutrino and outgoing positron in

the lab frame:

$$q^2 = t = m_e^2 - 2E_{\bar{\nu}}E_e(1 - v_e \cos \theta). \quad (\text{D.4})$$

The differential cross section in momentum transfer, accounting for an inner nucleon radiative correction  $\Delta_{\text{inner}}^R$  (taken to be = 0.024), can be written as:

$$\frac{d\sigma}{dq^2} = \frac{|\mathcal{M}|^2}{\pi(2M_p E_{\bar{\nu}})}(1 + \Delta_{\text{inner}}^R). \quad (\text{D.5})$$

The differential cross section in  $\cos \theta$  can be calculated with the Jacobian  $dq^2/d\cos\theta = 2E_{\bar{\nu}}p_e$ , using  $v_e = p_e/E_e$ . Expanding  $|\mathcal{M}|^2$  and applying the infinite nucleon mass assumption yields:

$$\frac{d\sigma}{d \cos \theta} = \sigma_0[(f^2 + 3g^2) + (f^2 - g^2)v_e \cos \theta]E_e p_e, \quad (\text{D.6})$$

where  $\sigma_0 = G_F^2 \cos \theta_C^{-2} (1 + \Delta_{\text{inner}}^R)/\pi$ . Integrating over  $\cos \theta$  yields the total cross section:

$$\sigma_{\text{tot}} = \sigma_0(f^2 + 3g^2)E_e p_e = 0.0952 \left( \frac{E_e p_e}{1 \text{MeV}^2} \right) \times 10^{-42} \text{ cm}^2. \quad (\text{D.7})$$

This can be related to the  $\beta$ -decay cross section and be rewritten in terms of the neutron lifetime  $\tau_n$ , including a phase space factor  $f_{p.s.}^R = 1.7152$  which includes corrections for Coulomb, weak magnetism, recoil, and outer radiative interactions, but does not include the inner radiative corrections [131]. The cross section below and in eqn. D.6 are used in simulations for the antineutrino analysis presented in this work

$$\sigma_{\text{tot}} = \frac{2\pi^2}{m_e^5 f_{p.s.}^R \tau_n} E_e p_e. \quad (\text{D.8})$$

# Bibliography

- [1] Pauli letter collection: letter to lise meitner. <https://cds.cern.ch/record/83282>.
- [2] The existence of a neutron. *Proceedings of the Royal Society of London. Series A, Containing Papers of a Mathematical and Physical Character*, 136(830), 1932.
- [3] Fred L. Wilson. Fermis theory of beta decay. *American Journal of Physics*, 36(12), 1968.
- [4] David J. Griffiths. *Introduction to elementary particles*. Wiley-VCH, 2020.
- [5] Kan Chang Wang. A suggestion on the detection of the neutrino. *Phys. Rev.*, 61:97–97, Jan 1942.
- [6] C. L. Cowan, F. Reines, F. B. Harrison, H. W. Kruse, and A. D. McGuire. Detection of the free neutrino: A Confirmation. *Science*, 124:103–104, 1956.
- [7] The nobel prize in physics 1957. <https://www.nobelprize.org/prizes/physics/1957/summary/>.
- [8] C. S. Wu, E. Ambler, R. W. Hayward, D. D. Hoppes, and R. P. Hudson. Experimental test of parity conservation in beta decay. *Phys. Rev.*, 105:1413–1415, Feb 1957.
- [9] Richard L. Garwin, Leon M. Lederman, and Marcel Weinrich. Observations of the failure of conservation of parity and charge conjugation in meson decays: the magnetic moment of the free muon. *Phys. Rev.*, 105:1415–1417, Feb 1957.
- [10] Carlo Giunti and Chung Wook. Kim. *Fundamentals of neutrino physics and astrophysics*. Oxford University Press, 2016.
- [11] R. P. Feynman and M. Gell-Mann. Theory of the fermi interaction. *Phys. Rev.*, 109:193–198, Jan 1958.
- [12] E. C. G. Sudarshan and R. E. Marshak. Chirality invariance and the universal fermi interaction. *Phys. Rev.*, 109:1860–1862, Mar 1958.
- [13] J. J. Sakurai. Mass reversal and weak interactions. *Il Nuovo Cimento*, 7(5):649–660, 1958.
- [14] L. D. Landau. On the conservation laws for weak interactions. *Nucl. Phys.*, 3:127–131, 1957.
- [15] T. D. Lee and C. N. Yang. Parity nonconservation and a two-component theory of the neutrino. *Phys. Rev.*, 105:1671–1675, Mar 1957.
- [16] Abdus Salam. Gauge Unification of Fundamental Forces. *Rev. Mod. Phys.*, 52:525–538, 1980.
- [17] M. Goldhaber, L. Grodzins, and A. W. Sunyar. Helicity of neutrinos. *Phys. Rev.*, 109:1015–1017, Feb 1958.
- [18] The nobel prize in physics 1988. <https://www.nobelprize.org/prizes/physics/1988/summary/>.

- [19] K. Kodama et al. Observation of tau neutrino interactions. *Physics Letters B*, 504(3):218–224, 2001.
- [20] B. Pontecorvo. Mesonium and antimesonium. *Journal of Experimental and Theoretical Physics*, 33:429, 1957.
- [21] B. Pontecorvo. Electron and Muon Neutrinos. *Zh. Eksp. Teor. Fiz.*, 37:1751–1757, 1959.
- [22] Sheldon L. Glashow. The renormalizability of vector meson interactions. *Nuclear Physics*, 10:107–117, 1959.
- [23] Abdus Salam and J. C. Ward. Weak and electromagnetic interactions. *Il Nuovo Cimento*, 11(4):568–577, 1959.
- [24] Steven Weinberg. A model of leptons. *Phys. Rev. Lett.*, 19:1264–1266, Nov 1967.
- [25] Robert Oerter. *The theory of almost everything: the standard model, the unsung triumph of modern physics*. Pi Press, 2006.
- [26] John N. Bahcall and Raymond Davis. Solar neutrinos: A scientific puzzle. *Science*, 191(4224):264–267, 1976.
- [27] Takaaki Kajita. Atmospheric neutrinos and discovery of neutrino oscillations. *Proceedings of the Japan Academy, Series B*, 86(4):303–321, 2010.
- [28] D. Casper et al. Measurement of atmospheric neutrino composition with the imb-3 detector. *Phys. Rev. Lett.*, 66:2561–2564, May 1991.
- [29] Y. Fukuda et al. Evidence for oscillation of atmospheric neutrinos. *Phys. Rev. Lett.*, 81:1562–1567, Aug 1998.
- [30] Q. R. Ahmad et al. Direct evidence for neutrino flavor transformation from neutral current interactions in the Sudbury Neutrino Observatory. *Phys. Rev. Lett.*, 89:011301, 2002.
- [31] A. Bellerive, J.R. Klein, A.B. McDonald, A.J. Noble, and A.W.P. Poon. The Sudbury Neutrino Observatory. *Nuclear Physics B*, 908:30–51, 2016. Neutrino Oscillations: Celebrating the Nobel Prize in Physics 2015.
- [32] G.T. Ewan and W.F. Davidson. Physics in canada. 61:339–346, 2005.
- [33] T. Araki et al. Measurement of neutrino oscillation with KamLAND: Evidence of spectral distortion. *Phys. Rev. Lett.*, 94:081801, 2004.
- [34] C. Giunti. No effect of majorana phases in neutrino oscillations. *Physics Letters B*, 686(1):41–43, 2010.
- [35] C. C. Nishi. Simple derivation of general fierz-type identities. *American Journal of Physics*, 73(12):1160–1163, 2005.

- [36] P. Langacker, S.t. Petcov, G. Steigman, and S. Toshev. Implications of the mikheyev-smirnov-wolfenstein (msw) mechanism of amplification of neutrino oscillations in matter. *Nuclear Physics B*, 282:589–609, 1987.
- [37] S Adrián-Martínez et al. Letter of intent for KM3NeT 2.0. *J. Phys. G: Nucl. Part. Phys.*, 43, 2016.
- [38] Bhag C. Chauhan, João Pulido, and E. Torrente-Lujan. KamLAND, solar antineutrinos, and the solar magnetic field. *Physical Review D*, 68(3), 2003.
- [39] Takaaki Kajita. Atmospheric neutrinos. *Advances in High Energy Physics*, 2012:1–24, 2012.
- [40] K. Abe, N. Abgrall, H. Aihara, Y. Ajima, J.B. Albert, D. Allan, P.-A. Amaudruz, C. Andreopoulos, B. Andrieu, M.D. Anerella, et al. The T2K experiment. *Nuclear Instruments and Methods*, 659(1):106–135, Dec 2011.
- [41] Justin Evans. The MINOS Experiment: Results and Prospects. *Adv. High Energy Phys.*, 2013:182537, 2013.
- [42] Jianming Bian. The NOvA Experiment: Overview and Status. In *Meeting of the APS Division of Particles and Fields*, 9 2013.
- [43] K. Abe et al. Hyper-Kamiokande Design Report. 5 2018.
- [44] B. Abi. The DUNE Far Detector Interim Design Report Volume 1: Physics, Technology and Strategies. 2019.
- [45] Jun Cao and Kam-Biu Luk. An overview of the Daya Bay reactor neutrino experiment. *Nuclear Physics B*, 908:62–73, 2016. Neutrino Oscillations: Celebrating the Nobel Prize in Physics 2015.
- [46] C. D. Shin, Z. Atif, G. Bak, J. H. Choi, H. I. Jang, J. S. Jang, S. H. Jeon, K. K. Joo, K. Ju, D. E. Jung, et al. Observation of reactor antineutrino disappearance using delayed neutron capture on hydrogen at reno. *Journal of High Energy Physics*, 2020(4), 2020.
- [47] Double chooz  $\theta_{13}$  measurement via total neutron capture detection. *Nature Physics*, 16(5):558–564, 2020.
- [48] F Perrot. Status and physics potential of the juno experiment. *Journal of Physics: Conference Series*, 1586:012047, 2020.
- [49] Fengpeng An et al. Neutrino Physics with JUNO. *J. Phys. G*, 43(3):030401, 2016.
- [50] Atsuto Suzuki. Antineutrino science in KamLAND. *The European Physical Journal C*, 74(10), 2014.
- [51] K. Eguchi et al. First results from KamLAND: Evidence for reactor anti-neutrino disappearance. *Phys. Rev. Lett.*, 90:021802, 2003.
- [52] S. Abe et al. Precision Measurement of Neutrino Oscillation Parameters with KamLAND. *Phys. Rev. Lett.*, 100:221803, 2008.

- [53] What is a Cleanroom? <https://www.cleanairtechnology.com/cleanroom-classifications-class.php>.
- [54] B. Aharmim et al. Measurement of the cosmic ray and neutrino-induced muon flux at the Sudbury neutrino observatory. *Phys. Rev. D*, 80:012001, Jul 2009.
- [55] SNO+ Collaboration. Measurement of the B8 solar neutrino flux in SNO+ with very low backgrounds. *Physical Review D*, 99(1), 2019.
- [56] V. Albanese et al. The SNO+ Experiment. 4 2021.
- [57] Robert Knapik, Richie Bonventre, and Tim Shokair. SNO+ Electronic Upgrades. *Nuclear Physics B - Proceedings Supplements*, 229-232:523, 2012. Neutrino 2010.
- [58] T. Undagoitia and L. Rauch. Dark matter direct-detection experiments. *arXiv: Instrumentation and Detectors*, 2015.
- [59] J Boger et al. The Sudbury Neutrino Observatory. *Nuclear Instruments and Methods in Physics Research Section A: Accelerators, Spectrometers, Detectors and Associated Equipment*, 449(1-2):172–207, 2000.
- [60] G. Doucas, N. A. Jelley, M. E. Moorhead, N. W. Tanner, S. Gil, L. McGarry, and C. E. Waltham. Light concentrators for the Sudbury Neutrino Observatory. *Nucl. Instrum. Meth. A*, 370:579–596, 1996.
- [61] J Rumleskie and C Virtue. Supernovae and SNO. *Journal of Physics: Conference Series*, 1342:012135, jan 2020.
- [62] SNO+ Collaboration. Search for invisible modes of nucleon decay in water with the SNO+ detector. *Physical Review D*, 99(3), 2019.
- [63] J. V. Jelley. Åerenkov radiation: Its origin, properties and applications. *Contemporary Physics*, 3(1):45–57, 1961.
- [64] Takao Itoh. Fluorescence and phosphorescence from higher excited states of organic molecules. *Chemical Reviews*, 112(8):4541–4568, 2012.
- [65] Delocalized Pi Bonds. <https://lavelle.chem.ucla.edu/forum/viewtopic.php?t=68610>.
- [66] Jonathan Clayden, Nick Greeves, and Stuart G. Warren. *Organic chemistry*. Oxford University Press, 2012.
- [67] David M. Jameson, John C. Croney, and Pierre D.J. Moens. Fluorescence: Basic concepts, practical aspects, and some anecdotes. In *Biophotonics, Part A*, volume 360 of *Methods in Enzymology*, pages 1–43. Academic Press, 2003.
- [68] John Betteley Birks. *The theory and practice of scintillation counting*. Pergamon Press, 1967.

- [69] M. R. Anderson et al. Development, characterisation, and deployment of the SNO+ liquid scintillator. *JINST*, 16(05):P05009, 2021.
- [70] B. von Krosigk. Measurement of proton and  $\alpha$ -particle quenching in LAB based scintillators and determination of spectral sensitivities to supernova neutrinos in the SNO+ detector (2015).
- [71] A. Wright. The Scintillation and Optical Properties of Linear Alkyl Benzene, SNO+ Internal Document 219.
- [72] S.D Biller, N.A Jelley, M.D Thorman, N.P Fox, and T.H Ward. Measurements of photomultiplier single photon counting efficiency for the Sudbury Neutrino Observatory. *Nuclear Instruments and Methods in Physics Research Section A: Accelerators, Spectrometers, Detectors and Associated Equipment*, 432(2-3):364–373, 1999.
- [73] Michael F. L’Annunziata and Michael J. Kessler.  ${}^5$  - liquid scintillation analysis: Principles and practice. In Michael F. L’Annunziata, editor, *Handbook of Radioactivity Analysis (Second Edition)*, pages 347–535. Academic Press, San Diego, second edition edition, 2003.
- [74] Steven Biller and Szymon Manecki. A New Technique to Load  ${}^{130}\text{Te}$  in Liquid Scintillator for Neutrinoless Double Beta Decay Experiments. *Journal of Physics: Conference Series*, 888:012084, 2017.
- [75] T. Kroupová. Improving the Sensitivity to Neutrinoless Double Beta Decay in SNO+ (2020).
- [76] A. Einstein. Über einen die erzeugung und verwandlung des lichtes betreffenden heuristischen gesichtspunkt. *Annalen der Physik*, 322(6):132–148, 1905.
- [77] Tanner Kaptanoglu. Characterization of the hamamatsu 8” r5912-mod photomultiplier tube. *Nuclear Instruments and Methods in Physics Research Section A: Accelerators, Spectrometers, Detectors and Associated Equipment*, 889:69–77, 2018.
- [78] B.a. Moffat, R.j. Ford, F.a. Duncan, K. Graham, A.l. Hallin, C.a.w. Hearns, J. Maneira, P. Skensved, and D.r. Grant. Optical calibration hardware for the sudbury neutrino observatory. *Nuclear Instruments and Methods in Physics Research Section A: Accelerators, Spectrometers, Detectors and Associated Equipment*, 554(1-3):255–265, 2005.
- [79] SNO+ Collaboration. The SNO experiment. *Journal of Instrumentation*, 16(08), 2021.
- [80] M.r. Dragowsky et al. The  ${}^{16}\text{n}$  calibration source for the sudbury neutrino observatory. *Nuclear Instruments and Methods in Physics Research Section A: Accelerators, Spectrometers, Detectors and Associated Equipment*, 481(1-3):284–296, 2002.
- [81] S. Agostinelli et al. Geant4 - a simulation toolkit. *Nuclear Instruments and Methods A*, 506(3), 2003.

- [82] Ianik Plante and Francis A Cucinotta. Cross sections for the interactions of 1eV–100MeV electrons in liquid water and application to Monte-Carlo simulation of HZE radiation tracks. *New Journal of Physics*, 11(6):063047, 2009.
- [83] Steven D. Biller, Edward J. Leming, and Josephine L. Paton. Slow fluors for effective separation of cherenkov light in liquid scintillators. *Nuclear Instruments and Methods in Physics Research Section A: Accelerators, Spectrometers, Detectors and Associated Equipment*, 972:164106, 2020.
- [84] Ziyi Guo, Minfang Yeh, Rui Zhang, De-Wen Cao, Ming Qi, Zhe Wang, and Shaomin Chen. Slow Liquid Scintillator Candidates for MeV-scale Neutrino Experiments. *Astroparticle Physics*, 109, 08 2017.
- [85] M. Yeh, S. Hans, W. Beriguete, R. Rosero, L. Hu, R.L. Hahn, M.V. Diwan, D.E. Jaffe, S.H. Kettell, and L. Littenberg. A new water-based liquid scintillator and potential applications. *Nuclear Instruments and Methods in Physics Research Section A: Accelerators, Spectrometers, Detectors and Associated Equipment*, 660(1):51–56, 2011.
- [86] J. Caravaca, B. J. Land, M. Yeh, and G. D. Orebi Gann. Characterization of water-based liquid scintillator for cherenkov and scintillation separation. *The European Physical Journal C*, 80(9), 2020.
- [87] Tanner Kaptanoglu, Meng Luo, Benjamin Land, Amanda Bacon, and Joshua R. Klein. Spectral photon sorting for large-scale cherenkov and scintillation detectors. *Phys. Rev. D*, 101:072002, Apr 2020.
- [88] J. Paton. Directionality studies with solar neutrinos, sno+ internal document 7063.
- [89] A. Mastbaum N. Barros T. Kaptanoglu, L. Segui and I. Coulter. Optics Overview and Proposed Changes to RAT, SNO+ Internal Document 3461.
- [90] J. Dunger. Topological and Time Based Event Classification for Neutrinoless Double Beta Decay in Liquid Scintillator (2018).
- [91] SNO+ Collaboration. Water UniDoc, SNO+ Internal Document 3461.
- [92] Eugene W. Beier. Isotropy Classifier, SNO+ Internal Document 2835.
- [93] J. Klein.  $\beta\beta$  summary collaboration meeting march 2021, sno+ internal document 6891.
- [94] Decay file:decay chain of thorium.svg search. [https://commons.wikimedia.org/wiki/File:Decay\\_Chain\\_of\\_Thorium.svg](https://commons.wikimedia.org/wiki/File:Decay_Chain_of_Thorium.svg). Accessed: 2021-09-25.
- [95] S. Andringa et al. Current Status and Future Prospects of the SNO+ Experiment. *Advances in High Energy Physics*, 2016:1–21, 2016.
- [96] Decay data search. <http://nucleardata.nuclear.lu.se/toi/>. Accessed: 2021-09-25.

- [97] J. Wang. Bipo background summary collaboration meeting march 2021, sno+ internal document 6851.
- [98] Ziyi Guo, Minfang Yeh, Rui Zhang, De-Wen Cao, Ming Qi, Zhe Wang, and Shaomin Chen. Slow liquid scintillator candidates for MeV-scale neutrino experiments. *Astroparticle Physics*, 109:33–40, 2019.
- [99] F. James. MINUIT Function Minimization and Error Analysis: Reference Manual Version 94.1. 1994.
- [100] G. Bellini et al. Lifetime measurements of  $^{214}\text{Po}$  and  $^{212}\text{Po}$  with the CTF liquid scintillator detector at LNGS. *Eur. Phys. J. A*, 49:92, 2013.
- [101] M. de Bruin. Glossary of terms used in nuclear analytical chemistry (provisional). *Pure and Applied Chemistry*, 54(8):1533–1554, 1982.
- [102] L. Dewayne Cecil and Jaromy R. Green. Radon-222. *Environmental Tracers in Subsurface Hydrology*, pages 175–194, 2000.
- [103] Comprehensive measurement of pp-chain solar neutrinos. *Nature*, 562(7728):505–510, 2018.
- [104] M. Ward. Rn task force walk around, sno+ internal document 6358.
- [105] M. Ward. Radon Task Force Status, SNO+ Internal Document 6530.
- [106] V. Lozza S. Manecki. Rn background detector correlations, SNO+ Internal Document 6644.
- [107] L. Pickard. Using  $^{210}\text{Po}$  to track in-situ ppo concentration, sno+ internal document 6345.
- [108] A. LaTorre. New Measurements for the Timing Spectrum of Electrons and Alphas in LAB+PPO, SNO+ Internal Document 4081.
- [109] T. Kaptanoglu. Scintillator timing measurement, sno+ internal document 5075.
- [110] T. Kaptanoglu. Measurements of 0.5 g/L LAB+PPO, SNO+ Internal Document 5997.
- [111] A. S. Inácio. Optical Calibration of the SNO+ Detector with the Laserball in the Water Phase, SNO+ Internal Document 5862.
- [112] L. Segui. Scintillator Model: comparison between new data and old model and its performance in RAT., SNO+ Internal Document 2774.
- [113] L. Lebanowski. Partial fill Analysis Requirements, SNO+ Internal Document 7064.
- [114] J. Paton. Directionality Studies With Solar Neutrinos, SNO+ Internal Document 7063.
- [115] Xin Qian and Jen-Chieh Peng. Physics with reactor neutrinos. *Reports on Progress in Physics*, 82(3):036201, feb 2019.
- [116] Feng Peng An et al. Improved Measurement of the Reactor Antineutrino Flux and Spectrum at Daya Bay. *Chin. Phys. C*, 41(1):013002, 2017.

- [117] Vedran Brdar, Patrick Huber, and Joachim Kopp. Antineutrino monitoring of spent nuclear fuel. *Phys. Rev. Applied*, 8(5):054050, 2017.
- [118] K. Schreckenbach, G. Colvin, W. Gelletly, and F. Von Feilitzsch. Determination of the antineutrino spectrum from  $^{235}\text{U}$  thermal neutron fission products up to 9.5 mev. *Physics Letters B*, 160(4-5):325–330, 1985.
- [119] A.A. Hahn, K. Schreckenbach, W. Gelletly, F. von Feilitzsch, G. Colvin, and B. Krusche. Antineutrino spectra from  $^{241}\text{Pu}$  and  $^{239}\text{Pu}$  thermal neutron fission products. *Physics Letters B*, 218(3):365–368, 1989.
- [120] P. Vogel, G. K. Schenter, F. M. Mann, and R. E. Schenter. Reactor antineutrino spectra and their application to antineutrino-induced reactions. ii. *Phys. Rev. C*, 24:1543–1553, Oct 1981.
- [121] Patrick Huber. Determination of antineutrino spectra from nuclear reactors. *Physical Review C*, 84(2), 2011.
- [122] Th. A. Mueller, D. Lhuillier, M. Fallot, A. Letourneau, S. Cormon, M. Fechner, L. Giot, T. Lasserre, J. Martino, G. Mention, , et al. Improved predictions of reactor antineutrino spectraimproved predictions of reactor antineutrino spectra. *Physical Review C*, 83(5), 2011.
- [123] Patrick Huber and Thomas Schwetz. Precision spectroscopy with reactor antineutrinos. *Phys. Rev. D*, 70:053011, Sep 2004.
- [124] N. Haag, A. Gütlein, M. Hofmann, L. Oberauer, W. Potzel, K. Schreckenbach, and F.M. Wagner. Experimental Determination of the Antineutrino Spectrum of the Fission Products of  $^{238}\text{U}$ . *Physical Review Letters*, 112(12), 2014.
- [125] A. Zummo. Reactor Isotope Variation, SNO+ Internal Document 7145.
- [126] X. B. Ma, W. L. Zhong, L. Z. Wang, Y. X. Chen, and J. Cao. Improved calculation of the energy release in neutron-induced fission. *Physical Review C*, 88(1), 2013.
- [127] Operating experience with nuclear power stations in member states. <https://www.iaea.org/publications/15004/operating-experience-with-nuclear-power-stations-in-member-states>. Accessed: 2021-09-25.
- [128] Pris home. <https://pris.iaea.org/pris/>. Accessed: 2021-09-25.
- [129] C. Mills. Reactor Flux Scaling , SNO+ Internal Document 6558.
- [130] 2021: Summary tables. [https://pdg.lbl.gov/2021/tables/contents\\_tables.html](https://pdg.lbl.gov/2021/tables/contents_tables.html). Accessed: 2021-09-25.
- [131] P. Vogel and John F. Beacom. Angular distribution of neutron inverse beta decay, anti-neutrino(e) + p → e+ + n. *Phys. Rev. D*, 60:053003, 1999.

- [132] A. Wright. Water updates, sno+ internal document 7074.
- [133] T. Kaptanoglu. Reactor Antineutrinos in the SNO+ Water Phase and Detector RD for Large-Scale Neutrino Detectors (2020).
- [134] Azusa Gando. Results from KamLAND-Zen. In *4th International Conference Current Problems in Nuclear Physics and Atomic Energy*, 2012.
- [135] F. P. et al An. New measurement of  $\theta_{13}$  via neutron capture on hydrogen at Daya Bay. *Phys. Rev. D*, 93:072011, Apr 2016.
- [136] Ondrej Sramek, Bedrich Roskovec, Scott A. Wipperfurth, Yufei Xi, and William F. McDonough. Revealing the Earth's mantle from the tallest mountains using the Jinping Neutrino Experiment. *Scientific Reports*, 6(1), 2016.
- [137] O. Smirnov. Experimental aspects of geoneutrino detection: Status and perspectives. *Progress in Particle and Nuclear Physics*, 109:103712, 2019.
- [138] G. Fiorentini, G. L. Fogli, E. Lisi, F. Mantovani, and A. M. Rotunno. Mantle geoneutrinos in KamLAND and Borexino. *Physical Review D*, 86(3), 2012.
- [139] Yu Huang, Viacheslav Chubakov, Fabio Mantovani, Roberta L. Rudnick, and William F. McDonough. A reference Earth model for the heat-producing elements and associated geoneutrino flux. *Geochemistry, Geophysics, Geosystems*, 14(6):2003–2029, 2013.
- [140] Yu Huang, Virginia Strati, Fabio Mantovani, Steven B. Shirey, and William F. McDonough. Regional study of the Archean to Proterozoic crust at the Sudbury Neutrino Observatory (SNO ), Ontario: Predicting the geoneutrino flux. *Geochemistry, Geophysics, Geosystems*, 15(10):3925–3944, 2014.
- [141] I. Semenec. SNO+ Geoneutrino Generator, SNO+ Internal Document 5512.
- [142] Geoneutrino spectrum and luminosity. <https://www.awa.tohoku.ac.jp/~sanshiro/research/geoneutrino/spectrum/>.
- [143] Particle Data Group. Particle Data Group - 2020 Archive. <https://pdg.lbl.gov/2020/>.
- [144] Adam M. Dziewonski and Don L. Anderson. Preliminary reference earth model. *Physics of the Earth and Planetary Interiors*, 25(4):297–356, 1981.
- [145] C Giunti, C.W Kim, and M Monteno. Atmospheric neutrino oscillations with three neutrinos and a mass hierarchy. *Nuclear Physics B*, 521(1):3–36, 1998.
- [146] Enomoto Sanshiro. Neutrino Geophysics and Observation of Geo-Neutrinos at KamLAND. Thesis, 2005.
- [147] David W. McKee, Jerome K. Busenitz, and Igor Ostrovskiy. A  $^{13}\text{C}^{16}\text{O}$  calibration source for KamLAND. *Nuclear Instruments and Methods in Physics Research Section A: Accelerators, Spectrometers, Detectors and Associated Equipment*, 587(2-3):272–276, 2008.

- [148] S. Ricetto. partial fill 365t re-proc+MC RAT6.18.9 - 210Po , SNO+ Internal Document 6794.
- [149] R. B. Walton, J. D. Clement, and F. Boreli. Interaction of Neutrons with Oxygen and a Study of the C<sup>13</sup>( $\alpha$ , n)O<sup>16</sup> Reaction. *Phys. Rev.*, 107:1065–1075, Aug 1957.
- [150] T. Murata et al. Evaluation of the ( $\alpha$ , xn) Reaction Data for JENDL/AN-2005. <https://wwwndc.jaea.go.jp/ftpnd/jendl/jendl-an-2005.html>, 2006.
- [151] K. K. Sekharan, A. S. Divatia, M. K. Mehta, S. S. Kerekatte, and K. B. Nambiar. <sup>13</sup>C( $\alpha$ , n)<sup>16</sup>O Reaction Cross Section between 1.95 and 5.57 MeV. *Phys. Rev.*, 156:1187–1190, Apr 1967.
- [152] J. K. Bair and F. X. Haas. Total Neutron Yield from the Reactions C-13 (alpha , n) O-16 and O-17, O-18 (alpha , n) Ne-20, Ne-21. *Phys. Rev. C*, 7:1356–1364, 1973.
- [153] S. Harissopoulos, H. W. Becker, J. W. Hammer, A. Lagoyannis, C. Rolfs, and F. Strieder. Cross section of the C13( $\alpha$ ,n)O16 reaction: A background for the measurement of geo-neutrinos. *Physical Review C*, 72(6), 2005.
- [154] Janis web  $\alpha$ -induced cross sections. <https://www.oecd-nea.org/janisweb/>. Accessed: 2021-09-17.
- [155] Interactions of ions with matter. <http://www.srim.org/>. Accessed: 2021-09-25.
- [156] W. A. Peters. Comment on “Cross section of the <sup>13</sup>C( $\alpha$ , n)<sup>16</sup>O reaction: A background for the measurement of geo-neutrinos”. *Phys. Rev. C*, 96:029801, Aug 2017.
- [157] Jie Zhao, Ze-Yuan Yu, Jiang-Lai Liu, Xiao-Bo Li, Fei-Hong Zhang, and Dong-Mei Xia. 13 C( $\alpha$ ,n) 16 O background in a liquid scintillator based neutrino experiment. *Chinese Physics C*, 38(11):116201, 2014.
- [158] O. Chkvoret. Leaching Studies , SNO+ Internal Document 2384.
- [159] M. Cox. AlphaN Related Analysis Antinu Workshop Update , SNO+ Internal Document 7040.
- [160] C. Andreopoulos, A. Bell, D. Bhattacharya, F. Cavanna, J. Dobson, S. Dytman, H. Gallagher, P. Guzowski, R. Hatcher, P. Kehayas, , et al. The genie neutrino monte carlo generator. *Nuclear Instruments and Methods in Physics Research Section A: Accelerators, Spectrometers, Detectors and Associated Equipment*, 614(1):87–104, 2010.
- [161] C. Lin. Atmospheric neutrinos in partial fill, SNO+ Internal Document 6958.
- [162] Antoine Kouchner. Next-generation atmospheric neutrino experiments. *Physics of the Dark Universe*, 4:60–74, 2014.
- [163] B. Liggins. Cosmic muon-induced neutrons in the SNO+ water phase, PhD Thesis, Queen Mary University of London (2020).
- [164] S. Abe et al. Production of Radioactive Isotopes through Cosmic Muon Spallation in KamLAND. *Phys. Rev. C*, 81:025807, 2010.

- [165] M. Agostini et al. Comprehensive geoneutrino analysis with Borexino. *Phys. Rev. D*, 101:012009, Jan 2020.
- [166] T. Bezerra. Updates on IBD Selection: mu -Tagging (VI), SNO+ Internal Document 7124.
- [167] William H. Press and William T. Vetterling. *Numerical recipes*. Cambridge Univ. Press, 1999.
- [168] Glen Cowan. *Statistical data analysis*. Clarendon Press, 1998.
- [169] D.A.S. Fraser N. Reid. Likelihood inference in the presence of nuisance parameters. *arXiv: Physics - Data Analysis, Statistics and Probability*, 2003.
- [170] Royal Statistical Society. *Journal of the Royal Statistical Society. Series B, (Methodological)*. Royal Statistical Society, London, 1959.
- [171] V. Lozza. Partial Fill background status , SNO+ Internal Document 6533.
- [172] Steven D. Biller and Scott M. Oser. Another look at confidence intervals: Proposal for a more relevant and transparent approach. *Nuclear Instruments and Methods in Physics Research Section A: Accelerators, Spectrometers, Detectors and Associated Equipment*, 774:103–119, 2015.
- [173] S. Riccetto. Full Fill 210Po , SNO+ Internal Document 7052.
- [174] H.M. O’Keeffe, E. O’Sullivan, and M.C. Chen. Scintillation decay time and pulse shape discrimination in oxygenated and deoxygenated solutions of linear alkylbenzene for the SNO experiment. *Nuclear Instruments and Methods in Physics Research Section A: Accelerators, Spectrometers, Detectors and Associated Equipment*, 640(1):119–122, 2011.
- [175] C. Mills. Alpha-n / IBD classifier , SNO+ Internal Document 6894.
- [176] T. Kaptanoglu. Scintillator Timing Measurement, SNO+ Internal Document 5075.
- [177] M. G. Aartsen et al. IceCube-Gen2: the window to the extreme Universe. *J. Phys. G*, 48(6):060501, 2021.
- [178] Zelimir Djurcic et al. JUNO Conceptual Design Report. *arXiv: Instrumentation and Detectors*, pages 1–300, 2015.
- [179] Xiang-Cui Lei et al. Evaluation of new large area PMT with high quantum efficiency. *Chinese Physics C*, 40(2):026002, 2016.
- [180] Refractive index of C<sub>2</sub>H<sub>4</sub>(OH)2 (Ethylene Glycol). [https://refractiveindex.info/?shelf=organic&book=ethylene\\_glycol&page=El-Kashef](https://refractiveindex.info/?shelf=organic&book=ethylene_glycol&page=El-Kashef).
- [181] O. Yu. Smirnov et al. Measurement of neutrino flux from the primary proton–proton fusion process in the Sun with Borexino detector. *Phys. Part. Nucl.*, 47(6):995–1002, 2016.

- [182] H. Back, M. Balata, A. Bari, T. Beau, A. Bellefon, G.B. Bellini, Jay Benziger, S. Bonetti, Augusto Brigatti, C. Buck, B. Caccianiga, Laura Cadonati, Frank Calaprice, G. Cecchet, M. Chen, A. Credico, O. Dadoun, D. D'Angelo, H. Haas, and G. Zuzel. Current status of the BOREXINO experiment. *Nuclear Physics B Proceedings Supplements*, 143:21–24, 06 2005.
- [183] Fumihiko Suekane, Toshiyuki Iwamoto, Hiroshi Ogawa, Osamu Tajima, and Hideki Watanabe. An overview of the KamLAND 1-kiloton liquid scintillator. *arXiv preprint physics/0404071*, 2004.
- [184] Jason A. Detwiler. Measurement of neutrino oscillation with KamLAND. Thesis, 2005.
- [185] Miao He and On behalf of the Atlas Collaboration. Double calorimetry system in JUNO. *Radiation Detection Technology and Methods*, 1:1–3, 2017.
- [186] Ari Rabl. Solar concentrators with maximal concentration for cylindrical absorbers. *Applied Optics*, 15(7):1871, 1976.
- [187] Joseph Perl. a Generic Interface Definition for HEP Event Display Representables. <https://www.slac.stanford.edu/~perl/heprep/index.html>.
- [188] M. Aker et al. The design, construction, and commissioning of the katrin experiment, 2021.
- [189] Benjamin Monreal. The Project 8 Radiofrequency Tritium Neutrino Experiment. *Physics Procedia*, 61:274–277, 2015. 13th International Conference on Topics in Astroparticle and Underground Physics, TAUP 2013.
- [190] K. Blaum et al. The Electron Capture  $^{163}\text{Ho}$  Experiment ECHo, 2013.
- [191] V. Yu. Kozlov et al. Physics and present status of the WITCH experiment. *Phys. Atom. Nucl.*, 67:1112–1118, 2004.
- [192] M. Aker et al. First direct neutrino-mass measurement with sub-eV sensitivity. 5 2021.
- [193] Julien Lesgourgues and Sergio Pastor. Neutrino mass from cosmology. *Advances in High Energy Physics*, 2012:1–34, 2012.
- [194] 2020: Neutrinos in Cosmology. <https://pdg.lbl.gov/2020/reviews/rpp2020-rev-neutrinos-in-cosmology.pdf>. Accessed: 2021-09-25.
- [195] N. Aghanim et al. Planck 2018 results. VI. Cosmological parameters. *Astron. Astrophys.*, 641:A6, 2020. [Erratum: Astron.Astrophys. 652, C4 (2021)].
- [196] Katrin sets first limit on neutrino mass. <https://cerncourier.com/a/katrin-sets-first-limit-on-neutrino-mass/>. Accessed: 2021-09-29.
- [197] H. Weyl. Gravitation and the electron. *Proceedings of the National Academy of Sciences*, 15(4):323–334, 1929.
- [198] W. Pauli. On the Earlier and more recent history of the neutrino. *Camb. Monogr. Part. Phys. Nucl. Phys. Cosmol.*, 14:1–22, 2000.

- [199] Ettore Majorana and Luciano Maiani. A symmetric theory of electrons and positrons. *Ettore Majorana Scientific Papers*, pages 201–233.
- [200] Yi Cai, Tao Han, Tong Li, and Richard Ruiz. Lepton number violation: Seesaw models and their collider tests. *Frontiers in Physics*, 6:40, 2018.
- [201] Robert H. Bernstein. The Mu2e Experiment. *Frontiers in Physics*, 7:1, 2019.
- [202] Elucidating the Fundamental Nature of Neutrinos with Double Beta Decay. [https://www.physik.uzh.ch/dam/jcr:407f9747-df4b-4158-a0ae-f5043ea7ba5b/baudis\\_higgs2020.pdf](https://www.physik.uzh.ch/dam/jcr:407f9747-df4b-4158-a0ae-f5043ea7ba5b/baudis_higgs2020.pdf).
- [203] J. Schechter and J. W. F. Valle. Neutrinoless Double beta Decay in SU(2) x U(1) Theories. *Phys. Rev. D*, 25:2951, 1982.
- [204] A. Gando et al. Search for Majorana Neutrinos Near the Inverted Mass Hierarchy Region with KamLAND-Zen. *Phys. Rev. Lett.*, 117:082503, Aug 2016.
- [205] Jonathan Engel and Javier Menéndez. Status and future of nuclear matrix elements for neutrinoless double-beta decay: a review. *Reports on Progress in Physics*, 80(4):046301, mar 2017.
- [206] Steven D. Biller. Combined constraints on majorana masses from neutrinoless double beta decay experiments. *Phys. Rev. D*, 104:012002, Jul 2021.
- [207] Laura Cardani. Neutrinoless double beta decay overview. *SciPost Physics Proceedings*, (1), 2019.
- [208] Andrea Giuliani and Alfredo Poves. Neutrinoless double-beta decay. *Advances in High Energy Physics*, 2012:1–38, 2012.
- [209] A. Li. Livetime Update, SNO+ Internal Document 6261.
- [210] H. O’Keefe V. Lozza, M. Chen. Expected radioactive backgrounds in SNO+, SNO+ Internal Document 507.
- [211] M. Luo and L. Lebanowski. External Energy Calibration with 16N for Water Phase, SNO+ Internal Document 6975.
- [212] P. Ravi. External K40 Background, SNO+ Internal Document 6858.